CO_2 Capture by Aqueous Absorption

Summary of First Quarterly Progress Reports 2012

by Gary T. Rochelle

Supported by the Luminant Carbon Management Program
and the
Industrial Associates Program for CO_2 Capture by Aqueous Absorption

Department of Chemical Engineering
The University of Texas at Austin

April 30, 2012

Introduction

This research program is focused on the technical obstacles to the deployment of CO_2 capture and sequestration from flue gas by alkanolamine absorption/stripping and on integrating the design of the capture process with the aquifer storage/enhanced oil recovery process. The objective is to develop and demonstrate evolutionary improvements to monoethanolamine (MEA) absorption/stripping for CO_2 capture from gas-fired and coal-fired flue gas. The Luminant Carbon Management Program and the Industrial Associates Program for CO_2 Capture by Aqueous Absorption support 17 graduate students and one visiting scholar. Most of these students have prepared detailed quarterly progress reports for the period January 1, 2012 to March 30, 2012.

Conclusions

Thermodynamics and Rates

An updated VLE model shows the capacity of the PRC 8 m PZ Fall 2011 pilot plant sample is 18% lower and the calculated heat of absorption for the pilot plant sample 6% higher than 8 m PZ. However, the difference between the CO_2 solubility for the pilot plant sample and laboratory grade 8 m PZ is small, especially at high temperature (above 100 °C).

The high temperature VLE measurements for 8 m PZ with 100 mM Inh A are systematically lower than the results for the pilot plant sample, but the difference is very small and likely within the error range of the experimental method.

High temperature P_{CO2}* measurements for 6 m PZ/2 m BAE are used to update the semi-empirical VLE model to give a solvent capacity of 0.69 mol/kg, which is 13% less than 8 m PZ. Solvent heat of absorption calculated by the model is 68 kJ/mol, which is 6% higher than 8 m PZ.

The group contribution model for amine Henry's constant predicts in order of increasing hydrophilicity, Ocy < O < OH < NH < N < Ncy < NH2. In order of increasing hydrophobicity, Ccy < CH2 (or CH) < CH3-(N) < CH3-(C) < CH3-(Ncy).

6 m PZ/4 m AMP is not a desirable blend owing to its narrow operating window.

Even though 6.5 m PZ/3 m AMP has a similar operating window to 8 m PZ, the viscosity, nearly twice that of 8 m PZ, limits its application.

For aqueous 5 m PZ/2.3 m AMP blend, solids are precipitated when the loading is lower than 0.3, but no solids are observed when CO_2 is kept loaded into this blend until the loading reaches 0.5.

The performance of aqueous 5 m PZ/2.3 m AMP is similar to 8 m PZ in terms of viscosity, heat of absorption, lean and rich loading departure. Due to lower total alkalinity, the CO_2 capacity is lower.

The mass transfer rates in 5 m PZ/2.3 m AMP are higher than in 8 m PZ when the loading is rich.

Both AMP and PZ degrade faster in blend than in a single system, and the main degradation product identified is 1,1-dimethyl-2-piperazin-1-ethylamine.

The high temperature VLE data for 2 m PZ/4 m AMP indicate that this blend has 0.89 mol/kg of CO_2 capacity and 74 kJ/mol of CO_2 heat of absorption. These properties are better than 8 m PZ. Another advantage of this blend is that it does not have a solid solubility problem.

The thermodynamic models for AMP/H_2O and AMP/CO_2/H_2O have been built in Aspen Plus® using VLE, heat capacity, volatility, and CO_2 solubility data. The pKa value of AMP was fitted by manually adjusting the standard free energy of formation and standard enthalpy of formation at infinite dilution of $AMPH^+$. The AMP/H_2O model represents the experimental data well, while the AMP/CO_2/H_2O model needs further testing by heat capacity data.

Modeling

The end effects in the air-water column provide total gas film transfer units of 0.5 in the top and 2.2 to 2.3 in the bottom.

With MP250Y, k_G varies with u_G^0.61.

Coal-based capacity will often supply marginal generation when gas prices are low, CO_2 prices are moderate, and net electricity load (demand, or load, minus wind production) exceeds 40 GW.

A typical design specification of a total LMTD of 5 °C is necessary to optimize a network of cross exchangers. An equivalent work of 29.2 kJ/mol CO_2 was obtained for a configuration of split heat exchangers with single-stage flash and warm rich bypass. For smaller values of bypass, it is optimum not to split the exchanger and to use only one exchanger.

An adiabatic LP column with HP flash gives an optimum equivalent work of 29 kJ/mol CO_2 with specification of 5 °C LMTD on all cross exchangers.

Preliminary results for amine scrubbing for natural gas usage indicate energy performance in the range of 36–39 kJ/mol CO_2.

Preliminary absorber design for gas combustion capture demonstrated the benefit of gas cooling in the column but is limited by a lean end pinch corresponding to a temperature bulge at the top of the column.

Optimized absorber design for economic analysis confirmed the potential benefit of low temperature absorber design (30°C) relative to standard design conditions (40°C) by reducing packing volume by as much as 25% and absolute solvent circulation rate by as much as 10% for holding all other design conditions constant.

Solvent Management

The MNPZ formation rate constant for 8 m PZ at 120 °C and a CO_2 loading of 0.3 is approximately $4*10^{-4}$ s^{-1}. $PZCOO^-$ catalyzes MNPZ formation but not MNPZ decomposition.

The MNPZ decomposition rate constant (s^{-1}) follows Arrhenius temperature dependence.

$$k_2(T) = 3.7 * 10^{-6} e^{\frac{92}{R}\left(\frac{1}{393}-\frac{1}{T}\right)}$$

The MNPZ steady state concentration should be about 0.8 mM with a sump operating at 150 °C, a sump residence time of 8 minutes, and a flue gas NO_2 concentration of 1 ppm. It takes 5 days to reach 90% of steady state MNPZ concentration at 150 °C and a total residence time 5 times longer than the sump residence time.

At 150 °C and 0.3 CO_2 loading, MEA reacts in 600 hours with PZ to produce aminoethylpiperazine (AEP) and diaminoethylpiperazine with a yield of 53 to 68%. No other significant products appeared in the available analytical methods.

CO_2 transfer to aerosols is liquid-film controlled. Particles less than 0.1 μm are in equilibrium to CO_2 for any starting PZ concentration.

Aerosol temperature will be approximately the wet bulb temperature of the gas.

5 m PZ/2 m AEP is thermally stable up to 150 °C. The thermal degradation were NH_4^+ > formate > PEP > NPZ, AEAEPZ Urea, an unknown product (retention time of 17.7), penta-amine, HEP > DMPZ, AEAEPZ, DAEP, and EPZ.

At 175 °C, the degradation of both PZ and AEP in this blend showed a fast phase in the first week, followed by a slow process in the following 4 weeks. Reversible SN_2 reactions may account for the fast degradation process in first week, and elimination reactions of AEP and the reaction between PZ and degradation products (such as AEAEPZ) contribute to the further slow degradation of PZ/AEP in the following 4 weeks.

Both the PRC solvent and PP2 solvent had degraded significantly by the end of their respective campaigns. A greater amount of degradation products were observed in Pilot Plant 2. Formate, N-formylpiperazine, and ethylenediamine were the most prevalent degradation products measured.

In Pilot Plant 2, oxidative degradation products such as amides and carboxylic acids did not begin to accumulate in significant amounts until approximately halfway through the campaign. This strongly correlated with the accumulation of dissolved metals from corrosion, indicating that these metal ions help to catalyze the radical mechanism believed to be responsible for oxidative degradation. The PRC solvent had a much lower concentration of dissolved metals, and also had far less oxidative degradation products, even though the synthetic flue gas for contained approximately 18 kPa O_2, while the PP2 real flue gas was on the order of 5 kPa.

N-formlypiperazine was the only major formamide present in both pilot plant solvents, accounting for about 50% of the total formate present. The heat-stable salt form of formate accounted for the remaining formate present in the solvents.

The thermal degradation products ethylenediamine (EDA), N-(hydroxyethyl)piperazine (HEP), and N-(aminoethyl)piperazine (AEP) all accumulated at a relatively constant rate early in the PP2 campaign. HEP and other unidentified thermal degradation products continued to accumulate at this rate for the entire campaign. However, EDA and AEP in the solvent decreased over time later in the campaign, indicating that both are intermediate degradation products that will degrade further.

Accumulation of nitrate and sulfate in the PP2 solvent was most likely the result of absorption of trace levels (ppm) of SO_x and NO_x from the flue gas.

N-nitrosopiperazine (MNPZ) accumulation in PP2 solvent agreed with the model developed by Fine, reaching a steady state due to the balancing effects of PZ reacting with nitrite absorbed from the flue gas and thermal degradation of MNPZ in the stripper.

Laboratory Safety

All experimental work is performed under the Laboratory Safety Guidelines (http://www.utexas.edu/safety/ehs/lab/manual/) of the University of Texas. The laboratory personnel have all completed four safety training courses certified by the University: general lab safety, hazardous materials, fire extinguisher, and site specific safety. Routine personal safety protection includes safety glasses, lab coats, gloves, long pants, and closed toe shoes. Goggles are used for specific hazardous operations. Food and drink are prohibited in the laboratories. Safety inspections of all labs are conducted by a different student every month. The University Safety Office conducts random safety evaluations of each lab, usually about twice a year.

Most of the experimental work with amines is conducted in exhaust hoods. We have recently added ventilated gas cabinets for cylinders of nitrogen mixed with ammonia, NO, NO_2, and SO_2. All work on undiluted nitrosamine samples is contained in one laboratory that has no desks assigned to students for continuous occupancy. We have developed a standard operating procedure to be used in an experiment with closed cylinders of amine solution heated to 175 ^oC in convection ovens. These experiments are also contained in the nitrosamines lab.

Dr. Rochelle is the Chairman of the Safety Committee of the Department of Chemical Engineering. The committee meets once a month to review safety issues, safety experiences, and address initiatives for improving safety.

1. CO_2 Solubility in Aqueous Amines p. 15

by Le Li

CO_2 solubility at high temperature was measured for three solvents: PRC pilot plant 8 m PZ Fall 2011 sample, 8 m PZ with 100 mM Inhibitor A (Inh A), and the blend of 6 m PZ/2 m bis(aminoethyl)ether (BAE). High temperature P_{CO2}* measurements are necessary to make accurate predictions in solvent capacity and heat of CO_2 absorption. A total pressure equilibrium reactor is used to measure P_{CO2}* at 100, 110, 120, 130, 140, 150, 160 °C. For the pilot plant sample, 18 P_{CO2}* data points was measured at various CO_2 loading. The new data points are used together with low temperature measurements and an updated semi-empirical model is calculated. For the pilot plant sample, the updated model give a capacity of 0.65 mol/kg, which is 18% lower than 8 m PZ, and heat of absorption of 68 kJ/mol, which is 6% higher than 8 m PZ. High temperature P_{CO2}* measurements for 8 m PZ Inh A compare closely with results for the pilot plant sample. The effect of Inh A (at the concentration typical in a CO_2 capture process) on solvent VLE is currently inconclusive, though it is expected to be insignificant. A total of 21 high temperature P_{CO2}* data points were collected for 6 m PZ/2 m BAE. The VLE model was regressed using 1) total pressure data, 2) WWC data at low temperatures, and 3) both data sets. The three models differ in mathematical form and generate different values for solvent capacity and heat of absorption. The third model is expected to have the best overall predictability since it uses all of the available data and the regression resulted in a high R^2 value of 0.994. The predicted solvent capacity for the blend is 0.69 mol/kg, which is 13% less than 8 m PZ. The heat of absorption calculated by the model is 68 kJ/mol, which is 6% higher than 8 m PZ.

2. Aqueous Amine Volatility in CO_2 Capture p. 29

by Thu Nguyen

Aqueous amine volatility in binary amine-water systems is crucial for: (1) proper design of water wash units in post-combustion CO_2 capture process and (2) accurate representation and modeling of the intrinsic interactions between amine and water. In this work, the volatilities of 19 amines considered to be viable for CO_2 capture, including monoethanolamine (MEA), piperazine (PZ), and n-methyldiethanolamine (MDEA), were measured for dilute amine concentrations from 0.1–1.05 m amine in water from 40–70 ˚C and 1 bar as these conditions represent the operating conditions of the CO_2 capture absorber. In using the volatility data for all the amines from this work along with 16 alkylamines from the literature, a group contribution model was developed to correlate functional group behavior to the aqueous amine Henry's constant at 40 ˚C. The Henry's constant is used as an indicator of the intrinsic amine volatility. The R^2 of this group contribution model is ~0.95. The model is able to represent the Henry's constants of the amines within ±25% within ±25% of the experimental values. Two of the unique features of this model are(1) distinction between cyclic and straight chained amines; (2) distinction between the different types of methyl groups based on the neighboring groups attached to them. In order to represent the Henry's constants of the amines between 25 ˚C and 70 ˚C, and to extrapolate outside this range, another group contribution model was developed to estimate the amine heats of solution which are then used to predict the H constants at the temperatures of interest given the values predicted at 40 ˚C. Overall, the predicted H constants are found to be well within an order of magnitude of the experimental H constants.

3. Characterization of AMP/PZ p. 45

by Han Li

Piperazine (PZ) has been investigated as a promising solvent for carbon dioxide capture. In this study, 2-amino-2-methyl-1-propanol (AMP) was chosen as an additive to PZ to increase CO_2 capacity and CO_2 heat of absorption and to avoid solids precipitation. Experimental results on solid solubility, CO_2 solubility, mass transfer rate, viscosity, volatility, heat capacity, NMR speciation and thermal degradation are given for 5 m (mol/kg H_2O) PZ/2.3 m AMP. 2 m PZ/4 m AMP was also investigated.

The goal of this study is to construct a thermodynamic model in Aspen Plus® to predict the properties of $PZ/AMP/CO_2/H_2O$ over a wide range of conditions and to develop a kinetic model to predict CO_2 mass transfer rates. The acquired thermodynamic data for 5 m PZ/2.3 m AMP and 2 m PZ/4 m AMP will be regressed with other data from the literature. The resulting models will be used in absorption/stripping process modeling. In this quarter, the thermodynamic model for AMP/H_2O, $AMP/AMPH^+$, and $AMP/CO_2/H_2O$ has been finished.

Piperazine (PZ) has been investigated as a promising solvent for carbon dioxide capture. In this study, 2-amino-2-methyl-1-propanol (AMP) was chosen as an additive to PZ to increase CO_2 capacity and CO_2 heat of absorption and to avoid solids precipitation. Experimental results on solid solubility, CO_2 solubility, mass transfer rate, viscosity, volatility, heat capacity, NMR

speciation and thermal degradation are given for 5 m (mol/kg H_2O) PZ/2.3 m AMP. 2 m PZ/4 m AMP was also investigated.

The goal of this study is to construct a thermodynamic model in Aspen Plus® to predict the properties of PZ/AMP/CO_2/H_2O over a wide range of conditions and to develop a kinetic model to predict CO_2 mass transfer rates. The acquired thermodynamic data for 5 m PZ/2.3 m AMP and 2 m PZ/4 m AMP will be regressed with other data from the literature. The resulting models will be used in absorption/stripping process modeling. In this quarter, the thermodynamic model for AMP/H_2O, AMP/$AMPH^+$, and AMP/CO_2/H_2O has been finished.

4. Modeling Amine Thermodynamics and Hydraulics p. 86

by Peter Frailie

The goal of this study is to evaluate the performance of an absorber/stripper operation that utilizes MDEA/PZ. Before analyzing unit operations and process configurations, thermodynamic, hydraulic, and kinetic properties for the blended amine must be satisfactorily regressed in Aspen Plus®. The approach used in this study is first to construct separate MDEA and PZ models that can later be reconciled via cross parameters to model accurately the MDEA/PZ blended amine. This study is currently in the process of updating Tthe MDEA/PZ model based on thermodynamic, hydraulic, and kinetic data is currently being updated. Separate MDEA and PZ models have been finished that accurately predict VLE, heat capacity, unloaded amine volatility, CO2 activity coefficient, and CO2 absorption rate over operationally significant temperature, amine concentration, and loading ranges. All available thermodynamic and hydraulic data for 7 m MDEA/2 m PZ and 5 m MDEA/5 m PZ have also been regressed. CO2 absorption rate data for 8 m PZ, 7 m MDEA/2 m PZ, and 5 m MDEA/5 m PZ are currently being regressed. The goal for the next quarter is to construct and optimize an absorption/stripping/compression operation in Aspen Plus® for both 7 m MDEA/2 m PZ and 5 m MDEA/5 m PZ.

5. Pilot Plant Testing of Advanced Process Concepts using Concentrated Piperazine p. 101

by Dr. Eric Chen

In this period, the final report for the second pilot plant campaign with the modified high temperature two-stage flash skid was completed. The campaign report was issued to the C2P3 sponsors and contains the details of the modifications made to the skid and pilot plant, the absorber and flash skid configuration, the startup, operation, and shutdown procedure, pilot plant and analytical data, and interpreted results.

A work plan was developed in preparation for the 2012 pilot plant campaign. The six objectives of the plan are: aerosol characterization and mitigation from the absorber column, evaluation of high temperature oxidation from oxygen entrainment in the absorber bottoms, addressing nitrosamine formation in the piperazine (PZ) solvent from oxidation and reaction with NO_x, development of a pilot-scale PZ reclaiming process, upgrade of steam heater capacity and installation of low temperature flash tank for new process configuration that minimizes oxidation and demonstrates thermal decomposition of nitrosamine, and development of process control strategy for pilot plant operation with minimized solvent inventory.

Pilot plant data validation for the October 2011 HTPZ-2 campaign showed that FT-200, the absorber bottom outlet flow measurement, had large standard deviations. FT-201, the skid return flow meter, may also have higher than expected standard deviations relative to the stated manufacturer's specifications. The deviations of FT-200 were also observed in an overall pilot plant material balance analysis, which compared the combined flow rates of the skid return, condensate, and CO_2 recycle mass flow rates as measured by the online instruments. Discussions with the Micro Motion sales representative revealed that the temperature measurement in the Coriolis flow meter do not directly contact the process fluid and should be carefully used.

Heat exchanger models were developed using Aspen Exchanger Design and Rating (EDR) for the high pressure cross-exchanger (H-520), low pressure cross-exchanger (H-113), high pressure steam heater (H-525), and low pressure steam heater (H-535). Also, Aspen Plus® models for the six control valves on the flash skid have been developed to help with data validation and provide better understanding of the process skid in terms of operating limitations and future equipment modifications.

Modifications to the CSIRO pilot plant are slowly proceeding under the assumption that the ANLEC agreement will be signed in the near future. Modifications are scheduled to be completed in mid-April and startup of the unit in late April to early May. The CSIRO pilot unit will evaluate concentrated PZ with high temperature simple stripping. The University of Texas will provide technical support and consultation.

A proposal has been submitted to DOE to revise the scope of work by URS with UT input. The new proposal will redirect funding originally allocated for the flash skid testing at CSIRO to a campaign with the flash skid at SRP in the fall of 2012. The proposal also forgoes fabrication of the 0.5 MW flash skid for the NCCC testing and proposes use of the existing high pressure simple stripper. The focus of the NCCC testing will be on aerosol emissions, nitrosamines, and reclaiming.

6. Pilot Plant Validation and Carbon Capture from Natural Gas Applications p. 103

by Darshan Sachde

During the first quarter of 2012, pilot plant data analysis continued as part of absorber model development and validation. The October 2011 campaign at J.J. Pickle Research Campus (PRC) was the focus of the recent work and included error quantification in mass balance (CO_2 and PZ) and CO_2 removal calculations. The CO_2 mass balance closed for 7 of 10 pilot plant runs within 1 standard deviation, and the PZ mass balance closed for 5 of 10 runs. Issues highlighted in the analysis included confirmation of reduced variation and improved accuracy in manual titration compared to auto titration, existence of potential bias in PZ auto titration, and offset in rich loading flow measurements. Finally, gas side CO_2 mass balance revealed statistically significant (at 95% confidence interval) improvement in CO_2 removal due to spray nozzle implementation in 2 of 3 runs.

The absorber model that was validated in Q4 2011 was used to develop design cases for natural gas combustion applications. A preliminary absorber design was developed for CO_2 capture from the flue gas of a combined cycle gas turbine. The novel absorber configuration includes lean gas cooling in the absorber column (no direct contact cooler) via rich amine recycle. Initial results for 8 m PZ with a lean loading of 0.27 mols CO_2/mols alkalinity, a 10:1 recycle rate in the 1 m bottom packed section, and a L/G of 1.65 have achieved 84% CO_2 removal with 15 m of total packed height (2250 m^3 packed volume). However, driving force analysis revealed a lean end pinch corresponding to a temperature bulge in the column. Methods to address these performance issues are discussed in detail in this report.

Finally, preliminary absorber designs for economic analysis of CO_2 capture from coal-fired combustion presented in the fourth quarter of 2011were optimized and finalized. The designs included cases at lean loadings 0.27 and 0.30 mols CO_2/mols alkalinity and at absorber operating temperatures of 30 °C and 40 °C. The low temperature absorber designs reduced packing volume by as much as 25% and absolute solvent circulation rates by as much as 10% relative to the analogous design at 40 °C. The report includes detailed design results for all cases.

7. Measurement of Packing Effective Area and Mass Transfer Coefficients p. 126

by Chao Wang

In this quarter, significant effort has been made troubleshooting the outlet SO_2 sampling system. The mass transfer characteristics of gas-film control systems and their physical properties make the solute gas very easy to remove. The high mass transfer efficiency of this system makes the outlet SO_2 concentration very low (ppb levels) after counter-contacting the solvent in just a few feet of packing. Thus, it is difficult to obtain a reliable outlet SO2 reading.

Several methods have been tried to obtain a reasonable SO2 outlet reading. To eliminate the water condensation in the outlet sample line, a Micro-GASSTM Gas Analysis Sampling System from PERMA PURE LLC has been installed based on recommendations of SO_2 analytical experts. The sample conditioner uses the hot exhaust gas from the analyzer as the drying gas. The sample gas and purge gas is contacted indirectly in a Nafion Membrane Dryer. Water vapor is then transferred from the wet sample gas through the membrane to the counter-current dry purge.

The outlet SO_2 analyzer was sent to the manufacturer to repair a hydrocarbon knockout component. Upon its return, the analyzer was carefully re-calibrated to ensure its accuracy.

The upper and lower end effects were measured this quarter during the SO_2 outlet troubleshooting. The upper end effect was measured by obtaining samples directly above the packing section and at the traditional outlet sample point above the Trutna tray de-entrainer. The NTU for the top end effect is approximately 0.5. The lower end effect was measured by obtaining samples at the traditional air inlet piping and immediately below the packing. The NTU_{bottom} was determined to be around 1.1–1.3.

In the course of systematically checking the outlet sampling system section, a leak was found associated with the membrane filter. The leak only occurred when the inlet of the membrane filter was under vacuum. No leak was present if the inlet was under positive pressure. This made the leak difficult to find and was a characteristic of the fitting assembly used. The fitting was changed and the vacuum leak stopped. The membrane filter is installed just before the SO_2 analyzer to make sure no liquid gets into the analyzer. After changing the fitting on the membrane filter, the outlet SO_2 analyzer responded more quickly and reliably.

The gas film mass transfer coefficient for Mellapak 250Y has been measured this quarter. MP250Y is a standard structured packing with a total area of 250 m^2/m^3 and corrugation angle of 45 degrees. It can be used as a baseline for our structured packing comparison. k_G for this packing is a function of liquid velocity and independent of gas velocity. The exponent of k_G

over u_G for this packing is 0.61 compared with values of 0.73 to 1 in previous result. The exponent after SO_2 sampling troubleshooting is lower than before, which suggests previous results should be explored further.

8. Modeling and simulation of complex stripping configurations p. 132

by Tarun Madan

Stripper complexity is an important area of research to minimize the energy penalty of CO_2 capture process from amine scrubbing of post combustion gases. Configurations such as the interheated stripper, multistage flash with cold rich bypass, and adiabatic lean flash have shown promising results in decreasing the overall energy requirement of the process. These results depend on the design specifications used in the process, especially the design specification for the cross-exchanger. The problem becomes more complex when multiple heat exchangers are used in the system. Practical design specifications that can be applied across the heat exchanger network must be identified.

An overall log mean temperature difference (LMTD) of 5 °C across the cross exchanger(s) was investigated and identified as a reasonable design specification. This specification allows us to compare configurations developed by splitting a single cross exchanger with LMTD of 5 °C into two or more cross exchangers with an overall LMTD across all the exchangers of 5 °C. Such a configuration was investigated with a single-stage flash and warm rich bypass to identify the optimum operating condition for 8 m PZ operating at 150 °C stripping. The effect of splitting the exchanger to multiple exchangers was studied for minimum equivalent work. A minimum equivalent work value of 29.2 kJ/mol CO_2 was achieved using this specification, corresponding to the operating condition of a single cross exchanger (or coldest possible temperature of bypass) and 0.33 lean loading (0.4 rich loading).

The complex configuration of a LP flash followed by a HP flash was optimized with an overall LMTD of 5 ^oC.

Amine scrubbing is being investigated for CO_2 removal from flue gas of natural gas fired power plants using 8 m PZ. Preliminary results for the interheated stripper configuration give an equivalent work of 39 kJ/mol CO_2 at the optimum lean loading for 0.33 rich loading.

Pilot plant reconciliation was continued from last quarter. On the stripper side, Aspen Plus® models were modified and shifted to adjust rich loading to close the mass balance. Energy balances were also closed out with this adjusted model. A single more rigorous model based on modeling of individual units of the pilot plant will be prepared in next quarter.

9. 2MPZ Heat Capacity, Speciation, and Process Modeling p. 149

by Brent Sherman

Creating a process model of 2-methylpiperazine (2MPZ) will allow us to understand how reaction rate affects all aspects of the amine scrubbing process. The existing 2MPZ model is unsuitable for creating a process model, and so it will be re-regressed as it is blended with the Fawkes model. In order to improve the quality of this regression, heat capacity and additional speciation data were sought. However, the available differential scanning calorimeter (DSC) failed to replicate results. Changing the equilibration time, scan rate, and reference resulted in only minor improvement. At higher loadings, the 4 m 2MPZ/4 m PZ blend NMR had merged peaks at 40 °C. This means speciation cannot be determined. Running at a lower temperature will give more peak separation. Results from this are pending. Work next quarter will focus on creating a 2MPZ process model as well as obtaining accurate heat capacities.

10. First-Principles Dynamic Model for a Flash Tank p. 157

by Matt Walters

Co-supervised by Thomas Edgar

A set of dynamic model equations has been developed for a flash tank, which represents the high pressure flash at the PRC pilot plant. Seven dynamic variables have been identified as defining the state of the flash tank system: total liquid molar hold-up, total vapor molar hold-up, mole fraction of CO_2 in the semi-rich liquid, mole fraction of PZ in the semi-rich liquid, mole fraction of CO_2 in the overhead vapor, temperature of the liquid hold-up, and temperature of the vapor hold-up. Additionally, this system has seven input variables associated with the material and energy streams: molar flow rate of the rich liquid feed, vapor overhead, and semi-rich liquid, mole fraction of CO_2 and PZ in the rich liquid feed, feed temperature, and heat duty. This seven input, seven output system will be used for modeling and control of a flash tank.

11. Electric Grid-Level Implications of Flexible CO_2 Capture Operation p. 164

by Stuart Cohen

Co-supervised by Michael Webber

Flexible post-combustion absorption/stripping that vents carbon dioxide (CO_2) or stores rich solvent at partial or zero load could add value to facilities with CO_2 capture by providing a facility with opportunities to perform electricity price arbitrage or provide grid reliability services (ancillary services, or AS). Work has continued this quarter on both the grid-level electricity dispatch model discussed in the Rochelle Group 3rd and 4th quarterly reports of 2011 and the single plant profit maximization model used in earlier work. The least-cost dispatch model uses performance parameters for each generation facility, electricity demand, wind-based electricity production, and AS requirements to determine the power plant operation that minimizes total dispatch costs. It is intended to determine whether flexible CO_2 capture increases AS revenues and improves grid reliability. The single plant model maximizes operating profits at a single facility with CO_2 capture in response to input electricity prices.

The following are key conclusions and accomplishments from this quarter.

- The grid-level least-cost dispatch model has been successfully tested with unit-specific data and demonstrates reasonable computation time under tested input conditions.
- A detailed description and scenario results from a single plant profit maximization model has been published in the *International Journal of Greenhouse Gas Control* under the title "Optimizing post-combustion CO_2 capture in response to volatile electricity prices."
- A new procedure has been developed to adjust historical electricity prices for changes in market prices of fuel (coal, natural gas) and CO_2. This procedure will supply input data to the single plant profit maximization model.
- Adjusting electricity prices for CO_2 prices by adding the average CO_2 emissions cost of gas-fired facilities provides conservative estimates of any electricity price increase.

- Coal-based capacity will often supply marginal generation when gas prices are low, CO_2 prices are moderate, and net electricity demand (demand, or load, minus wind production) exceeds 40 gigawatts.

12. Synthesis of Aminoethylpiperazine via Monoethanolamine and Piperazine at Stripper Conditions p. 181

by Omkar Namjoshi

The selective production of aminoethylpiperazine (AEP) has been investigated this quarter. AEP can be blended with PZ to widen the solid solubility window while maintaining competitive CO_2 absorption rates, capacities, and degradation characteristics compared to 8 m PZ. AEP can be produced in the stripping column of the amine plant by reaction between the monoethanolamine (MEA) oxazolidinone, and piperazine (PZ). Another major synthesis product is diaminoethylpiperazine, or DAEP.

The synthesis of AEP was studied at 150 ^{o}C with an initial loading of 0.3 mol CO_2 / mol alkalinity with two blends: 7 m PZ/2 m MEA and 6 m PZ/4 m MEA. A combined AEP/DAEP yield of 68% was obtained with 89% of the total alkalinity present as PZ, AEP, or DAEP over 840 hours for the 7 m PZ/2 m MEA system. A combined AEP/DAEP yield of 52% was obtained with 77% of the total alkalinity present as PZ, AEP, or DAEP for the 6 m PZ/4 m MEA system. Ureas appear to be the greatest contributor to alkalinity loss. MEA degradation products and formates do not appear to significantly contribute to alkalinity loss.

13. Aqueous piperazine/aminoethylpiperazine for CO_2 Capture p. 193

by Yang Du

Thermal degradation of piperazine (PZ)/aminoethylpiperazine (AEP) was investigated in this quarter. Degradation products were identified using cation and anion chromatography and mass spectrometry, and degradation pathways were inferred.

NH_4^+ and formate were the two most abundant products for PZ/AEP thermal degradation, and consistently increased in thermal degradation experiments. PEP was the next most abundant product and reached equilibrium in first week. The production of FPZ, AEAEPZ Urea, DMPZ, and HEP showed a fast phase in the first week, followed by a slow process within the following 4 weeks. A certain penta-amine and an unknown product (retention time of 17.7) also showed a similar process. The concentration of AEAEPZ reached its maximum after around 1 to 3 weeks and then decreased during the rest time of the 5 weeks degradation experiment. DAEP and EPZ were only positively identified by IC after 3 weeks degradation.

At 175 °C, the degradation of both PZ and AEP in this blend showed a fast phase in the first week, followed by a slow process in the following 4 weeks. Generally, reversible SN_2 reactions account for the fast degradation process in first week, and elimination reactions of AEP and the reaction between PZ and degradation products (such as AEAEPZ) contribute the further slow degradation of PZ/AEP in the following 4 weeks. At 150 °C, this blend showed a consistently slow degradation within 5 weeks, in terms of both PZ and AEP components, due to the fact that at lower temperature, reactions take more time to reach equilibrium. Degradation kinetics was modeled using a 2-stage first order model at 175 °C and a single-stage first order model at 150 °C.

The apparent first order rate constant (k_1) representing the PZ degradation rate in 5 m PZ/2 m AEP is similar to that of pure PZ at 175 °C for the first 5 weeks, but faster at 150 °C. The AEP degradation rate in 5 m PZ/2 m AEP should be slower than that of pure AEP. When compared to MEA and 6 m PZ/4 m AMP blend, 5 m PZ/2 m AEP is obviously more thermally stable at 150 °C in terms of k_1. The different degradation performance of PZ or AEP in blend system and pure system at 150 °C is expected to be the result of synergism/inhibition effect of these two components.

14. Amine Degradation in CO_2 Capture p. 210

by Alex Voice

N-nitroso-piperazine (MNPZ) was produced at a net rate of 3.5 µMol/kg/hr in 8 m piperazine (PZ) in the integrated solvent degradation apparatus (ISDA). MNPZ formation was due to production of nitrite from degradation of PZ.

Addition of 7.2 mMol/kg of sodium nitrite to the solution resulted in an equimolar amount of MNPZ formed in less than 24 hours. The MNPZ then degraded over the course of the experiment.

The first-order thermal degradation rate constant of MNPZ at 120 °C was 0.599 day^{-1}, compared with a rate constant of 0.299 day^{-1} in batch cylinders (Rochelle, 2011). The difference is likely due to errors in correctly estimating the temperature and residence time of the amine in various parts of the ISDA. The thermal degradation rate of MNPZ was not affected by the presence of dissolved oxygen.

Geometry of the bubble removal vessel in the ISDA did not affect total formate production. Total formate was not produced in the absence of oxygen.

The presence of manganese increased the oxidation rate of monoethanolamine (MEA) by more than a factor of two. Normalized MEA loss was the same for three solutions with initial MEA concentration from 2.9 to 5.3 mol/kg MEA. No significant difference in MEA loss or total formate production was observed between solutions containing Mn(II), Mn(III), or Mn(IV). In all cases with manganese present, MEA loss leveled out at 70% after six days.

15. Aerosol and Volatile Emission Control in CO_2 Capture p. 222

by Steven Fulk

In this quarter, an aerosol growth model was developed in Microsoft® Excel to gain a semi-quantitative understanding of aerosol size behavior throughout an absorber with a water wash section. Heat and mass transfer to aerosol particles was assumed to have negligible impact on the bulk gas and liquid mass and energy balances. Gas-phase properties for integration were calculated from Aspen Plus® simulations using a modified version of the Fawkes model developed in the Rochelle group. Mass, heat, and momentum balances for aerosol particles were modeled assuming homogeneous spheres traveling through an infinite, quiescent gas.

H_2O and piperazine (PZ) mass transfer were assumed to be gas-film controlled; however, CO_2 mass transfer was found to be liquid-film controlled for particle sizes down to 5 µm and initial PZ concentrations greater than 1 molal. Particles less than 0.1 µm are in equilibrium to CO_2 for any starting PZ concentration.

Aerosol size is driven by water mass transfer since gas phase concentrations of PZ are very low and CO_2 quickly reaches equilibrium upon entering the absorber or further upstream where nucleation sites first become available. Water mass transfer dominates the all latent effects in the aerosol such that the heat flux to the droplet equals the latent heat of condensation or evaporation. The aerosol is at the wet bulb temperature of the gas.

Goals for next quarter include coding a steady-state mass and heat transfer model into Matlab® with a long term goal of including sulfuric acid into rigorous speciation calculations.

16. Piperazine Degradation in Pilot Plants *p. 244*

by Paul Nielsen

This progress report discusses the findings made in the characterization of solvent degradation at the pilot-plant scale. Degraded 8 m piperazine (PZ) was analyzed from 2 pilot plant campaigns, one run at the Pickle Research Campus (PRC) in October 2011 and one run at “Pilot Plant 2” (PP2). The PRC campaign used synthetic flue gas consisting of air mixed with 12 kPa CO_2, while the PP2 campaign used a slip stream of real flue gas from a coal-fired power plant. Data from these campaigns can be used to determine the degradation rate of PZ and the formation of byproducts.

The major thermal degradation products detected in both pilot plant solvents included ethylenediamine, N-(aminoethyl)piperazine, and N-(hydroxyethyl)piperazine. Oxidative degradation products including formate, acetate, oxalate, and N-formlypiperazine were also detected. The formation of the oxidative degradation products was observed to be catalyzed by the accumulation of dissolved metal ions from corrosion in PP2.

N-nitrosopiperazine, a known carcinogen that forms when PZ reacts with nitrite absorbed from flue gas, was also observed in PP2 solvent at a steady state of 1 mmol/kg. The accumulation of MNPZ seems to be limited by its thermal degradation in the stripper.

17. N-Nitrosopiperazine Kinetics in CO_2 Capture *p. 270*

by Nathan Fine

This quarter, high temperature kinetics for the formation and decomposition of N-Nitrosopiperazine (MNPZ) were studied. MNPZ formation is first order with respect to nitrite concentration, and MNPZ decomposition is first order with respect to MNPZ concentration. Both reactions are irreversible. A temperature dependent model was determined for MNPZ decomposition from 120 °C to 150 °C. However, MNPZ formation was too fast to analyze at 135 °C and 150 °C using the current methodology. Stainless steel ions were found to have no effect on MNPZ decomposition. Piperazine carbamate (PZCOO-) catalyzes MNPZ formation, but has no effect on MNPZ decomposition. Current data suggests that MNPZ decomposition is first order with respect to protonated piperazine (+HPZ).

The MNPZ kinetics were used to calculate the transient and steady state MNPZ concentration in a carbon capture absorption-stripping unit. The steady state concentration can be lowered by decreasing the residence time in the stripping sump, decreasing the NO2 concentration in the flue gas, or increasing the temperature in the sump. At a sump temperature of 150 °C and a total residence time 5 times the sump residence time, nitrosamine concentration should reach 90% of steady state after 5 days.

Appendix

Omkar Namjoshi Safe Operating Practices p. 284

CO_2 Solubility in Aqueous Amines

January 1 – March 31, 2012

by Le Li

Supported by the Luminant Carbon Management Program

Department of Chemical Engineering
The University of Texas at Austin

April 30, 2012

Abstract

CO_2 solubility at high temperature was measured for three solvents: PRC pilot plant 8 m PZ Fall 2011 sample, 8 m PZ with 100 mM Inhibitor A (Inh A), and the blend of 6 m PZ/2 m bis(aminoethyl)ether (BAE). High temperature P_{CO2}* measurements are necessary to make accurate predictions in solvent capacity and heat of CO_2 absorption. A total pressure equilibrium reactor is used to measure P_{CO2}* at 100, 110, 120, 130, 140, 150, 160 °C. For the pilot plant sample, 18 P_{CO2}* data points was measured at various CO_2 loading. The new data points are used together with low temperature measurements and an updated semi-empirical model is calculated. For the pilot plant sample, the updated model give a capacity of 0.65 mol/kg, which is 18% lower than 8 m PZ, and heat of absorption of 68 kJ/mol, which is 6% higher than 8 m PZ. High temperature P_{CO2}* measurements for 8 m PZ Inh A compare closely with results for the pilot plant sample. The effect of Inh A (at the concentration typical in a CO_2 capture process) on solvent VLE is currently inconclusive, though it is expected to be insignificant. A total of 21 high temperature P_{CO2}* data points were collected for 6 m PZ/2 m BAE. The VLE model was regressed using 1) total pressure data, 2) WWC data at low temperatures, and 3) both data sets. The three models differ in mathematical form and generate different values for solvent capacity and heat of absorption. The third model is expected to have the best overall predictability since it uses all of the available data and the regression resulted in a high R^2 value of 0.994. The predicted solvent capacity for the blend is 0.69 mol/kg, which is 13% less than 8 m PZ. The heat of absorption calculated by the model is 68 kJ/mol, which is 6% higher than 8 m PZ.

Introduction

CO_2 solubility data at high temperature are crucial in accurately predicting solvent performance. The CO_2 vapor-liquid equilibrium for a solvent determines solvent capacity and heat of absorption. In practice, solvent vapor liquid equilibrium (VLE) is characterized using a semi-empirical model (Equation 1).

$$\ln(P^*_{CO_2}) = a + b/T + c\cdot\alpha + d\cdot\alpha^2 + e\cdot\frac{\alpha}{T} + f\cdot\frac{\alpha^2}{T} \tag{1}$$

The parameters in the model are calculated from regressing experimentally measured VLE data. Thus, the quality of the experimental data directly affects the accuracy of the calculated solvent capacity and heat of absorption. The accuracy of each measured VLE data point is specific to the experimental method, and is largely limited by the bias and error in the apparatus and procedures. The accuracy of the model can be improved by collecting additional data 1) using an alternative experimental method, or 2) expanding the range of experimental conditions. Data measured using alternative experimental methods, although it may introduce new errors, can be used to check the bias in the original method. Incorporating data at new experimental conditions improves the overall predictability of the model, especially properties with theoretical dependency of the varied condition. In this case, since the heat of absorption of CO_2 for a solvent is defined as the temperature dependence of the solvent CO_2 solubility (Equation 2), data at additional temperature conditions can improve the model prediction in $-H_{abs}$ values.

$$H_{abs} = -R \cdot \frac{\partial(lnP^*_{CO_2})}{\partial(\frac{1}{T})} = -R \cdot (b + d \cdot ldg + f \cdot ldg^2) \quad (2)$$

Typically, for each solvent CO_2 solubility at low temperature is measured using the wetted wall column (WWC). The WWC generates 15 to 20 CO_2 equilibrium partial pressure measurements at various CO_2 loading and 20, 40, 60, 80, and 100 ˚C. VLE models can be regressed using the WWC results alone. However, the model is best used for interpolating property values within the temperature and CO_2 loading range where the data were collected. Also, error and inconsistency in temperature control of the WWC experimental procedure will be reflected as inaccurate temperature dependence of measured equilibrium values. Thus, solvent heat of absorption calculated using the WWC VLE model contains inaccuracies which are a direct function of the errors in the temperature measurement of the experiment.

The VLE of CO_2 at high temperature was measured using a total pressure equilibrium reactor. The standard experimental procedure typically generates 20 to 24 equilibrium partial pressure measurements at seven temperatures between 100 and 160 ˚C and various CO_2 loadings. This approach efficiently improves the accuracy of the VLE model by simultaneously doubling the total number of collected data and expanding the temperature range of the data set.

The sample from the PRC pilot plant 8 m PZ campaign in Fall 2011 was tested in the WWC during the last quarter. Equilibrium data collected at low temperature show slight change in capacity and heat of absorption for the pilot plant sample from bench scale 8 m PZ results (Rochelle, 2012). High temperature CO_2 VLE was measured for the pilot plant sample in the total pressure apparatus during this quarter. The new equilibrium data were analyzed together with the low temperature data to generate an updated semi-empirical model. Solvent capacity and heat of absorption calculated from the updated model are compared against results for laboratory grade 8 m PZ.

Previous low temperature VLE measurement suggests the pilot plant sample is distinctly different in its CO_2 solubility from bench scale fresh 8 m PZ. One difference between the two is the presence of 100 mM Inh A in the pilot plant sample. The effect of Inh A on the CO_2 solubility for 8 m PZ should be determined to understand the change in solvent performance for the PRC samples. Fresh 8 m PZ solvent was prepared with Inh A and tested in the total pressure apparatus to characterize VLE at high temperature. The measured data was compared with the high temperature data of the pilot plant sample.

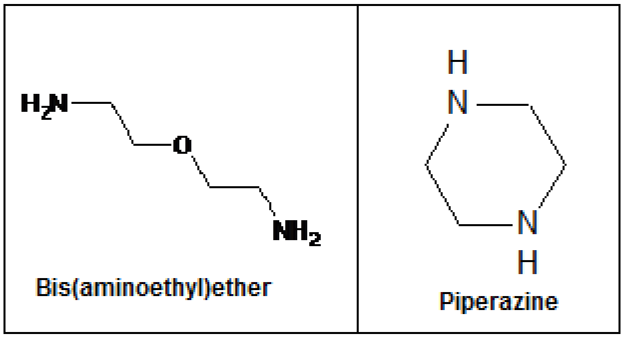

Figure 1: Molecular structure of BAE and PZ

6 m PZ/2 m Bis(aminoethyl)ether (BAE) was characterized using the WWC last quarter, and shows attractive properties as a solvent for CO_2 absorption (Rochelle, 2012). The molecular structures of BAE and PZ are shown in Figure 1. This quarter, additional equilibrium data were measured for the blend using the total pressure apparatus at 100–160 ˚C and various CO_2 loadings. A semi-empirical model was regressed using 1) low temperature data (WWC), 2) high temperature data (total pressure), and 3) both sets of VLE data. The three VLE models predict different values for solvent capacity and heat of absorption. Comparing the form and statistical significance of model parameters improves understanding of the bias of experimental data for both the WWC and total pressure methods.

Experimental Methods

A total pressure equilibrium reactor is used to measure CO_2 partial pressure at high temperature. The experimental apparatus and procedure are identical to those used by Xu (2011). During an experiment, the equilibrium reactor is assumed to be a closed system which contains the solvent sample and gaseous nitrogen (N_2). The pressure of the entire system is measured continuously as the reactor is heated to target temperature. At each temperature, the reactor is maintained at equilibrium for 10 to 20 minutes. The measured system pressure during the equilibrium phase is averaged and reported (P_{meas}). The CO_2 partial pressure of the system (P_{CO2}) is calculated from the measured P_{meas}. An example of the total pressure raw experimental data is shown in Figure 2.

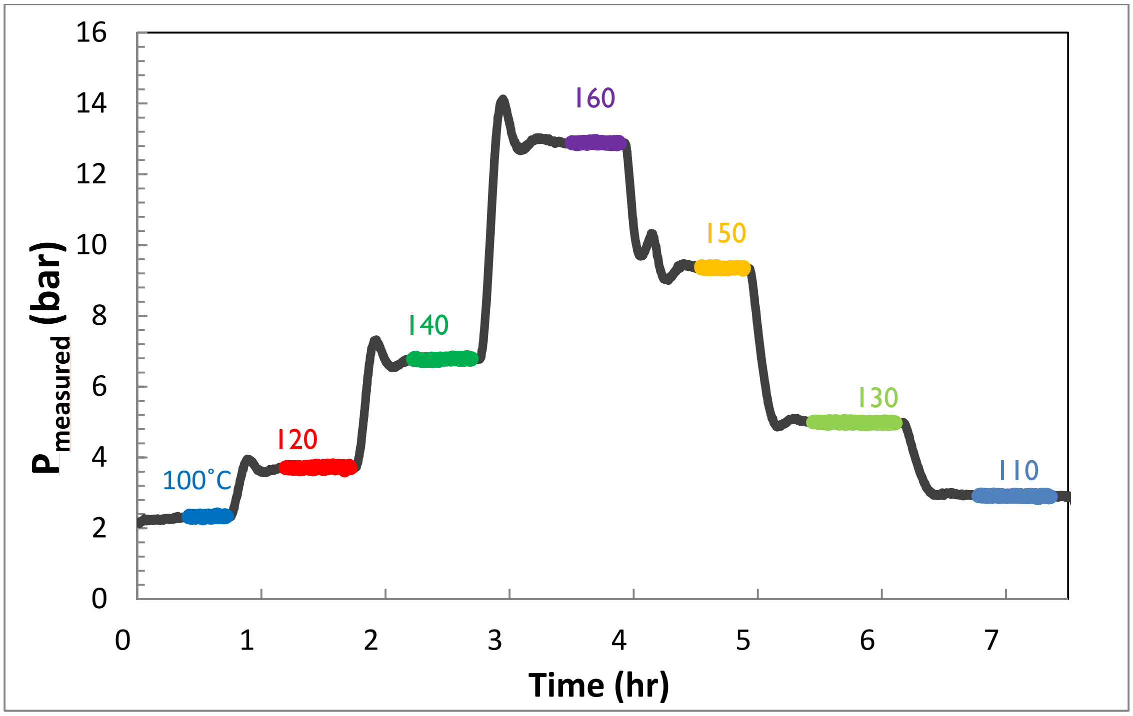

Figure 2: Example total pressure measurement (pilot plant sample)

First, the partial pressure of nitrogen (P_{N2}) is subtracted from the measured pressure to give the total pressure of the solvent (Equation 3).

$$P_{total} = P_{meas} - P_{N_2} \qquad (3)$$

$$P_{N_2} = T \cdot \frac{P_{N_2\,initial}}{T_{initial}} \qquad (4)$$

$$P_{CO_2} = P_{total} - P_{H_2O} - P_{amine} = P_{total} - P^*_{H_2O} \cdot x_{H_2O} - P^*_{amine} \cdot x_{amine} \qquad (5)$$

The initial pressure of N_2 ($P_{N2initial}$) and temperature are recorded and used in the ideal gas law to calculate P_{N2} at each experimental temperature (Equation 4). The partial pressure of CO_2 (P_{CO2}) is then calculated by subtracting the partial pressure of water (P_{H2O}) and amines (P_{amine}) from P_{total} (Equation 5). The partial pressures of water and amine are calculated using Raoult's law: the partial pressure of a species in the gas phase equals the vapor pressure of the species multiplied by its liquid phase mole fraction. Literature values for water vapor pressures are used for P_{H2O}* (DIPPR). Vapor pressure of the amine (P_{amine}*) is assumed to be zero since its value is expected to be negligible relative to the vapor pressure of other species.

To accurately report the CO_2 content in the liquid phase, the liquid sample is analyzed at room temperature at the beginning and the end of each experiment. However, the true liquid phase CO_2 loading during the experiment is expected to change significantly from measured values due to the high CO_2 partial pressure at high temperatures. Therefore, the reported CO_2 loading values are calculated by subtracting the moles CO_2 in the vapor phase (n_{CO_2V}) from total CO_2 in the original sample (n_{CO_2T}) as in Equation 6. The vapor phase CO_2 (n_{CO_2V}) is calculated using ideal gas law (Equation 7), where V_{vap} is the vapor volume of the equilibrium reactor (approx 135 mL).

$$\propto = \frac{n_{CO_2T} - n_{CO_2V}}{n_{alkalinity}} \quad (6)$$

$$n_{CO_2V} = \frac{P_{CO_2}V_{vap}}{RT} \quad (7)$$

Detailed results are reported in the appendix.

Materials

The amine solvents were prepared gravimetrically. To achieve each CO_2 loading, gaseous CO_2 (99.99%, Matheson Tri-Gas) was bubbled into the solvent. The chemicals used in solvent preparation are listed in Table 1.

The 2011 8 m PZ pilot plant sample used in the total pressure experiment was the absorber lean amine sample collected from the skid. The high CO_2 loading conditions were achieved by bubbling CO_2 into the collected sample.

Table 1: Materials Used for Solvent Preparation

Chemical	Purity	Source
Bis(aminoethyl)ether	99%	Huntsman
Piperazine	98%	Sigma-Aldridge
Methyldiethanolamine	98.5%	Huntsman
DDI Water	100.00%	Millipore, Direct-Q

Analytical Methods

Liquid samples for each experiment were analyzed for CO_2 content and total alkalinity. The total inorganic carbon (TIC) method is used to measure the total moles of CO_2 per unit mass of liquid sample. The acid titration method is used to determine the total moles of alkalinity in the samples. For each sample, both analysis methods were performed in triplicate and the average value was reported. The apparatus and method for both TIC and acid titration are identical to those used by Freeman (2011).

Laboratory Safety

The apparatus for the total pressure experiment is located in a functional and properly vented fume hood. The system typically operates at high temperatures (+100 °C) and high pressures (2–25 bar) continuously for 6–8 hours. The fume hood is clear of other equipment to avoid damage in case of leakage of high pressure gas. The system is designed to hold pressure up to 30 bar. In case of system pressure reaching above 30 bar, pressure will be released through the imperfect spring seal of the reactor. Proper venting of the hood is ensured during the course of the experiment so that released gas will be immediately vented and will not be released into the lab. The apparatus is disassembled after cooling the reactor to room temperature. Venting outlets of the reactor are first opened to release any potential system pressure prior to disassembling of the reactor. Directly touching the heated reactor is avoided during the operation of the experiment. All liquid samples are handled at room temperature.

Chemicals are prepared, loaded, and handled using standard laboratory safety guidelines. Gloves, long pants, closed-toed shoes, and goggles are worn at all times.

Results and Discussion

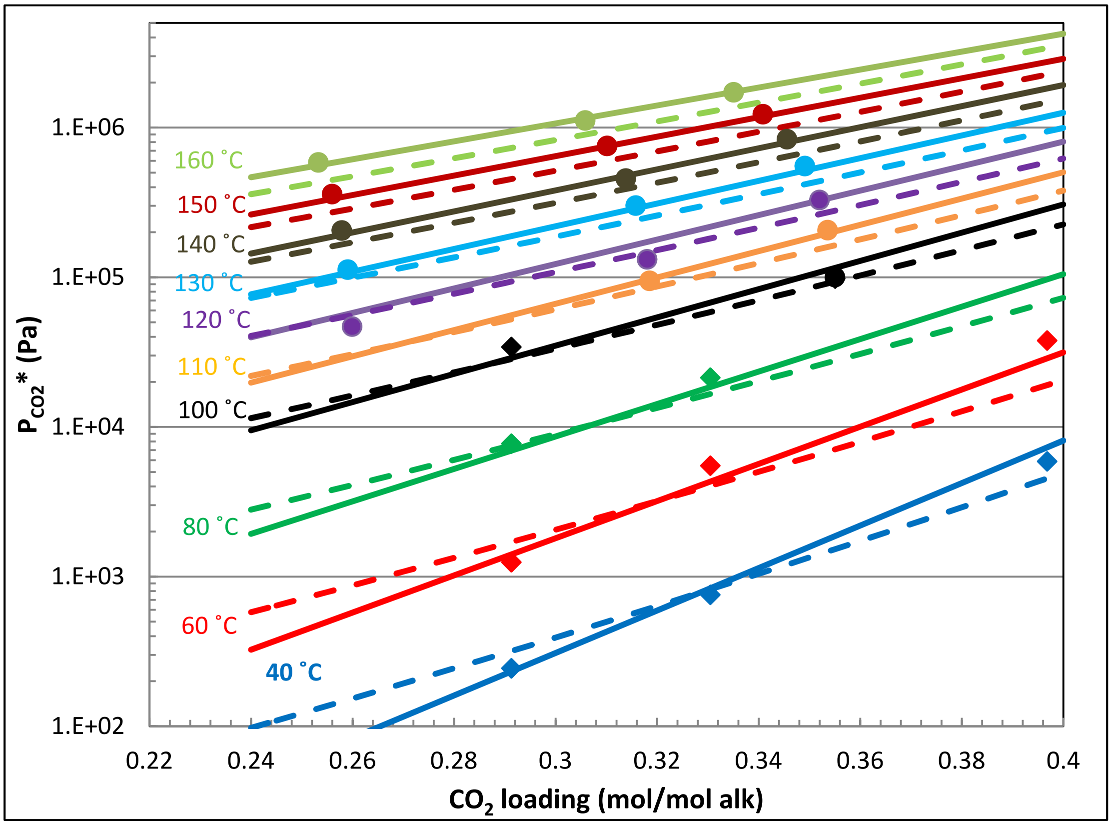

Figure 3: CO_2 solubility in PRC 8 m PZ Fall 2011 campaign pilot plant sample. Circles: total pressure; diamonds: wetted wall column; solid lines: pilot plant semi-empirical model (Table 2); dashed lines: 8 m PZ semi-empirical model (Table 2).

For the PRC 8 m PZ Fall 2011 pilot plant campaign sample, 18 P_{CO2}* data points were collected using the total pressure method at 100–160 °C between the nominal lean and rich loading of the solvent. Together with 9 P_{CO2}* data points collected at low temperature using the WWC (Rochelle, 2012), a total of 27 data points were regressed to obtain the semi-empirical model for the pilot plant sample (Table 2). The measured P_{CO2}* plotted with the semi-empirical model result, is also compared against the semi-empirical model result of 8 m PZ (Figure 3). The measured values from the two different methods agreed well with each other. The semi-empirical model is able to fit both sets of data closely. The model regression has a relatively high R^2 value (0.997) Compared to the model results of 8 m PZ, the CO_2 solubility curve of the pilot plant sample has a smaller slope. Considering the errors associated with the experimental data, this observed difference in the model results is likely within the variability of the data used. Mathematically, the regressed model for PRC pilot plant and 8 m PZ differs in the functional dependency of P_{CO2}* and loadings and temperatures. The predicted capacity of the pilot plant sample is significantly lower than 8 m PZ, by 18%. The calculated heat of absorption for the pilot plant sample is 6% higher than 8 m PZ. Detailed P_{CO2}* data for the pilot plant sample are summarized in Table 3.

Table 2: Semi-empirical model (Equation 1) parameters for pilot plant sample and 8 m PZ

	PRC pilot plant		8 m PZ (Xu, 2011)	
	Value	Std Error	Value	Std Error
a	45.8	1.9	35.3	0.3
b	-15604.3	727.7	-11054	120
c	-35.4	6.0	/	/
d	/	/	-18.9	2.7
e	21322.6	2227.7	4958	347
f	/	/	10163	1085
R^2	0.997		0.993	
Capacity (mol/kg solv)	0.65		0.79	
$-H_{abs}$ @ 1.5 kPa (kJ)	68		64	

Table 3: Detailed high temperatures P_{CO2}* results for PRC 8 m PZ Fall 2011 pilot plant sample

Temperature	**CO_2 ldg**	**P_{CO2}**	Raw Data		Sample analysis		
			P_{meas}	P_{tot}	CO_2	Alkalinity	CO_2 ldg
(°C)	mol/mol	kPa	kPa	kPa	mol/kg	mol/kg	mol/mol
120	0.260	47	372	220	2.22	8.53	0.261
130	0.259	113	499	348			
140	0.258	205	677	521			
150	0.256	360	936	775			
160	0.253	586	1289	1125			
110	0.318	95	323	220	2.62	8.19	0.320
120	0.318	132	439	306			
130	0.316	301	646	538			
140	0.314	457	899	774			
150	0.310	755	1300	1172			
160	0.306	1116	1789	1658			
100	0.355	100	322	189	2.95	8.26	0.356
110	0.354	207	460	332			
120	0.352	329	642	502			
130	0.349	554	924	789			
140	0.346	837	1295	1152			
150	0.341	1230	1791	1645			
160	0.335	1722	2411	2261			

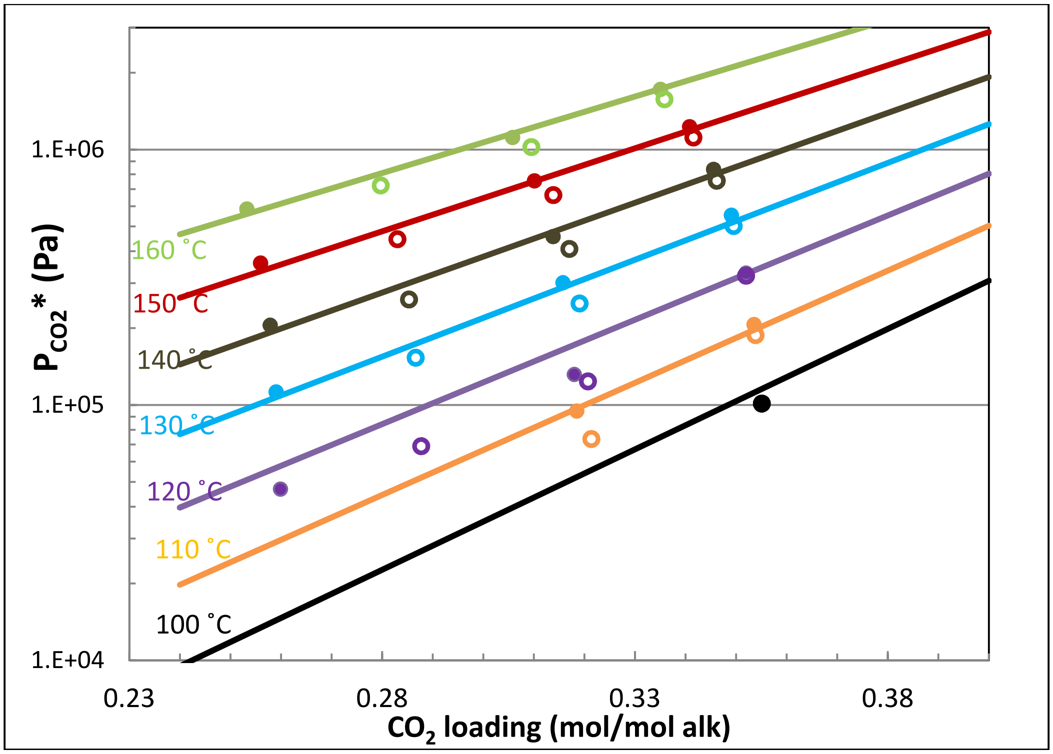

Figure 4: CO_2 solubility at high temperatures for 8 m PZ + 100 mM Inh A. Solid circles: PRC pilot plant sample; empty circles: 8 m PZ + Inh A; solid lines: pilot plant semi-empirical model (Table 2).

P_{CO2}* data were collected at high temperature using the total pressure method for 8 m PZ with 100 mM Inh A. The 8 m PZ/Inh A data are plotted against measurements and model results for the PRC pilot plant sample (Figure 4). At high temperatures, the CO_2 solubility for 8 m PZ/Inh A compares closely to that of the pilot plant sample. The measured P_{CO2}* values for 8 m PZ/Inh A are systematically lower than both the measured data and model results for the PRC sample. However, the difference is small and within the error margin of the experimental method. Thus, additional data at low temperatures are necessary to perform further comparison on the CO_2 solubility of the two systems. The detailed measurement of high temperature P_{CO2}* for 8 m PZ/Inh A is summarized in Table 4.

Table 4: Detailed high temperatures P_{CO2}* results for 8 m PZ + 100 mM Inh A

T	**CO_2 ldg**	**P_{CO2}**	Raw Data		Sample analysis		
			P_{meas}	P_{tot}	CO_2	Alkalinity	CO_2 ldg
(°C)	mol/mol	kPa	kPa	kPa	mol/kg	mol/kg	mol/mol
120	0.288	69	405	243	2.39	8.28	0.289
130	0.287	153	552	390			
140	0.285	259	744	576			
150	0.283	446	1035	863			
160	0.280	724	1442	1266			
110	0.321	74	334	199	2.64	8.20	0.322
120	0.321	124	441	298			

130	0.319	250	628	487			
140	0.317	409	873	725			
150	0.314	664	1232	1081			
160	0.310	1023	1720	1565			
100	0.355	101	319	190			
110	0.354	188	423	314			
120	0.352	321	630	495			
130	0.350	502	855	739	2.89	8.09	0.357
140	0.346	756	1203	1072			
150	0.342	1115	1666	1533			
160	0.336	1575	2253	2117			

The total pressure method is used to collect high temperature P_{CO2}* data for the amine blend of 6 m PZ/2 m BAE. A total of 21 data points were measured at 100–160 °C and various CO_2 loadings. A semi-empirical VLE model is regressed using the total pressure measurements. The experimentally measured data and the model results are plotted together (Figure 5). Statistically, the linear regression calculation resulted in a relatively low value of R^2, suggesting variability in the total pressure data (Table 5: model 1).

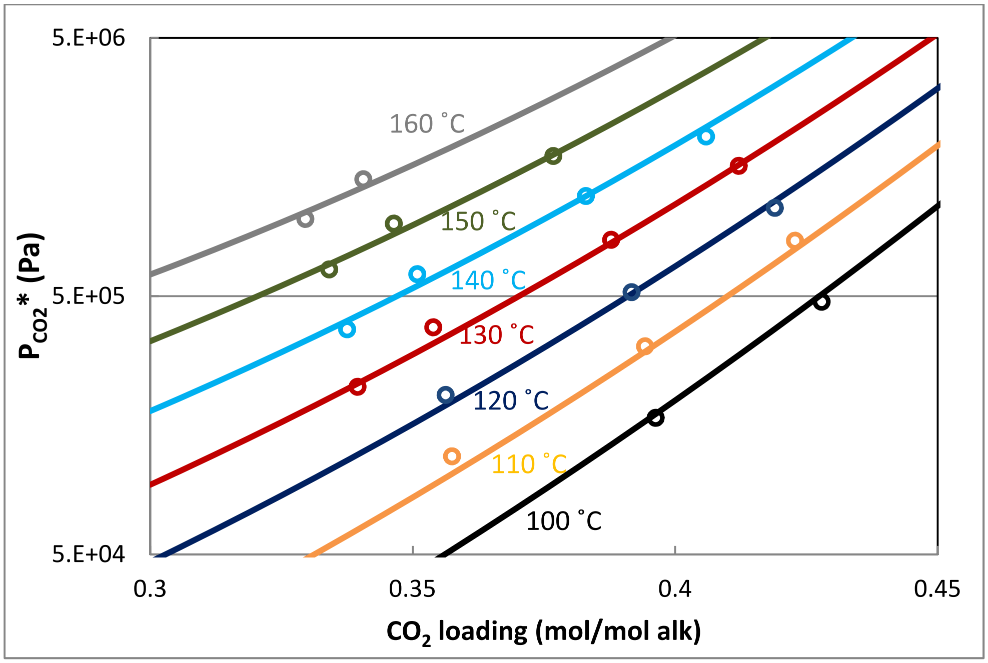

Figure 5: CO_2 solubility at high temperatures for 6 m PZ/2 m BAE. Empty circles: total pressure; solid lines: total pressure semi-empirical model (Table 5: model 1).

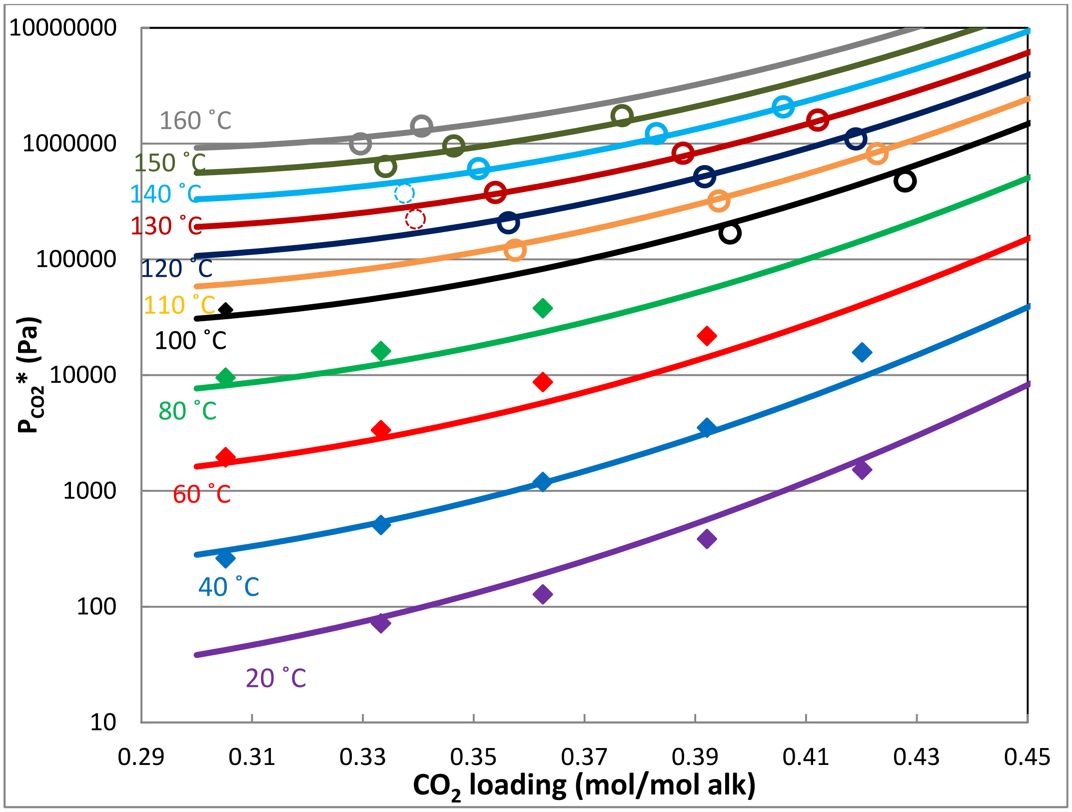

Figure 6: CO_2 solubility for 6 m PZ 2 m BAE. Empty circles: total pressure; diamonds: WWC (Rochelle 2012); solid lines: all data semi-empirical model (Table 5: model 3).

High temperature P_{CO2}* measurement is then compared with low temperature data from the WWC (Figure 6). A model is regressed using data at low and high temperatures together (38 data points). The model result should, in theory, minimize the experimental bias of both methods. For the WWC data, the model fits best at low loadings. At high loadings, the model under-predicts the data at 60 °C and 80 °C. The poorer fit suggests a greater error in the WWC measurements at these conditions. For the total pressure data, the model fits the data well, except for the lowest loading point at each temperature. The model suggests significant error in the 130 and 140 °C points (Figure 6: dashed circles). Statistically, the R^2 value of this model is higher than the total pressure only model, suggesting improved overall predictability.

Table 5: Three sets of semi-empirical model (Equation 1) parameters for 6 m PZ/2 m BAE

	1) total pressure		2) WWC (Rochelle, 2012)		**3) All Data**	
	Value	Std error	Value	Std error	Value	Std error
a	51	7	38	1	**53**	6
b	-17343	3059	-8410	1172	**-13249**	1273
c	-53	18	/	/	**-96**	28
d	21443	8138	-16668	6316	**13676**	3461
e	36	14	/	/	**114**	33
f	/	/	37391	8733	/	/
R^2	0.987		0.995		**0.994**	

Capacity (mol/kg solv)	0.49	0.62	**0.69**
$-H_{abs}$ @ (1.5kPa) (kJ)	74	79	**68**

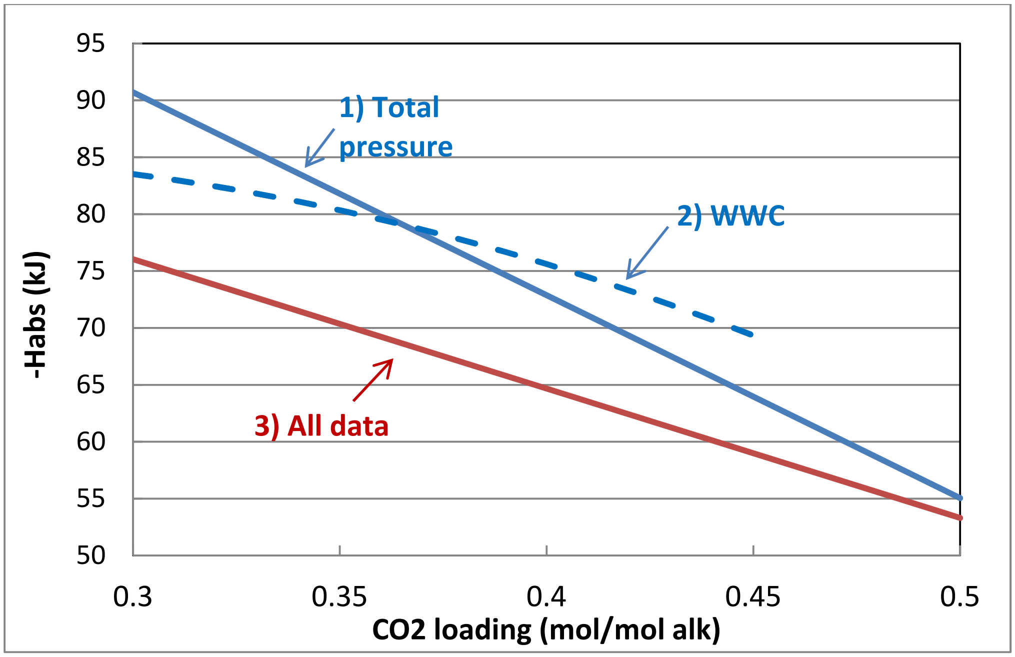

Figure 7: Heat of absorption of 6 m PZ/2 m BAE predicted by three semi-empirical VLE models (Table 5)

Together with a previously regressed model using only the WWC VLE data, a total of three VLE models were regressed for 6 m PZ/2 m BAE (Table 5). Mathematically, the functional form of the WWC differs slightly from the other models. Solvent performance properties calculated using the three models differ significantly. For solvent capacity, the total pressure model predicts a much lower value (0.49 mol/kg) than the other models (0.62 and 0.69 mol/kg). The heat of absorption of CO_2 for this blend is 74 and 79 kJ/mol by the total pressure and WWC models, respectively, whereas model 3 calculates a heat of absorption of 68 kJ/mol, which is approximately 10% lower than the other models. This difference in heat of absorption prediction is presented graphically in Figure 7. It is expected that model 3, which uses both data sets, will predict values between the results by the models using the total pressure data or the WWC alone. However, across the tested loading range, model 3 consistently predicts heat of absorption about 10 kJ lower than the other models. This observation is likely due to error in the experimental measurements, which reduces the accuracy in the temperature dependence extracted from the data. Without additional data, model 3 is used to represent the blend, since it used the largest number of data and also has satisfactory R^2 value.

The details of the high temperature $P_{CO2}*$ measurements for 6 m PZ/2 m BAE are summarized in Table 6.

Table 6: Detailed high temperature P_{CO2}* results for 6 m PZ/2 m BAE

T	**CO_2 ldg**	**P_{CO2}**	Raw Data		Sample analysis		
			P_{meas}	P_{tot}	CO_2	Alkalinity	CO_2 ldg
(°C)	mol/mol	kPa	kPa	kPa	mol/kg	mol/kg	mol/mol
130	0.339	223	598	460	2.71	7.91	0.343
140	0.338	372	841	690			
150	0.334	635	1208	1053			
160	0.330	995	1697	1538			
110	0.357	120	373	246	2.84	7.90	0.359
120	0.356	207	516	382			
130	0.354	379	750	616			
140	0.351	609	1065	926			
150	0.346	955	1515	1373			
160	0.341	1418	2106	1961			
100	0.396	169	391	257	3.23	8.11	0.399
110	0.394	320	577	444			
120	0.392	518	831	691			
130	0.388	827	1201	1062			
140	0.383	1221	1680	1535			
150	0.377	1745	2308	2159			
100	0.428	476	694	565	3.34	7.66	0.435
110	0.423	820	1009	946			
120	0.419	1099	1410	1273			
130	0.412	1598	1902	1836			
140	0.406	2077	2500	2394			

Conclusions

An updated VLE model shows the capacity of the PRC 8 m PZ Fall 2011 pilot plant sample is 18% lower and the calculated heat of absorption for the pilot plant sample 6% higher than 8 m PZ. Based on the measured data, the difference between the CO_2 solubility for the pilot plant sample and laboratory grade 8 m PZ is small, especially at high temperature (above 100 °C). The high temperature VLE measurements for 8 m PZ with 100 mM Inh A are systematically lower than the results for the pilot plant sample, but the difference is very small and likely within the error range of the experimental method. Additional data at low temperature are required to conclusively determine the effect of Inh A on solvent VLE. High temperature P_{CO2}* measurements for 6 m PZ/2 m BAE are used to update the semi-empirical VLE model for the solvent. The updated model uses 38 data points and has an R^2 value of 0.994. The model predicts a solvent capacity of 0.69 mol/kg, which is 13% less than 8 m PZ. Solvent heat of absorption calculated by the model is 68 kJ/mol, which is 6% higher than 8 m PZ. The accuracy of model prediction in heat of absorption needs to be further analyzed.

Future Work

Equilibrium measurements at high temperature will be taken for more solvents, including PZ blends and amino acids. The wetted wall column method will undergo troubleshooting by performing equipment calibration and measurement error analysis. Measurement of absorption rates and low temperature VLE for 8 m PZ will be repeated as part of the troubleshooting effort. Meanwhile the wetted wall column apparatus will be used to measure absorption rate of NO_2 into amine solvents.

References

DIPPR, 1998-Provo, UT: BYU DIPPR, Thermophysical Properties Laboratory, 1998-Version 13.0.

Freeman SA. *Thermal degradation and oxidation of aqueous piperazine for carbon dioxide capture*. The University of Texas at Austin. Ph.D. Dissertation. 2011.

Rochelle GT et al. "CO_2 Capture by Aqueous Absorption, Fourth Quarterly Progress Report 2011." Luminant Carbon Management Program. The University of Texas at Austin. 2012.

Xu Q. *Thermodynamics of CO_2 loaded aqueous amines*. The University of Texas at Austin. Ph.D. Dissertation. 2011.

Appendix

Table A1: Supporting measurements for the total pressure experiment for PRC 8 m PZ Fall 2011 pilot plant sample

Sample loading mol/mol alk		T F	$P_{N2initial}$ bar	Sample mass g
0.261	Initial	62	1.12	392.3
	After	60	1.08	
0.320	Initial	63	1.04	405.3
	After	60	0.97	
0.356	Initial	65	0.98	404.8
	After	60	0.77	

Table A2: Supporting measurements for the total pressure experiment for 8 m PZ + 100 mM Inh A

Sample loading mol/mol alk		T F	$P_{N2initial}$ bar	Sample mass g
0.289	Initial	65	1.20	406.6
	After	61	1.16	
0.322	Initial	66	1.06	402.4
	After	62	1.02	
0.357	Initial	68	1.01	389.7
	After	60	0.83	

Table A3: Supporting measurements for the total pressure experiment for 6 m PZ/2 m BAE

Sample CO_2 ldg mol/mol alk		T F	$P_{N2\ initial}$ bar	Sample Mass g
0.343	Initial	67	1.14	400.7
	After	62	0.992	
0.359	Initial	66	0.995	400.1
	After	62	0.962	
0.399	Initial	68	1.05	418.7
	After	61	1.00	
0.435	Initial	64	1.01	401.1
	After	60	0.472	

Aqueous Amine Volatility in CO_2 Capture

Quarterly Report for January 1 – March 31, 2012

by Thu Nguyen

Supported by the Luminant Carbon Management Program

Department of Chemical Engineering

The University of Texas at Austin

April 30, 2012

Abstract

Aqueous amine volatility in binary amine-water systems is crucial for: (1) proper design of water wash units in post-combustion CO_2 capture process and (2) accurate representation and modeling of the intrinsic interactions between amine and water. In this work, the volatilities of 19 amines considered to be viable for CO_2 capture, including monoethanolamine (MEA), piperazine (PZ), and n-methyldiethanolamine (MDEA), were measured for dilute amine concentrations from 0.1–1.05 m amine in water from 40–70 ˚C and 1 bar as these conditions represent the operating conditions of the CO_2 capture absorber. In using the volatility data for all the amines from this work along with 16 alkylamines from the literature, a group contribution model was developed to correlate functional group behavior to the aqueous amine Henry's constant at 40 ˚C. The Henry's constant is used as an indicator of the intrinsic amine volatility. The R^2 of this group contribution model is ~0.95. The model is able to represent the Henry's constants of the amines within ±25% of the experimental values. Two of the unique features of this model are(1) distinction between cyclic and straight chained amines; (2) distinction between the different types of methyl groups based on the neighboring groups attached to them. In order to represent the Henry's constants of the amines between 25 ˚C and 70 ˚C, and to extrapolate outside this range, another group contribution model was developed to estimate the amine heats of solution which are then used to predict the H constants at the temperatures of interest given the values predicted at 40 ˚C. Overall, the predicted H constants are found to be well within an order of magnitude of the experimental H constants.

Introduction

The study of amine volatility in dilute amine-water systems provides key understanding that is crucial to the design of water wash units used in the CO_2 capture process. Typical water wash operations involve treating only a few ppm of amine in more than 15 mole % of water. In addition to the need to size the water wash, there is also a scientific interest in exploring dilute aqueous amine volatility in an effort to better understand amine/water interactions. Proper understanding of these interactions enables one to generalize, and effectively predict, the volatilities of a large number of amines used in CO_2 capture without the need for extensive experimentation.

While there are published measurements on the VLE of amine-water systems, only a few of them measure the vapor phase mole fraction of the amine. This work is among the few that measure the vapor composition of the amines, particularly at very dilute amine concentrations, to develop proper understanding of the intrinsic amine-water interactions. Furthermore, this work is believed to provide one of the largest collections of experimental data of amine volatility in water for as many as 19 amines that are relevant to CO_2 capture. Other work that investigated aqueous amine volatilities will now be summarized. Lenard et al. (1990) measured the gas phase composition of MEA in binary aqueous solution (343K and 363K) using gas chromatography. These data were represented using a three-parameter Redlich-Kister expansion. Pappa et al. (2006) made isobaric T-x-y measurements for the AMP-H_2O system at 66.7, 80.0, and 101.3 kPa using a modified Swietoslawski ebulliometer with sample compositions being determined using a standard curve of refractive index for this system at 25 ˚C. Kim et al. (2008) also used this ebulliometer technique to determine the total pressure along with the liquid and vapor mole fractions of MEA, MDEA, and MAPA. Cai et al. (1996) measured isobaric VLE at 101.3 kPa and 66 kPa (373K - 443K) using the standard curve of refraction index versus mole fraction of the binary mixture at 20 ºC. The liquid phase activity coefficients were calculated with the UNIFAC group contribution model as published by Larsen et al. (1987).

This work investigates the aqueous volatility of 19 amines that are useful to CO_2 capture. Among them are MEA), PZ, and MDEA. The amine partial pressures were obtained experimentally at absorber operating conditions of 40–70 ˚C and 1 atm using a hot gas FTIR. Given the partial pressures, the amine Henry's constants can be determined and are used as the primary indicator of amine volatility in this work. A group contribution model is developed using experimental H constants from this work along with those of 16 alkylamines obtained from the literature. This model is believed to be more reliable and accurate in the prediction of amine volatility for CO_2 capture amines compared to existing group contribution models such as UNIFAC and that of Hine and Mookerjee (1975). Although these other models are regressed using a larger database of compounds, they nonetheless fail to predict the experimental volatilities of CO_2 capture amines accurately since alkylamines were used to regress the group parameters. Meanwhile, the amines used for CO_2 capture application are much more structurally complex than alkylamines. In the case of the non-alkylamines, the presence of hydroxyl and ether groups can influence the interaction of the amine group with water differently than how the alkyl groups in alkylamines affect the interaction of the amine group with water. Thus, amine group parameters regressed from alkylamine data are not reliable in predicting the volatility of non-alkylamines such as the ones used in CO_2 capture.

Experimental Apparatus

Amine Concentration Determination

The amine concentration was determined by acid titration with an automatic Titrando series titrator with automatic equivalence point detection. A 300X diluted sample was titrated with 0.1 N H_2SO_4 to a pH of 2.4. The amount of acid needed to reach the equivalence point at a pH of 3.9 was used to calculate the total amine concentration. The reproducibility of this method is about 1%.

Amine Volatility

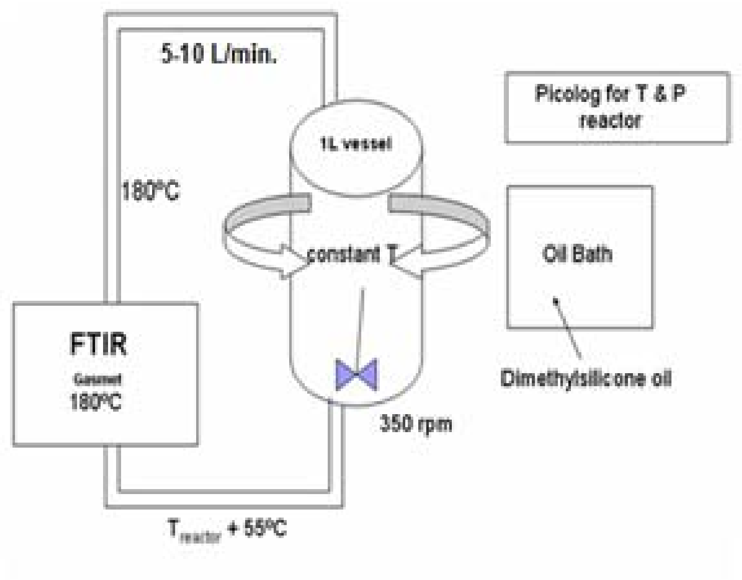

Figure 1: FTIR System for Amine Volatility

Amine volatility was measured in a stirred reactor coupled with a hot gas FTIR analyzer (Fourier Transform Infrared Spectroscopy, Temet Gasmet Dx-4000) as shown in Figure 1. This was the same method and apparatus used by Nguyen et al. (2010) and Hilliard (2008) to measure amine volatility and CO_2 partial pressure in loaded solutions. The 1 L glass reactor was agitated at 350 rpm ± 5 rpm. Temperature in the reactor was controlled to ±0.1 °C by circulating dimethylsilicone oil. The reactor was insulated with thick aluminum insulation. The temperature inside the reactor was measured with a platinum resistance thermometer with an accuracy of ± 0.01 °C. Vapor from the headspace of the reactor was circulated at a rate of ~5–10 L/min. by a heated sample pump to the FTIR through a heated Teflon line. Both the line and analyzer were maintained at 180 °C to prevent possible condensation or adsorption of amine. The FTIR measured amine and water concentration in the gas. The relative standard uncertainty in the vapor phase measurement was reported to be ±2% by Goff (2005). After the gas passed through the FTIR, it was returned to the reactor through a heated line maintained ~ 55 °C hotter than the reactor. With the 55 °C difference, the measured water concentrations were found to remain consistent, within 0.5–1%, between continuous instrument samplings at a given temperature. Upon completion of a given experiment, approximately 25 mL of liquid sample was taken to verify the amine concentration using acid titration.

FTIR calibration for each amine was performed with a syringe pump, a manual needle valve, and a stainless steel injection chamber. A known nitrogen flow rate, typically 2 SLPM, is introduced to the calibrator at room temperature via a mass flow controller. The syringe pump injects a known and very precise flow of the target amine to be calibrated into the nitrogen flow in a heated injection chamber kept at 180 °C. This produces a continual flow of a known concentration calibration gas that is introduced into the FTIR analyzer at 180 °C. A spectrum of a known mixture of the target gas and N_2 is measured and saved as a reference calibration.

Calibration is performed at each concentration of interest. If the target amine is a solid at room temperature, it is necessary to dilute it in deionized water up to the point where it is soluble. The diluted amine-water mixture is then injected into the heated chamber. In this case, the water component is subtracted from the overall spectra leaving the target amine as the remaining residual spectra. The amine residual is then saved as a reference calibration. PZ was calibrated by this method because it is a solid at room temperature.

Theory

Amine volatility is expressed using the Henry's constant (H) given by

$$H_{amine} = P_{amine} / \gamma_\infty * x_{amine} \tag{1}$$

where:

P_{amine} is the amine partial pressure
x_{amine} is the amine liquid phase mole fraction
γ_∞ is the asymmetric amine activity coefficient defined at the reference state of infinite dilution of amine in water

At the dilute amine concentrations used in the experiments (0.1–1.5 m amine in H_2O), the amine asymmetric activity coefficients are assumed to be 1. In actuality, extrapolating the data from the dilute experimental amine concentration to infinite dilution shows that the asymmetric activity coefficients are usually within ±10% of unity. This result will be demonstrated in the *Results and Discussion* section.

The temperature dependence of the amine Henry's constants is assumed to obey the Gibbs-Helmholtz relation as follows:

$$-d(\ln H_{amine}) / d(1/T) = \Delta H_{solution}/R \tag{2}$$

The Henry's constant is estimated as a function of temperature by::

$$H_{amine}(T) = H_{amine,313.15K} * \exp[-\Delta H_{sol}/R(1/T - 1/313.15K)] \tag{3}$$

Data

Table 1 gives the experimental amine partial pressures and Henry's constants for the 20 CO_2 capture amines investigated in this work. Amine and water partial pressures are estimated to have ±6% error. The experimental amine H constants are expected to have ±10% error in consideration of: (1) experimental uncertainty and (2) deviation of experimental condition from infinite dilution of amine in water.

Table 1: Amine and Water Partial Pressures for Amines Investigated from 40–70 ˚C

T (C)	P_{amine} (Pa)	P_{H2O} (kPa)	H_{amine} (Pa)		T (C)	P_{amine} (Pa)	P_{H2O} (kPa)	H_{amine} (Pa)
0.5 m MDEA (N-Methyldiethanolamine)					**0.09 m 1,4 DMPZ (1,4-Dimethyl Piperazine)**			
40	0.265	7.39	29.7		40	2.71	6.87	1510
45	0.288	9.38	32.3		45	4.44	8.63	2470
50	0.312	12.6	35.0		50	8.15	11.4	4540

55	0.369	15.9	41.4		55	12.9	14.8	7160
60	0.455	19.8	51.0		60	21.0	18.6	11700
65	0.593	25.4	66.5		65	33.8	24.1	18800
70	0.767	31.4	85.9		70	53.1	30.7	29500
0.48 m PZ (Piperazine)					**0.47 m DMAEE (2,2-Dimethylamino Ethoxy Ethanol)**			
40	0.399	7.27	46.6		40	0.504	7.05	60.0
45	0.516	9.17	60.2		45	0.614	8.74	73.2
50	0.630	12.2	73.5		50	0.803	11.5	95.8
55	0.930	15.5	109		55	1.46	14.9	174
60	1.36	19.3	159		60	2.04	18.8	243
65	2.11	25.0	246		65	3.69	24.3	440
70	3.09	31.7	361					
					0.57 m DMEA (Dimethylethanolamine)			
0.45 m DGA$^{®}$ (Diglycolamine$^{®}$)					40	21.4	6.93	2110
40	0.153	7.06	19.1		45	31.5	8.72	3100
45	0.159	8.95	19.8		50	47.7	11.5	4700
50	0.169	11.7	21.0		55	69.7	15.0	6860
55	0.202	15.3	25.1		60	96.9	18.9	9540
60	0.261	19.0	32.5		65	139	24.4	13700
65	0.382	24.5	47.5		70	194	30.8	19200
0.49 m MAPA (3-Methylamino Propylamine)					**0.48 m MORPH (Morpholine)**			
40	1.28	9.11	147		40	8.78	7.05	1020
45.1	1.56	12.0	178		45	13.1	8.94	1530
50	2.54	16.3	291		50	19.0	11.8	2220
55	3.34	20.5	382		55	26.6	15.1	3100
60	4.96	26.3	567		60	39.6	19.2	4620
65.2	7.47	33.8	855		65	54.7	24.7	6380
					70	76.5	31.0	8930
0.5 m EDA (Ethylenediamine)					**0.28 m DMORPH (Dimorpholino Diethyl Ether)**			
40	0.892	7.29	100		40	0.254	6881	50.7
45	1.03	9.19	116		45	0.263	8675	52.5

50	1.59	12.2	179		50	0.283	11567	56.5
55	2.09	15.8	234		55	0.371	15057	74.0
60	3.05	19.7	342		60	0.394	19046	78.5
65	4.10	25.3	459		65	0.465	24730	92.7
					70	0.491	31112	97.8
0.7 m MEA (Ethanolamine) (Kim et al., 2008)					**0.13 m HEP (Hydroxyethyl Piperazine)**			
40	0.728	7.28	60.0		40	0.089	7172	38.0
60	5.87	19.6	432		45	0.168	9065	72.1
80	13.9	46.4	954		50	0.341	11854	146
100	49.8	99.5	3481		55	0.393	15341	169
					60	0.460	19226	197
0.3 m DAP (1,2-Diaminopropane)					65	0.506	24804	217
40	0.636	5.76	118		70	0.596	31279	255
45	1.21	7.54	226					
50.2	1.59	10.0	295		**0.22 m DL-ALA (DL-Alaninol)**			
55	2.13	13.1	397		40	0.680	7075	172
60.1	3.01	17.3	561		45	0.839	9068	213
65	4.03	22.1	750		50	1.12	11858	285
					55	1.67	15147	424
1.05 m 1MPZ (1-Methyl Piperazine)					60	2.55	18934	645
40	2.65	6.87	143		65	4.20	24215	1065
45	4.94	8.82	266					
50	7.51	12.3	405		**0.5 m DEA (Diethanolamine)**			
55	11.6	14.6	628		40.1	0.178	7387	19.9
60	18.7	18.6	1010		45	0.199	9283	22.3
65	29.1	23.7	1566		50	0.215	12078	24.1
					55	0.227	15771	25.4
0.44 m AMP (2-Amino-2-Methyl-1-Propanol)					60	0.240	19565	26.9
40	2.48	7.27	316		65	0.243	25154	27.2
45	3.60	9.19	458					
50	5.71	12.2	727		**0.95 m 2MPZ (2-Methyl Piperazine)**			
55	8.50	15.9	1082		40	0.811	6758	48.2
60	12.2	19.8	1547		45	1.26	8674	75.0

65	18.2	25.5	2315		50	2.13	10850	127
					55	2.87	13685	170
0.1 m HMDA (Hexamethylenediamine)					60	4.46	17798	265
40	0.265	6.98	148		65	7.24	21681	431
45	0.277	8.78	154		70	10.6	33589	630
50	0.284	11.6	158					
55	0.366	14.9	204					
60	0.530	18.7	295					
65	0.809	24.2	450					
70	0.931	29.5	518					

Table 2 displays the experimental H constants for 16 alkylamines at 25 ˚C (Hine & Mookerjee, 1975).

Table 2: Henry's Constants for 16 Alkylamines at 25 ˚C

Amine	**H_{amine} (Pa)**
Ethylamine	57100
Propylamine	68700
Butylamine	84500
Pentylamine	137000
Hexylamine	150000
Dimethylamine	99200
Diethylamine	143000
Dipropylamine	286000
Dibutylamine	509000
Piperidine	24900
Pyrrolidine	13400
Hexamethyleneimine	34400
Trimethylamine	584000
Triethylamine	826000
N-Methylpyrrolidine	169000
N-Methylpiperidine	194000

Amine Structures

Figure 2 shows the structures for all 19 amines that were investigated in this work.

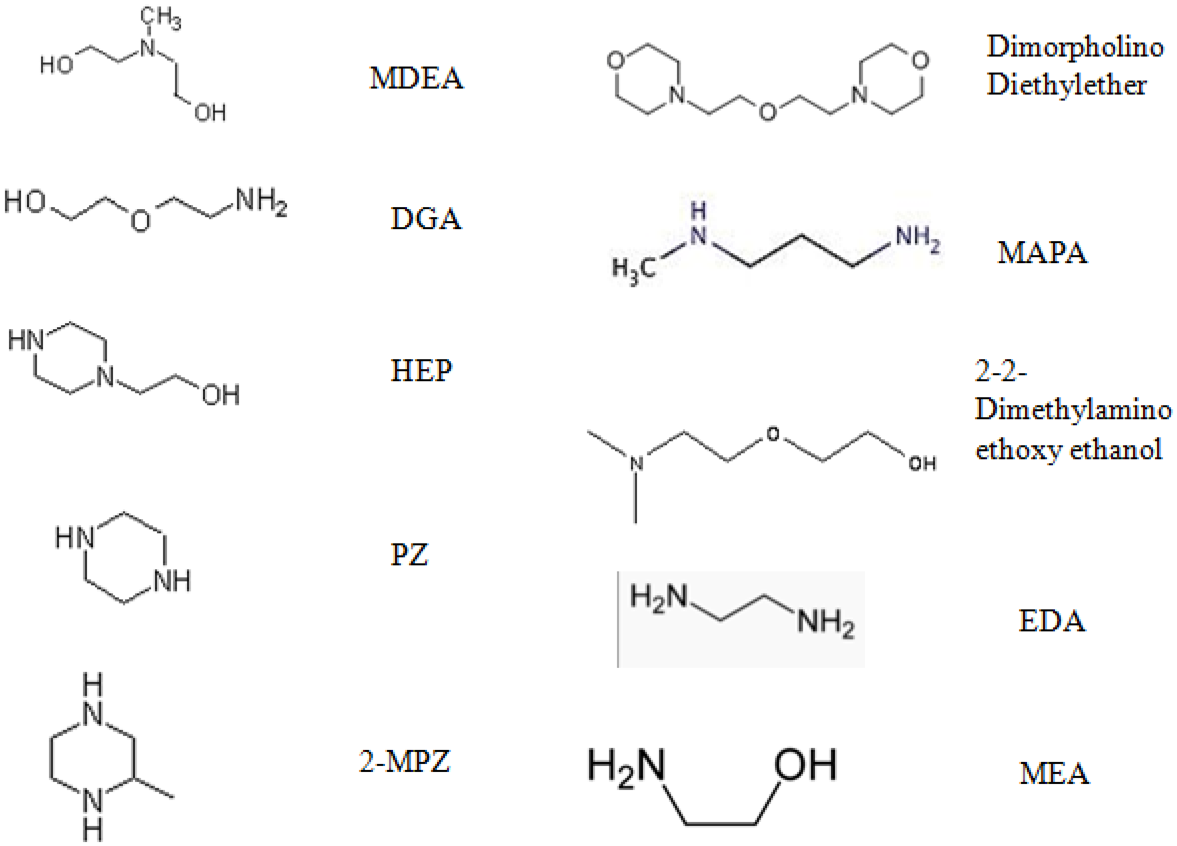

Figure 2: Amine Structures

HMDA

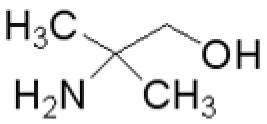

AMP

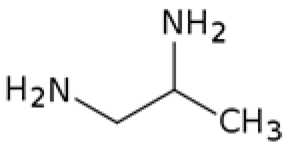

1,2-Diaminopropane

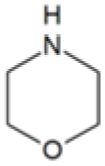

Morpholine

1-Methyl PZ

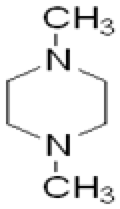

1,4 DMPZ

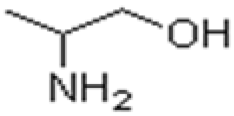

DL-Alaninol

DMMEA

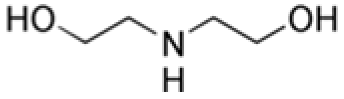

Diethanolamine

Figure 3: Amine Structures (Continued)

Results and Discussion

This work assumes that the experimental Henry's constant is within ±10% of the Henry's constant at infinite dilution in water. Figure 4 shows how the experimental (asymmetric) activity coefficient of PZ in H_2O varies with PZ concentration at 60 ^{o}C.

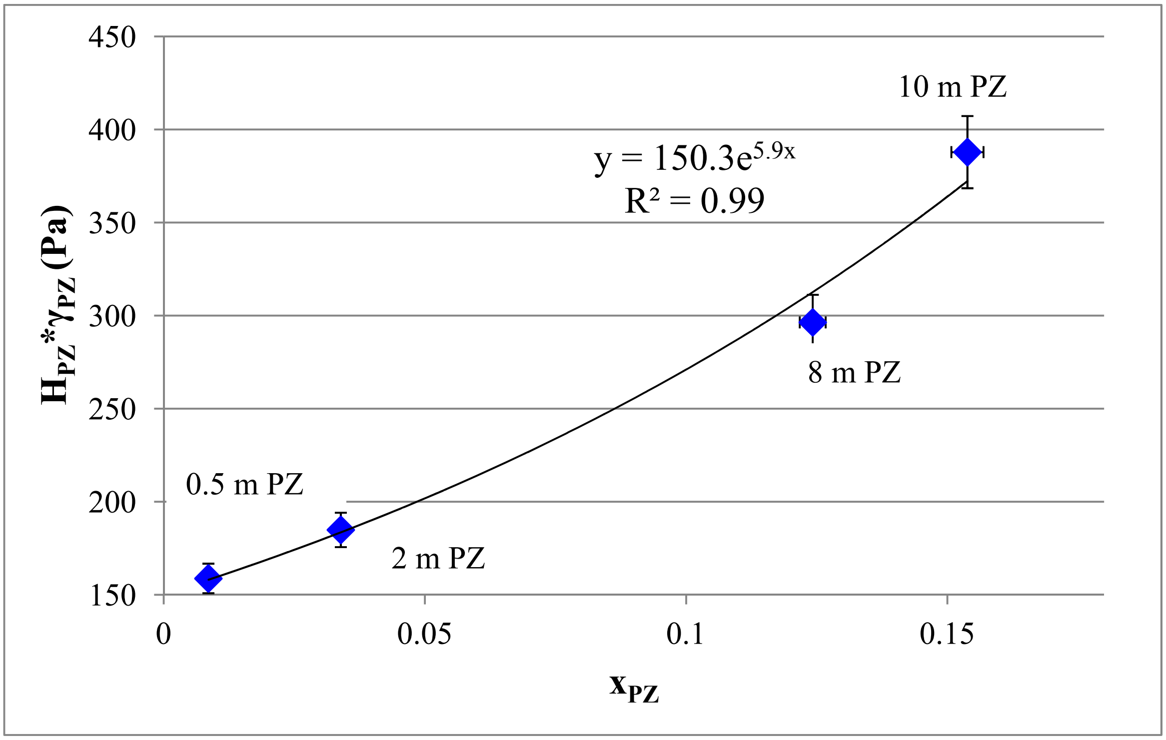

Figure 4: Behavior of Asymmetric PZ Activity Coefficient in H_2O at 60 ˚C

The true Henry's constant determined by the extrapolation of this data to zero PZ is ~150 Pa. Table 3 summarizes the estimated PZ activity coefficient at other PZ concentrations.

Table 3: PZ Activity Coefficient for 0.5–10 m PZ at 60 ˚C, $H_{PZ,60C}$ = 150 Pa

PZ (m)	x_{PZ}	$\gamma_{PZ,60C}$
0.5 m	8.57E-03	1.05
2 m	3.39E-02	1.22
8 m	1.24E-01	2.08
10 m	1.54E-01	2.48

The experimental PZ Henry's constant at 60 ˚C was determined at the most dilute PZ concentration where volatility was still detectable by the FTIR (0.5 m PZ). At this concentration, the asymmetric PZ activity coefficient is estimated to be 1.05 which is only 5% from unity which is the value of the activity coefficient at infinite dilution of PZ in water. The true H constant at infinite dilution is estimated to be ~150 Pa whereas the experimental H constant, determined at 0.5 m PZ condition, is ~158.9 Pa. This difference between the true versus experimental H constant is only 6%; therefore, the experimental H constant can be justifiably assumed to be the true H constant of an amine in water within such margin of error (attributed to deviation in the amine activity coefficient from unity). For all other amine systems studied, the experimental H constants are generally assumed to have a ±10% margin of error as the amine concentrations vary between 0.1 and 1.05 m amine. The exact percentage of error cannot be determined for each amine because no extensive data was taken to study amine volatility as a function of concentration.

The empirical model of aqueous amine Henry's constants consist of two parts: (1) a correlation of H constants at 40 ˚C (313.15K) to molecular structures using a group contribution method; (2) an empirical extrapolation of H constants as a function of temperature using estimated values of the amine heats of solution which are also correlated to structures.

In developing a correlation between amine H constants at 40 ˚C and molecular structures, it was necessary to obtain estimates of the alkylamine H constants at 40 ˚C using the published values at 25 ˚C along with the measured heats of solution for some of the alkylamines. For those alkylamines without heats of solution reported, it was necessary to estimate these enthalpies based on the presence of functional groups and how they contributed to the enthalpies measured for similar alkylamines. For example, the heat of solution for propylamine in water can be estimated from reported heats of solution for methylamine and ethylamine. Given that $\Delta H_{sol}/R$ of methylamine (1 CH_3 + 1 NH_2) is reported ~2600 K and that of ethylamine (1 CH_2 + 1 CH_3 + 1 NH_2) is ~3600K by Sander et. al (1999), one can deduce that the CH_2 group contributes ~1000 K to the enthalpy of solution of ethylamine. Using this rationale, the enthalpy of solution of propylamine, which has yet one more CH_2 group attached to ethylamine, one can estimate that its heat of solution is approximately ~4600K due to the presence of this additional CH_2 group. Table 4 provides the estimated heats of solution and H constants at 40 ˚C for all of the alkylamines considered in this work. The experimental H constants for the alkylamines are from Hine and Mookerjee (1975) whereas the heats of solution are obtained from Sander et al. (1999).

Table 4: Henry's Constants of Alkylamines at 298K and 313K

Alkylamine	H_{298K} (experimental)	$\Delta H_{sol}/R$ (K)	H_{313K} (est.)
Pyrrolidine	13388	7600	45394
Piperidine	24930	7900	88701
Hexamethyleneimine	34413	8200	128487
Ethylamine	57111	3600	101836
Propylamine	68662	4600 (est.)	143772
Butylamine	84473	5600 (est.)	207706
Dimethylamine	99247	4000	188717
Pentylamine	136999	6600 (est.)	395568
Diethylamine	143456	10000	715237
Hexylamine	150217	7600 (est.)	598091
N-Methylpyrrolidine	168546	7600	571471
N-Methylpiperidine	193517	7900	688536
Dipropylamine	286232	16000 (est.)	3741872
Dibutylamine	509001	22000 (est.)	17447283
Trimethylamine	584411	6000 (est.)	1532348
Triethylamine	825503	15000 (est.)	9190004

The H constants for alkylamines were estimated by invoking Equation 3 provided that the reported H constants at 298.15K and the heats of solution were now determined already. The experimental H constants at 40 ˚C for 19 of the CO_2 capture amines studied in this work and for 16 alkylamines were correlated to molecular structures in the following semi-empirical model:

$$\ln H_{amine,313.15K} = \text{Intercept} + \sum k_j * n_j \tag{4}$$

where:

k_j is the parameter value for functional group j
n_j is the number of occurrences of group j in an amine structure

A total of 35 data points, representing H constants for 35 amines at 40 ˚C, were regressed in Excel to provide the functional group parameter values. Table 5 summarizes the parameter results for Equation 4.

Table 5: Functional Group Parameter Values for Aqueous H Constant Estimates at 40 ˚C

Group j	Parameter Value	Standard Error
NH_2	-6.63	0.82
N_{cy}	-6.60	0.67
N	-5.51	1.59
NH	-5.46	1.15
OH	-5.14	0.58
O	-3.91	1.06
O_{cy}	-1.73	0.90
C_{cy}	0.67	0.34
CH_2 or CH	0.81	0.21
CH_3-(N)	1.15	0.76
CH_3-(C)	1.23	0.53
CH_3-(N_{cy})	1.58	0.64
Intercept	14.8	1.4

The model differentiates between primary (NH_2), secondary (NH), and tertiary (N) amines. There are also two other important distinctions made among the groups: (1) cyclic (cy) versus non-cyclic structure – this distinction is not found in the earlier group contribution model by Hine and Mookerjee (1975) but is warranted in this work; (2) differentiation among methyl groups by the neighboring groups attached to them – in this case, the neighboring group attached to the methyl can either be a straight chained amine (N), a cyclic amine (N_{cy}), or a straight chained carbon (C). The goodness of fit statistic R^2 is ~0.95 which indicates a robust fit of the experimental H. The parameter values are all statistically significant as they are larger than their corresponding standard errors.

In Table 5, the functional group parameters are ranked from top to bottom in the order of most polar to most non-polar as given by their signed magnitudes. Polar groups, such as the amines and ether, are hydrophilic in nature. The presence of hydrophilic groups tends to lower the tendency to volatilize into the vapor phase; thus, hydrophilic groups are seen to have negative parameter values as they decrease the magnitudes of the H constants. Conversely, non-polar groups such as the alkyl groups tend to increase the tendency to volatilize; therefore, they have positive parameter values which increase the magnitudes of the H constants. Finally, the relative order of the groups matches intuition in that amine groups are more polar than hydroxyl (OH) which in turn are more polar than the ether (O) group.

Figure 5 shows how the natural log of the amine H constants calculated from the model compare to experimental values.

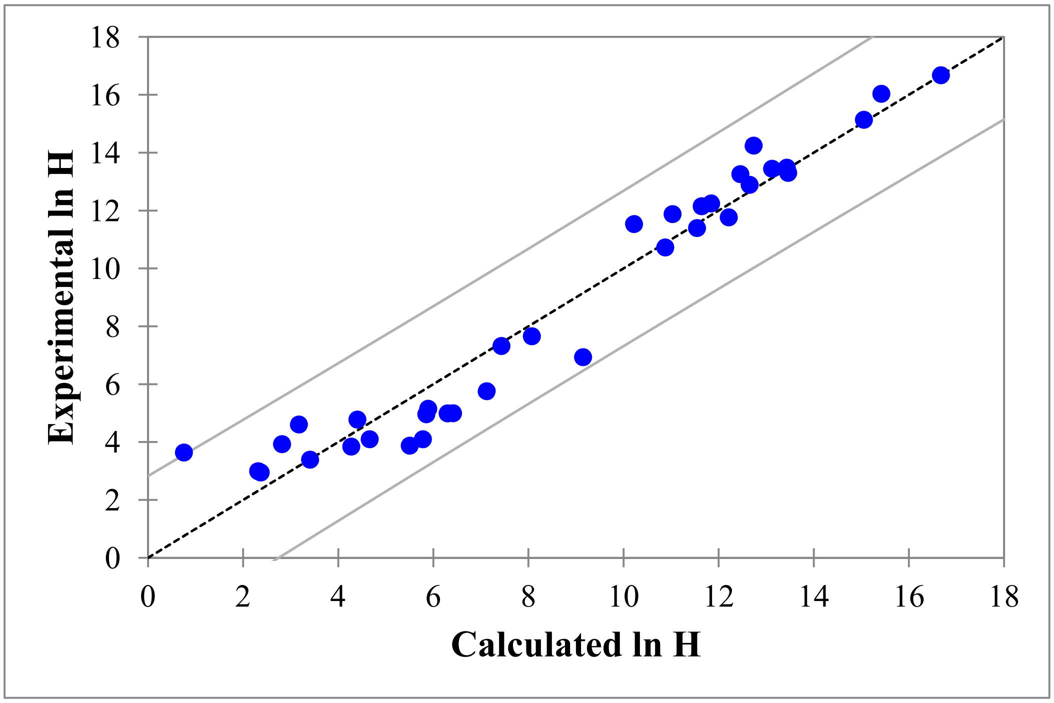

Figure 5: Evaluation of Aqueous Amine H Constant Model (40 ˚C)

It can be seen that the model can represent the majority of the experimental data to well within ±25%.

The second half of the modeling efforts involves capturing the temperature behavior of the amine Henry's constants between 25–70 ˚C. In theory, the model should be able to extrapolate even outside this temperature range, given its form. The experimental heats of solution for all 35 amines are correlated to the functional groups presented earlier according to the following form:

$$\Delta H_{sol}/R = \text{Intercept} + \sum k_j * n_j \qquad (5)$$

Table 6 summarizes the functional group parameter values for the heat of solution correlation.

Table 6: Functional Group Parameter Values for Amine Heat of Solution Estimates

Group j	$\Delta H_{sol}/R$ Contribution (K)	Standard error
O_{cy}	-3270	1986
OH	2044	1286

NH$_2$	-852	1818
O	-618	2343
CH$_3$-(N)	-339	1669
C$_{cy}$	443	744
N$_{cy}$	597	1481
C	625	455
CH$_3$-(N$_{cy}$)	1403	1419
NH	2218	2528
CH$_3$-(C)	2355	1165
N	2930	3500
Intercept	4587	3075

The R^2 for the heat of solution fit is only ~0.64 which indicates that the fit is not very robust. Bawsed on their associated standard errors, some of the parameters are not statistically significant. These observations suggest that there is not as strong an intrinsic correlation between the amine heat of solution and molecular structures as there is between the latter and aqueous volatility. Nevertheless, a group contribution method must also be used to represent the amine heats of solution for purposes of representation and prediction of new amines in the future.

Figure 6 shows how the amine heats of solution predicted using group contribution parameters from Table 6 compare to experimental values.

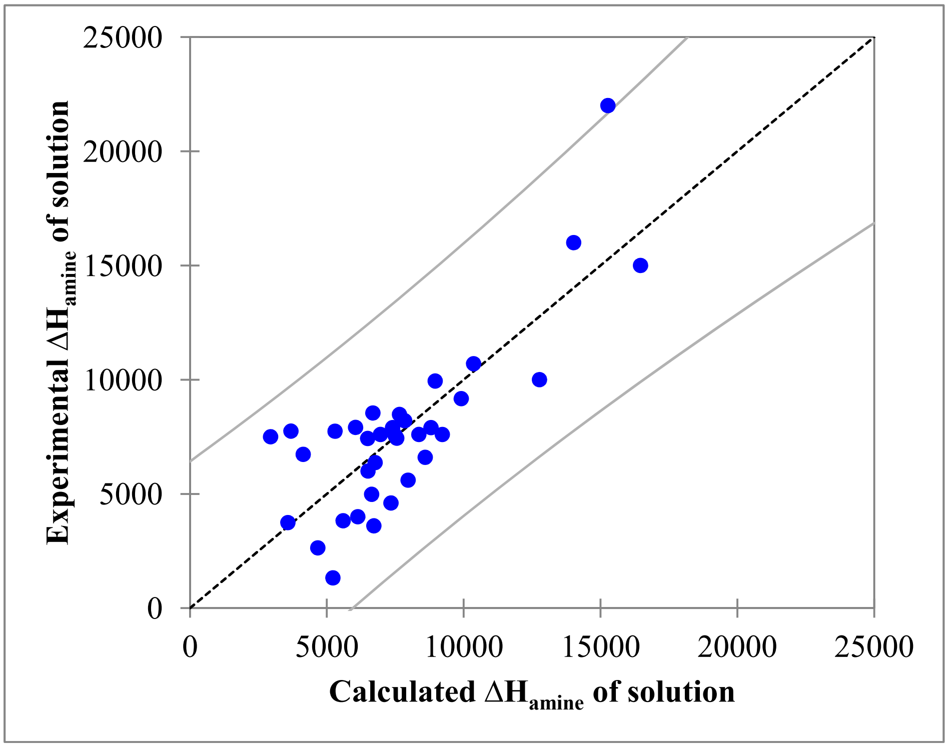

Figure 6: Evaluation of Predicted Amine Heats of Solution

In Figure 6, the predicted heats of solution for the majority of the amines were well within ±33% of the experimental values.

Provided the estimated amine Henry's constant at 40 ˚C (Equation 4) and the heat of solution (Equation 5), one can predict the amine Henry's constant at a temperature of interest using Equation 3. Figure 7 compares the experimental and predicted values of amine Henry's constant for all 35 amines (19 CO_2 capture amines and 16 alkylamines) considered in this work for the range of temperature from 25–70 ˚C.

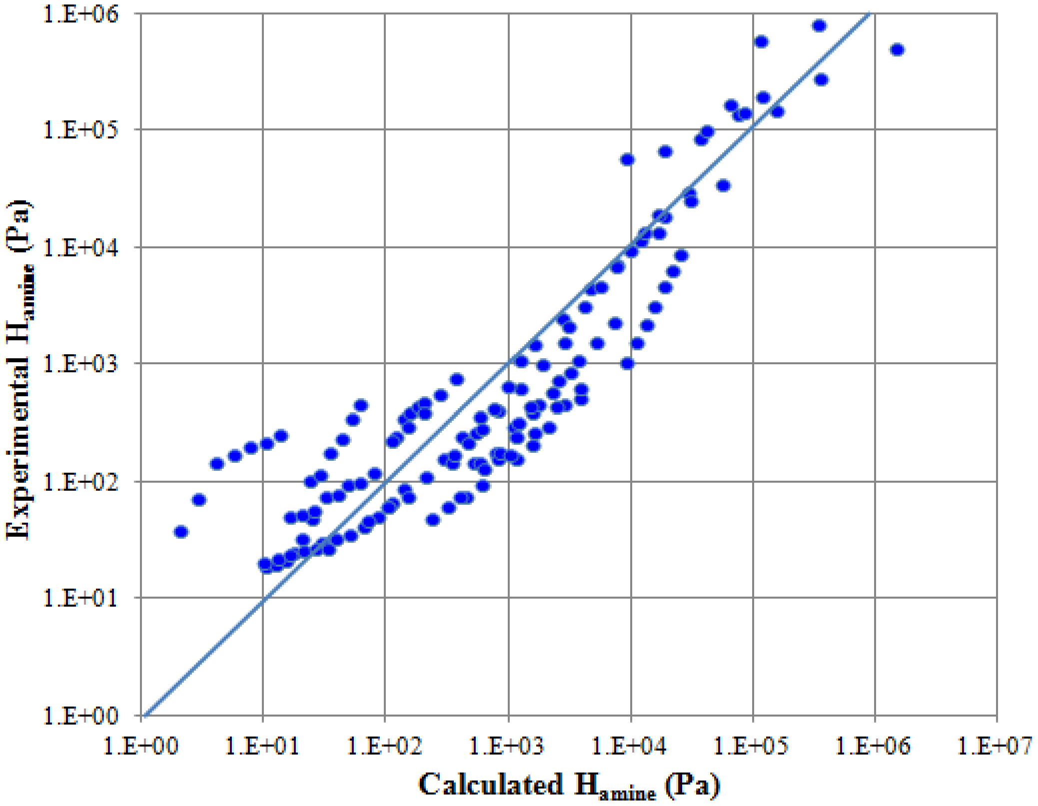

Figure 7: Evaluation of Predicted Amine Henry's Constants from 25–70 ˚C

In Figure 7, it can be seen that the group contribution model within this work does a fair job of representing the Henry's constants of all 35 amines from 25–70 ˚C. The predictions are within an order of magnitude of the experimental values. .

Conclusions

1.Given the dilute amine concentrations at which the Henry's constants are measured, these constants are expected to be ±10% from the true H constants at infinite dilution of amine in water.

2. Polar groups (such as the amine, hydroxyl, and ether groups) have favorable interactions with water and thereby decrease an amine's tendency to volatilize into the vapor phase. In order of increasing hydrophilicity, $O_{cy} < O < OH < NH < N < N_{cy} < NH_2$.

3. Non-polar groups have unfavorable interactions with water which result in the amine having a greater tendency to volatilize from the aqueous solution. In order of increasing hydrophobicity, $C_{cy} < CH_2$ (or CH) $< CH_3$-(N) $< CH_3$-(C) $< CH_3$-(N_{cy}).

4. The group contribution model developed was able to represent the natural log of the experimental amine H constants at 40 ˚C, for both the 19 CO_2 capture amines from this work and 16 alkylamines, to well within ±25%.

5. For temperature between 40 ˚ - 70 ˚C, the calculated H constants estimated by the model were found to be well within an order of magnitude of the experimental values.

References

Cai Z, Xie R, Wu Z. "Binary Isobaric Vapor-Liquid Equilibria of Ethanolamines + Water." *J Chem Eng Data*. 1996;41:1101–1103.

Goff GS. *Oxidative Degradation of Aqueous Monoethanolamine in CO_2 Capture Processes: Iron and Copper Catalysis, Inhibition, and O_2 Mass Transfer*. The University of Texas at Austin. Ph.D. Dissertation. 2005.

Hilliard MD. *A Predictive Thermodynamic Model for an Aqueous Blend of Potassium Carbonate, Piperazine, and Monoethanolamine for Carbon Dioxide Capture from Flue Gas*. The University of Texas at Austin. Ph.D. Dissertation. 2008.

Kim I, Svendsen HF, Borresen E. "Ebulliometric Determination of Vapor-Liquid Equilibria for Pure Water, Monoethanolamine, N-Methyldiethanolamine, 3-(Methylamino)-propylamine, and Their Binary and Ternary Solutions." *J Chem Eng Data*. 2008;53:2521–2531.

Larsen BL, Rasmussen P, Fredenslund A. "A Modified UNIFAC Group Contribution Model for Prediction of Phase Equilibria and Heats of Mixing." *Ind Eng Chem Res*. 1987;26:2274–2286.

Lenard J, Rousseau R, Teja A. "Vapor-Liquid Equilibria for Mixtures of 2-aminoethanol + water." *AIChE Symp Ser*. 1990;86.

Mookerjee PK, Hine J. "The Intrinsic Hydrophilic Character of Organic Compounds. Correlations in terms of Structural Contributions." *J Org Chem*. 1975;40:292–295.

Nguyen T., Hilliard MD, Rochelle GT. "Amine Volatility in CO_2 Capture." *Int J Greenh Gas Con*. 2010;4:707–715.

Pappa G, Anastasi C, Voutsas E. "Measurement and thermodynamic modeling of the phase equilibrium of aqueous 2-amino-2-methyl-1-propanol solutions." *Fluid Phase Equilib*. 2006;243:193–197.

Sander R, "Compilation of Henry's Law Constants for Inorganic and Organic Species of Potential Importance in Environmental Chemistry." Version 3. 1999.

Characterization of AMP/PZ

Quarterly Report for January 1 – March 31, 2012

by Han Li

Supported by the Luminant Carbon Management Program

Department of Chemical Engineering
The University of Texas at Austin

April 30, 2012

Abstract

Piperazine (PZ) has been investigated as a promising solvent for carbon dioxide capture. In this study, 2-amino-2-methyl-1-propanol (AMP) was chosen as an additive to PZ to increase CO_2 capacity and CO_2 heat of absorption and to avoid solids precipitation. Experimental results on solid solubility, CO_2 solubility, mass transfer rate, viscosity, volatility, heat capacity, NMR speciation and thermal degradation are given for 5 m (mol/kg H_2O) PZ/2.3 m AMP. 2 m PZ/4 m AMP was also investigated.

The goal of this study is to construct a thermodynamic model in Aspen Plus® to predict the properties of PZ/AMP/CO_2/H_2O over a wide range of conditions and to develop a kinetic model to predict CO_2 mass transfer rates. The acquired thermodynamic data for 5 m PZ/2.3 m AMP and 2 m PZ/4 m AMP will be regressed with other data from the literature. The resulting models will be used in absorption/stripping process modeling. In this quarter, the thermodynamic model for AMP/H_2O, AMP/$AMPH^+$, and AMP/CO_2/H_2O has been finished.

Introduction

PZ is a cyclic amine with two secondary amine nitrogens, which has the advantages of fast reaction rate, high capacity, and resistance to oxidation and thermal degradation. However, the solid solubility results show that for 8 m PZ, the critical CO_2 loading to inhibit crystallization at 0 °C is about 0.3 mol/mol alkalinity (Freeman, 2010). AMP is a hindered amine. The lean/rich loading for 4.8 m AMP is 0.27/0.56 mol/mol alkalinity (Chen, 2011), which has the advantages of high capacity, low regeneration heat, resistance to oxidation, and thermal degradation, but the reaction rate between 4.8 m AMP and CO_2 is only one third of 8 m PZ.

CO_2 solubility, heat capacity, CO_2 absorption rate, density, and viscosity of the AMP/PZ blend have been investigated by several researchers, but they focused on the physical properties of the unloaded blend and the highest experimental temperature was 80 °C. In this study, AMP will be examined as an additive to PZ, measuring unloaded and loaded physical properties, high temperature CO_2 solubility, mass transfer rates, and speciation.

Based on all the experimental results, the thermodynamic model will be built for the use of absorption/stripping process modeling. The method is to reconcile the separate AMP and PZ models via cross parameters to accurately model PZ/AMP blended amines. The PZ model has been finished by Frailie (2011).

This is a cumulative report on the solvent system PZ/AMP. In this quarter, results are added on the thermal degradation for 5 m PZ/2.3 m AMP with a loading of 0.4 mol CO_2/mol alkalinity. The solid solubility and total pressure measurement for 2 m PZ/4 m AMP are discussed. Initial thermodynamic models for AMP/H_2O and AMP/CO_2/H_2O are presented.

Literature Review

There are 12 references related to PZ/AMP blends. The CO_2 absorption rate, CO_2 solubility, heat capacity, and physical properties such as density and viscosity for PZ/AMP/CO_2/H_2O were studied. The modeling of the mass transfer process was discussed.

Physical Properties

The physical properties of blends of AMP and PZ, as measured in the literature, are listed in Table 1. In addition to density and viscosity, Sun (2002) measured the diffusivity of N_2O in these solutions and these measurements are applied to estimate CO_2 diffusivity. This experiment was performed in a wetted wall column with a reported error of 2%. Paul (2006) and Samanta (2006) correlated the results as a function of temperature and amine concentration, while Murshid (2011) regressed them as a function of temperature.

Table 1: Physical properties measured in literature

Author Year	Properties	Temperature/K	Concentration
Sun **2002**	Density Viscosity	303.15-313.15	AMP: 1.0, 1.5 M PZ: 0.1-0.4 M
Paul **2006**	Density Viscosity	288-333	Total: 30 wt % PZ: 3-12 wt %
Samanta **2006**	Density Viscosity	298-333	Total: 30 wt % PZ: 2-8 wt %
Dash **2011**	Density Viscosity	303-323	Total: 40 wt % PZ: 2-8 wt %
Murshid **2011**	Density Viscosity Surface tension Refractive index	298.15-333.15	Total: 30 wt % PZ: 1.74-10.35 wt %

Chen **2009**	Heat capacity	303.2-353.2	14 different concentrations

Chen (2010) reported heat capacity data for the system (AMP-PZ-H_2O) and applied the Redlich-Kister-type model to estimate excess molar heat capacities, keeping the mole fractions of water at 0.6, 0.7, 0.8, and 0.9. All the solutions are investigated without CO_2 loading.

Reaction kinetics

Table 2 lists research on the reaction kinetics in PZ/AMP. PZ was in all cases regarded as an activator.

Table 2: Reaction Kinetics Summary in Literature

Amines	Rate Constants $k_{2,AMP}$ m^3/kmol/s	Temperature	Concentration	CO_2 partial pressure	Author Year
HMDA+AMP **MDEA+AMP** **PZ+AMP**	$k_H=3.84\times10^{10}\exp\left(-\frac{5361}{T/K}\right)$ $k_M=6.60\times10^{9}\exp\left(-\frac{4959}{T/K}\right)$ $k_P=9.09\times10^{9}\exp\left(-\frac{5058}{T/K}\right)$	303-343K	1 wt %, 3 wt %, 5 wt % additives + 30 wt % AMP	/	Choi 2007
PZ+AMP	/	298-313K	2-8 wt % PZ added to keep the total 30 wt %	2-14kPa	Samanta 2008
AMP **AMP+PZ**	AMP: 1150 at 303K 1241 at 313K AMP+PZ: 1500 at 303K 1771 at 313K	303-313K	0.55-3.35 M AMP + 0.115-0.233 M PZ	/	Seo 2000
PZ **PZ+AMP**	$3.13\times10^{7}\exp\left(-\frac{3034}{T/K}\right)$	303.15-313.15K	1-1.5 M AMP + 0.1-0.4 M PZ	/	Sun 2002
PZ+AMP	/	303-323K	2-8 wt % PZ added to keep the total 40 wt %	5-15kPa	Dash 2011

The zwitterion mechanism is generally accepted as the reaction mechanism between CO_2 and PZ-activated aqueous AMP. The reaction of CO_2 and AMP is second order. Choi (2007) conducted the measurements in a stirred cell reactor and compared the enhancement of absorption rate by different additives. The results showed that HMDA promoted the rate most.

Samanta (2008) developed a coupled mass transfer-reaction kinetics-equilibrium model according to Higbie's penetration theory, to predict the absorption rates and enhancement factors. The predicted results were compared with experimental data of absorption of CO_2 into AMP+PZ in a wetted wall contactor. By parametric sensitivity analysis, the author suggests that formation of PZ-dicarbamate is important in the overall kinetics of CO_2-AMP-PZ. Seo (2000) used a wetted sphere absorber. Sun (2002) modeled the kinetic data with a hybrid reaction rate model, a second-order reaction for the reaction of CO_2 with PZ, and a zwitterion mechanism for the reaction of CO_2 with AMP. The overall pseudo first-order reaction rate constants were obtained through measurements in a wetted wall absorber. The author's calculation showed that there was a small difference between the overall and apparent rate constant. Dash (2011) modeled the mass transfer process through Aspen Plus® to predict CO_2 absorption rate and enhancement factor. The results showed that 35 wt % AMP + 5 wt % PZ appeared to produce the optimum absorption rate.

CO_2 Solubility

Yang (2009) measured CO_2 solubility in an aqueous mixture of PZ and AMP, in which PZ acts as a promoter. The apparatus used was a 1.0 L stainless steel vapor-recirculation equilibrium cell. The temperature and pressure were controlled at the range of 313.2–353.2 K and up to 152 kPa. The concentrations of AMP were 2 and 3 M, while those of PZ were 0.5–1.5 M. The Kent-Eisenberg model was adapted to represent the data. Dash (2011) also measured CO_2 solubility with a high pressure stainless steel stirred equilibrium cell at 303–323 K and 298–328 K. The CO_2 partial pressure was controlled at 0.1–140 kPa and 0.1–1450 kPa. 2–8 wt % PZ was added to the aqueous AMP solutions to keep the total concentration at 30 wt % and 40 wt %. An e-NRTL model was adapted in Aspen Plus®. This model was used to predict speciation, heat of absorption, pH of the CO_2 loaded solution, and amine volatility, but the model was not verified.

Experimental Methods

Solvents used in this research are listed in Table 3.

Table 3: Chemical Species Used for Solvent Preparation

Chemical	Purity	Source	CAS#
Piperazine	98%	Sigma-Aldridge	110-85-0
2-amino-2-methyl-1-propanol	99%	Acros Organics	124-68-5

Loaded solutions were prepared gravimetrically on a scale. The calculated amounts of DDI water and amines were weighed and mixed in a 500 mL flask. The well mixed solution was transferred to the loader and a gas sparging cap was placed on top of the loader. The CO_2 inlet lines and CO_2 vent lines were attached to the glass flanges on the gas sparger. TheCO_2 flow was started until the desired amount of CO_2 was absorbed by the solution, as determined gravimetrically.

Solid solubility experiments were conducted in a water bath with the temperature maintained within the range of 0–80 °C. The solution was prepared at loadings of 0.05, 0.10, 0.15, 0.20, 0.25, 0.30, 0.35, 0.40, and 0.45 mol CO_2/equiv amine. The loaded and unloaded samples were set at 40 °C, 30 °C, and 25 °C overnight to have a feel for the transition temperature. The temperature of the water bath was then carefully increased to melt the slurry. The melting temperature is regarded as the transition temperature.

Two experiments on aqueous AMP solution were performed in a jacketed loader with a stirring bar. The initial concentrations of the experiments were 12 m AMP and 10 m AMP. The solution was loaded until solids precipitated. Then the temperature was increased to 35 °C, 40 °C, 50 °C, and 60 °C and samples were taken at each point. 8 to 10 hours were allowed to reach the solid-liquid equilibrium. The samples were immediately diluted in DDI water to prevent crystallization.

The low temperature CO_2 solubility data and mass transfer rates from 20 to 100 °C were measured using the wetted wall column. The method is identical to that used by Hilliard (2008).

The high temperature CO_2 solubility data were obtained from total pressure measurement with a sealed autoclave. The experimental method can be found in Xu's progress report (Rochelle, 2010).

Amine volatility measurements were performed in a volatility apparatus equipped with a heat-insulated glass reactor and a FTIR to analyze the gas composition and a computer to record the FTIR results online. The detailed operation is described in Hilliard (2008).

Thermal degradation: The thermal degradation experimental method was developed by Davis (2009). Half-inch 316L stainless steel tubing was cut into 10 cm segments and fitted on each end with Swagelok® endcaps. The endcaps were tightened as much as possible to hold high pressures and maintain the concentration of amine and carbon dioxide in solution. A set of cylinders loaded with the same solution was created and placed in an oven. Individual sample cylinders were removed at specified time intervals and cooled to room temperature before opening for analytical testing.

Analytical Methods

Amine titration: An automatic Titrando series titrator with an acid dispenser and a pH probe to determine the concentration of total alkalinity of an amine solution at room temperature was used (Hilliard, 2008). The acid is 0.2 N H_2SO_4. 0.2 g of sample combined with 60 mL DDI water was used for each titration. Throughout the titration, PC control automatically recorded the volume of acid added and current pH. The titrator would stop when the pH reached 2.4 and the Titrando then gave the equivalence point by judging the change in slope of the titration curve and the amount of acid needed to reach that point.

Total inorganic carbon (TIC) measurement: The apparatus used to measure the concentration of CO_2 in amine consists of a rotameter type gas flow meter, glass injection tube with injection port and frit, two glass cylinders used as desiccant tubes, CO_2 detector, and a computer (Hilliard, 2008). 1 to 1.5 mL of phosphoric acid (H_3PO_4) was injected into the injection port and 100X dilute sample was introduced into the same port. The released CO_2 was carried by nitrogen (N_2), whose flow rate was maintained at a reading of 12 by the rotameter, to travel through the acid and desiccant and finally reach the Horiba PIR 200 infrared detector. PicoLog software recorded the change in voltage. A calibration curve was produced at the end of each analysis using a 1000 ppm standard inorganic carbon solution, a mixture of Na_2CO_3 and $NaHCO_3$.

Cation chromatography: A Dionex ICS-2100 modular IC system with AS-DV autosampler was used to determine amine concentration by identifying and quantifying positively charged ions in solution (Freeman, 2011). An IonPac CG17 guard column (4 x 50 mm) and an IonPac CS17 analytical column (4 x 250 mm) were used for the separation based on adhesion properties of different molecules to the medium, which was ethylvinylbenzene cross-linked with 55% divinylbenzene resin. A 10,000X dilute sample was sent to the eluent stream, onto the columns, then to a 4-mm Cationic Self-Regenerating Suppressor (CSRS) to remove anionic species. The eluent stream contained varying concentrations of methanesulfonic acid (MSA) in analytical grade water. Finally, the stream reached the conductivity detector (CD). Changes in solution conductivity were detected in the CD and were used to create a chromatogram.

Mass spectrometry (MS): Samples were introduced directly by syringe pump injection to the electrospray ionization (ESI) unit. A detector measured the amount of ionized particles of each mass and the result was a spectrum. MS was mainly used to qualitatively determine the molecular weight of unknown molecules of interest (Freeman, 2011).

Rheometer: Viscosity was measured using a Physica MCR 301 cone and plate rheometer (Freeman, 2011). This apparatus controlled temperatures from -30 to 150 °C. By assuming Newtonian fluids, the viscosity was determined by measuring the torque applied to the fluid during the rotation of the cone, which was proportional to the shear stress in the fluid.

Results and Discussion

Aqueous AMP solution

Solid solubility of loaded aqueous AMP solutions is shown in Table 4. As the most concentrated solution used in previous research is 4.8 m, no solid issues are reported.

Table 4: Solid solubility of loaded AMP aqueous solution

T °C	α mol CO_2/mol alkalinity	AMP mol AMP/kg H_2O
21	0.11	11.01
35	0.31	5.22
35	0.47	6.69
40	0.398	8.23

40	0.474	6.67
50	0.40	8.90
60	0.394	9.36

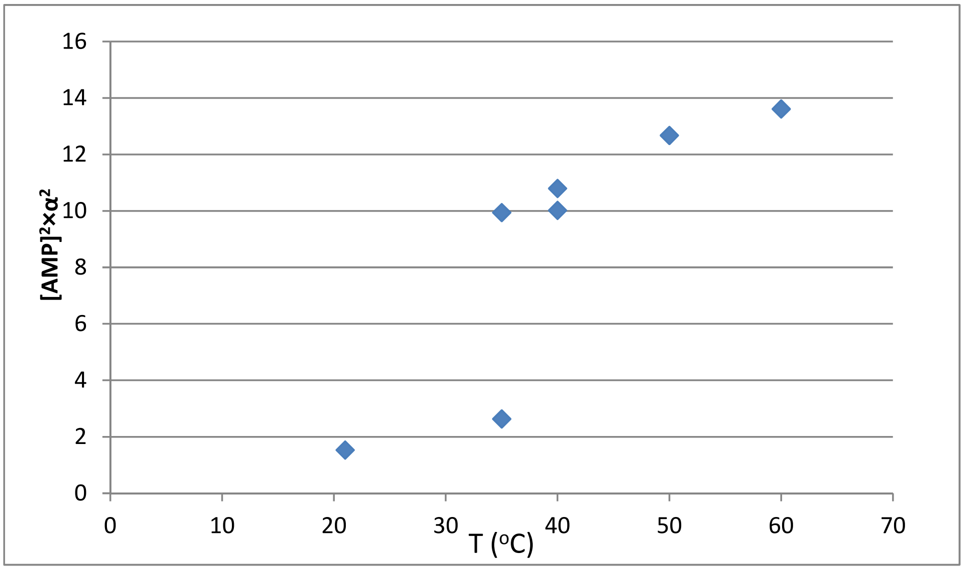

Figure 1: Relationship between $\alpha^2 * [AMP]^2$ and temperature

As AMP-carbamate is not stable, we can ignore its existence. We assume that the composition of the loaded solution includes AMPH$^+$, HCO$_3^-$, and free AMP. The solid may be (AMPH$^+$)(HCO$_3^-$), whose equilibrium in solution is as follows:

$$(AMPH^+)(HCO_3^-) \overset{K_{sp}}{\Leftrightarrow} AMPH^+ + HCO_3^-$$

K_{sp}, which is a function of temperature, can be expressed as $K_{sp} = [AMPH^+] * [HCO_3^-]$, in which:

$$[HCO_3^-] = [AMPH^+] = \alpha * [AMP]$$

The relationship between $\alpha^2 * [AMP]^2$ and temperature is shown in Figure 1.

The results in Figure 1 are not consistent with assumption that the solid is (AMPH$^+$)(HCO$_3^-$). There may be two different solid phases, one at high temperature and one at low temperature respectively, which need additional investigation.

6 m PZ/4 m AMP

The transition temperature of loaded 6 m PZ/4 m AMP and 6.5 m PZ/3 m AMP is listed in Table 5. The comparison of the solubility window with 8 m PZ (Freeman, 2011) is shown in Figure 2.

Table 5: Transition temperature of loaded 6 m PZ/4 m AMP

α mol CO_2/mol alkalinity	Transition T/℃
0	37.0
0.043	34.0
0.097	30.0
0.145	26.0
0.163	24.0
0.225	15.0
0.292	3.0
0.309	0.0
0.337	0.0
0.341	40.0

Figure 2 shows that substituting 2 m PZ with 4 m AMP will narrow the solubility window and present a smaller rich loading boundary, which will also reduce the operating range. To find a possible concentration that will not precipitate at room temperature, the supernatant of the slurry with a total 0.41 loading at room temperature was analyzed. The results from cation chromatography and total inorganic carbon analyzer showed that 6 m PZ/3.2 m AMP with a loading of 0.44 will be soluble.

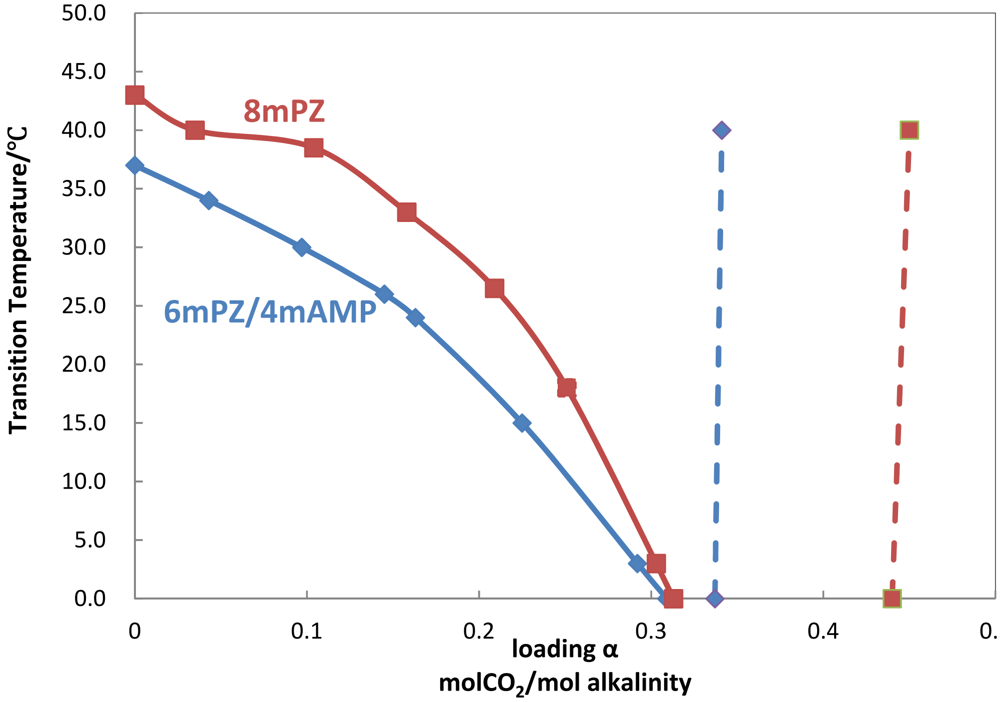

Figure 2: Comparison of solubility window between 6 m PZ/4 m AMP and 8 m PZ

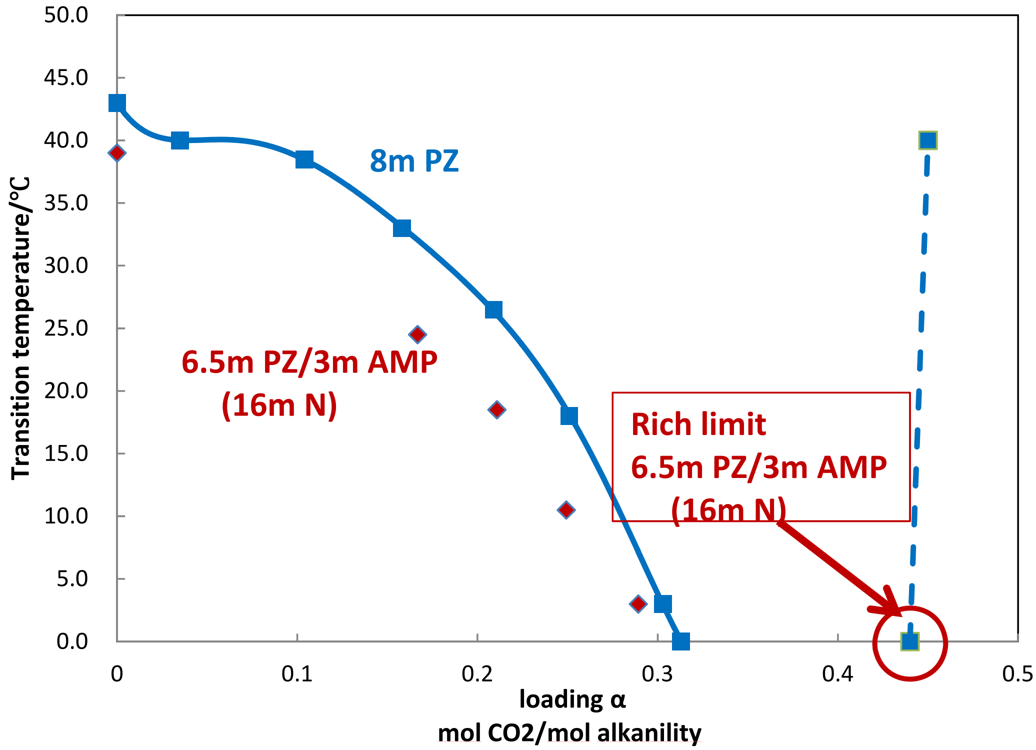

Figure 3: Comparison of solubility window between 6.5 m PZ/3 m AMP and 8 m PZ

6.5 m PZ/3 m AMP

To obtain a comparable CO_2 capacity with 8 m PZ, 16 m alkalinity is kept when preparing the blend. Thus 6.5 m PZ/3 m AMP was chosen as the second blend to be researched. The transition temperature of loaded solution is listed in Table 6.

Table 6: Transition temperature of loaded 6.5 m PZ/3 m AMP

6.5 m PZ/3 m AMP	
α mol CO_2/mol alkanility	Transition T/℃
0	39.0
0.167	24.5
0.211	18.5
0.249	10.5
0.289	3.0
0.445	0

Figure 2 shows the comparison of solid solubility window between this blend and 8 m PZ. They have similar lean and rich boundary at 0 °C.

The total pressure over the loaded blend was measured at 100–160 °C. The partial pressure of CO_2 was calculated by subtracting the partial pressure of N_2 and water from the pressure. P_{water} was assumed to follow the Raoult's Law and P_{amine} was neglected.

Table 7: Total pressure and CO_2 partial pressure in 6.5 m PZ/3 m AMP

PZ/AMP		T	CO_2 ldg	Pt	P_{CO2}	PZ/AMP		T	CO_2 ldg	Pt	P_{CO2}
m		C	mol/mol alk	kPa	kPa	m		C	mol/mol alk	kPa	kPa
6.5	3	100	0.271	102	21.2	6.5	3	150	0.291	1141	764
6.5	3	120	0.270	243	84.9	6.5	3	160	0.283	1688	1199
6.5	3	130	0.269	370	154	6.5	3	100	0.440	469	392
6.5	3	140	0.266	580	291	6.5	3	120	0.429	1052	900
6.5	3	150	0.263	882	501	6.5	3	130	0.418	1673	1466
6.5	3	160	0.257	1311	817	6.5	3	140	0.409	2228	1951
6.5	3	120	0.303	293	135	6.5	3	150	0.393	3193	2828
6.5	3	130	0.300	470	256	6.5	3	160	0.378	4131	3658
6.5	3	140	0.297	734	447						

The liquid composition has been corrected for 100–160 °C data because the CO_2 loading in the liquid phase differs significantly from that measured at room temperature, especially at high temperature and high loading.

The total pressure and CO_2 partial pressure of this blend are listed in Table 7. An empirical model was developed by regressing CO_2 partial pressure as a function of temperature and CO_2 loading in the liquid phase.

$$lnP_{CO2} = (42.4 \pm 1.2) + (-16.5 \pm 3.5)\alpha + \frac{(-13811 \pm 487)}{T} + (12433 \pm 1408)\frac{\alpha}{T} \qquad (1)$$

The heat of absorption can be derived from the CO_2 partial pressure model according to the Gibbs-Helmholtz equation.

$$\Delta H_{abs} = -R\frac{\partial lnP_{CO2}}{\partial \frac{1}{T}} = -R(-13811 + 12433\alpha) \qquad (2)$$

The CO_2 loading at 40 °C when the CO_2 partial pressure is 0.5 kPa and 5.0 kPa can also be predicted from the CO_2 partial pressure model, which is exactly the definition of lean and rich loading. Then the CO_2 capacity of this blend can be obtained.

$$Capacity = mol\ CO_2/kg\ solvent = \frac{(\alpha_{rich} - \alpha_{lean}) \cdot mol\ alkalinity}{kg\ solvent} \qquad (3)$$

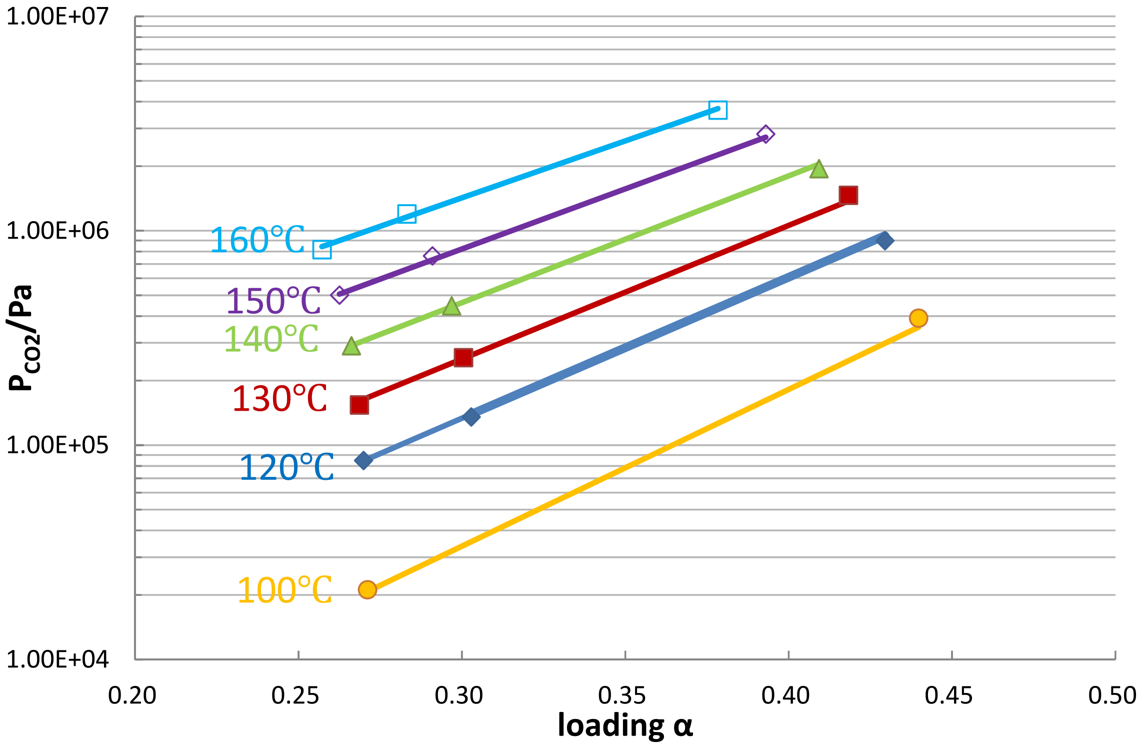

Figure 4: CO_2 solubility in aqueous 6.5 m PZ/3 m AMP [Points: experimental data. Lines: model (Equation 1)]

Figure 4 gives the CO_2 partial pressure from 100 to 160 °C at variable loading. The model fits the data well. The predicted CO_2 capacity, lean and rich loading and heat of absorption are listed in Table 8.

Table 8: Predicted properties of 6.5 m PZ/3 m AMP

CO_2 Capacity (mol CO_2/kg solvent)	0.87
Lean loading (mol CO_2/mol alkalinity)	0.342
Rich loading (mol CO_2/mol alkalinity)	0.441
$-\Delta H_{abs}$ @P_{CO2}=1.5 kPa (kJ/mol)	75

Table 9: Viscosity of loaded 6.5 m PZ/3 m AMP

T (°C)	25	40	60	80
CO_2 ldg (mol CO_2/mol alk)	**μ(cP)**	**μ(cP)**	**μ(cP)**	**μ(cP)**
0.448	37.96	22.05	11.29	6.95
0.305	27.54	15.35	7.53	4.57
0.271	29.83	15.82	8.93	4.83

The viscosity of 6.5 m PZ/3 m AMP at rich loading when the temperature is 40 °C is 22 cP, as listed in Table 9, while that of 8 m PZ at the same condition is 12 cP. But the viscosity is expected to be not much higher than 8 m PZ because high viscosity may reduce the mass transfer rate and affect the performance of the heat exchanger.

5 m PZ/2.3 m AMP

To achieve a lower viscosity than 6.5 m PZ/3 m AMP without significantly decreasing the CO_2 capacity and heat of absorption, the 6.5 m PZ/3 m AMP blend was diluted by 80%. The new blend is 5 m PZ/2.3 m AMP.

Viscosity

The viscosity of this blend was shown in Table 10. When the temperature is 40 °C, the viscosity is 11.63 cP at rich loading, which is acceptable.

Solid Solubility Observation

No solids were observed even when the loading was 0.5 at 0 °C, which means that there may be no rich boundary in this blend, but precipitation of solids began when the loading was lower than 0.3. The operating window is a little wider than 8 m PZ.

Table 10: Viscosity of loaded 5 m PZ/2.3 m AMP

T (°C)	40	60	80
CO_2 ldg (mol CO_2/mol alk)	**μ(cP)**	**μ(cP)**	**μ(cP)**
0.482	11.63		
0.387	10.37	5.79	3.93
0.302	8.53	4.85	3.19

CO_2 Solubility

The total pressure over the loaded blend was measured at 100–160 °C. The partial pressure of CO_2 was calculated by subtracting the partial pressure of N_2 and water from the pressure. P_{water} was assumed following the Raoult's Law and P_{amine} was neglected.

Table 11: Total pressure and CO_2 partial pressure in 5 m PZ/2.3 m AMP

PZ/AMP		**Temp**	**CO_2 ldg**	**Pt**	**P_{CO2}**	**PZ/AMP**		**Temp**	**CO_2 ldg**	**Pt**	**P_{CO2}**
m		**C**	**mol CO_2/mol alk**	**kPa**	**kPa**	**m**		**C**	**mol CO_2/mol alk**	**kPa**	**kPa**
5	2.3	120	0.297	285	120	5	2.3	100	0.436	347	264
5	2.3	130	0.295	447	222	5	2.3	110	0.432	530	413
5	2.3	140	0.291	680	378	5	2.3	120	0.427	823	661
5	2.3	150	0.286	1023	626	5	2.3	130	0.418	1255	1035
5	2.3	160	0.279	1500	974	5	2.3	140	0.410	1730	1436
5	2.3	120	0.382	531	368	5	2.3	150	0.397	2425	2037
5	2.3	130	0.376	840	617	5	2.3	100	0.494	751	670
5	2.3	140	0.369	1246	949	5	2.3	130	0.466	2119	1902
5	2.3	150	0.359	1821	1430	5	2.3	150	0.439	3619	3237
5	2.3	160	0.347	2528	2020						

The liquid composition has been corrected for 100–160°C data because the CO_2 loading in the liquid phase differs significantly from that measured at room temperature, especially at high temperature and high loading.

The total pressure and CO_2 partial pressure of this blend from 100 to 160 °C are listed in Table 11.

Table 12: CO_2 partial pressure in 5 m PZ/2.3 m AMP from wetted wall column

PZ/AMP		**Temp**	**CO_2 ldg**	**P_{CO2}**	**PZ/AMP**		**Temp**	**CO_2 ldg**	**P_{CO2}**
m		**C**	**mol CO_2/mol alk**	**Pa**	**m**		**C**	**mol CO_2/mol alk**	**Pa**
5	2.3	40	0.310	325	5	2.3	40	0.380	2204
5	2.3	60	0.310	2742	5	2.3	60	0.380	11464
5	2.3	80	0.310	11146	5	2.3	80	0.380	49169
5	2.3	100	0.310	59912	5	2.3	20	0.420	676
5	2.3	20	0.350	93	5	2.3	40	0.420	5325
5	2.3	40	0.350	844	5	2.3	60	0.420	26451
5	2.3	60	0.350	5979	5	2.3	20	0.465	2963
5	2.3	80	0.350	27778	5	2.3	40	0.465	17617
5	2.3	20	0.380	229					

Together with the low temperature data from 20 to 100 °C, which are shown in Table 12, an empirical model was generated by regressing CO_2 partial pressure as a function of temperature and CO_2 loading in the liquid phase.

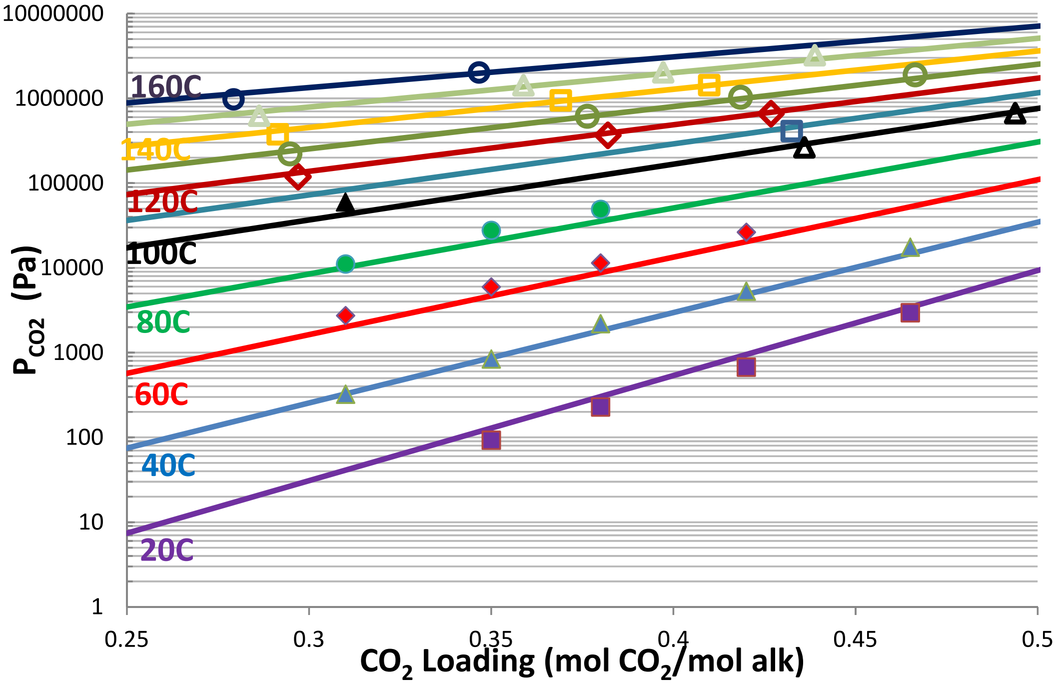

Figure 5: CO_2 Solubility for 5 m PZ/2.3 m AMP [Filled points: from wetted wall column. Empty points: from total pressure measurement. Lines: Eq. 4]

$$lnP_{CO2} = (46.7 \pm 2.6) + (-34.0 \pm 6.7)\alpha + \frac{(-15186 \pm 958)}{T} + (18338 \pm 2500)\frac{\alpha}{T} \qquad (4)$$

The heat of absorption can be derived from the CO_2 partial pressure model according to the Gibbs-Helmholtz Equation.

$$\Delta H_{abs} = -R\frac{\partial lnP_{CO2}}{\partial \frac{1}{T}} = -R(-15186 + 18338\alpha) \qquad (5)$$

The CO_2 loading at 40 °C when the CO_2 partial pressure is 0.5 kPa and 5.0 kPa can also be predicted from the CO_2 partial pressure model, which is exactly the definition of lean and rich loading. Then the CO_2 capacity of this blend can be obtained by Equation 3.

The comparison of CO_2 capacity, loading range, and heat of absorption between 5 m PZ/2.3 m AMP and 8 m PZ, and 4.8 m AMP is shown in Table 13. This blend has an unexpectedly lower CO_2 capacity than other two solvents. The delta loading of this blend is a little bit larger than 8 m PZ, the loss of CO_2 capacity is because of smaller total alkalinity in this blend. The heat of absorption of three solvents is comparable when the equilibrium partial pressure of CO_2 is 1.5 kPa.

Table 13: Comparison of 5 m PZ/2.3 m AMP, 8 m PZ, and 4.8 m AMP

	5 m PZ/2.3 m AMP	**8 m PZ**	**4.8 m AMP**
CO_2 Capacity (mol CO_2/kg solvent)	0.71	0.79	0.96
Lean loading (mol CO_2/mol alkalinity)	0.328	0.31	0.27
Rich loading (mol CO_2/mol alkalinity)	0.422	0.39	0.56
$-\Delta H_{abs}$ @P_{CO2}=1.5 kPa (kJ/mol)	69	70	73

CO2 mass transfer rates

As a complement to Table 12, Table 14 lists the CO_2 mass transfer rates in 5 m PZ/2.3 m AMP.

The detailed wetted wall column results are included in Appendix A.

Figure 6 compares the CO_2 mass transfer rates of this blend, 8 m PZ, and 4.8 m AMP (Chen, 2011). The rates of this blend are always much higher than those of 4.8 m AMP, but a little bit lower than those of 8 m PZ when the CO_2 loading is low. As the CO_2 loading gets richer, the difference in rates between this blend and 8 m PZ becomes smaller and this blend transfers CO_2 faster than 8 m PZ after a certain loading point.

Table 14: k_g' Measured for 5 m PZ/2.3 m AMP

CO_2 loading	**Temperature**	**k_g'**
mol CO_2/mol alk	°C	$\times 10^7$ (mol/s·Pa·m^2)
0.350	20	12.90
0.380	20	9.53
0.420	20	5.19
0.465	20	2.62
0.310	40	18.90
0.350	40	12.60
0.380	40	10.00
0.420	40	5.62
0.465	40	2.36
0.310	60	17.10
0.350	60	13.00
0.380	60	9.16
0.420	60	4.56
0.310	80	18.20
0.350	80	10.10
0.380	80	5.69

0.310	100	6.59

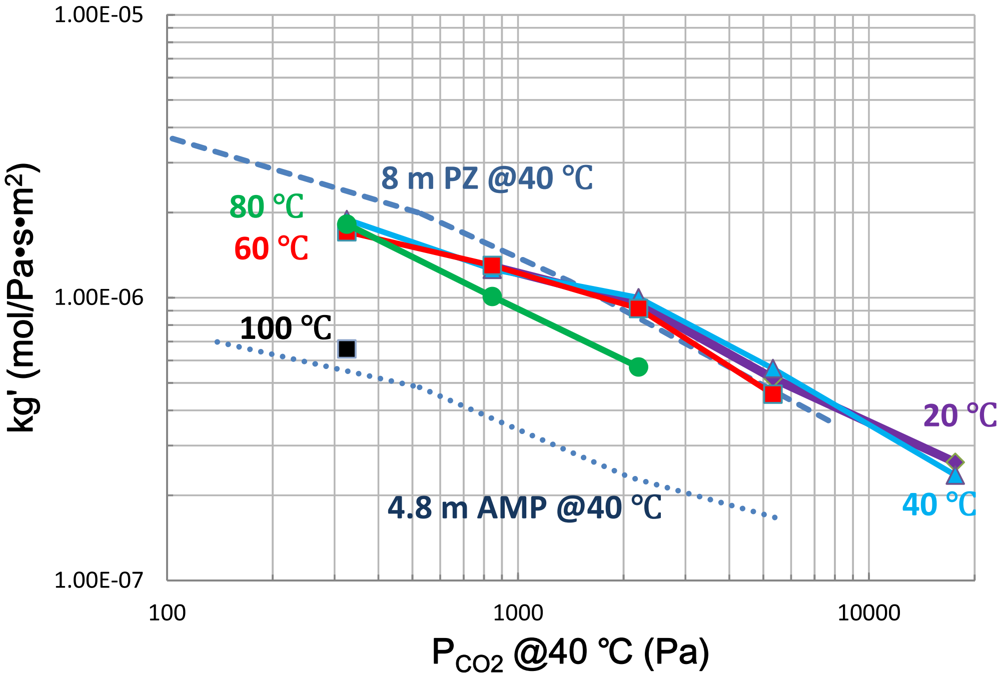

Figure 6: **CO_2 Liquid Phase Mass Transfer Coefficient (k_g')** **in 5 m PZ/2.3 m AMP**

Volatility

Partial pressures for amine, water, and carbon dioxide are calculated using the concentration readings from the FTIR multiplied by atmospheric pressure.

$$P_{amine} = P_{atm} \times \frac{\text{amine [ppm]}}{1{,}000{,}000}$$

$$P_{H_2O} = P_{atm} \times \frac{H_2O\text{ [ppm]}}{1{,}000{,}000}$$

$$P_{CO_2} = P_{atm} \times \frac{CO_2\text{ [ppm]}}{1{,}000{,}000}$$

After calculation, the volatility and CO_2 solubility for unloaded and loaded 5 m PZ/2.3 m AMP are shown in Table 15.

Table 15: Volatility and CO_2 solubility for unloaded and loaded 5 m PZ/2.3 m AMP

PZ/AMP		**T**	**CO_2 ldg**	**P_{PZ}**	**P_{AMP}**	**P_{H2O}**	**P_{CO2}**
m		**C**	**mol /mol alk**	**Pa**	**Pa**	**Pa**	**Pa**
5	2.3	40.1	0	4.78	12.15	5911	0
5	2.3	45	0	5.21	13.80	7130	0

5	2.3	50	0	8.46	21.06	9449	0
5	2.3	55	0	13.52	31.06	12203	0
5	2.3	60	0	15.46	40.17	15378	0
5	2.3	40	0.299	0.60	5.71	5723	244
5	2.3	45	0.299	0.65	8.24	7310	407
5	2.3	50.1	0.299	1.23	12.57	9757	677
5	2.3	55.1	0.299	1.90	17.65	12568	914
5	2.3	60	0.299	2.69	23.44	15822	1338
5	2.3	65	0.299	4.14	34.35	20050	2190

Figures 7–8 demonstrate that AMP is much more volatile than PZ. The volatility of PZ and AMP both decrease when CO_2 is loaded into the solution because of the decreasing concentration of free amine. But the volatility of PZ decreases faster than that of AMP, which suggests that CO_2 reacts first with PZ.

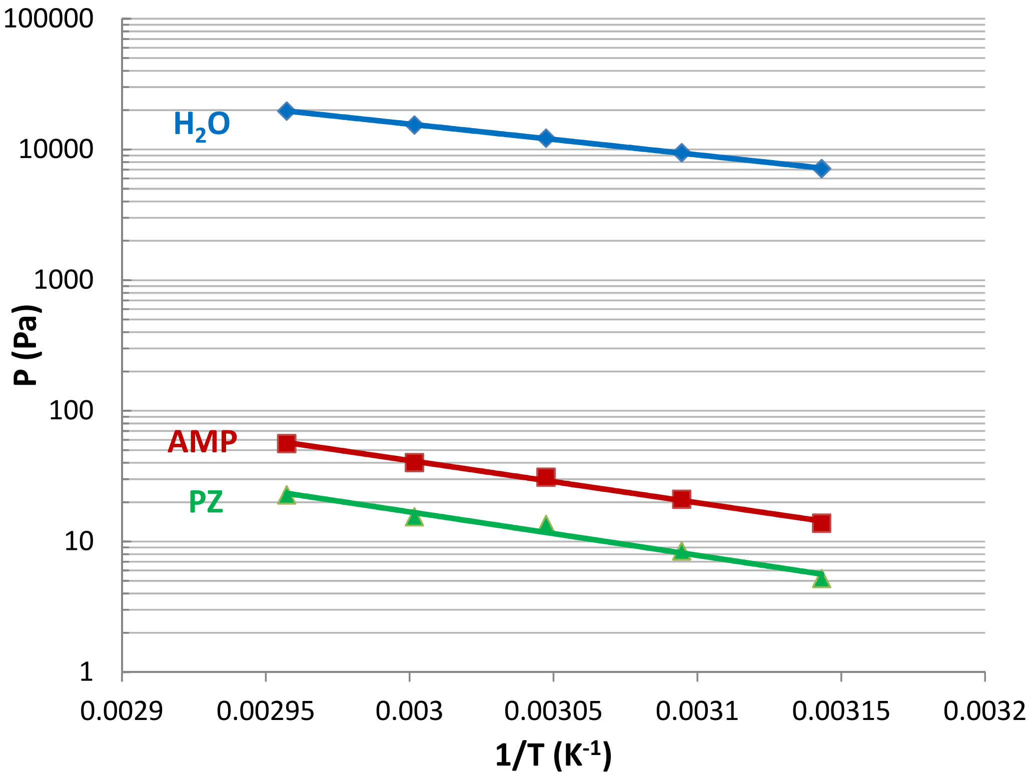

Figure 7: Amine volatility in aqueous unloaded 5 m PZ/2.3 m AMP

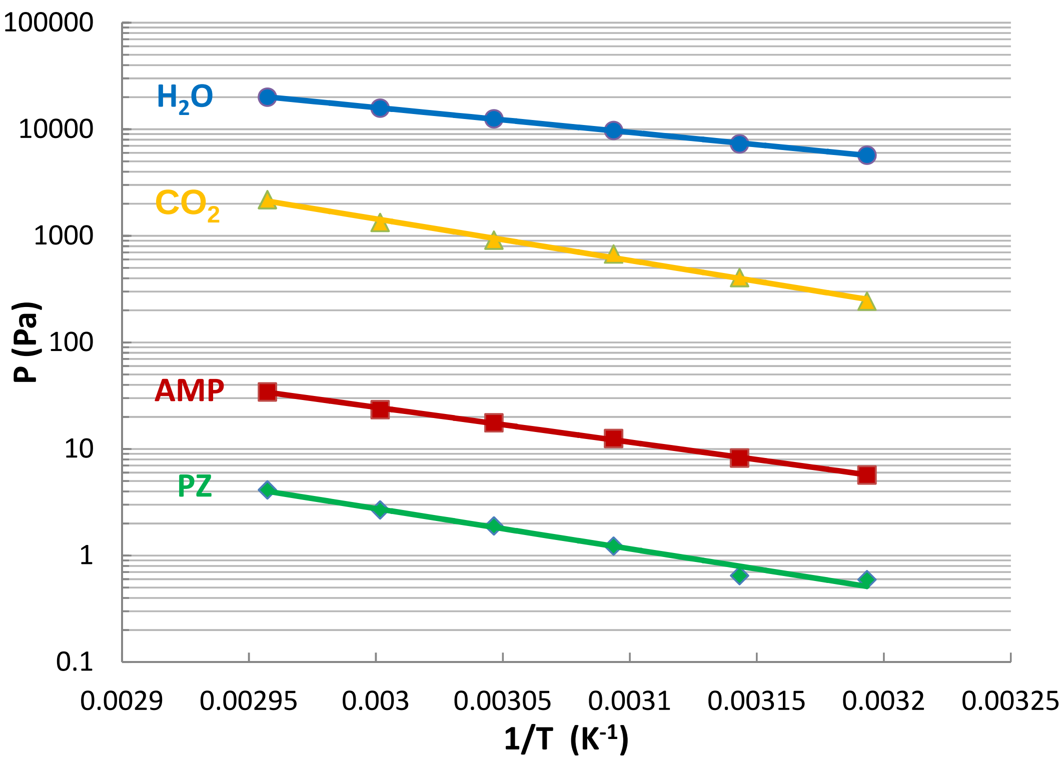

Figure 8: Amine volatility in aqueous 5m PZ/2.3m AMP when α = 0.3

Thermal degradation

Two parallel sets of experiments were performed for thermal degradation with 5 m PZ/2.3 m AMP loaded with 0.4 mol CO_2/mol alkalinity at 135 and 150 °C. Data can only be obtained for six weeks in the first set because of leakage. The second set is still ongoing. The raw data for the first set are listed in Appendix B.

Figures 9 and10 are typical cation chromatograms for degraded PZ/AMP. Figure 11 shows the concentration of PZ and AMP in degraded samples during the experiment.

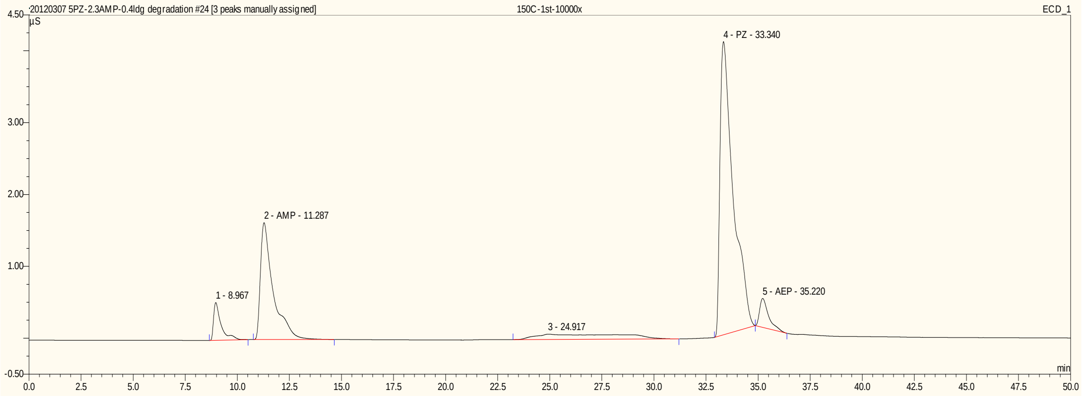

Figure 9: Cation chromatogram for thermally degraded 5 m PZ/2.3 m AMP, α = 0.4, T = 150 °C, t = 1 week

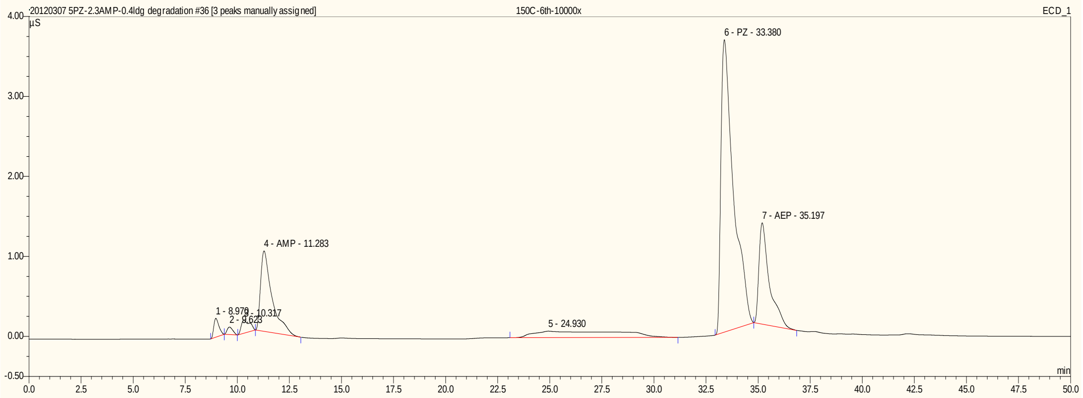

Figure 10: Cation chromatogram for thermally degraded 5 m PZ/2.3 m AMP, α = 0.4, T = 150 °C, t = 6 weeks

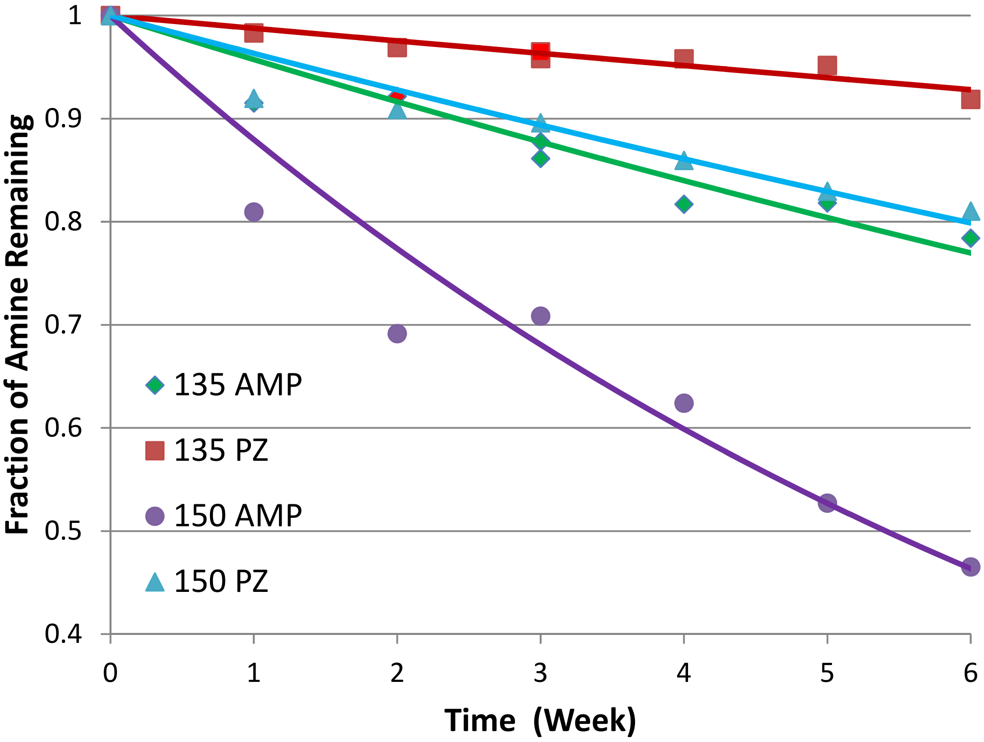

Figure 11: Thermal degradation of 5 m PZ/2.3 m AMP with 0.4 CO_2 loading

In Figures 9 and10, the x-axis represents the response time, while the y-axis is the response signal. The response time was used to identify the component referenced to the calibration curve, while the area under the peak was to quantify the concentration.

The area under the peaks at 9 min and 27 min does not change with reaction time, suggesting that these peaks are not degradation products. The area under the peak at 36 min shows obvious increasing trend with time, suggesting a possible main degradation product. The peaks at 11 min and 23.5 min have been identified as AMP and PZ.

AMP and PZ both degraded in the solution. The possible reaction pathway has been suggested by Zhou (Rochelle, 2009). From her analysis, the main degradation product is 1,1-dimethyl-2-piperazin-1-ethylamine (DPE), whose structure is shown in Figure 12.


1,1-dimethyl-2-piperazin-1-ethylamine (DPE) 1-(2-aminoethyl) piperazine (AEP)

Figure 12: Molecule structure

There is no commercial source of DPE, but 1-(2-aminoethyl) piperazine (AEP) has a similar structure to DPE, which is also shown in Figure 12. The concentration of DPE was estimated by the standard calibration of AEP. The molecular weight of DPE is 157.25.

Figure 13 gives the full MS scan for 5 m PZ/2.3 m AMP with 0.4 loading degraded for 6 weeks at 135 °C. The peak marked as 158.10 verifies the main degradation product as DPE.

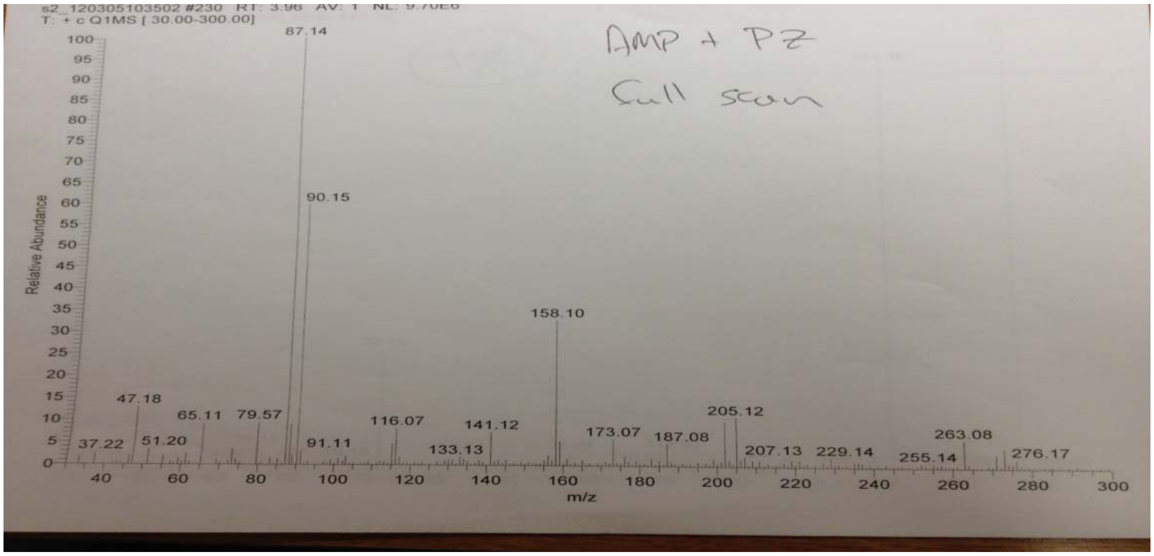

Figure 13: MS spectrum for degraded 5 m PZ/2.3 m AMP with a loading of 0.4 moles CO_2 per mole of alkalinity held at 135 °C for 6 weeks and injected by syringe pump

The loss rate of amine in thermal degradation was calculated by assuming that the total reaction was pseudo-first order. The method was suggested by Davis (2009).

where:

$C_{amine,0}$ is the initial concentration of amine,
C_{amine} is the concentration of amine at certain week,
t represents time,
k_1 is the reaction constant.

This can be put in the Arrhenius equation related to activation energy:

$$k_1 = A \cdot exp\left(\frac{E_A}{R} \cdot \frac{1}{T}\right) \qquad (7)$$

Davis determined that the acceptable operating temperature for 7 m MEA is 122 °C (Davis, 2009). This temperature corresponds to an apparent first order constant value of 2.91×10^{-8} s^{-1} and a loss of approximately 2% of the initial amine per week. Based on the acceptable loss rate of 7 m MEA, a tolerable stripper temperature can be determined for any amine.

A comparison of the reaction rate, activation energy, and estimated stripper temperature for different amines can be found in Table 16.

Table 16: Apparent first order rate constants, activation energy, and estimated stripper temperature of different amines

Amine	Components	Conc. (m)	Ldg (mol/mol alk)	$k_1\times10^9$ (s^{-1})		Act. Energy (kJ/mol)	T giving k_1 = 2.9e9 s^{-1} (°C)	Ref.
				135C	150C			
PZ	PZ	8	0.3	1	6	184	163	Freeman
PZ	PZ	8	0.4	0.5	8	191	162	Freeman
AMP	AMP	7	0.4	21	86	112	137	Davis
MEA	MEA	11	0.2	69	-	-	-	Davis
MEA	MEA	3.5	0.2	41	-	-	-	Davis
MEA	MEA	7	0.2	90	397	123	121	Davis
MEA	MEA	7	0.4	134	828	157	121	Davis
MEA	MEA	7	0.5	201	1300	162	-	Davis
MEA	MEA	11	0.4	174	-	-	-	Davis
MEA	MEA	11	0.5	249	-	-	-	Davis
MEA	MEA	3.5	0.5	137	-	-	-	Davis
PZ	PZ/AMP	6/4	0.4	32	92	-	-	Zhou et al
AMP	PZ/AMP	6/4	0.4	67	249	-	-	Zhou et al
PZ+ AMP	PZ/AMP	6/4	0.4	46	144	PZ(184)	134	Zhou et al
PZ	PZ/AMP	5/2.3	0.4	21	64	108	139	This work
AMP	PZ/AMP	5/2.3	0.4	72	214	104	123	This work
PZ+ AMP	PZ/AMP	5/2.3	0.4	36	103	102	132	This work

Both PZ and AMP have higher rate constant in PZ/AMP blend than in single amine system, but lower than MEA. Also, the estimated stripper temperature for PZ/AMP blend is lower than single PZ and AMP system, but still higher than MEA solution.

2 m PZ/4 m AMP

To characterize PZ/AMP, properties for different ratios of PZ to AMP are needed. Even though many researchers have performed experiments on this blend with less PZ than AMP, data is limited to low temperatures and unloaded solution. For solid solubility and viscosity reasons, 2 m PZ/4 m AMP was chosen.

Solid solubility observation

A set of solid solubility experiments for different ratios of PZ to AMP was performed at 0, 0.5, 0.55 loadings. The purpose was to find a blend that did not have the lean and rich boundary. The results at room temperature are shown in Table 17.

Table 17: Solid solubility observation

Ratios (m PZ/m AMP)	**Loading (mol CO_2/mol alka)**		
	0	0.50	0.55
3/6	S	NS	-
2/6	S	NS	
1.5/6	S	NS	-
3/5	NS	-	-
2/5	S	-	NS
2/4	S	-	S

(S represents soluble, NS represents non-soluble)

The unloaded solution was soluble for all the ratios besides the 3/5 blend, which was unusual. When 6 m AMP existed in the solution, the solids would precipitate at 0.5 loading even when the concentration of PZ was as low as 1.5 m. This observation showed that it was the excess AMP that led to the crystallization. But precipitation also occurred in 5 m AMP combined solution when the loading was 0.55. 2/4 blend was not observed to precipitate at either the lean or rich boundary.

Total pressure measurement

The total pressure over the loaded blend was measured at 100–160 °C. The partial pressure of CO_2 was calculated by subtracting the partial pressure of N_2 and water from the pressure. P_{water} was assumed following the Raoult's Law and P_{amine} was neglected.

Table 18: Total pressure and CO_2 partial pressure in 2 m PZ/4 m AMP

PZ/AMP		**Temp**	**CO_2 ldg**	**Pt**	**P_{CO2}**	**PZ/AMP**		**Temp**	**CO_2 ldg**	**Pt**	**P_{CO2}**
m		**C**	**mol CO_2/mol alk**	**kPa**	**kPa**	**m**		**C**	**mol CO_2/mol alk**	**kPa**	**kPa**
2	4	100	0.302	130	38.5	2	4	100	0.406	215	123
2	4	110	0.301	208	78.6	2	4	110	0.403	351	221

2	4	120	0.298	337	157	2	4	120	0.397	579	399
2	4	130	0.294	525	281	2	4	130	0.390	878	634
2	4	140	0.288	804	478	2	4	140	0.377	1367	1041
2	4	150	0.280	1180	751	2	4	150	0.363	1929	1499
2	4	160	0.268	1703	1145	2	4	160	0.345	2689	2131
2	4	100	0.351	170	78.8	2	4	100	0.442	284	192
2	4	110	0.349	264	134	2	4	110	0.437	465	335
2	4	120	0.345	448	269	2	4	120	0.429	751	572
2	4	130	0.341	654	410	2	4	130	0.420	1129	885
2	4	140	0.333	973	647	2	4	140	0.405	1680	1354
2	4	150	0.321	1470	1040	2	4	150	0.388	2342	1912
2	4	160	0.307	2076	1518						

The liquid composition has been corrected for 100–160 °C data because the CO_2 loading in the liquid phase differs significantly from that measured at room temperature, especially at high temperature and high loading.

The total pressure and CO_2 partial pressure of this blend from 100 to 160 °C were listed in Table 18.

An empirical model was generated by regressing CO_2 partial pressure as a function of temperature and CO_2 loading in the liquid phase.

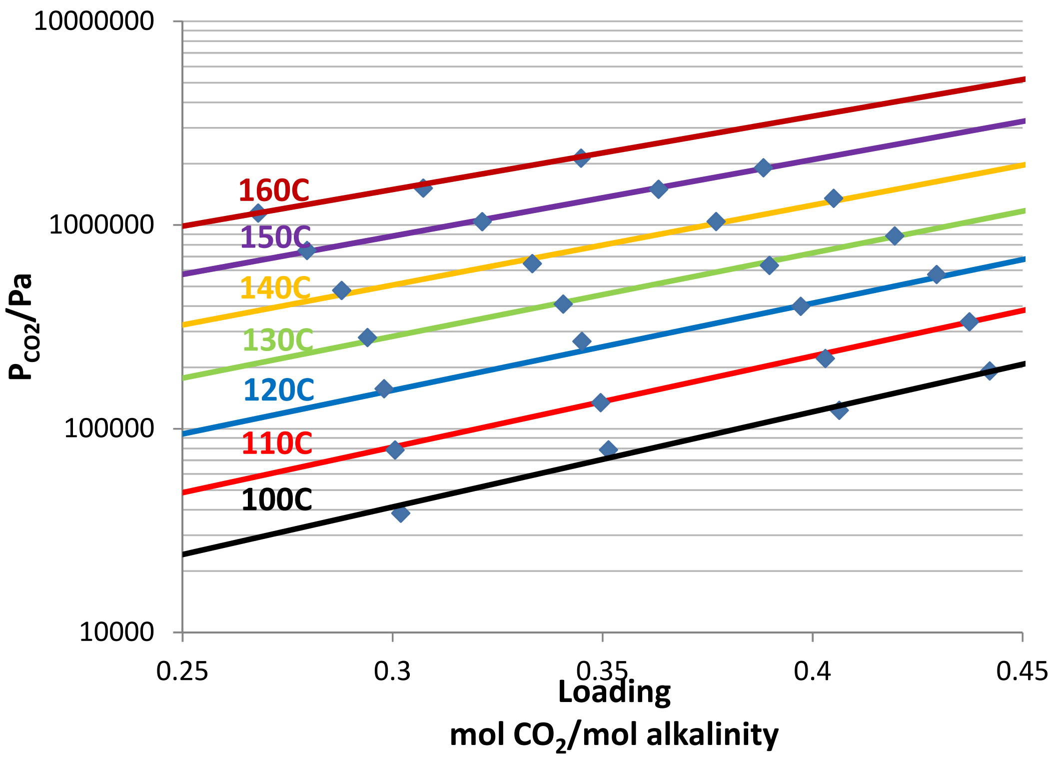

Figure 14: CO_2 Solubility for 2 m PZ/4 m AMP [Filled points: from total pressure measurement. Lines: Equation 8]

$$lnP_{CO2} = (38.7 \pm 1.4) + (-7.1 \pm 3.9)\alpha + \frac{(-11667 \pm 544)}{T} + (6662 \pm 1551)\frac{\alpha}{T} \qquad (8)$$

The heat of absorption can be derived from the CO_2 partial pressure model according to the Gibbs-Helmholtz Equation.

$$\Delta H_{abs} = -R\frac{\partial lnP_{CO2}}{\partial \frac{1}{T}} = -R(-11667 + 6662\alpha) \qquad (9)$$

The CO_2 loading at 40 °C when the CO_2 partial pressure is 0.5 kPa and 5.0 kPa can also be predicted from the CO_2 partial pressure model, which is exactly the definition of lean and rich loading. Then the CO_2 capacity of this blend can be obtained by Equation 3.

The predicted CO_2 capacity, lean and rich loading, and heat of absorption are listed in Table 19.

Table 19: Predicted properties of 2 m PZ/4 m AMP

CO_2 Capacity (mol CO_2/kg solvent)	0.89
Lean loading (mol CO_2/mol alkalinity)	0.34
Rich loading (mol CO_2/mol alkalinity)	0.501
$-\Delta H_{abs}$ @P_{CO2}=1.5 kPa (kJ/mol)	74

AMP Thermodynamic Model

To accurately predict the vapor-liquid equilibrium (VLE), heat capacity, amine volatility, CO_2 activity coefficient, and CO_2 heat of absorption for PZ/AMP aqueous solution, the sequential regression method was applied. Phase equilibrium such as vapor-liquid equilibrium, chemical equilibrium, and heat are primary properties for a system in a thermal process. AMP was always treated as a Henry's component, so Henry's law was adopted to characterize VLE for AMP. Aspen Plus® used Equation 10 to calculate the Henry's constant. Constants A, B, C, and D were regressed.

$$lnH_i = A_i + \frac{B_i}{T} + C_i lnT + D_i T \tag{10}$$

The activity coefficient is always introduced to describe the non-ideal behavior of a system. If the solution is ideal, the activity coefficient γ_i will be 1. γ_i could be larger or smaller than 1 depending on the reference state. One is called asymmetric reference state, which assumes γ_i to be 1 when x_i approaches 0. The other is called symmetric reference state, which assumes γ_i to be 1 when x_i approaches 1. The displacement to 1 represents the non-ideality in the solution. The symmetric convention for definition of activity coefficient was applied for water as a solvent, whereas for other molecular and ionic species, the asymmetric reference state was used. NRTL and e-NRTL thermodynamic models were used to characterize AMP/H_2O and AMP/CO_2/H_2O systems separately. In Aspen Plus®, the temperature dependence of the e-NRTL parameters is expressed in the following relationships:

Molecule-Molecule Binary Parameters

$$\tau_{mm'} = A_{mm'} + \frac{B_{mm'}}{T} + F_{mm'} lnT + G_{mm'} T \tag{11}$$

Electrolyte-Molecule Pair Parameters

$$\tau_{ca,m} = C_{ca,m} + \frac{D_{ca,m}}{T} + E_{ca,m}[\frac{(T_{ref} - T)}{T} + \ln(\frac{T}{T_{ref}})] \tag{12}$$

Molecule-Electrolyte Pair Parameters

$$\tau_{m,ca} = C_{m,ca} + \frac{D_{m,ca}}{T} + E_{m,ca}[\frac{(T_{ref} - T)}{T} + \ln(\frac{T}{T_{ref}})] \tag{13}$$

Where T_{ref}=298.15K. As electrolyte concentration approaches zero, the e-NRTL model is reduced to the NRTL model. For molecule-molecule interaction, the non-randomness parameter $\alpha = 0.3$; for molecule-ion pair interaction or ion pair-ion pair interaction, $\alpha = 0.1$.

There are two methods to calculate chemical equilibrium constants. One is based on the concentration of products and reactants, while the other the standard free energy of formation (ΔG_{form}, ΔH_{form}) of products and reactants. The second method was always applied in the following modeling work. Only ΔG_{form}, ΔH_{form} for $AMPH^+$ were adjusted, while the values for other components were set default.

Heat capacity is a fundamental property in calculating all the properties related to heat. The values for heat capacity parameters for AMP/H_2O and AMP/CO_2/H_2O were regressed in this work. The equation used to calculate ideal gas heat capacity is:.

$$CPIG = A + BT + CT^2 + DT^3 \qquad (14)$$

The data regression system (DRS) in Aspen Plus® was used for the regression of relevant parameters based on the experimental data sets from this work and the literature. The Britt-Luecke algorithm was applied to minimize the Maximum Likelihood objective function, in which errors in all measured variables were taken into account.

The thermodynamic model built for AMP was based on the Fawkes v3.0 model for PZ developed by Frailie et al. (Frailie, Plaza et al., 2011).

AMP/H_2O Regression

The first set of data incorporated into the AMP/H_2O thermodynamic model was unloaded amine volatility data measured by Nguyen (Rochelle, 2009). Figure 15 compares the experimental data and the Aspen Plus® predictions for low temperature AMP volatility in unloaded solutions of 0.29, 0.92, 4.6, and 11.5 m.

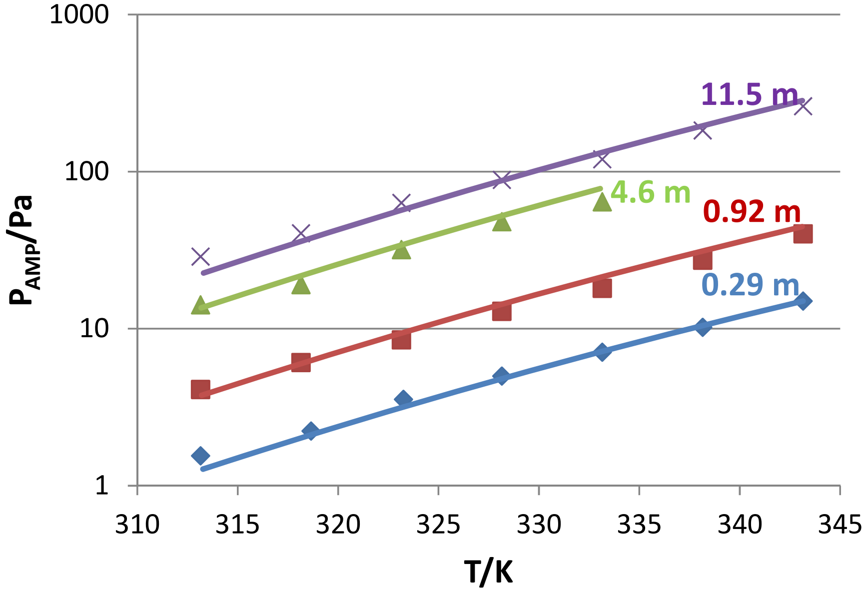

Figure 15: AMP volatility as a function of temperature for 0.29, 0.92, 4.6, and 11.5 m unloaded solutions between 40 and 70 °C. (Points: experimental data; Lines: Aspen Plus® predictions.)

The next regression included isobaric VLE over the whole mole fraction range at 66.7, 80.0, and 101.3 kPa of aqueous unloaded AMP solutions. The VLE data were measured by Pappa (Pappa et al., 2006). Figure 16 compares the experimental data and the Aspen Plus® predictions.

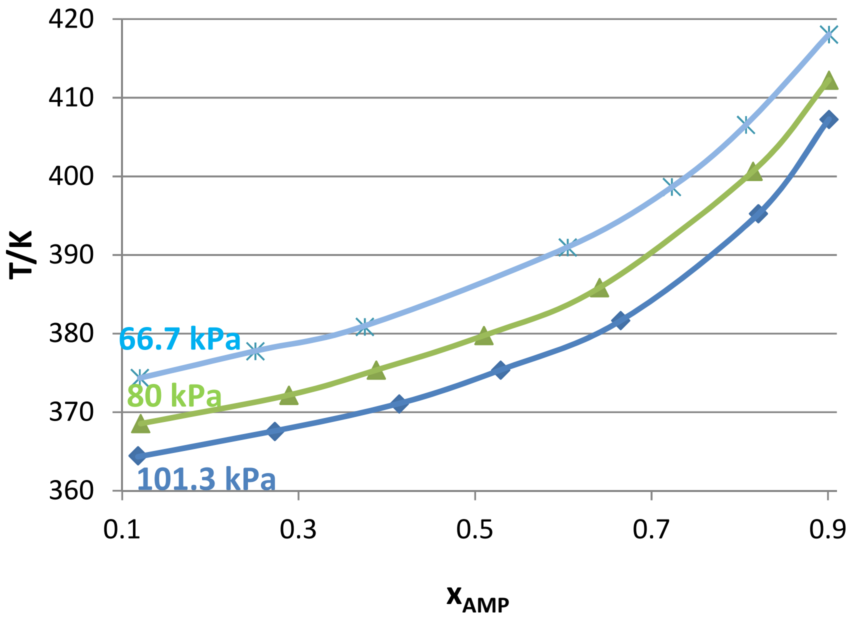

Figure 16: Experimental data (points) and Aspen Plus® predictions (lines) for isobaric VLE of unloaded AMP solutions

The last set of data incorporated into the AMP/H_2O thermodynamic model was unloaded amine heat capacity data measured by Chiu (Chiu et al., 1999) and Zhang (Zhang et al., 2002). Totally 244 data points were used over the whole mole fraction range between 5 °C and 90 °C. Figure 17 compares the experimental data (Chiu et al., 1999) and Aspen Plus® predictions between 30 °C and 80 °C.

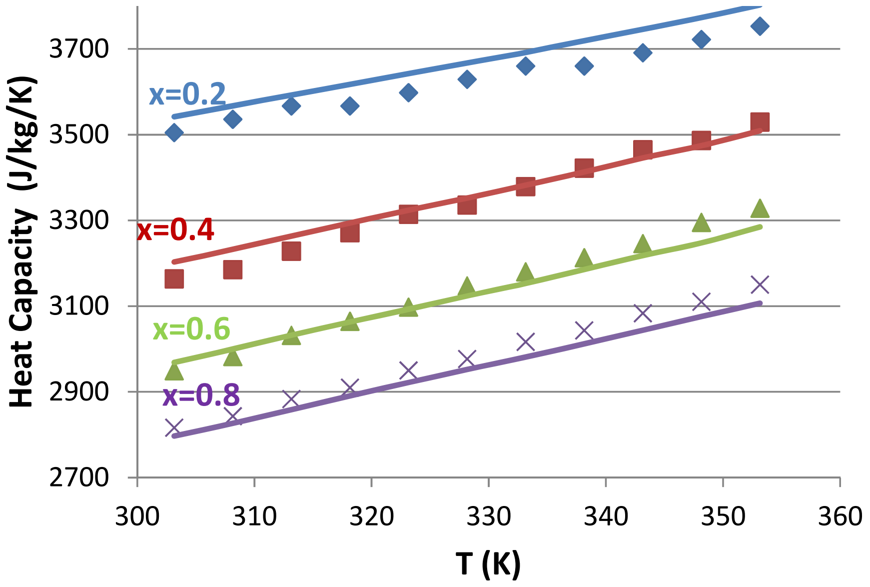

Figure 17: Experimental data (points) and Aspen Plus® predictions (lines) for heat capacity of unloaded AMP solutions

The parameters used to fit unloaded AMP volatility, VLE, and heat capacity, are ideal gas heat capacity, infinite dilution activity coefficients, and Henry's constant in water. The relative weighting of the heat capacity data set was set at 2. Table 20 summarizes all of the parameters and their standard deviations.

Table 20: Parameters used to model unloaded AMP solution (C_p^{ig}: J/kmol•K; Henry's Law: Pa)

Parameter	Species	Value	Std. Dev.
CPIG/2	AMP	7129	643
CPIG/3	AMP	-33.70	3.74
CPIG/4	AMP	0.0355	0.0054
NRTL/1	AMP/H_2O	0.647	0.001
NRTL/1	AMP/H_2O	0.667	0.0008
NRTL/2	AMP/H_2O	0.629	0.001
NRTL/2	AMP/H_2O	58.48	0.09
NRTL/5	AMP/H_2O	0.0986	1.19E-04
NRTL/5	AMP/H_2O	0.115	1.60E-04
NRTL/6	AMP/H_2O	-0.0056	9.25E-06
NRTL/6	AMP/H_2O	0.0012	6.81E-06
HENRY/1	AMP	-711	36
HENRY/2	AMP	6655	974
HENRY/3	AMP	136	6.3
HENRY/4	AMP	-0.269	0.010

AMP/CO_2/H_2O Regression

ΔG_{form}, ΔH_{form}, and C_P^{aq} of $AMPH^+$ were firstly manually adjusted to fit pKa data for AMP between 20 and 90 °C (Little et al., 1990; Hamborg et al., 2009; Kim et al., 2011). Figure 18 compares the experimental data and Aspen Plus® predictions for the pKa of AMP.

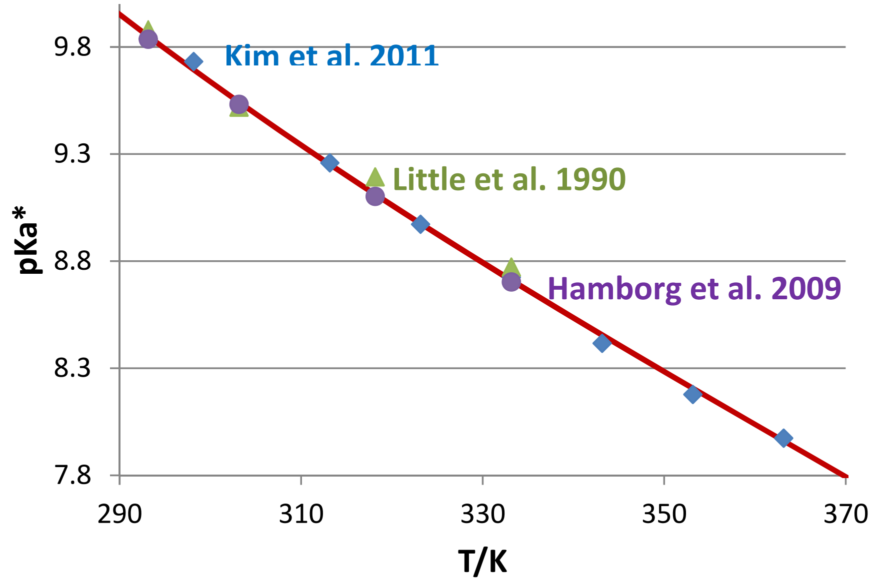

Figure 18: pKa* of unloaded AMP (Points: experimental data; Lines: Aspen Plus® predictions).

The pKa value in literature was based on molality, whereas in this work it was calculated based on the mole fraction. The correlation between these base cases can be expressed using the following equation:

$$pKa = pKa^{*} + ln\left(\frac{1000}{MW_w}\right)\sum_{i \neq w} v_i \qquad (15)$$

where:

pKa* is mole fraction-based,
pKa is molarity-based,
MW_w is the molecule weight of water.

The next regression included VLE for loaded AMP solutions between 20 and 100 °C. Table 21 lists all the VLE data used in modeling AMP/CO_2/H_2O.

Table 21: VLE data for loaded AMP solution from literature

Author	Concentration (mol AMP/kg H_2O)	Temperature (°C)	Loading (mol CO_2/mol AMP)	Number
Teng et al.	2.46	40-70	0.03-1.3	24
Tontiwachwuthikul et al.	2.46, 4.15	20-80	0.1-1	40
Li et al.	4.8	40-100	0.04-0.9	28
Dash et al.	3.16, 4.8, 8.2	25-55	0.2-1.2	166
Chen et al.	4.8	40-100	0.15-0.6	13

Figures 19–20 compare the experimental data and Aspen Plus® predictions for 4.8 m AMP loaded solution between 25 and 100 °C.

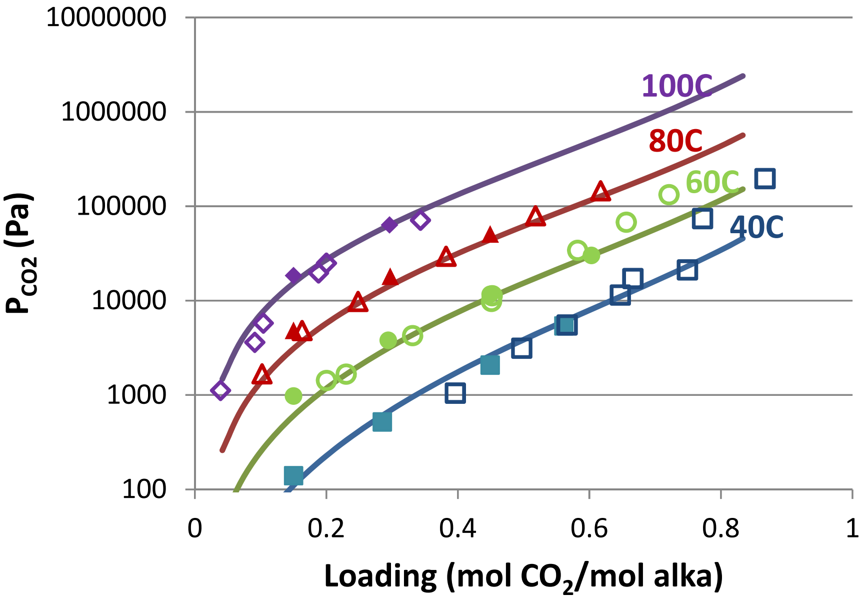

Figure 19: VLE of loaded 4.8 m AMP (Filled points: Xi et al.; Open points: Li et al.; Lines: Aspen Plus® predictions).

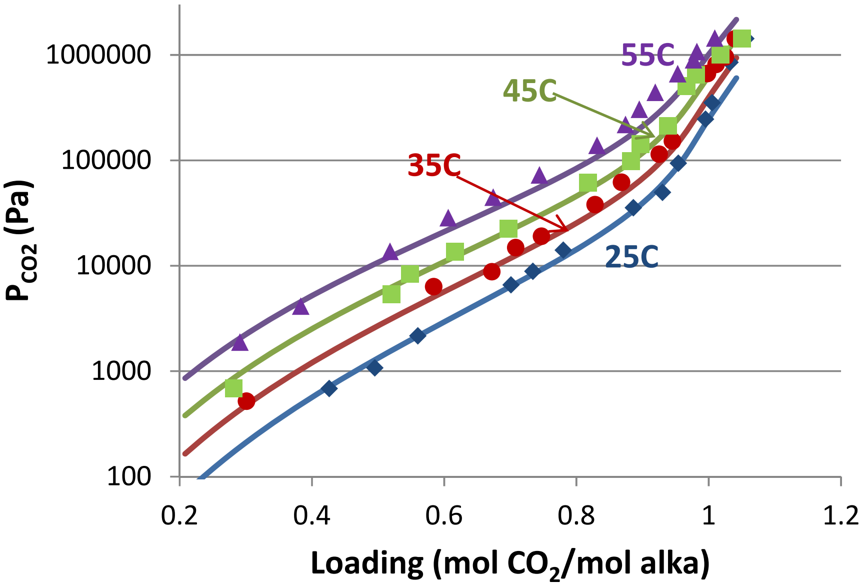

Figure 20: VLE of loaded 4.8 m AMP (Points: Dash et al.; Lines: Aspen Plus® predictions).

Table 22 reports the regressed parameters and their values.

Table 22: Parameters used to model loaded AMP solution

Parameter	Species	Value	Std. Dev.	Units
GMELCC/1	$H_2O/(AMPH^+,HCO_3^-)$	25.27	2.73	N/A
GMELCC/1	$(AMPH^+,HCO_3^-)/H_2O$	-11.32	1.31	N/A
GMELCC/1	$AMP/(AMPH^+,HCO_3^-)$	21.56	2.61	N/A
GMELCC/1	$(AMPH^+,HCO_3^-)/AMP$	-5.05	1.42	N/A
GMELCD/1	$H_2O/(AMPH^+,HCO_3^-)$	-4918	873	°K
GMELCD/1	$(AMPH^+,HCO_3^-)/H_2O$	2253	421	°K
GMELCD/1	$AMP/(AMPH^+,HCO_3^-)$	-5179	669	°K

The parameters will be updated once the heat capacity and volatility are incorporated into Aspen Plus®. The model also needs to predict speciation and heat of absorption data adequately. Though these data sets will not be regressed directly, they need to be checked periodically to ensure reasonable results. This analysis will be discussed in the next quarter.

Conclusions

1. 6 m PZ/4 m AMP is not a desirable blend owing to its narrow operating window.
2. Even though 6.5 m PZ/3 m AMP has a similar operating window to 8 m PZ, the viscosity, nearly twice that of 8 m PZ, limits its application.
3. For aqueous 5 m PZ/2.3 m AMP, solids are precipitated when the loading is lower than 0.3, but no solids are observed when CO_2 is kept loaded into this blend until the loading reaches 0.5.
4. The performance of aqueous 5 m PZ/2.3 m AMP is similar to 8 m PZ in terms of viscosity, heat of absorption, lean and rich loading departure. Due to lower total alkalinity, the CO_2 capacity is lower.
5. The mass transfer rates in 5 m PZ/2.3 m AMP are higher than in 8 m PZ when the loading is rich.
6. Both AMP and PZ degrade faster in a blend than in a single system, and the main degradation product identified is 1,1-dimethyl-2-piperazin-1-ethylamine.
7. The disadvantage of this blend is that more solvent will be lost because of its high volatility.
8. The high temperature VLE data for 2 m PZ/4 m AMP indicate that this blend has 0.89 mol/kg of CO_2 capacity and 74 kJ/mol of CO_2 heat of absorption. These properties are better than 8 m PZ. Another advantage of this blend is that it does not have a solid solubility problem.
9. The thermodynamic models for AMP/H_2O and $AMP/CO_2/H_2O$ have been built in Aspen Plus® using VLE, heat capacity, volatility, and CO_2 solubility data. The pKa value of AMP was fitted by manually adjusting the standard free energy of formation and standard enthalpy of formation at infinite dilution of $AMPH^+$. The AMP/H_2O

model represents the experimental data well, while the AMP/CO_2/H_2O model needs further testing by heat capacity data.

Future Work

The heat capacity and NMR speciation for loaded 5 m PZ/2.3 m AMP and 2 m PZ/4 m AMP will be measured next. Low temperature gas liquid equilibrium data for loaded 2 m PZ/4 m AMP and CO_2 Liquid Phase Mass Transfer Coefficient (k_g') will be determined using the wetted wall column.

The PZ/AMP/CO_2/H_2O thermodynamic and dynamic model will be finalized.

One paper on experiments and another on modeling will be finished.

Safety

In the total pressure experiments, high temperature up to 160 °C makes the surface of the autoclave hot. Therefore the SOP includes a waiting period to refrain from touching the autoclave until it cools down to room temperature. Insulated gloves are used to take cylinders out of the oven. Because the cylinders will be under high pressure when they are taken out, they are not opened until they cool down to room temperature.

References

Chen X. *Carbon Dioxide Thermodynamics, Kinetics, and Mass Transfer in Aqueous Piperazine Derivatives and Other Amines.* The University of Texas at Austin. Ph.D. Dissertation. 2011.

Chen X, Closmann FB, Rochelle GT. "Accurate screening of amine by the wetted wall column". *Energy Proc.* 2011;4:101–108.

Chen Y-R, Caparanga AR, Soriano AN, Li M-H. "Liquid heat capacity of the solvent system (piperazine + 2-amino-2-methyl-1-propanol + water)". *J Chem Thermodynamics*. 2010;42:518–523.

Chiu L-F, Li M-H. "Heat capacity of alkanolamine aqueous solutions". *J Chem Eng Data.* 1999;44:1396–1401.

Choi W-J, Cho K-C, Shim J-G, Hwang H-R, Park S-W, Oh K-J. "Removal of carbon dioxide by absorption into blended amines: kinetics of absorption into aqueous AMP/HMDA, AMP/MDEA, AMP/piperazine solutions". *Green Chemistry*. 2007;9:594–598.

Dash SK, Samanta AN, Bandyopadhyay SS. "Solubility of carbon dioxide in aqueous solution of 2-amino-2-methyl-1-propanol and piperazine". *Fluid Phase Equil*. 2011;307:166–174.

Dash SK, Samanta A, Samanta AN, Bandyopadhyay SS. "Absorption of carbon dioxide in piperazine activated concentrated aqueous 2-amino-2-methyl-1-propanol solvent". *Chem Eng Sci*. 2011;66:3223–3233.

Dash SK, Samanta AN, Bandyopadhyay SS. "(Vapour + liquid) equilibria (VLE) of CO_2 in aqueous solutions of 2-amino-2-methyl-1-propanol: New data and modeling using Enrtl-equation". *J Chem Thermodynamics.* 2011;43:1278–1285.

Davis JD. *Thermal Degradation of Aqueous Amines Used for Carbon Dioxide Capture.* The University of Texas at Austin. Ph.D. Dissertation. 2009.

Frailie PT, Plaza JM, Van Wagener DH, Rochelle GT. "Modeling piperazine thermodynamics". *Energy Proc*. 2011;4:35–42.

Freeman SA, Dugas RE, Van Wagener DH, Nguyen T, Rochelle GT. "Carbon dioxide capture with concentrated, aqueous piperazine". *IJGGC.* 2010;4:119–124.

Freeman SA. *Thermal Degradation and Oxidation of Aqueous Piperazine for Carbon Dioxide Capture.* The University of Texas at Austin. Ph.D. Dissertation. 2011.

Hamborg ES, Versteeg GF. "Dissociation constants and thermodynamic properties of amines and alkanolamines from (293 to 353) K". *J Chem Eng Data.* 2009;54:1318–1328.

Hilliard MD. *A Predictive Thermodynamic Model for an Aqueous Blend of Potassium Carbonate, Piperazine, and Monoethanolamine for Carbon Dioxide Capture from Flue Gas.* The University of Texas at Austin. Ph.D. Dissertation. 2008.

Kim I, Jens CM, Grimstvedt A, Svendsen HF. "Thermodynamics of protonation of amines in aqueous solutions at elevated temperatures". *J Chem Thermodynamics*. 2011;43:1754–1762.

Li M-H, Chang B-C. "Solubility of carbon dioxide in water + monoethanolamine + 2-amino-2-methyl-1-propanol". *J Chem Eng Data.* 1994;39:448–452.

Little RJ, Bos M, Knoop GJ. "Dissociation constants of some alkanolamines at 293, 303, 318, and 333 K". *J Chem Eng Data.* 1990;35:276–277.

Murshid G, Shariff AM, Keong LK, Bustam MA. "Physical properties of aqueous solutions of piperazine and (2-amino-2-methyl-1-propanol + piperazine) from (298.15 to 333.15) K". *J Chem Eng Data*. 2011;56:2660–2663.

Paul S, Mandal B. "Density and viscosity of aqueous solutions of (N-methylkiethanolamine + piperazine) and (2-amino-2-methyl-1-propanol + piperzine) from (288 to 333) K". *J Chem Eng Data*. 2006;51:1808–1810.

Pappa GD, Anastasi C, Voustsas EC. "Measurement and thermodynamic modeling of the phase equilibrium of aqueous 2-amino-2-methyl-1-propanol solutions". *Fluid Phase Equilibrium*. 2006;243:193–197.

Rochelle GT et al. "CO_2 Capture by Aqueous Absorption, Third Quarterly Progress Reports 2009." Luminant Carbon Management Program. The University of Texas at Austin. 2009.

Rochelle GT et al. "CO_2 Capture by Aqueous Absorption, Fourth Quarterly Progress Reports

2009." Luminant Carbon Management Program. The University of Texas at Austin. 2010.

Rochelle GT et al. "CO_2 Capture by Aqueous Absorption, Second Quarterly Progress Reports 2010." Luminant Carbon Management Program. The University of Texas at Austin. 2010.

Samanta A, Bandyopadhyay SS. "Density and viscosity of aqueous solutions of piperazine and (2-amino-2-methyl-1-propanol + piperazine) from 298 to 333 K". *J Chem Eng Data*. 2006;51:467–470.

Samanta A, Bandyopadhyay SS. "Absorption of carbon dioxide into aqueous solutions of piperazine activated 2-amino-2-methyl-1-propanol". *Chem Eng Sci*. 2009;64:1185–1194.

Seo DJ, Hong WH. "Effect of piperazine on the kinetics of carbon dioxide with aqueous aqueous solutions of 2-amino-2-methyl-1-propanol". *Ind Eng Chem Res*. 2000;39:2062–2067.

Sun W-C, Yong C-B, Li M-H. "Kinetics of the absorption of carbon dioxide into mixed aqueous solutions of 2-amino-2-methyl-1-propanol and piperazine". *Chem Eng Sci*. 2005;60:503–516.

Teng TT, Mather AE. "Solubility of CO_2 in an AMP solution". *J Chem Eng Data.* 1990;35: 411–414.

Tontiwachwuthikul P, Melsen A, Lim CJ. "Solubility of CO_2 in 2-amino-2-methyl-1-propanol solutions". *J Chem Eng Data.* 1991;36:130–133.

Yang Z-Y, Soriano AN, Caparanga AR, Li M-H. "Equilibrium solubility of carbon dioxide in (2-amino-2-methyl-1-propanol + piperazine + water)". *J Chem Thermodynamics*. 2010;42:659–665.

Zhang K, Hawrylak B. "Thermodynamics of aqueous amines: excess molar heat capacities, volumes, and expansibilities of {water + methyldiethanolamine (MDEA)} and {water + 2-amino-2-methyl-1-proponal (AMP)}". *J Chem Thermodynamics*. 2002;34:679–710.

Zhou S, Chen X, Nguyen T, Voice AK, Rochelle GT. "Aqueous ethylenediamine for CO_2 capture". *ChemSusChem.* 2010;3:913–918.

Appendix

Table A-1: Detailed Wetted Wall Column Data for 5 m PZ/2.3 m AMP

PZ/AMP		CO_2 ldg	P^*_{CO2}	Temp	Pressure	Gas_{Dry}	Gas_{Wet}	$P_{CO2in, dry}$	$P_{CO2in, wet}$	$P_{CO2out, dry}$	$P_{CO2out, wet}$	CO_2 flux	KG	kg	KG/kg	kg'
m		mol CO_2/mol alk	Pa	C	psig	Std L/min	Std L/min	Pa	Pa	Pa	Pa	mol/s cm^2	mol/s Pa cm^2	mol/s Pa cm^2		mol/s Pa cm2
5	2.3	0.309	325	40	20	5	5.16	0.00	0.00	93.04	90.17	-3.76E-08	1.34E-10	4.57E-10	0.292	1.89E-10
								62.90	60.96	138.01	133.75	-3.03E-08				
								109.31	105.93	170.78	165.51	-2.48E-08				
								475.49	460.82	432.44	419.10	1.74E-08				
								527.40	511.12	477.65	462.91	2.01E-08				
								570.21	552.61	507.07	491.42	2.55E-08				
5	2.3	0.309	2742	60	20	5	5.45	0.00	0.00	755.82	692.83	-3.05E-07	1.27E-10	4.83E-10	0.262	1.71E-10
								557.29	510.85	1131.33	1037.05	-2.32E-07				
								1112.20	1019.51	1604.91	1471.17	-1.99E-07				
								3274.40	3001.53	3233.74	2964.26	1.64E-08				
								3826.91	3508.00	3590.12	3290.94	9.56E-08				
5	2.3	0.309	11146	80	40	5	5.72	0.00	0.00	4098.42	3583.47	-1.05E-06	1.16E-10	3.21E-10	0.361	1.82E-10
								4441.52	3883.47	7065.72	6177.95	-6.72E-07				
								8019.63	7012.00	9490.08	8297.70	-3.76E-07				
								12732.62	11132.83	12921.14	11297.66	-4.83E-08				
								23704.46	20726.12	20575.03	17989.89	8.01E-07				
								27474.85	24022.78	22837.27	19967.89	1.19E-06				
								31132.13	27220.55	24571.65	21484.35	1.68E-06				

Table A-2: Detailed Wetted Wall Column Data for 5 m PZ/2.3 m AMP

PZ/AMP		CO_2 ldg	P^*_{CO2}	Temp	Pressure	Gas_{Dry}	Gas_{Wet}	$P_{CO2in, dry}$	$P_{CO2in, wet}$	$P_{CO2out, dry}$	$P_{CO2out, wet}$	CO_2 flux	KG	kg	KG/kg	kg'
m		mol CO_2/mol alk	Pa	C	psig	Std L/min	Std L/min	Pa	Pa	Pa	Pa	mol/s cm^2	mol/s Pa cm^2	mol/s Pa cm^2		mol/s Pa cm2
5	2.3	0.309	59912	100	60	5	6.22	0.00	0.00	16250.13	13052.47	-3.05E-06	5.23E-11	2.54E-10	0.206	6.59E-11
								25981.67	20869.07	33859.59	27196.79	-1.48E-06				
								50233.30	40348.52	55330.77	44442.92	-9.56E-07				
								89005.00	71490.82	86533.49	69505.65	4.63E-07				
								95492.69	76701.88	91270.54	73310.56	7.92E-07				
								102598.26	82409.24	92403.31	74220.43	1.91E-06				
5	2.3	0.351	93	20	20	5	5.05	0.00	0.00	21.29	21.08	-8.59E-09	1.00E-10	4.46E-10	0.224	1.29E-10
								22.00	21.79	37.55	37.18	-6.27E-09				
								34.44	34.11	47.84	47.37	-5.41E-09				
								59.56	58.97	65.78	65.13	-2.51E-09				
								141.84	140.45	130.83	129.55	4.44E-09				
								191.11	189.24	170.78	169.11	8.21E-09				
5	2.3	0.351	844	40	20	5	5.16	0.00	0.00	186.32	180.57	-7.52E-08	9.85E-11	4.57E-10	0.215	1.26E-10
								202.59	196.34	324.81	314.79	-4.93E-08				
								385.80	373.90	486.50	471.48	-4.06E-08				
								758.21	734.81	793.61	769.12	-1.43E-08				
								1124.63	1089.93	1098.32	1064.43	1.06E-08				
								1486.04	1440.18	1344.92	1303.42	5.70E-08				
								1832.85	1776.29	1619.98	1569.99	8.59E-08				

Table A-3: Detailed Wetted Wall Column Data for 5 m PZ/2.3 m AMP

PZ/AMP		CO_2 ldg	P^*_{CO2}	Temp	Pressure	Gas_{Dry}	Gas_{Wet}	$P_{CO2in,\ dry}$	$P_{CO2in,\ wet}$	$P_{CO2out,\ dry}$	$P_{CO2out,\ wet}$	CO_2 flux	KG	kg	KG/kg	kg'
m		mol CO_2/mol alk	Pa	C	psig	Std L/min	Std L/min	Pa	Pa	Pa	Pa	mol/s cm^2	mol/s Pa cm^2	mol/s Pa cm^2		mol/s Pa cm2
5	2.3	0.351	5979	60	40	5	5.28	0.00	0.00	1760.77	1667.69	-4.51E-07	9.06E-11	2.98E-10	0.304	1.30E-10
								1474.22	1396.29	2846.65	2696.16	-3.51E-07				
								2933.37	2778.29	3940.06	3731.77	-2.58E-07				
								9033.86	8556.29	8317.49	7877.79	1.83E-07				
								10391.20	9841.88	9184.68	8699.13	3.09E-07				
								11823.95	11198.88	10240.39	9699.03	4.05E-07				
5	2.3	0.351	27778	80	40	5	5.72	0.00	0.00	8095.03	7077.94	-2.07E-06	7.70E-11	3.21E-10	0.240	1.01E-10
								6786.71	5933.99	11903.13	10407.56	-1.31E-06				
								12732.62	11132.83	17143.98	14989.93	-1.13E-06				
								37466.39	32758.94	36222.16	31671.04	3.19E-07				
								49870.99	43604.96	44818.66	39187.43	1.29E-06				
								63142.77	55209.21	56582.29	49473.02	1.68E-06				
5	2.3	0.381	229	20	20	5	5.05	0.00	0.00	43.05	42.63	-1.74E-08	7.85E-11	4.46E-10	0.176	9.53E-11
								59.56	58.97	88.26	87.40	-1.16E-08				
								116.00	114.87	134.90	133.58	-7.63E-09				
								328.40	325.19	308.78	305.77	7.92E-09				
								378.63	374.93	354.23	350.77	9.85E-09				
								429.09	424.90	395.61	391.74	1.35E-08				

Table A-4: Detailed Wetted Wall Column Data for 5 m PZ/2.3 m AMP

PZ/AMP		CO_2 ldg	P^*_{CO2}	Temp	Pressure	Gas_{Dry}	Gas_{Wet}	$P_{CO2in, dry}$	$P_{CO2in, wet}$	$P_{CO2out, dry}$	$P_{CO2out, wet}$	CO_2 flux	KG	kg	KG/kg	kg'
m		mol CO_2/mol alk	Pa	C	psig	Std L/min	Std L/min	Pa	Pa	Pa	Pa	mol/s cm^2	mol/s Pa cm^2	mol/s Pa cm^2		mol/s Pa cm2
5	2.3	0.381	2204	40	20	5	5.16	0.00	0.00	406.61	394.06	-1.64E-07	8.23E-11	4.57E-10	0.180	1.00E-10
								727.11	704.68	1002.17	971.25	-1.11E-07				
								1449.44	1404.71	1583.39	1534.52	-5.41E-08				
								3011.30	2918.38	2906.06	2816.38	4.25E-08				
								3736.03	3620.73	3501.63	3393.57	9.46E-08				
								4470.31	4332.36	4039.79	3915.12	1.74E-07				
5	2.3	0.381	11464	60	40	5	5.28	0.00	0.00	2752.39	2606.88	-7.05E-07	7.01E-11	2.98E-10	0.235	9.16E-11
								2925.82	2771.15	4905.28	4645.97	-5.07E-07				
								6021.32	5703.00	7491.77	7095.72	-3.76E-07				
								17634.13	16701.91	16616.12	15737.72	2.61E-07				
								20537.33	19451.63	18576.73	17594.68	5.02E-07				
								23440.53	22201.36	20688.15	19594.48	7.05E-07				
5	2.3	0.381	49169	80	50	5	5.59	0.00	0.00	11265.15	10068.51	-2.44E-06	4.69E-11	2.67E-10	0.176	5.69E-11
								12915.23	11543.31	19337.17	17283.07	-1.39E-06				
								25268.54	22584.38	29282.25	26171.74	-8.69E-07				
								75796.70	67745.18	72987.10	65234.03	6.08E-07				
								82129.44	73405.23	78338.71	70017.17	8.21E-07				
								88997.35	79543.59	81817.26	73126.21	1.55E-06				

Table A-5: Detailed Wetted Wall Column Data for 5 m PZ/2.3 m AMP

PZ/AMP		CO$_2$ ldg	P*$_{CO2}$	Temp	Pressure	Gas$_{Dry}$	Gas$_{Wet}$	P$_{CO2in, dry}$	P$_{CO2in, wet}$	P$_{CO2out, dry}$	P$_{CO2out, wet}$	CO$_2$ flux	KG	kg	KG/kg	kg'
m		mol CO$_2$/mol alk	Pa	C	psig	Std L/min	Std L/min	Pa	Pa	Pa	Pa	mol/s cm^2	mol/s Pa cm^2	mol/s Pa cm^2		mol/s Pa cm2
5	2.3	0.420	676	20	20	5	5.05	0.00	0.00	75.58	74.84	-3.05E-08	4.65E-11	4.46E-10	0.104	5.19E-11
								107.39	106.34	168.62	166.98	-2.47E-08				
								200.20	198.24	250.90	248.45	-2.05E-08				
								960.08	950.70	929.94	920.85	1.22E-08				
								1136.35	1125.25	1086.84	1076.22	2.00E-08				
								1314.55	1301.70	1247.57	1235.38	2.70E-08				
5	2.3	0.420	5325	40	20	5	5.16	0.00	0.00	662.53	642.09	-2.67E-07	5.01E-11	4.57E-10	0.109	5.62E-11
								734.29	711.63	1260.49	1221.59	-2.12E-07				
								1475.75	1430.21	1896.71	1838.18	-1.70E-07				
								8911.93	8636.91	8529.24	8266.03	1.54E-07				
								9581.64	9285.95	9127.19	8845.53	1.83E-07				
								10299.18	9981.36	9749.06	9448.21	2.22E-07				
5	2.3	0.420	26451	60	40	5	5.28	0.00	0.00	3989.08	3778.20	-1.02E-06	3.96E-11	2.98E-10	0.133	4.56E-11
								6809.33	6449.36	9448.60	8949.11	-6.76E-07				
								12841.96	12163.07	14727.15	13948.61	-4.83E-07				
								24982.62	23661.93	25397.37	24054.75	-1.06E-07				
								43570.66	41267.32	41836.28	39624.62	4.44E-07				
								50168.85	47516.70	47303.35	44802.68	7.34E-07				
								62988.18	59658.34	57860.45	54801.68	1.31E-06				

Table A-6: Detailed Wetted Wall Column Data for 5 m PZ/2.3 m AMP

PZ/AMP		CO_2 ldg	P^*_{CO2}	Temp	Pressure	Gas_{Dry}	Gas_{Wet}	$P_{CO2in, dry}$	$P_{CO2in, wet}$	$P_{CO2out, dry}$	$P_{CO2out, wet}$	CO_2 flux	KG	kg	KG/kg	kg'
m		mol CO_2/mol alk	Pa	C	psig	Std L/min	Std L/min	Pa	Pa	Pa	Pa	mol/s cm^2	mol/s Pa cm^2	mol/s Pa cm^2		mol/s Pa cm2
5	2.3	0.449	2963	20	20	5	5.05	0.00	0.00	196.13	194.21	-7.92E-08	2.48E-11	4.46E-10	0.056	2.62E-11
								751.03	743.69	875.41	866.85	-5.02E-08				
								1112.20	1101.33	1219.83	1207.91	-4.34E-08				
								2190.91	2169.50	2222.00	2200.29	-1.25E-08				
								5895.84	5838.23	5728.41	5672.44	6.76E-08				
								6709.06	6643.51	6493.80	6430.35	8.69E-08				
								7450.52	7377.73	7187.42	7117.20	1.06E-07				
5	2.3	0.449	17617	40	40	5	5.10	0.00	0.00	1564.71	1534.08	-4.01E-07	2.18E-11	2.87E-10	0.076	2.36E-11
								6692.45	6561.43	7484.23	7337.72	-2.03E-07				
								10085.80	9888.36	10651.36	10442.85	-1.45E-07				
								24828.04	24342.00	24337.89	23861.44	1.25E-07				
								30898.37	30293.50	29842.66	29258.45	2.70E-07				
								37421.15	36688.58	35875.29	35172.99	3.96E-07				

Table B: Thermal degradation of 5 m PZ/2.3 m AMP with 0.4 loading

Experimental Time (Weeks)		0	1	2	3	4	5	6
Piperazine (mM)	135 ℃	3.06	3.01	2.96	2.93	2.93	2.91	2.81
	150 ℃	3.06	2.81	2.78	2.74	2.63	2.54	2.48
2-amino-2-methyl-1-propanol (mM)	135 ℃	1.34	1.22	1.23	1.15	1.09	1.09	1.05
	150 ℃	1.34	1.08	0.92	0.95	0.83	0.71	0.62
1,1-dimethyl-2-piperazin-1-ethylamine (mM)*	135 ℃	0	0.011	0.046	0.073	0.099	0.13	0.16
	150 ℃	0	0.099	0.20	0.23	0.33	0.40	0.40

*the concentration of 1,1-dimethyl-2-piperazin-1-ethylamine (DPE) is calculated using 1-(2-aminoethyl)piperazine (AEP) standard calibration

Modeling Amine Thermodynamics and Hydraulics

Quarterly Report for January 1 – March 31, 2012

by Peter Frailie

Supported by the Luminant Carbon Management Program

Department of Chemical Engineering
The University of Texas at Austin

April 30, 2012

Abstract

The goal of this study is to evaluate the performance of an absorber/stripper operation that utilizes MDEA/PZ. Before analyzing unit operations and process configurations, thermodynamic, hydraulic, and kinetic properties for the blended amine must be satisfactorily regressed in Aspen Plus®. The approach used in this study is first to construct separate MDEA and PZ models that can later be reconciled via cross parameters to model accurately the MDEA/PZ blended amine. The MDEA/PZ model based on thermodynamic, hydraulic, and kinetic data is currently being updated. Separate MDEA and PZ models have been finished that accurately predict VLE, heat capacity, unloaded amine volatility, CO_2 activity coefficient, and CO_2 absorption rate over operationally significant temperature, amine concentration, and loading ranges. All available thermodynamic and hydraulic data for 7 m MDEA/2 m PZ and 5 m MDEA/5 m PZ have also been regressed. CO_2 absorption rate data for 8 m PZ, 7 m MDEA/2 m PZ, and 5 m MDEA/5 m PZ are currently being regressed. The goal for the next quarter is to construct and optimize an absorption/stripping/compression operation in Aspen Plus® for both 7 m MDEA/2 m PZ and 5 m MDEA/5 m PZ.

Introduction

The removal of CO_2 from process gases using alkanolamine absorption/stripping has been extensively studied for several solvents and solvent blends. An advantage of using blends is that the addition of certain solvents can enhance the overall performance of the CO_2 removal system. A disadvantage of using blends is that they are very complex compared to a single solvent, thus making them much more difficult to model.

This study will focus on a blended amine solvent containing piperazine (PZ) and methyldiethanolamine (MDEA). Previous studies have shown that this particular blend has the potential to combine the high capacity of MDEA with the attractive kinetics of PZ (Bishnoi, 2000). These studies have supplied a rudimentary Aspen Plus®-based model for an absorber with MDEA/PZ. This previous work recommended that that more kinetic and thermodynamic data should be acquired concerning the MDEA/PZ blend before the model can be significantly improved. Three researchers in the Rochelle lab have been acquiring these data, which are being incorporated into the model. One of the major goals of this study will be to improve the supplied Aspen Plus® absorber model with up-to-date thermodynamic and kinetic data. Another major goal of this study will be to make improvements to the MDEA and PZ thermodynamic models, which should simplify the construction of the blended amine model.

Methods and Discussion

During the past quarter the MDEA, PZ, and MDEA/PZ thermodynamic models were updated to include additional experimental data. The correlations used to calculate hydraulic properties were modified to improve accuracy at low amine concentrations. What follows is a description of the sequential regression used to develop the models, as well as a brief discussion of each of the incorporated data sets.

Amine/Water Regression

The methodology used in the development of the Fawkes model thermodynamics was modified to regress all amine water properties simultaneously. In earlier models the MDEA/H_2O, PZ/H_2O, and MDEA/PZ/H_2O systems were regressed separately to ensure adherence to sequential regression methodology. However, this approach limits the set of parameters available to regress MDEA/PZ/H_2O to only MDEA/PZ interaction parameters, which is inadequate to represent all available experimental data. Table 1 reports the parameters used to regress amine volatility and heat capacity data for MDEA/H_2O, PZ/H_2O, and MDEA/PZ/H_2O along with their standard deviations.

Table 1: Parameters used to regress MDEA/H_2O, PZ/H_2O, and MDEA/PZ/H_2O

Parameter	Components	St. Dev.
NRTL/1	MDEA/H_2O	0.00348
NRTL/2	MDEA/H_2O	0.952
NRTL/5	MDEA/H_2O	0.000624
NRTL/6	MDEA/H_2O	0.000111
HENRY/1	MDEA/H_2O	1.11
HENRY/2	MDEA/H_2O	221
HENRY/4	MDEA/H_2O	0.00153
NRTL/1	PZ/H_2O	0.00441
NRTL/2	PZ/H_2O	1.36
HENRY/1	PZ/H_2O	1.46
HENRY/2	PZ/H_2O	300
HENRY/4	PZ/H_2O	0.00201

It should be noted that the MDEA/PZ interaction parameters were not needed to represent MDEA/PZ/H_2O data. Figures 1, 2, 3, and 4 show partial pressure of amine as a function of temperature and amine concentration for MDEA, PZ, 7 m MDEA/2 m PZ, and 5 m MDEA/5 m PZ, respectively.

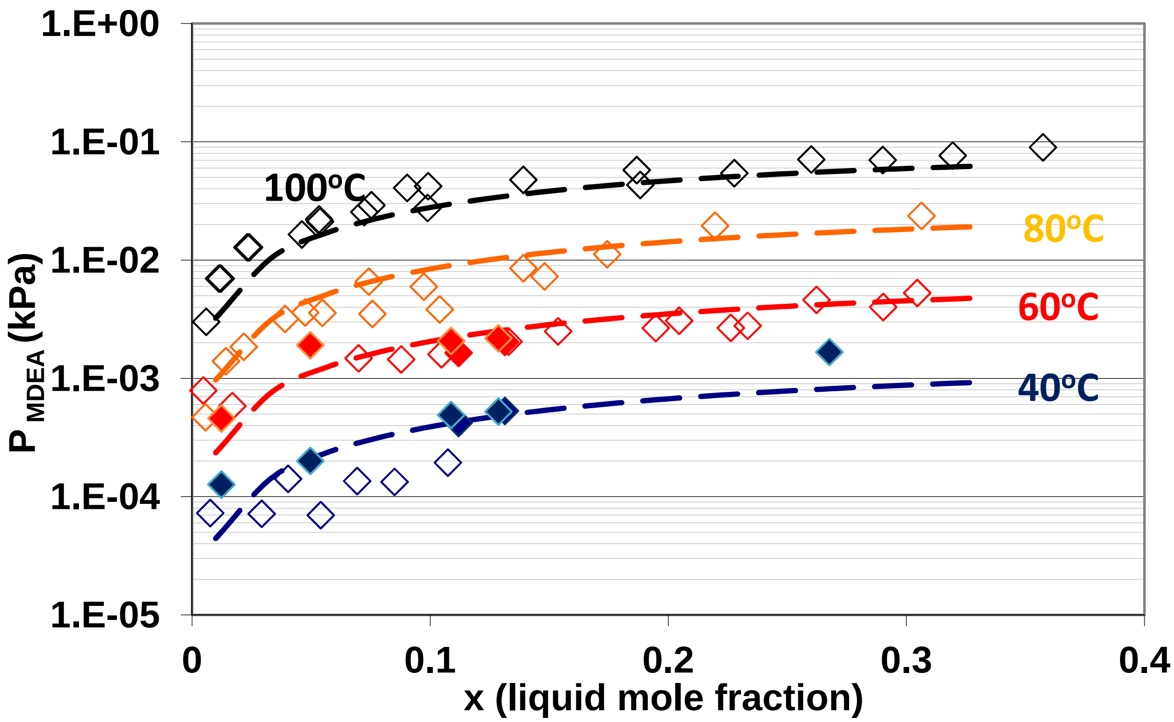

Figure 1: Experimental data from Nguyen (2009, closed points) and Kim (2008, open points) and Aspen Plus® predictions for partial pressure of MDEA as a function of amine concentration from 40–100 °C

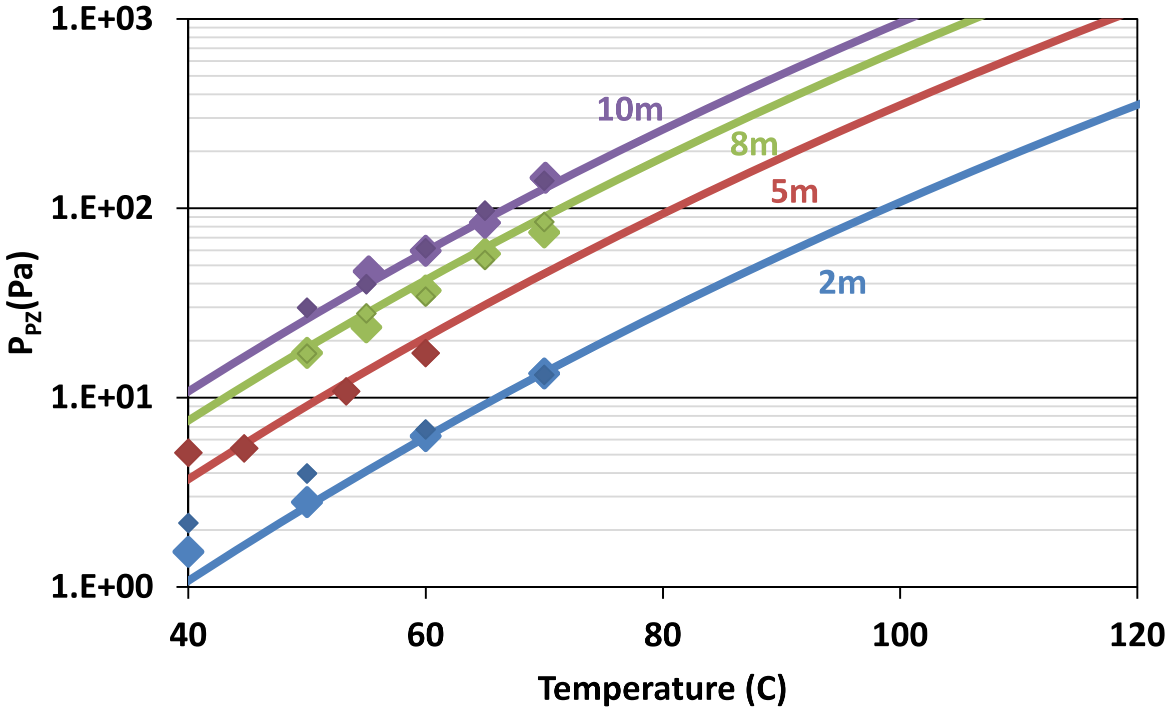

Figure 2: Experimental data from Nguyen (2009) and Aspen Plus® predictions (lines) for partial pressure of 2 m, 5 m, 8 m, and 10 m PZ from 40–70 °C

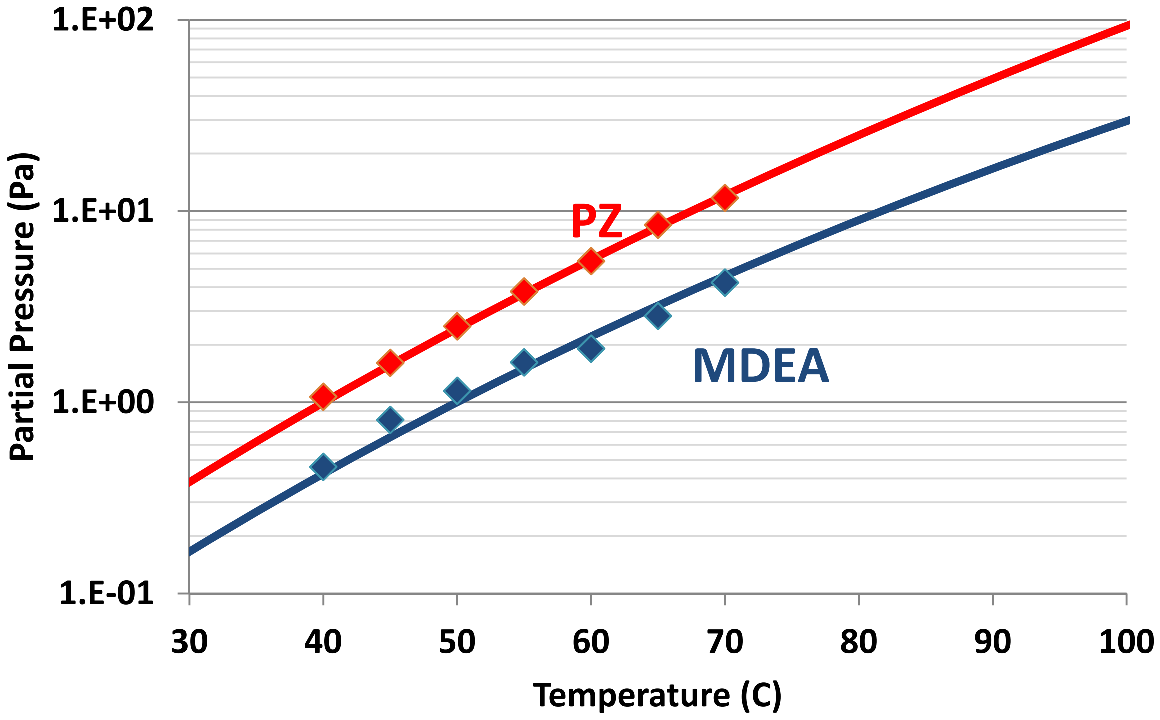

Figure 3: Experimental data from Nguyen (2012) and Aspen Plus® predictions (lines) for partial pressure of 7 m MDEA/2 m PZ from 40-–70 °C

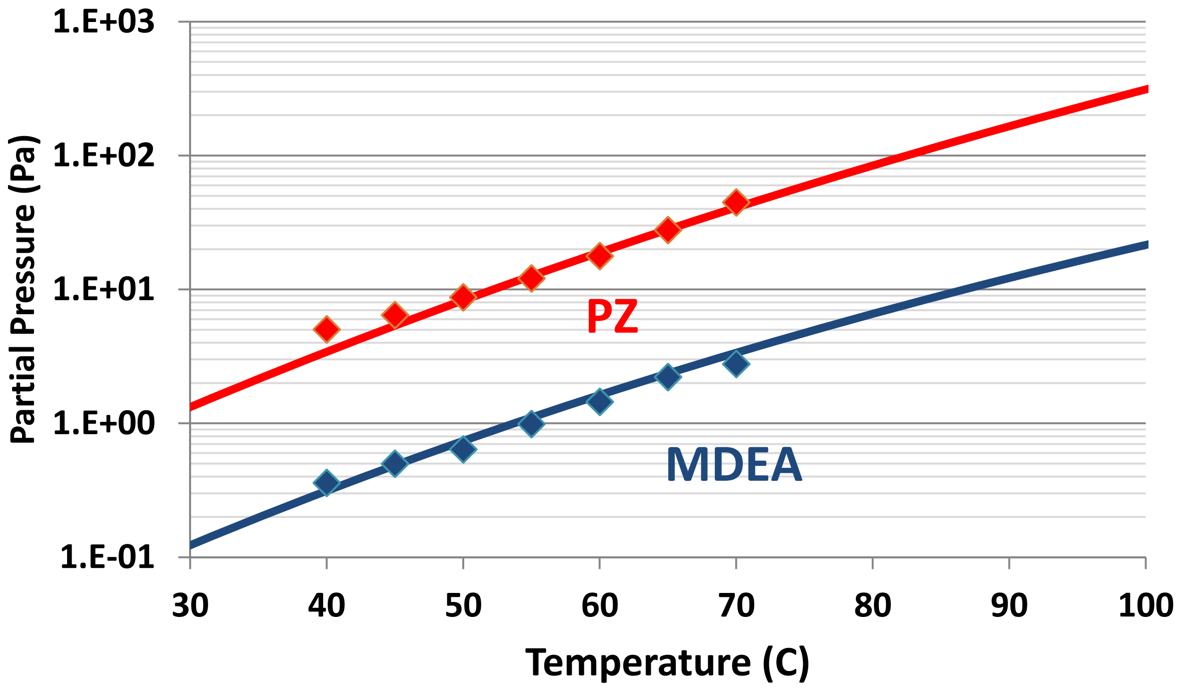

Figure 4: Experimental data from Nguyen (2012) and Aspen Plus® predictions (lines) for partial pressure of 5 m MDEA/5 m PZ from 40–70 °C

MDEA/H_2O/CO_2 Regression

Two major modifications were made to the MDEA/H_2O/CO_2 model: (1) inclusion of VLE data down to 25 wt % MDEA, and (2) addition of the carbonate species to system chemistry. The first modification is simply an effort to expand the capabilities of the model. The second modification is intended to improve model accuracy at low loadings. Table 2 reports the parameters used to regress CO_2 solubility and loaded heat capacity data for MDEA/H_2O/CO_2 along with their standard deviations.

Table 2: Parameters used to regress MDEA/H_2O/CO_2

Parameter	Components	St. Dev.
CPAQ0/1	$MDEAH^+$	4090
τ_{m-ca}/1	$H_2O/(MDEAH^+/HCO_3^-)$	0.109
τ_{ca-m}/1	$(MDEAH^+/HCO_3^-)/H_2O$	0.047
τ_{m-ca}/1	$H_2O/(MDEAH^+/CO_3^{2-})$	0.097
τ_{ca-m}/1	$(MDEAH^+/CO_3^{2-})/H_2O$	0.045
τ_{m-ca}/2	$H_2O/(MDEAH^+/HCO_3^-)$	3.77
τ_{m-ca}/1	$MDEA/(MDEAH^+/HCO_3^-)$	0.351
τ_{ca-m}/1	$(MDEAH^+/HCO_3^-)/MDEA$	0.086
τ_{m-ca}/1	$MDEA/(MDEAH^+/CO_3^{2-})$	0.136
τ_{ca-m}/1	$(MDEAH^+/CO_3^{2-})/MDEA$	0.024
τ_{m-ca}/2	$MDEA/(MDEAH^+/HCO_3^-)$	97.8

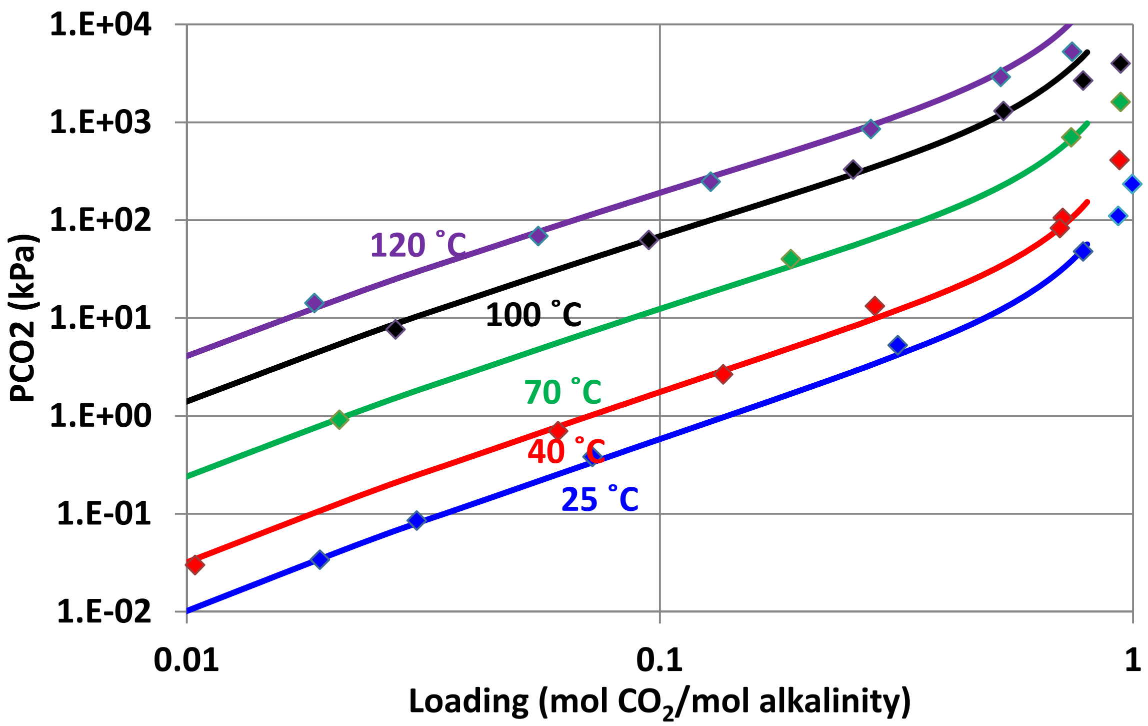

Figure 5: Experimental data from Jou (1982) and Aspen Plus® predictions (lines) for CO_2 solubility in 50 wt % MDEA between 40 °C and 120 °C

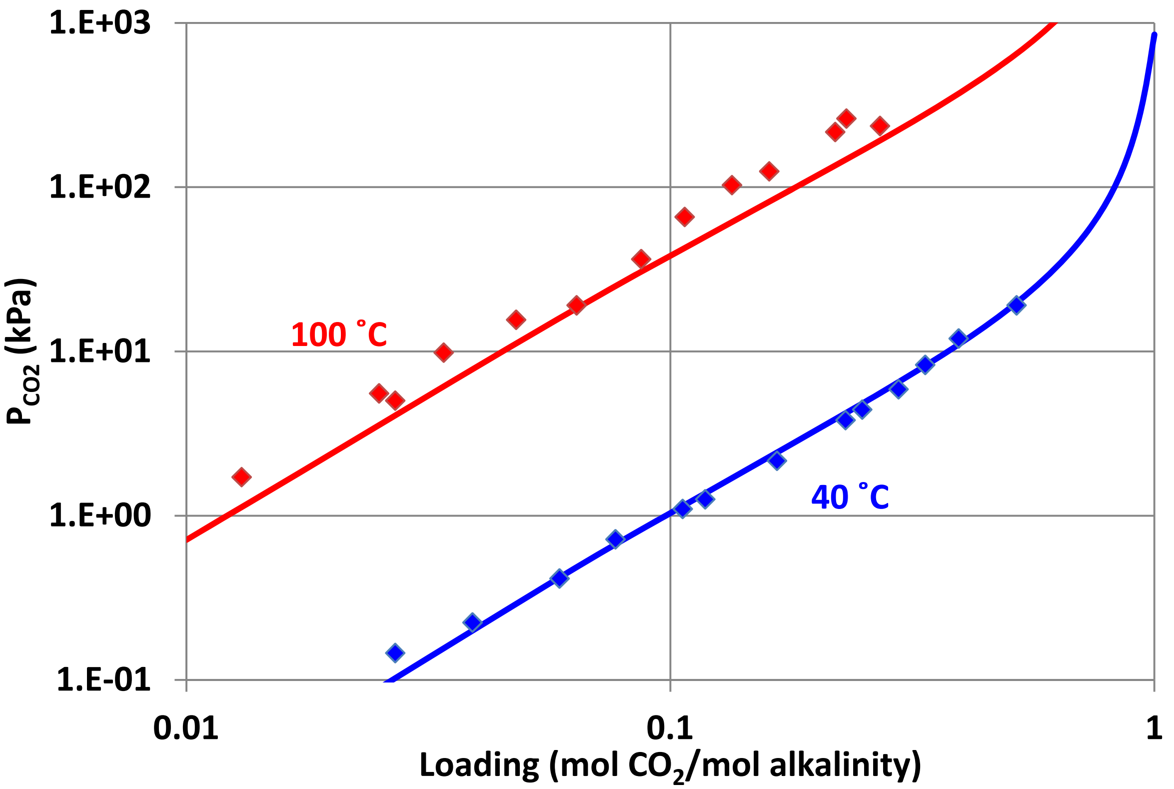

Figure 6: Experimental data from Jou (1993) and Aspen Plus® predictions (lines) for CO_2 solubility in 35 wt % MDEA between 40 °C and 100 °C

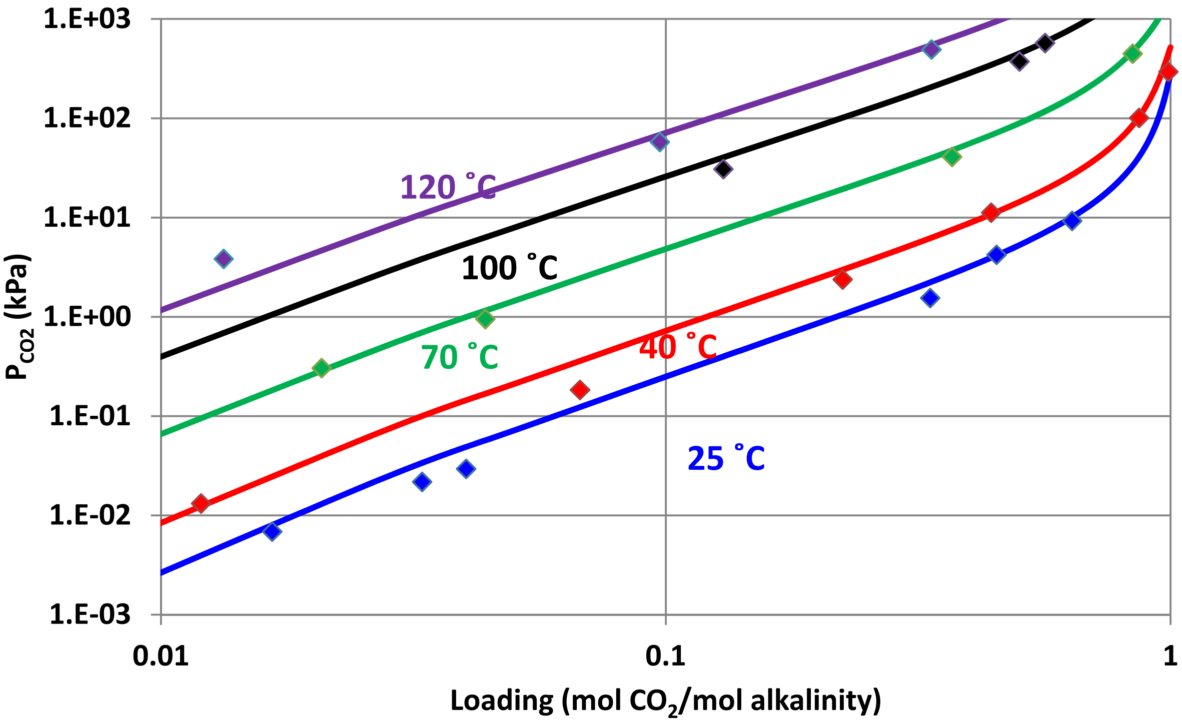

Figure 7: Experimental data from Jou (1982) and Aspen Plus® predictions (lines) for CO_2 solubility in 25 wt % MDEA between 40 °C and 120 °C

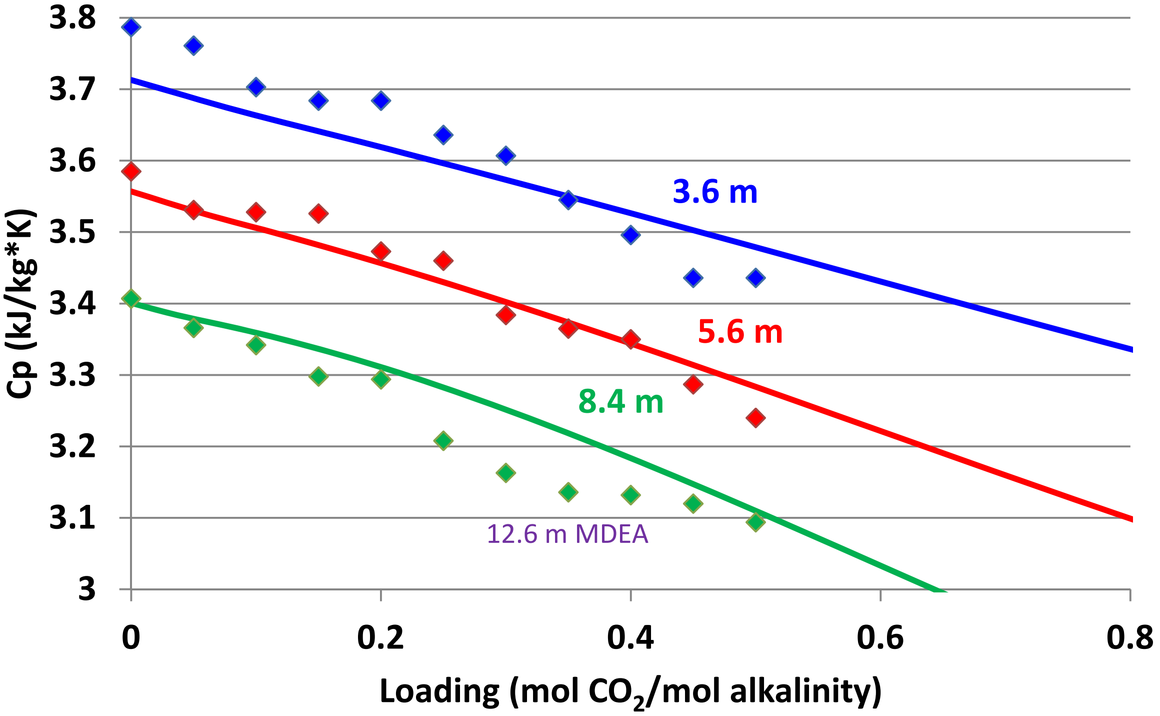

Figure 8: Experimental data from Weiland (1997) and Aspen Plus® predictions (lines) for MDEA C_P in 30–50 wt % MDEA at 25 °C

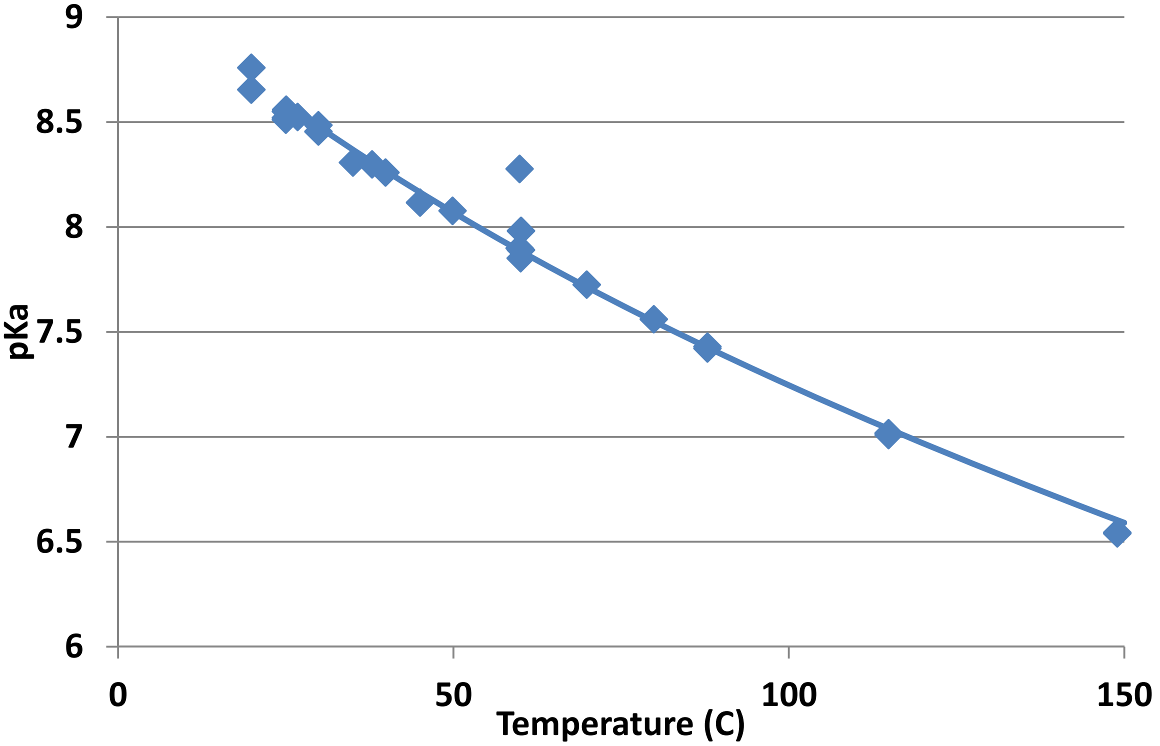

Figure 9: Experimental data from Hamborg (2007) and Aspen Plus® predictions (lines) for MDEA pKa in 50 wt % MDEA between 25 °C and 150 °C

Figures 5, 6, and 7 compare experimental data and Aspen Plus® predictions for CO_2 solubility in 50, 35, and 25 wt % MDEA, respectively. Figure 8 compares experimental data and Aspen Plus® predictions for loaded MDEA heat capacity at 25 °C. It should be noted that the Gibbs energy of formation (DGAQFM) and enthalpy of formation (DHAQFM) for $MDEAH^+$ were set by fitting MDEA pKa data from Hamborg (2007), the results of which can be found in Figure 9.

PZ/H_2O/CO_2 Regression

Just as with the Fawkes model, the PZ/H_2O/CO_2 regression focused on fitting experimental data for concentrated PZ solutions. The H^+PZCOO^- zwitterion was treated as a Henry's component with a Henry's constant on the order of 10^{-9} to ensure a minimal vapor concentration. The remaining parameters were fit by regressing CO_2 solubility and speciation data. Table 3 reports the parameters used in this regression with their standard deviations.

Table 3: Parameters used to regress MDEA/H_2O/CO_2

Parameter	Components	St. Dev.	Units
DGFORM	H^+PZCOO^-	1.75E5	J/kmol
DHFORM	H^+PZCOO^-	FIXED	J/kmol
CPIG/1	H^+PZCOO^-	FIXED	J/kmol.K
CPIG/2	H^+PZCOO^-	FIXED	J/kmol.K
DGAQFM	$PZCOO^-$	4.90E5	J/kmol
DHAQFM	$PZCOO^-$	1.01E5	J/kmol
CPAQ0/1	$PZCOO^-$	FIXED	J/kmol.K
CPAQ0/2	$PZCOO^-$	FIXED	J/kmol.K
CPAQ0/1	PZH^+	FIXED	J/kmol.K
CPAQ0/2	PZH^+	FIXED	J/kmol.K
DGAQFM	$PZ(COO)_2^{2-}$	FIXED	J/kmol
DHAQFM	$PZ(COO)_2^{2-}$	6.49E10	J/kmol
CPAQ0/1	$PZ(COO)_2^{2-}$	FIXED	J/kmol.K
CPAQ0/2	$PZ(COO)_2^{2-}$	FIXED	J/kmol.K
$\tau_{m-ca}/1$	$H_2O/(PZH^+,PZCOO^-)$	0.103	N/A
$\tau_{ca-m}/1$	$(PZH^+,PZCOO^-)/H_2O$	0.065	N/A
$\tau_{m-ca}/1$	$H_2O/(PZH^+,PZ(COO)_2^{2-})$	0.137	N/A
$\tau_{ca-m}/1$	$(PZH^+,PZ(COO)_2^{2-})/H_2O$	0.056	N/A
$\tau_{m-ca}/1$	$PZ/(PZH^+,PZCOO^-)$	0.262	N/A
$\tau_{ca-m}/1$	$(PZH^+,PZCOO^-)/PZ$	0.066	N/A
$\tau_{m-ca}/1$	$PZ/(PZH^+,PZ(COO)_2^{2-})$	0.140	N/A
$\tau_{ca-m}/1$	$(PZH^+,PZ(COO)_2^{2-})/PZ$	0.030	N/A
$\tau_{m-ca}/1$	$H^+PZCOO^-/(PZH^+,PZCOO^-)$	0.135	N/A
$\tau_{ca-m}/1$	$(PZH^+,PZCOO^-)/H^+PZCOO^-$	0.033	N/A
$\tau_{m-ca}/1$	$H^+PZCOO^-/(PZH^+,PZ(COO)_2^{2-})$	0.118	N/A
$\tau_{ca-m}/1$	$(PZH^+,PZ(COO)_2^{2-})/H^+PZCOO^-$	0.074	N/A
$\tau_{m-ca}/1$	$H^+PZCOO^-/(PZH^+,HCO_3^-)$	0.100	N/A
$\tau_{ca-m}/1$	$(PZH^+,HCO_3^-)/H^+PZCOO^-$	0.050	N/A

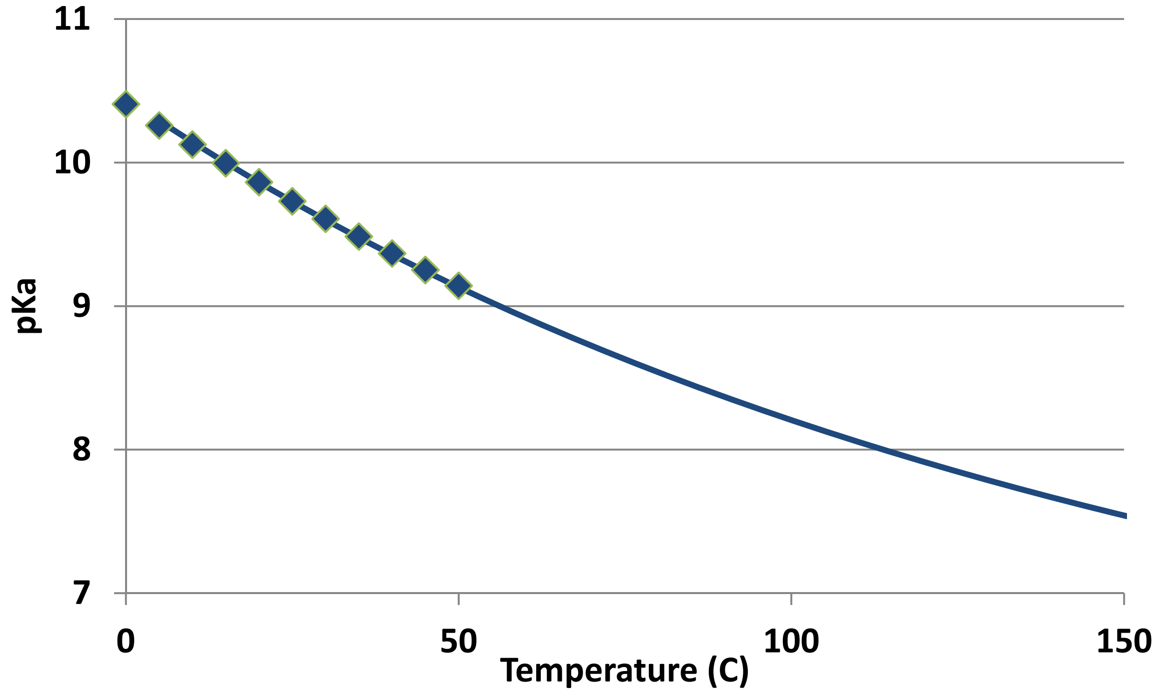

Figure 10: Experimental data from Hetzer, 1968 (points) and Aspen Plus® predictions (lines) for PZ pKa between 0 °C and 50 °C

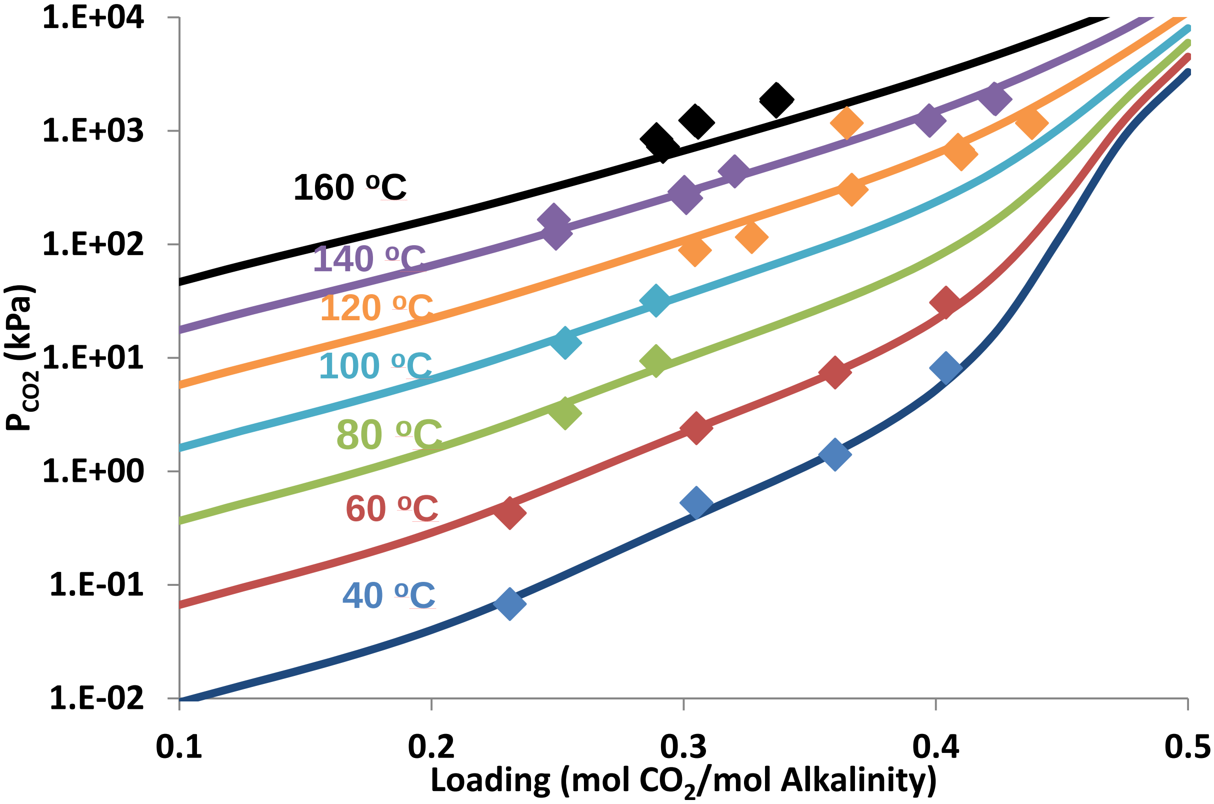

Figure 11: Experimental data from Dugas (2009) and Xu (2011) and Aspen Plus® predictions for CO_2 solubility in 8 m PZ pKa between 40 °C and 160 °C

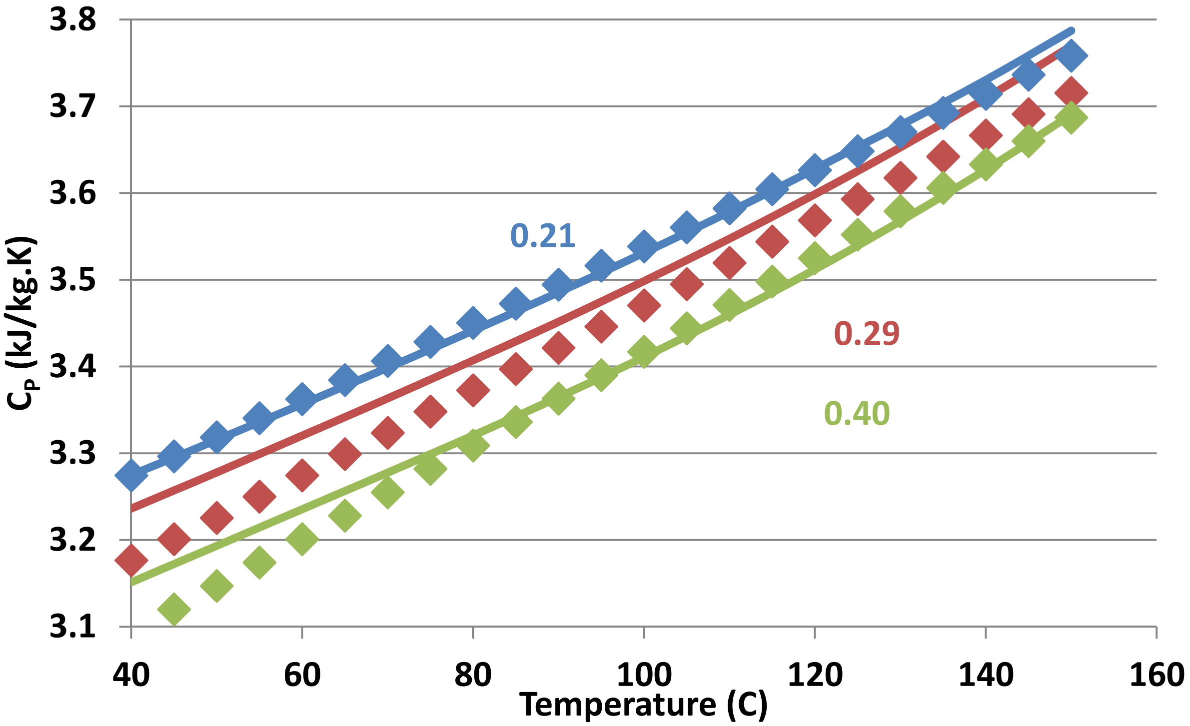

Figure 12: Experimental data and Aspen Plus® predictions for heat capacity of 8 m PZ pKa between 40 °C and 150 °C at loadings of 0.21 (blue), 0.29 (red) and 0.40 (green)

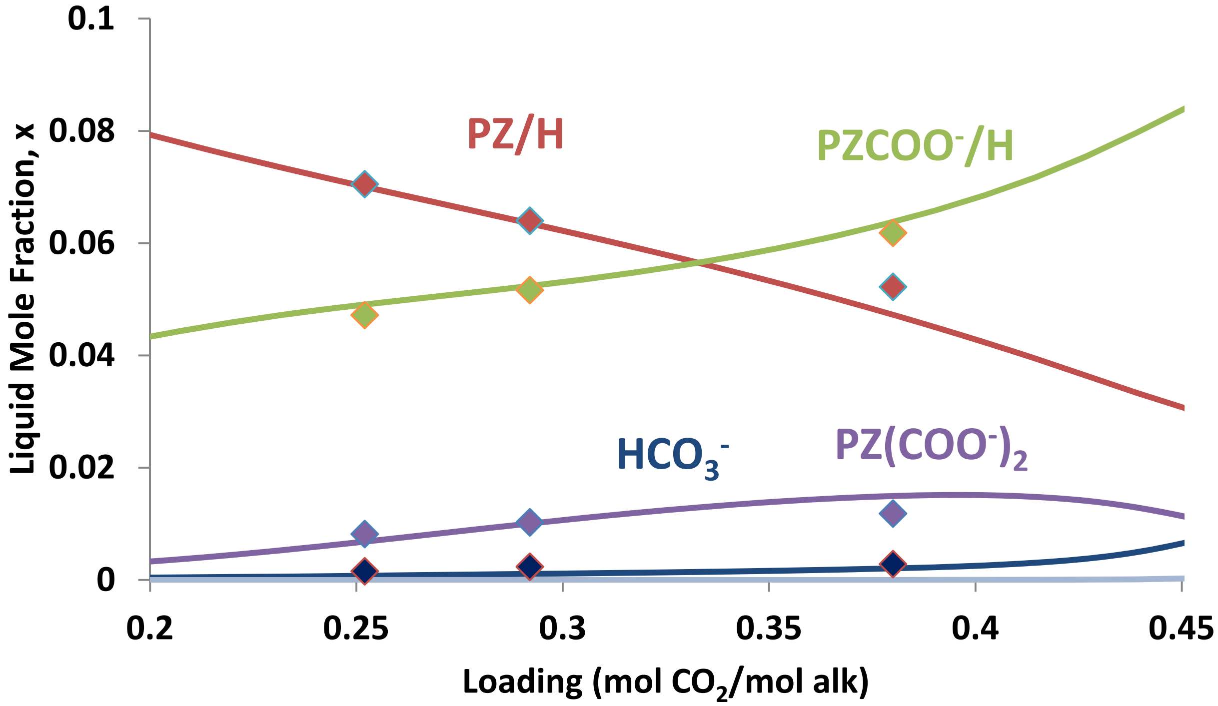

Figure 13: Experimental data from Nguyen (2012) and Aspen Plus® predictions for speciation of 8 m PZ at 40 °C

Gibbs energy of formation (DGAQFM) and the enthalpy of formation (DHAQFM) for PZH^+ were set by fitting PZ pKa data from Hetzer (1968), the results of which can be found in Figure 10. Figures 11, 12, and 13 compare 8 m PZ experimental and predicted CO_2 solubility, loaded heat capacity, and speciation, respectively.

MDEA/PZ/H_2O/CO_2 Regression

Because the ΔG_{form}, ΔH_{form}, and $C_{P,aq}$ of all species present in MDEA/PZ/H_2O/CO_2 have already been regressed, the only remaining adjustable parameters were the cross parameters used in the calculation of activity coefficients. These parameters were used to fit 7 m MDEA/2 m PZ and 5 m MDEA/5 m PZ VLE data (Chen, 2010; Xu, 2010) between 40 °C and 160 °C. Table 4 reports the parameters used to regress CO_2 solubility data for MDEA/PZ/H_2O/CO_2 along with their standard deviations.

Table 3: Parameters used to regress MDEA/PZ/H_2O/CO_2

Parameter	Components	St. Dev.	Units
τ_{ca-m}/1	($MDEAH^+$,$PZ(COO)_2^{2-}$)/H_2O	0.049	N/A
τ_{ca-m}/2	($MDEAH^+$,$PZCOO^-$)/MDEA	665.5	K
τ_{ca-m}/2	(PZH^+,HCO_3^-)/MDEA	1045	K
τ_{ca-m}/1	($MDEAH^+$,HCO_3^-)/H^+PZCOO^-	0.600	N/A
τ_{ca-m}/2	($MDEAH^+$,$PZCOO^-$)/H^+PZCOO^-	557	K
τ_{ca-m}/2	($MDEAH^+$,HCO_3^-)/H^+PZCOO^-	196	K
τ_{ca-m}/1	($MDEAH^+$,$PZCOO^-$)/PZ	0.050	N/A

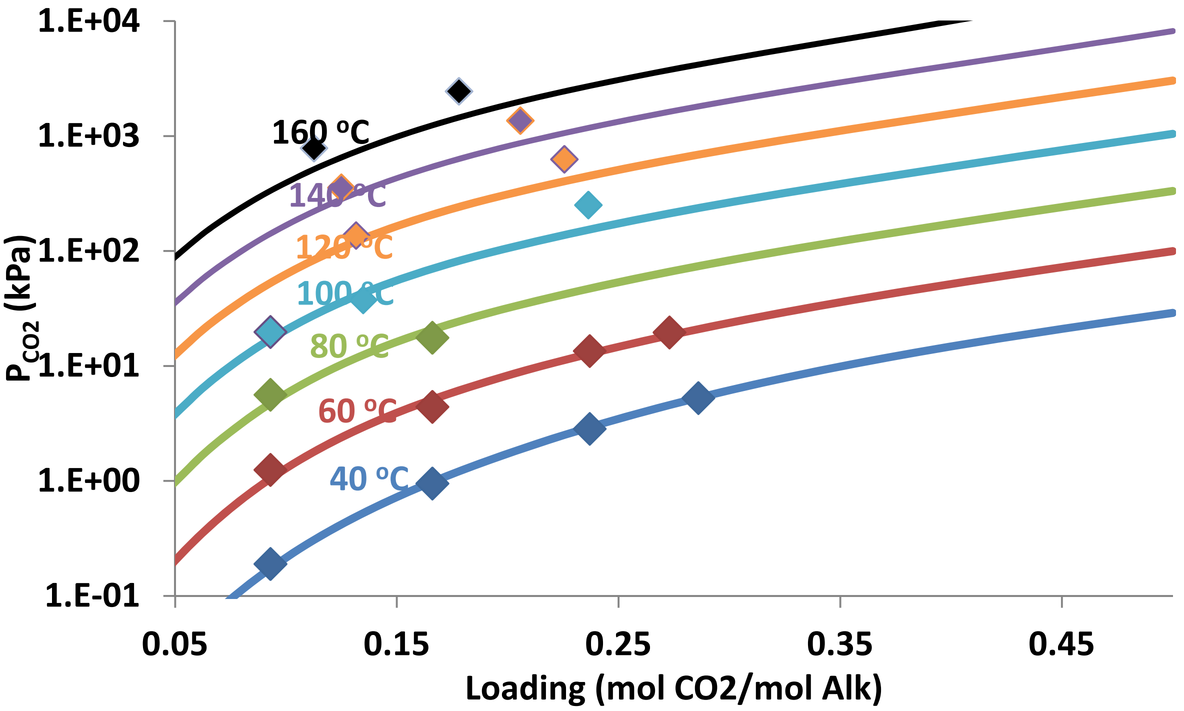

Figure 14: Aspen Plus® predictions (lines) and experimental data from Chen (2011) and Xu (2010) for VLE of 7 m MDEA/2 m PZ between 40 °C and 160 °C

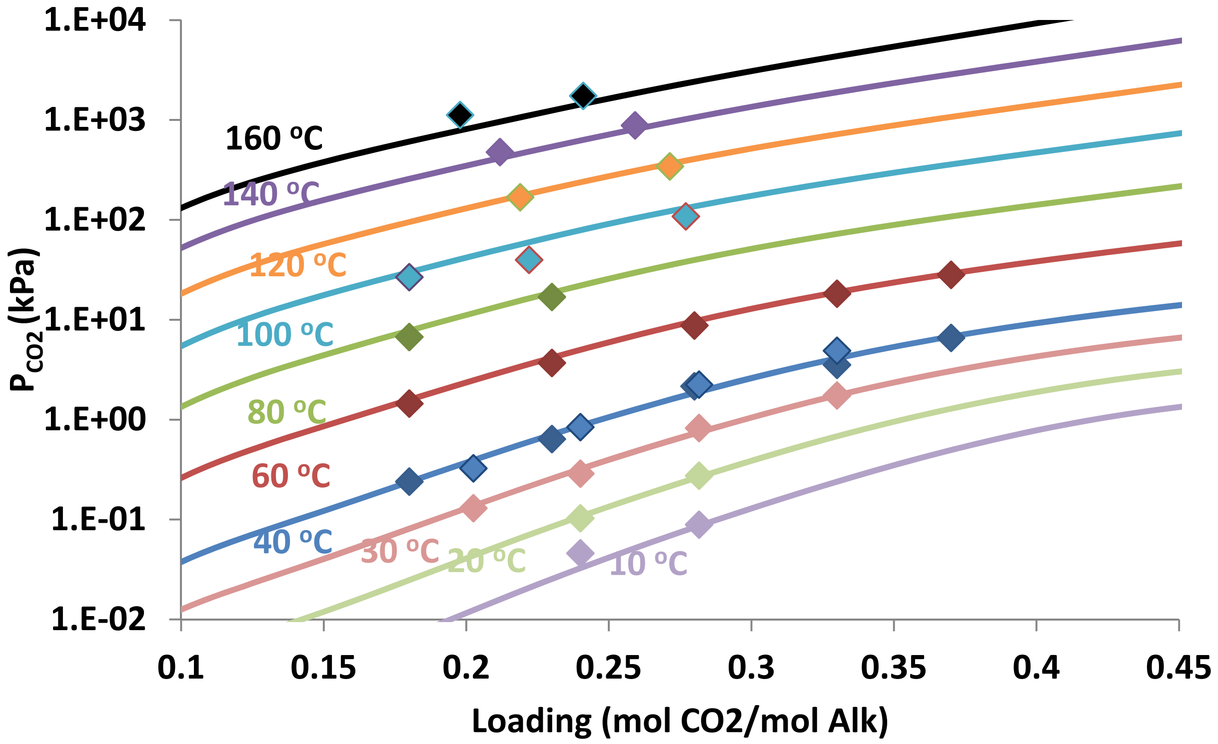

Figure 15: Experimental data from Chen (2011), Xu (2010), and Li (2011) and Aspen Plus® predictions (lines) for VLE of 5 m MDEA/5 m PZ between 10 °C and 160 °C

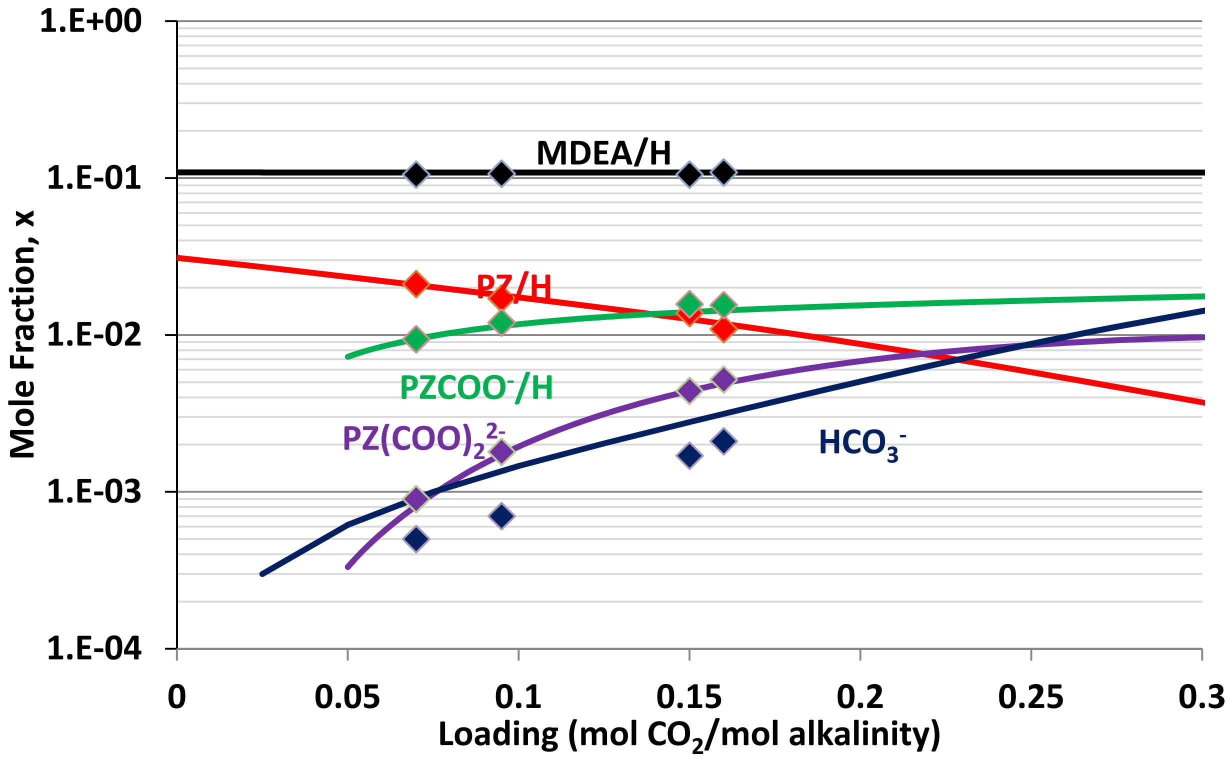

Figure 16: Experimental data from Nguyen (2012) and Aspen Plus® predictions (lines) for speciation of 7 m MDEA/2 m PZ at 40 °C

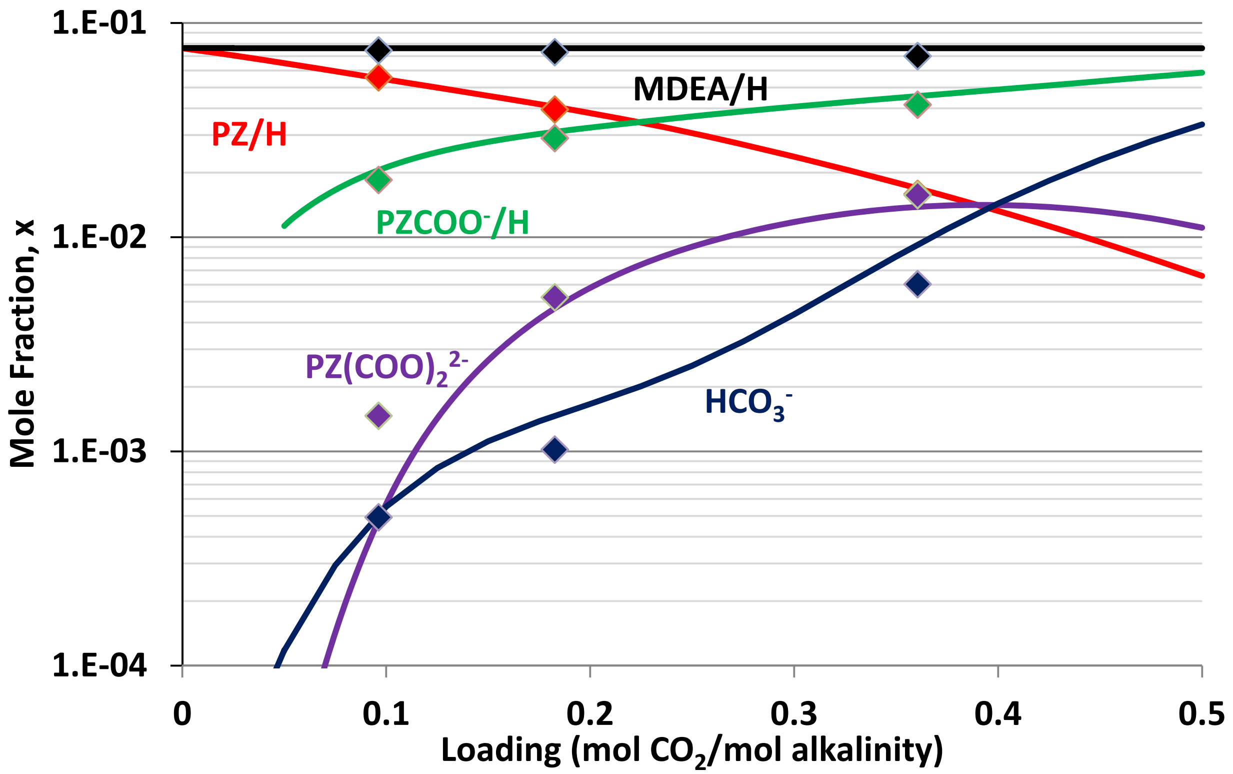

Figure 17: Experimental data from Nguyen (2012) and Aspen Plus® predictions (lines) for speciation of 5 m MDEA/5 m PZ at 40 °C

Figure 14 compares the experimental data and Aspen Plus® predictions for 7 m MDEA/2 m PZ between 40 °C and 160 °C, and Figure 15 compares the experimental data and Aspen Plus® predictions for 5 m MDEA/5 m PZ between 10 °C and 160 °C. Figures 16 and 17 compare experimental speciation data and Aspen Plus® predictions for 7 m MDEA/2 m PZ and 5 m MDEA/5 m PZ, respectively.

It should be noted that all other parameters in all regressions were left at Aspen Plus® default values. The new thermodynamic model uses more non-default parameter values than the Fawkes model, but that is to be expected. The new model includes VLE data down to 10 °C, a wider range of MDEA concentrations, and a new species (CO_3^{2-}).

MDEA/PZ Hydraulic Model

The correlations used to calculate density and viscosity have been modified to match pure water properties. This modification is intended to improve the accuracy of model predictions at water wash conditions. Density and viscosity were calculated using Equations 1 and 2, respectively.

$$\begin{aligned}\rho = (x_{H_2O})(\rho_{H_2O}) + (x_{MDEA})(AT+B) + (x_{PZ})(CT+D) + (x_{CO_2})(ET+F) + \ldots \\ \ldots + (x_{CO_2})(x_{MDEA}+x_{PZ})(GT+H)\end{aligned} \tag{1}$$

$$\frac{\mu}{\mu_{H_2O}} = \exp\left[\frac{[(Aw_{Am}+B)T+(Cw_{Am}+D)][\alpha(Ew_{Am}+FT+G)+1]w_{Am}}{T^2}\right] \tag{2}$$

In Equations 1 and 2, x_i is component mole fraction, w_{Am} is weight fraction of amine, α is loading, and T is temperature in K. Both of these equations are similar in form to those developed by Weiland (1998). Weiland calculates molar volume as a mole fraction basis and includes a term for the interaction between water and amine. Both equations had to be modified to include terms for both MDEA and PZ. Every weight fraction of amine term (w_{Am}) in Equation 2 was split into w_{MDEA} and w_{PZ}.

Conclusions

The thermodynamics and hydraulics of PZ (5 m–12 m), MDEA (2.8 m–8.4 m), 7 m MDEA/2 m PZ, and 5 m MDEA/5 m PZ were incorporated into Aspen Plus®. The model adequately predicts VLE, density, viscosity, heat capacity, speciation, and amine volatility data over significant loading and temperature ranges for each of these amines. Regressed expressions for the density and viscosity for each of these amines can be easily incorporated into Aspen Plus® using user-supplied FORTRAN subroutines. Experimental data concerning absorption rates of CO_2 are still being incorporated.

Future Work

The kinetics of MDEA/PZ will be the top priority for the next quarter. This will include fitting rate data for 7 m MDEA/2 m PZ and 5 m MDEA/5 m PZ with the WWC simulation in Aspen Plus®. Once this is completed, an absorption/stripping/compression process will be designed and optimized.

References

Bishnoi S. *Carbon Dioxide Absorption and Solution Equilibrium in Piperazine Activated Methyldiethanolamine*. The University of Texas at Austin. Ph.D. Dissertation. 2000.

Chen X. Accurate screening of amines by the Wetted Wall Column. *GHGT-10*. Amsterdam, NL: Elsevier, 2010.

Cullinane JT. *Thermodynamics and Kinetics of Aqueous Piperazine with Potassium Carbonate for Carbon Dioxide Absorption*. The University of Texas at Austin. Ph.D. Dissertation. 2005.

Dugas RE. *Carbon Dioxide Absorption, Desorption, and Diffusion in Aqueous Piperazine and Monoethanolamine*. The University of Texas at Austin. Ph.D. Dissertation. 2009.

Hamborg ES, Niederer JPM, Versteeg GF. Dissociation Constants and Thermodynamic Properties of Amino Acids Used in CO_2 Absorption from (293 to 353) K. *J Chem Eng Data*. 2007;52:2491–2502.

Hetzer HB, Robinson RA, Bates RG. Dissociation Constants of Piperazinium Ion and Related Thermodynamic Quantities from 0 to 50°. *J Phys Chem.* 1968;72(6):2081–2086.

Jou FY, Mather AE, Otto FD. Solubility of hydrogen sulfide and carbon dioxide in aqueous methyldiethanolamine solutions. *Ind Eng Chem. Process Des Dev.* 1982; 21(4): 539–544.

Jou FY, Carroll JJ, Mather AE Otto FD. The Solubility of Carbon Dioxide and Hydrogen Sulfide in a 35 wt % Aqueous Solution of Methyldiethanolamine. *Can J Chem Eng.* 1993; 71: 264–268.

Kim I, Svendsen HF, Borresen E. Ebulliometric Determination of Vapor-Liquid Equilibria for Pure Water, Monoethanolamine, N-Methyldiethanolamine, 3-(Methylamino)-propylamine, and Their Binary and Ternary Solutions. *J Chem Eng Data*. 2008; 53: 2521–2531.

Li, personal communication, 2011.

Nguyen, personal communication, July 20, 2009.

Nguyen, personal communication, January 18, 2012.

Weiland RH, Dingman, JC, Cronin DB. Heat Capacity of Aqueous Monoethanolamine, Diethanolamine, N-Methyldiethanolamine, and N-Methyldiethanolamine-Based Blends with Carbon Dioxide. *J Chem Eng. Data.* 1997; 42: 1004–1006.

Weiland RH, Dingman, JC, Cronin, DB, Browning, GJ. Density and Viscosity of Some Partially Carbonated Aqueous Alkanolamine Solutions and Their Blends. *J Chem Eng Data*. 1998; 43:378–382.

Xu Q. Total Pressure and CO_2 Solubility at High Temperatures in Aqueous Amines. *GHGT-10*. Amsterdam, NL: Elsevier, 2010.

Pilot Plant Testing of Advanced Process Concepts using Concentrated Piperazine

Quarterly Report for January 1 – March 31, 2012

by Eric Chen

Supported by the Luminant Carbon Management Program, the Industrial Associates Program for CO_2 Capture by Aqueous Absorption,

the CO_2 Capture Pilot Plant Project of the Process Science and Technology Center

and the U.S. Department of Energy

Department of Chemical Engineering

The University of Texas at Austin

April 30, 2012

Summary

In this period, the final report for the second pilot plant campaign with the modified high temperature two-stage flash skid was completed. The campaign report was issued to the C2P3 sponsors and contains the details of the modifications made to the skid and pilot plant, the absorber and flash skid configuration, the startup, operation, and shutdown procedure, pilot plant and analytical data, and interpreted results.

A work plan was developed in preparation for the 2012 pilot plant campaign. The six objectives of the plan are: aerosol characterization and mitigation from the absorber column, evaluation of high temperature oxidation from oxygen entrainment in the absorber bottoms, addressing nitrosamine formation in the piperazine (PZ) solvent from oxidation and reaction with NO_x, development of a pilot-scale PZ reclaiming process, upgrade of steam heater capacity and installation of low temperature flash tank for new process configuration that minimizes oxidation and demonstrates thermal decomposition of nitrosamine, and development of process control strategy for pilot plant operation with minimized solvent inventory.

Pilot plant data validation for the October 2011 HTPZ-2 campaign showed that FT-200, the absorber bottom outlet flow measurement, had large standard deviations. FT-201, the skid return flow meter, may also have higher than expected standard deviations relative to the stated manufacturer's specifications. The deviations of FT-200 were also observed in an overall pilot plant material balance analysis, which compared the combined flow rates of the skid return, condensate, and CO_2 recycle mass flow rates as measured by the online instruments. Discussions with the Micro Motion sales representative revealed that the temperature measurement in the Coriolis flow meter do not directly contact the process fluid and should be carefully used.

Heat exchanger models were developed using Aspen Exchanger Design and Rating (EDR) for the high pressure cross-exchanger (H-520), low pressure cross-exchanger (H-113), high pressure steam heater (H-525), and low pressure steam heater (H-535). Also, Aspen Plus® models for the

six control valves on the flash skid have been developed to help with data validation and provide better understanding of the process skid in terms of operating limitations and future equipment modifications.

Modifications to the CSIRO pilot plant are slowly proceeding under the assumption that the ANLEC agreement will be signed in the near future. Modifications are scheduled to be completed in mid-April and startup of the unit in late April to early May. The CSIRO pilot unit will evaluate concentrated PZ with high temperature simple stripping. The University of Texas will provide technical support and consultation.

A proposal has been submitted to DOE to revise the scope of work by URS with UT input. The new proposal will redirect funding originally allocated for the flash skid testing at CSIRO to a campaign with the flash skid at SRP in the fall of 2012. The proposal also forgoes fabrication of the 0.5 MW flash skid for the NCCC testing and proposes use of the existing high pressure simple stripper. The focus of the NCCC testing will be on aerosol emissions, nitrosamines, and reclaiming.

Pilot Plant Validation and Carbon Capture from Natural Gas Applications

Quarterly Report for January 1 – March 31, 2012

by Darshan Sachde

Supported by the Luminant Carbon Management Program
and by the PSTC Project on CO_2 Capture from Natural Gas Combustion (funded by TOTAL)

Department of Chemical Engineering
The University of Texas at Austin

April 30, 2012

Abstract

During the first quarter of 2012, pilot plant data analysis continued as part of absorber model development and validation. The October 2011 campaign at J.J. Pickle Research Campus (PRC) was the focus of the recent work and included error quantification in mass balance (CO_2 and PZ) and CO_2 removal calculations. The CO_2 mass balance closed for 7 of 10 pilot plant runs within 1 standard deviation, and the PZ mass balance closed for 5 of 10 runs. Issues highlighted in the analysis included confirmation of reduced variation and improved accuracy in manual titration compared to auto titration, existence of potential bias in PZ auto titration, and offset in rich loading flow measurements. Finally, gas side CO_2 mass balance revealed statistically significant (at 95% confidence interval) improvement in CO_2 removal due to spray nozzle implementation in 2 of 3 runs.

The absorber model that was validated in Q4 2011 was used to develop design cases for natural gas combustion applications. A preliminary absorber design was developed for CO_2 capture from the flue gas of a combined cycle gas turbine. The novel absorber configuration includes lean gas cooling in the absorber column (no direct contact cooler) via rich amine recycle. Initial results for 8 m PZ with a lean loading of 0.27 mols CO_2/mols alkalinity, a 10:1 recycle rate in the 1 m bottom packed section, and a L/G of 1.65 have achieved 84% CO_2 removal with 15 m of total packed height (2250 m^3 packed volume). However, driving force analysis revealed a lean end pinch corresponding to a temperature bulge in the column. Methods to address these performance issues are discussed in detail in this report.

Finally, preliminary absorber designs for economic analysis of CO_2 capture from coal-fired combustion presented in the fourth quarter of 2011were optimized and finalized. The designs included cases at lean loadings 0.27 and 0.30 mols CO_2/mols alkalinity and at absorber operating temperatures of 30 °C and 40 °C. The low temperature absorber designs reduced packing volume by as much as 25% and absolute solvent circulation rates by as much as 10% relative to the analogous design at 40 °C. The report includes detailed design results for all cases.

Introduction

During the past quarter, pilot plant data from the October 2011 campaign at PRC was analyzed for mass balance closure and to quantify uncertainty in measurement data. The mass balance data were also used to compare analytical methods for CO_2 and PZ measurement as well reliability of flow measurement data. The results of the analysis will be used as part of data reconciliation analysis in Aspen Plus® to further validate the 5deMayo 8 m PZ model and to evaluate the performance of the spray nozzle used in the intercooling loop during the campaign.

In addition to the pilot plant work, design cases were developed for carbon capture from a natural gas application. The absorber design omits a direct contact cooler from standard coal designs and implements a cold rich recycle in the bottom packed section of the column. A preliminary base case design has been developed and key design constraints have been identified for continued optimization.

October 2011 Pilot Plant Campaign

The October 2011 campaign at PRC used 8 m PZ with 6.1 m of GTC 350Z packing in the absorber. Intercooling was used in all runs of the campaign, with 3 of the runs including the use of a spray nozzle on the intercooling return to the column. The nozzle was located between the top and bottom sections of packing oriented towards the top of the column; therefore, the spray impacted the top section of packing on its return to the column. The use of the nozzle was expected to provide additional mass transfer area relative to the standard intercooling return.

Methodology

Data Reconciliation

The data from the pilot plant provide an opportunity to validate heat and material balances as predicted by the 5deMayo 8 m PZ model developed in Aspen Plus® by Plaza (2011). As reported in Q4 2011, the data reconciliation tool uses pilot plant data in an error minimization routine to adapt the absorber model to reflect field performance (Rochelle et al., 2011; Plaza, 2011). Figure 1 summarizes the data reconciliation process.

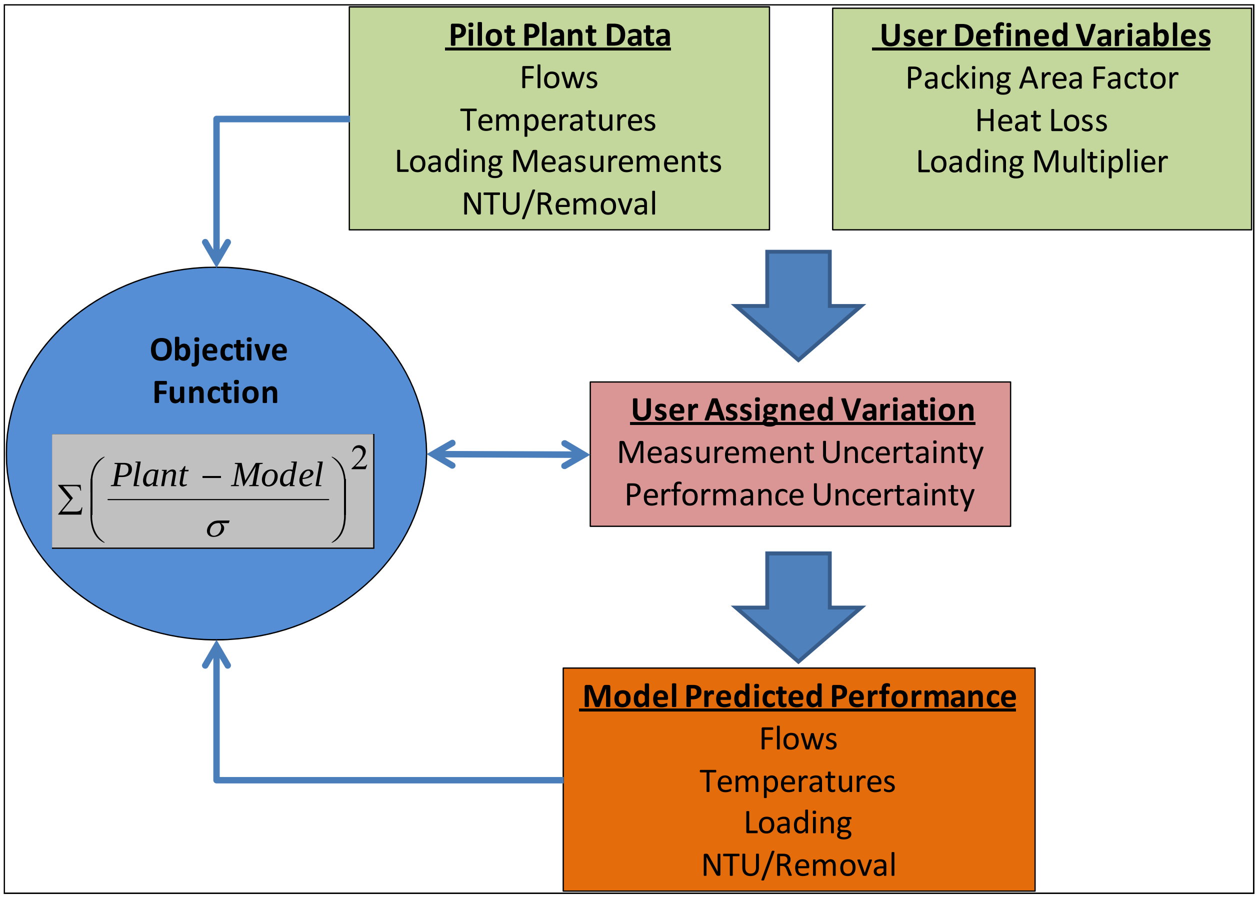

Figure 1: Data Reconciliation Overview as implemented in Aspen Plus®

The reconciliation process uses both user-defined variables and the variation associated with the pilot plant data to fit the model to the reported field performance data. The user-defined parameters, or fitting parameters, are in turn permanently incorporated into the validated absorber model.

For example, to isolate the effect of the spray nozzle on absorber performance, the nozzle will be modeled as a packed section in the absorber column in Aspen Plus® with an "area factor" or fitting parameter that will be allowed to vary during the reconciliation process. The modification to the packing area model developed by Wang is as follows (Rochelle et al., 2011):

$$\frac{a_e}{a_p} = \mathbf{A_F} * C_A \left(\frac{\rho_L}{\sigma}\right)^{0.116} (v_L)^{0.155} \tag{1}$$

where:

a_e = Specific wetted area (effective area);
a_p = Specific area of packing;
$\mathbf{A_F}$ = Area factor for spray nozzle data-fitting;
C_A= Experimental constant (based on packing type);
ρ_L = Liquid density;
σ = Liquid surface tension;
v_L = Liquid superficial velocity.

The area factor modification represents the mass transfer area generated by the spray nozzle in operation relative to a packed section of column.

The spray nozzle modeling effort emphasizes the importance of error quantification; if pilot plant data uncertainty is improperly quantified or heat and material balances do not close within reported uncertainty, user-defined variables (e.g., area factor for the spray nozzle) may no longer represent physical parameters but rather error fitting parameters to compensate for shortcomings in pilot plant data. Therefore, the first step in model development and validation for the October 2011 campaign was error quantification; the following section outlines the procedure used in this work.

Mass Balance and Error Analysis

The pilot plant error analysis over the past quarter focused on mass balance data around the absorber; performance parameters such as CO_2 removal or loadings are representations of mass balance results. Figure 2 depicts a simplified absorber process flow diagram (PFD) from the pilot plant at PRC including flow and analytical measurement points used in the current analysis. Table 1 provides additional detail on the measurements.

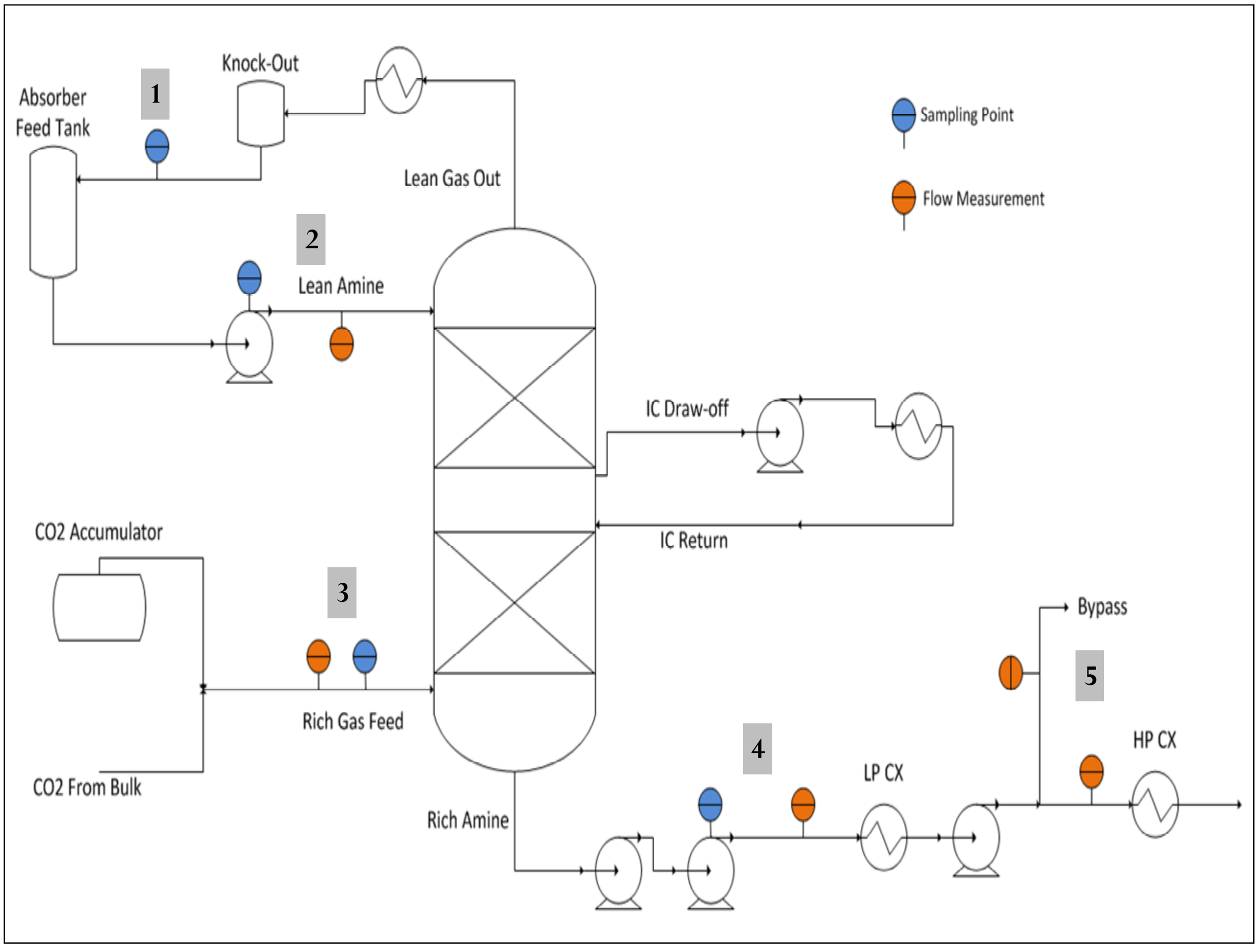

Figure 2: Simplified Absorber PFD with indications for sampling and measurement points used in the mass balance in this report. Points 1 through 5 are with corresponding descriptions in Table 1.

Table 1: Flow and Analytical Measurements Available for Pilot Plant Mass Absorber Mass Balance

Stream and ID	CO2		PZ	
	Flow	Analytical	Flow	Analytical
Lean Amine (Point 2 in Figure 2)	Micro Motion® Coriolis Flow Meters	Auto Titration Manual Titration TIC	Micro Motion® Coriolis Flow Meters	Auto Titration Manual Titration
Rich Amine (Points 4 and 5 in Figure 2)	Micro Motion® Coriolis Flow Meter	Auto Titration Manual Titration TIC	Micro Motion® Coriolis Flow Meter	Auto Titration
Lean Gas (Point 1 in Figure 2)	Rosemount® Annubar (Differential Pressure) Meter	Vaisala® GMT220 CO_2 Sensor (NDIR Sensor)	N/A	N/A**
Rich Gas (Point 3 in Figure 2)	Inferred from Inlet	Vaisala® GMT220 CO_2 Sensor (NDIR Sensor)	N/A	N/A
**FTIR Data available for PZ, CO_2 in Gas Outlet; Not used in this analysis				

The data from the flow meters (coriolis and annubar) and the inline CO_2 gas concentration (NDIR sensor) were averaged over the duration of a run at steady state; the corresponding standard deviation represented the random error associated with the inline measurements. The titration and TIC data were analyzed in triplicate for each pilot plant run; the average and standard deviation of the three samples were used in the error analysis. The gas outlet flow rate was calculated by using the compositions of the inlet and outlet streams and assuming constant mass flow of air in and out of the column. The flow data and analytical measurements were sufficient to complete a mass balance around the absorber for CO_2 and PZ; the error in the individual measurements was propagated through all calculations to provide a range around the mass balance closure numbers. In addition, CO_2 removal calculations were performed for each run based on gas and liquid data.

Note that the error analysis only considered random variation; no data regarding bias were available, but quantification of the random variation will allow inference about the presence of bias in the subsequent analysis.

Results

CO_2 Mass Balance

The CO_2 mass balance included a comparison between auto and manual titration by evaluating mass balance closure and variability in the data using each of the analytical methods. TIC data were insufficient to complete mass balances in several of the pilot plant runs, so it is excluded here. Figures 3 and 4 show CO_2 mass balance closure results using auto and manual titration, respectively.

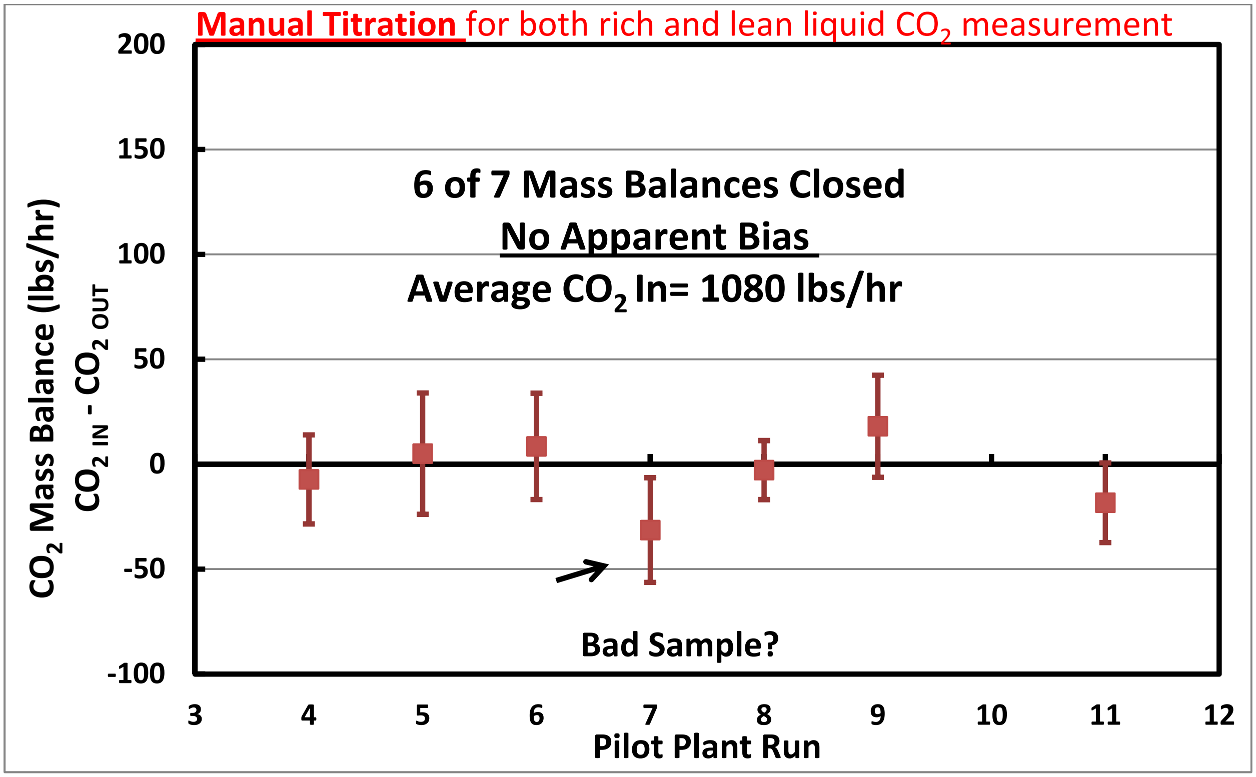

Figure 3: CO_2 mass balance (CO_2 In, Liquid and Gas – CO_2 Out, Liquid and Gas) results using manual titration for lean and rich concentrations and rich amine flow at position 4 in Figure 2. Y = 0 line indicates perfect mass balance closure. Error bars represent 1 standard deviation error about the mean.

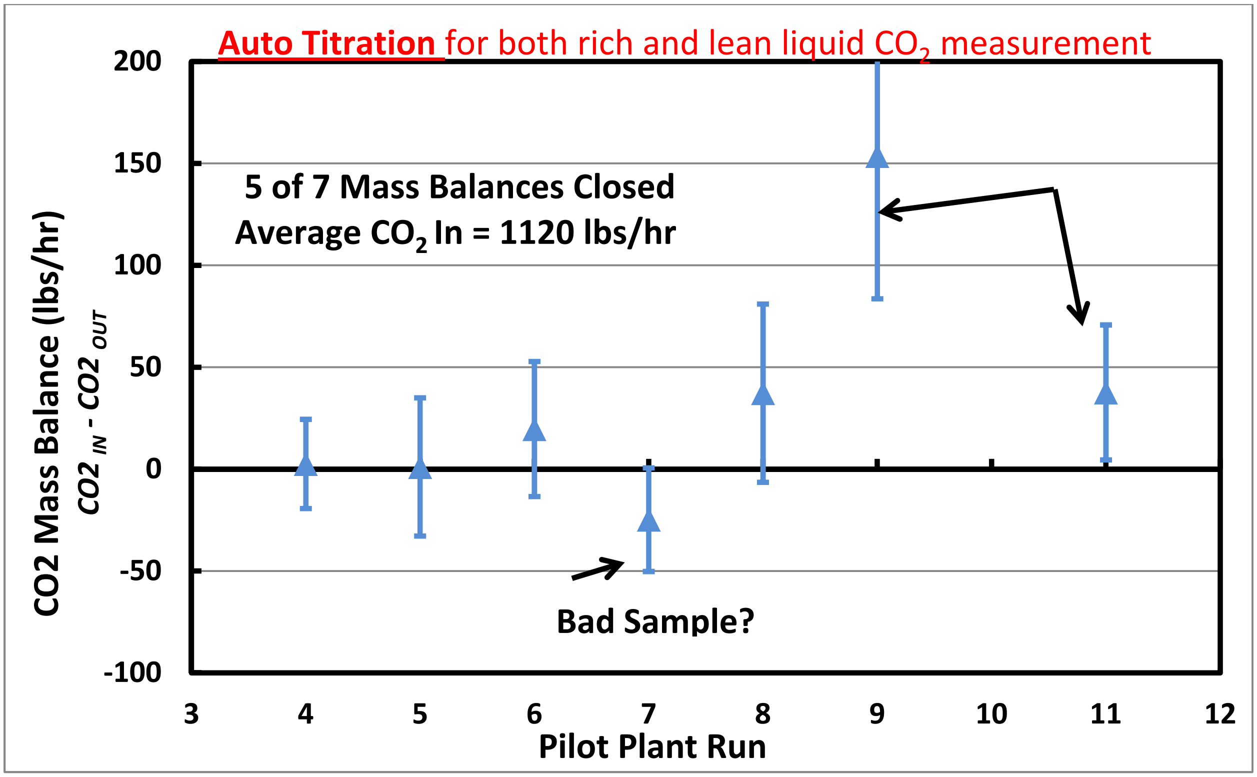

Figure 4: CO_2 mass balance (CO_2 In, Liquid and Gas – CO_2 Out, Liquid and Gas) results using auto titration for lean and rich concentrations and rich amine flow at position 4 in Figure 2. Y = 0 line indicates perfect mass balance closure. Error bars represent 1 standard deviation error about the mean.

Runs 1 through 3 are omitted due to lack of rich flow data at position 4; run 10 was omitted for lack of titration data. The two figures reveal that the manual titration outperforms auto titration in terms of mass balance closure (6 of 7 runs vs. 5 of 7 runs) and shows considerably less variation. The average relative standard error (RSE) (standard deviation in mass balance closure to total CO_2 transferred) for manual titration was 7.5% whereas for auto-titration it was 11.7%. Run 7 is the only run not closed for the manual titration case; the Run 7 mass balance is low in the auto-titration data as well, indicating potential bad data.

CO_2 removal numbers were calculated on both the liquid and gas side, with removal defined as follows:

Liquid Side:

$$CO_2Removed(\%) = \left(\frac{Liquid\ CO_2Out - Liquid\ CO_2In}{Gas\ CO_2In}\right) \tag{2}$$

Gas Side:

$$CO_2Removed(\%) = \left(\frac{Gas\ CO_2In - Gas\ CO_2Out}{Gas\ CO_2In}\right) \tag{3}$$

Figure 5 compares the results of the manual titration liquid side numbers (i.e., most accurate and precise liquid side numbers) and the gas side removal.

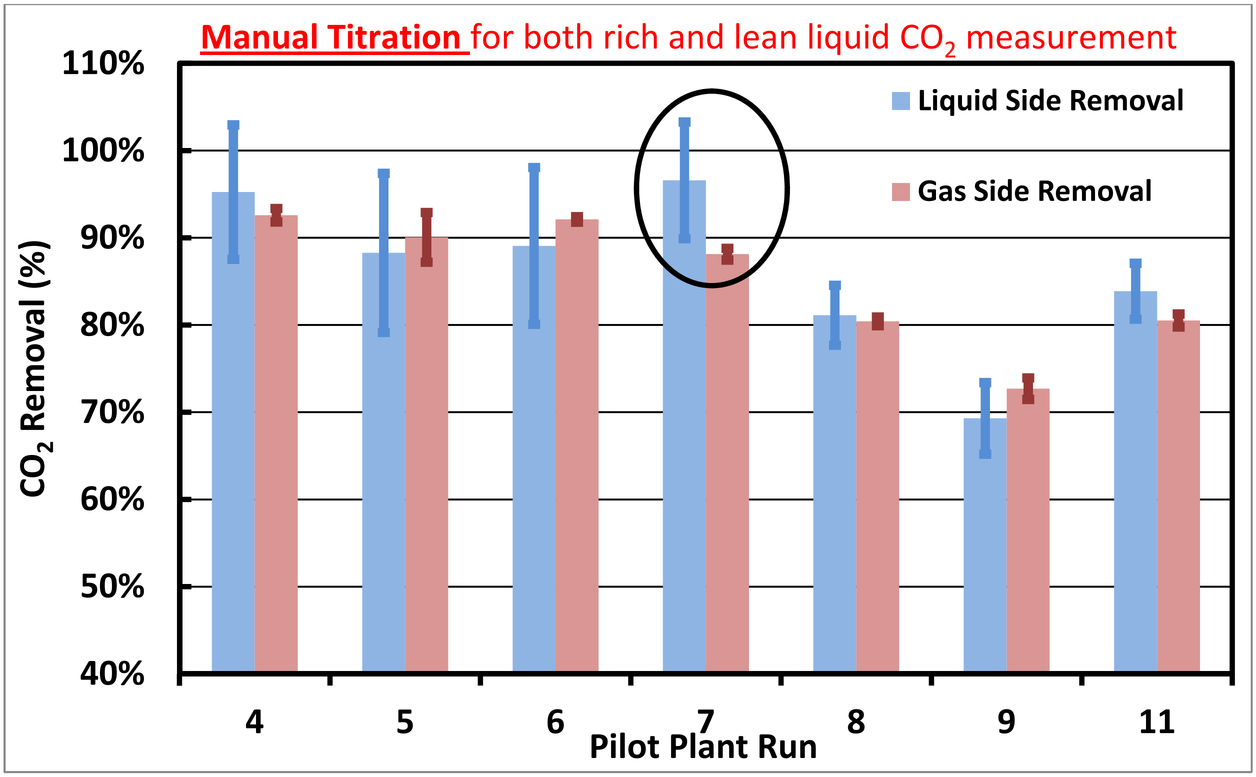

Figure 5: CO_2 removal, gas side vs. liquid side (manual titration, rich amine flow point 4). Error bars represent 1 standard deviation error about the mean.

The liquid side removal matches the gas side removal within variation in the data (as represented by the error bars) in all cases except run 7; this was expected as the liquid side mass balance did not close for run 7 due to potentially bad data. In addition, Figure 5 reveals significantly lower variation in the gas side measurements; the average RSE for removal on the liquid side was 10.9% compared to 1.2% on the gas side. This is explained in part by the fact that gas side concentrations are measured continuously inline, allowing averaging over a large number of data points relative to the triplicate liquid measurements sampled at a single time in each run.

With error quantified for removal calculations, spray nozzle performance could be evaluated by parametric testing.

Evaluating Spray Nozzle Performance

Table 2 summarizes pilot plan runs used to evaluate spray nozzle performance; the runs are paired by common gas rates and nearly identical operating conditions with the nozzle on and the nozzle off (the runs were consecutive to minimize variation).

Table 2: Spray nozzle testing, runs paired for comparison with nozzle on and off

RUN	Spray	Gas Rate (ACFM)	L/G	Lean Loading ($molCO_2/molPZ$)
1	**OFF**	**350**	**4**	**0.246**

2	**ON**	**350**	**4.2**	**0.243**
8	**OFF**	**475**	**3.8**	**0.243**
7	**ON**	**475**	**4.1**	**0.245**
10	**OFF**	**675**	**3.1**	**0.256**
9	**ON**	**675**	**3.1**	**0.242**

It should be noted that runs 1 and 2 did not have rich amine flow data at point 4 in Figure 2; for evaluation of nozzle performance, rich amine flow at point 5 was substituted for these runs only. Run 10 had no liquid side analytical data, so only gas side removal can be used to compare runs 9 and 10. Figures 6 and 7 compare nozzle performance based on liquid side removal calculations and gas side calculations, respectively. The error bars in these plots represent +/- 2 standard deviations or a 95% confidence interval around the expected value.

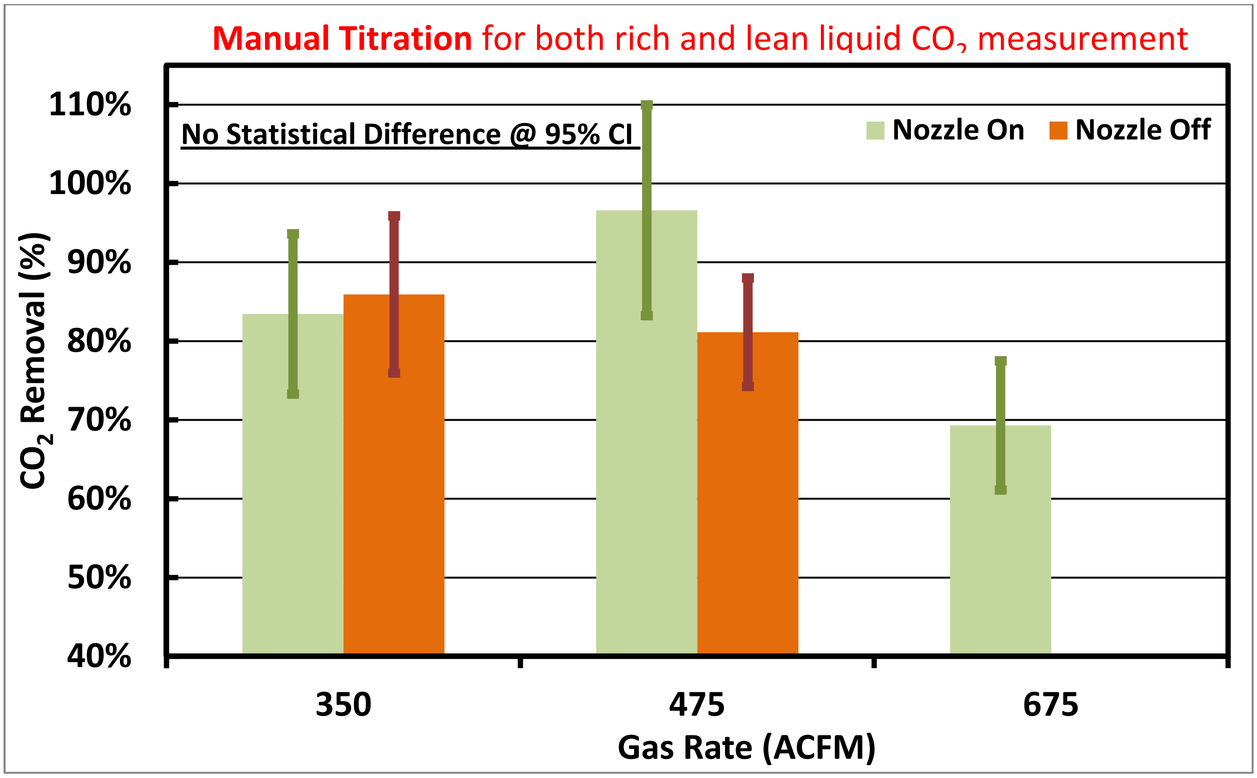

Figure 6: CO_2 Removal, Liquid Side (Manual Titration) – spray nozzle on vs. off. Error bars represent 95% confidence intervals.

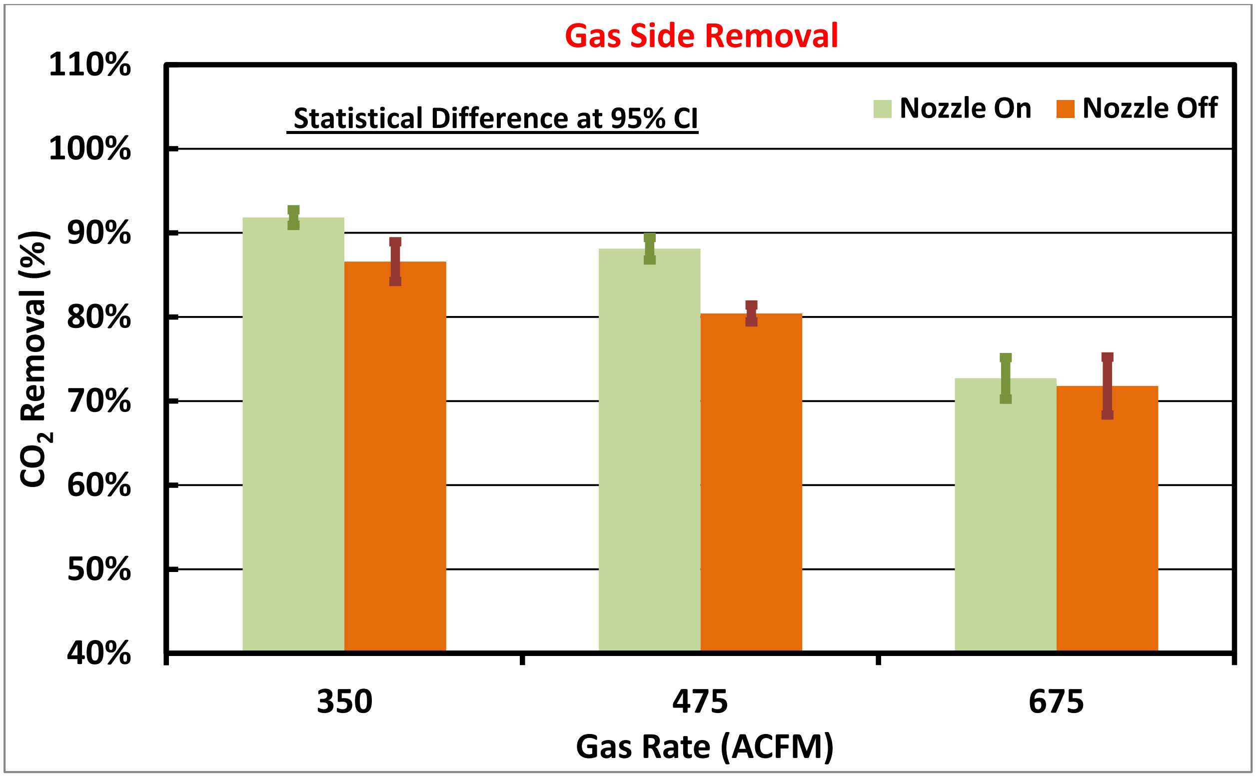

Figure 7: CO_2 Removal, Gas Side – spray nozzle on vs. off. Error bars represent 95% confidence intervals.

The preceding figures show that the best liquid side removal data (manual titrations) still have too much variation to evaluate performance after equipment modification (i.e., spray nozzle implementation); the difference with and without the nozzle is not statistically significant at a 95% confidence interval. In contrast, the gas side results in Figure 7 show that the removal with the spray nozzle at 350 ACFM and 475 ACFM is statistically higher than the corresponding runs without the nozzle. At 675 ACFM, the difference in removal is not statistically significant; this case merits further investigation to isolate spray nozzle performance.

The temperature profiles for the runs with the spray nozzle activated are compared in Figure 8.

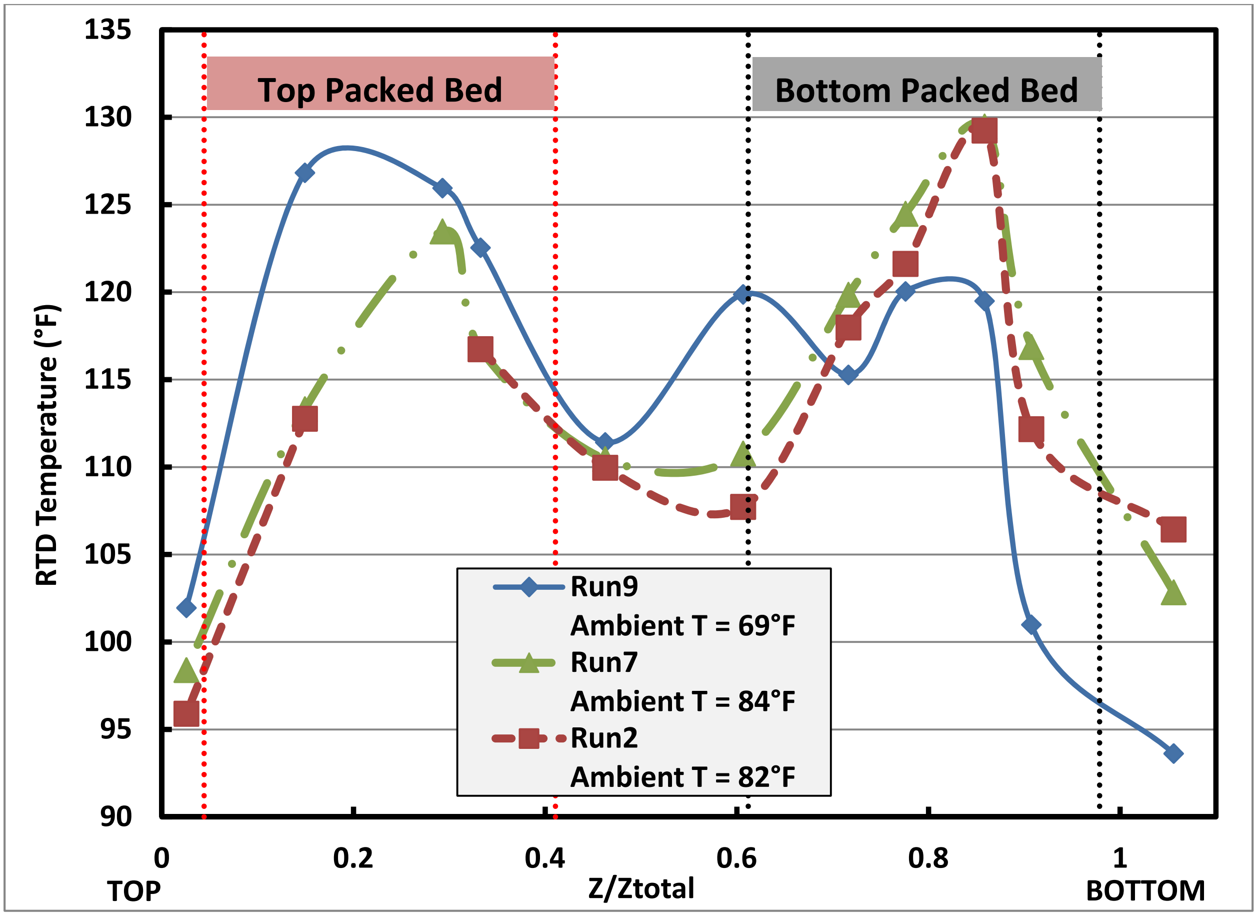

Figure 8: Column temperature profiles for Runs 2, 7 and 9 (spray nozzle activated). Total height (Z_{total}) is defined as distance between top and bottom body flanges on column at PRC. Location of packed beds is demarcated in figure relative to these reference flanges. Spray intercooling located at approximately $Z/Z_{Total} = 0.5$.

The temperature profile for run 9 shows deviations from runs 2 and 7. Run 9 was the only run that did not show statistically significant improvement with implementation of the spray nozzle and was operated at the highest gas rate and lowest L/G of the three spray nozzle runs. As the temperature profile shows, run 9 may be exhibiting a lean end (top of the column) pinch associated with the temperature bulge. If the performance is temperature limited at the top of the column, the implementation of the intercooling at the middle of the column will have minimal benefit. This may partially explain the reduced performance in run 9 relative to the other spray nozzle runs. In addition, the temperature profiles for runs 2 and 7 exhibit distinct spikes in the bottom section of packing likely corresponding to an increased mass transfer and reaction in the bottom section of packing. Run 9 does not exhibit the same distinct spike, though differences in the absolute temperatures for the 3 runs may be skewed by a lower ambient temperature during run 9 (i.e., greater heat loss in run 9). The improved performance in runs 2 and 7 relative to run 9 may not exclusively be explained by the spray nozzle; the high gas rate and lower relative L/G may also be associated with gas and liquid distribution problems that could have hindered performance in run 9.

PZ Mass Balance

The PZ mass balance was performed analogously to the CO_2 mass balance with the exception that manual titration was only available on the lean stream samples; therefore, only auto titration data for PZ is considered in this work. Figure 9 summarizes the PZ mass balance around the absorber.

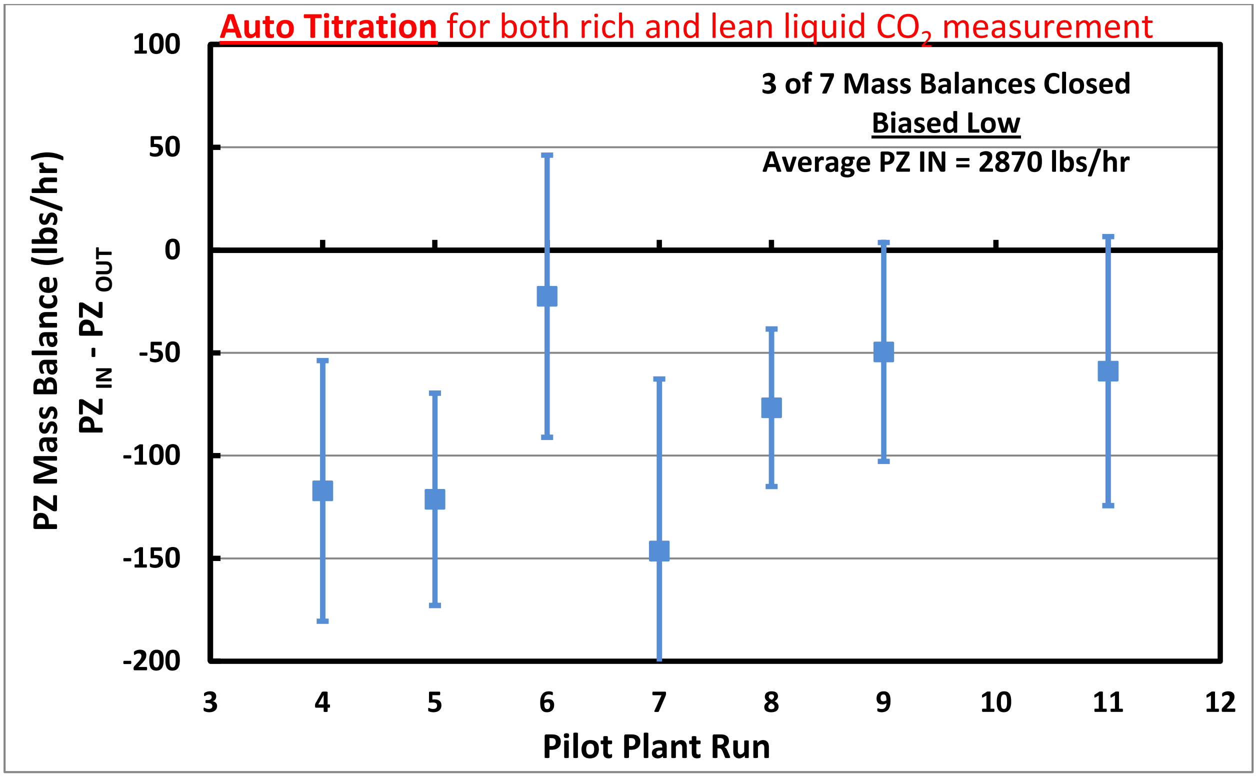

Figure 9: PZ mass balance (PZ In, Liquid – PZ Out, Liquid) results using auto titration for lean and rich concentrations and rich amine flow at position 4 in Figure 2. Y = 0 line indicates perfect mass balance closure. Error bars represent 1 standard deviation error about the mean.

As the figure shows, the PZ mass balance closure is poor when using auto titration for liquid side concentrations; only 3 of 7 mass balances closed within the variation in the measurements. It appears that the PZ mass balance numbers are consistently biased low (PZ out is high relative to PZ in); given that the CO_2 mass balance used the same flow rate data and did not show a discernible bias, this indicates a potential systematic offset in auto-titration numbers for PZ. The relative error in PZ numbers (standard deviation in mass balance relative to PZ recirculation rate) is 2.1%. The high PZ flow rates relative to CO_2 flow rates make the relative variation in the measurement data less significant for PZ.

Rich Amine Flow Rate Discrepancy

As noted, the mass balance analysis to this point has only considered rich amine flow rates at point 4 in Figure 2 (downstream from the rich amine pumps). Point 5 provides a second measure of rich amine flow data downstream from the high pressure cross exchanger (composed of bypass stream and skid feed stream flows). Given the appearance of bias in PZ numbers, the full error analysis was repeated using the skid rich amine flow rate at point 5. All of the results are not enumerated here; however several key observations are summarized. Figure 10 compares the *absorber rich flow* (point 4) to the *skid rich flow* (point 5).

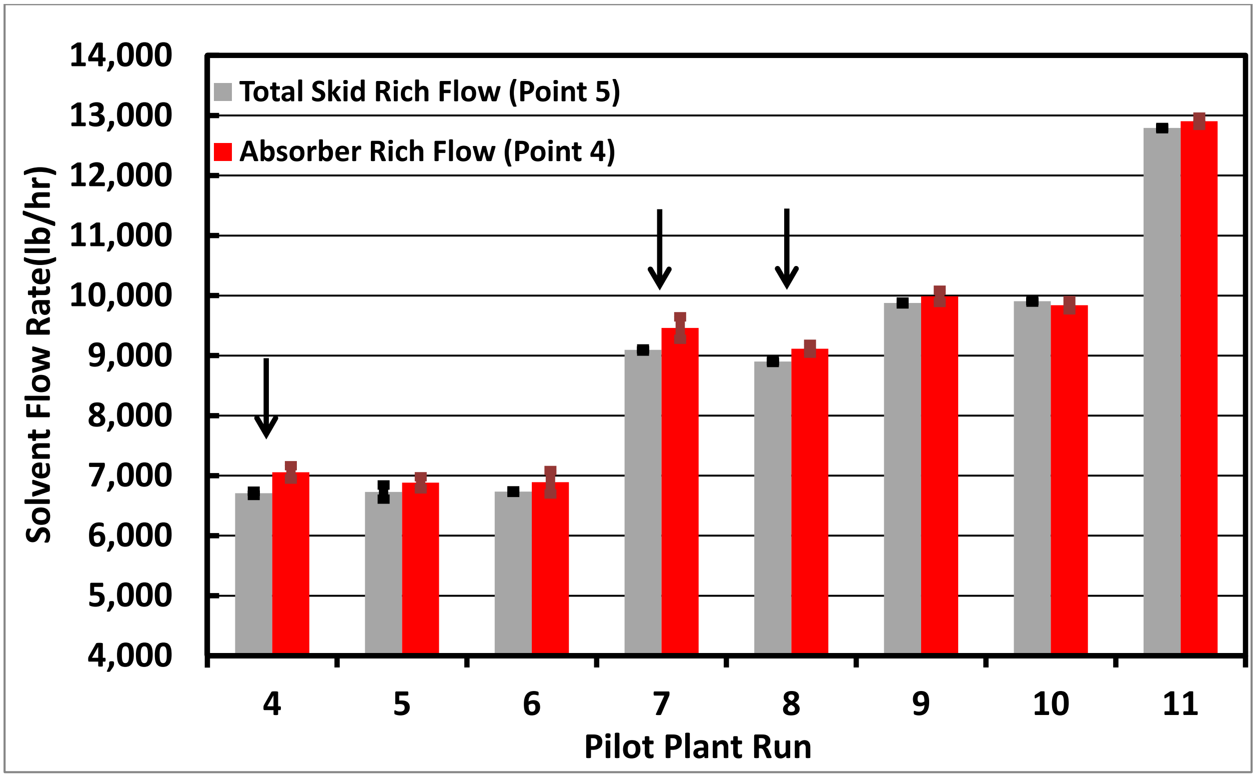

Figure 10: Comparison of 2 rich amine flow measurements. Error bars represent one standard deviation about the mean. Arrows identify runs in which flow rates do not match within error (runs 4, 7 and 8).

The figure shows that the absorber rich flow is consistently higher than the skid rich flow in all but one run (run 10). The RSE in the absorber rich flow is 1.38%, whereas the skid rich flow RSE is 0.39%. Though 5 of the 8 runs in Figure 10 match within the variation in the data, the combination of the systematic difference in flow rates and the higher variation in the absorber rich meter indicate potential bias in the rich amine flow data. The CO_2 mass balance and PZ mass balance results were compared with both flow rates to assess the existence of bias; Figures 11 and 12 summarize the results.

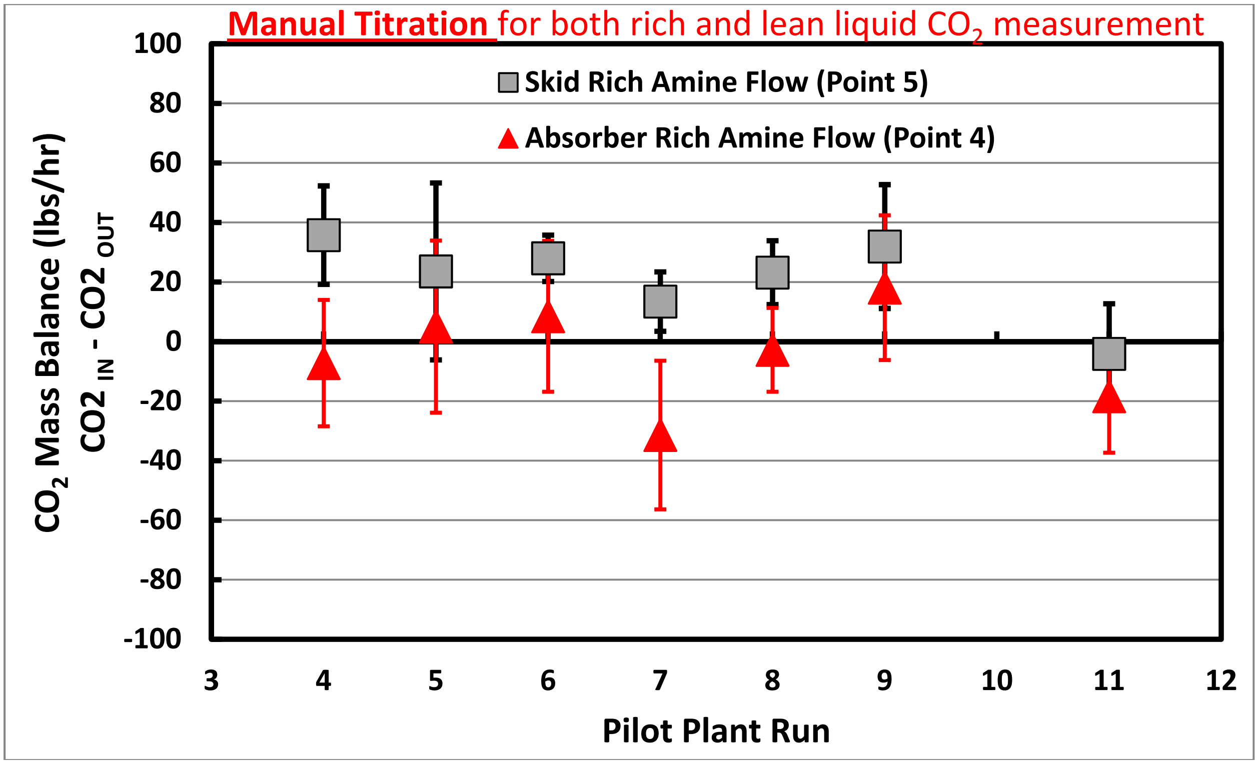

Figure 11: Comparison of CO_2 mass balance using both rich flow measurements. Error bars represent one standard deviation about the mean.

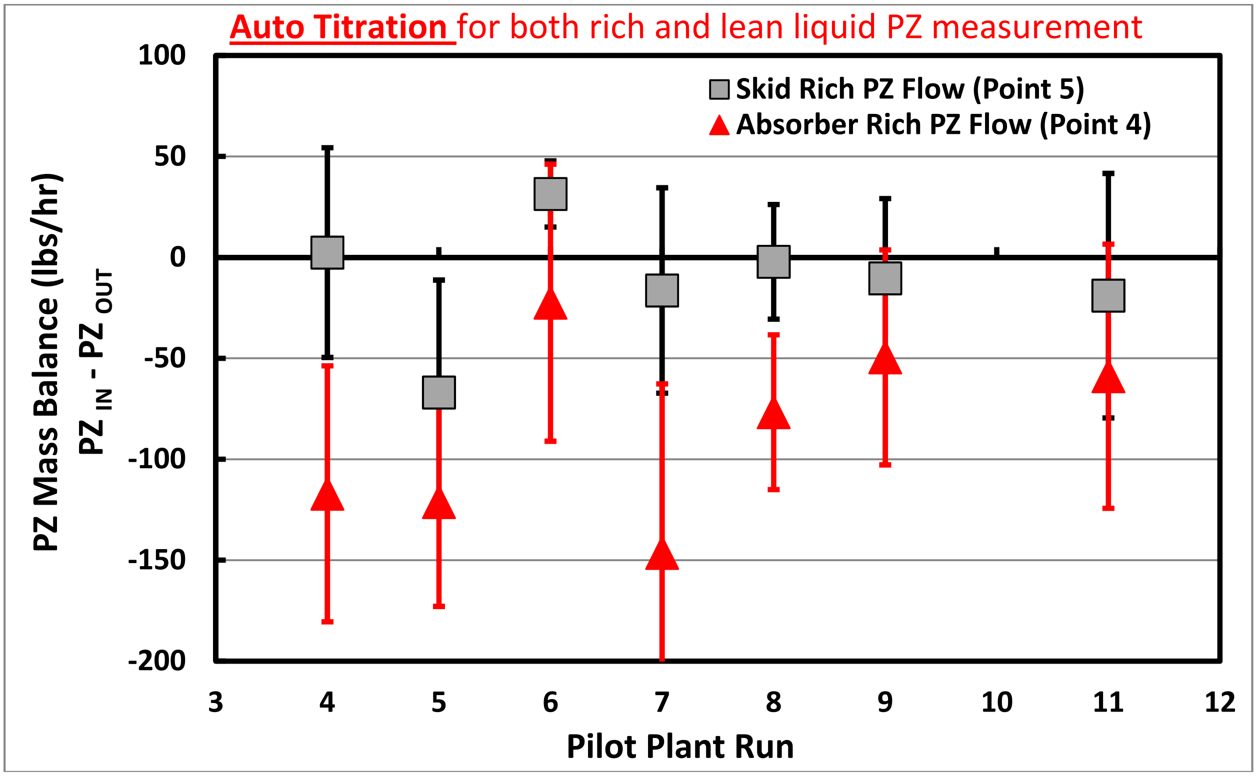

Figure 12: Comparison of PZ mass balance using both rich flow measurements. Error bars represent one standard deviation about the mean.

As expected, the use of the skid rich flow (point 5) shifts the mass balance closure data upwards for both CO_2 and PZ (lower flow rates out of the column relative to absorber rich measurement). While this appears to improve PZ mass balance and partially correct for the observed bias (5 of 7 runs closed with skid rich flow compared to 3 of 7 with absorber rich flow), the CO_2 mass balance is adversely impacted (2 of 7 runs closed with skid rich flow compared to 6 of 7 with absorber rich flow). This indicates that neither flow meter can unequivocally be designated as the more accurate meter; side-by-side calibration against a reference standard is needed. In addition, the use of either flow results in an apparent mass balance bias (bias low for PZ with absorber rich flow data, bias high for CO_2 with skid rich flow data). Therefore, the bias is not in the flow rate alone but also likely in an analytical measurement. Further study is needed to isolate the bias.

Discussion

Evaluation of the mass balance with accompanying error analysis has identified several key items as the data reconciliation moves forward. First, error analysis confirmed that manual titration data is both more accurate and precise than auto titration in CO_2 analysis; it should be the only data used in data reconciliation process. The PZ mass balance revealed potential bias in the auto titration data (manual titration data is only available on the lean side); to use PZ data in the data analysis, either wide error bands must be included (e.g., 2 standard deviations around measurements) or experimental bias must be quantified by running control experiments. Finally, the two liquid side flow measurements appear systematically offset; use of either flow rate leads to problems in mass balance closure. Calibration of the meters against a reference is needed before the rich amine flows can be used reliably.

The gas side data from the pilot plant showed low variation and removal calculations on the gas side were in agreement with liquid side removal within one standard deviation. This allowed comparison of column performance with and without the spray nozzle; results indicated that there was a statistically significant increase in removal in two of three trials with the nozzle compared to without the nozzle.

Development of Absorber Models for Gas-Fired Combustion

(a Project of the Process Science and Technology Center supported by TOTAL)

In parallel to model validation work, new design cases were developed for carbon capture from natural gas combustion sources. The case described in Table 3 was evaluated during the course of the past quarter. Figure 13 is a PFD of the absorber design for this case.

Table 3: Combined Cycle Gas Turbine Flue Gas Information

Case 1: Combined Gas Cycle Turbine	
Flow rate (kmol/h)	40,473
Flow rate (t/h)	1,161
Temperature (°C)	121
Pressure (kPag)	0
Molar Composition (%)	
H_2O	6.51
CO_2	3.31
N_2	75.48
Ar	0.91
O_2	13.79
He (ppmv)	15
CO (ppmv)	50
NOx (ppmv) – NO_2/NOx	30
Particles & unburned HC (kg/h)	15

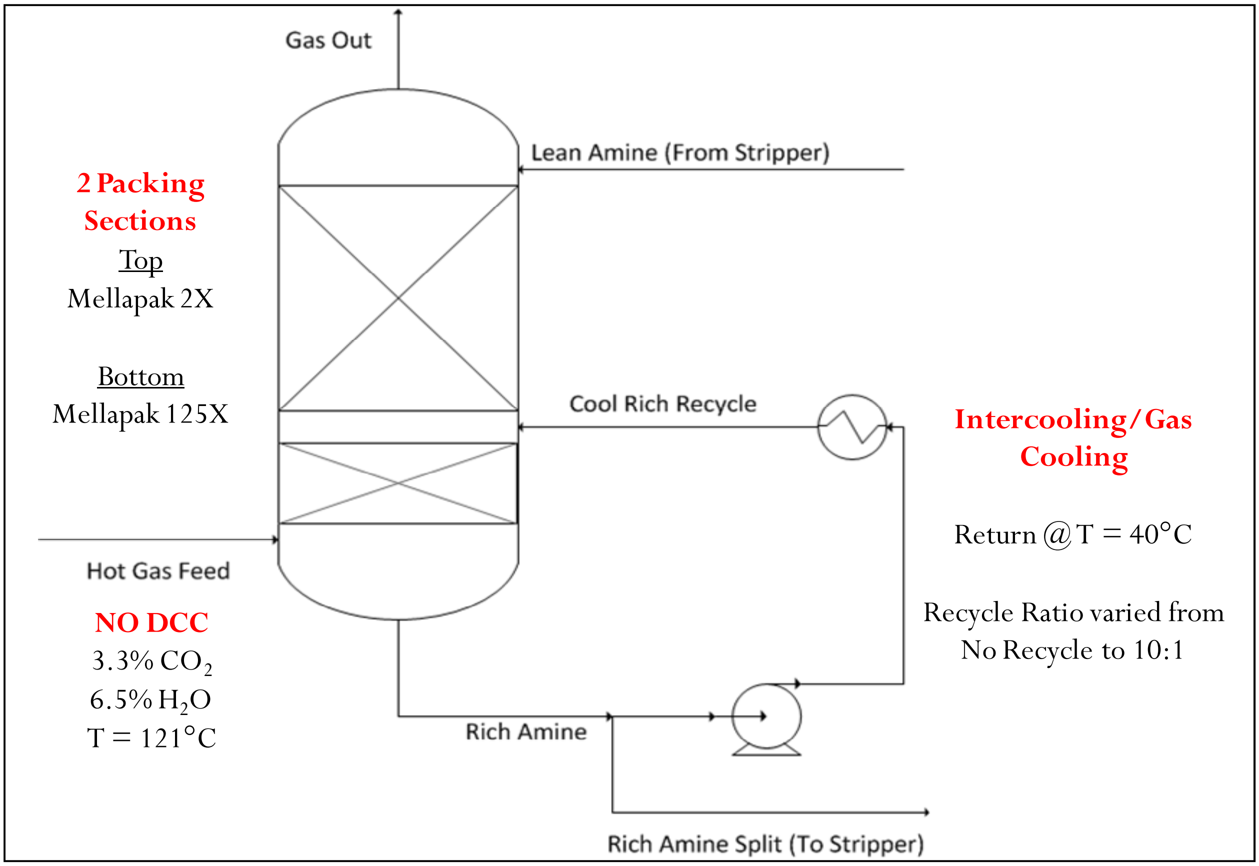

Figure 13: Case 1 Absorber PFD, Combined Cycle Gas Turbine.

The PFD for this case highlights the novel design features integrated for the combined cycle flue gas stream. Due to the low water content in the gas feed, a direct contact cooler was omitted from the design; water does not need to be removed from the gas during cooling. Instead, the gas will be cooled with a rich amine recycle stream in the lower packed section of the column. This accomplishes the necessary cooling of the gas and allows for absorption of CO_2 during the cooling process. The recycle of solvent in the bottom 1 meter packed section results in high pressure drop through this section; coarse structured packing was used in the bottom section to minimize pressure drop.

Case 1 Design Results

Preliminary results have been developed for a base case using the flue gas parameters described in the previous section and the absorber design parameters summarized in Table 4.

Table 4: Combined Cycle Gas Turbine Flue Gas Information

Case 1: Absorber Design Parameters	
Lean Loading (mols CO_2/mols alkalinity)	0.27
Target CO_2 Removal (%)	90%
Lean Amine Temperature (°C)	40
Intercooling/Recycle T (°C)	40
Rich Gas Feed T (°C)	121
Packing Type: Top Section	Mellapak 2X
Packing Type: Bottom Section	Mellapak 125X
Packing Height: Bottom Section	1 m

Figure 14 illustrates the performance benefit of the recycle gas cooling method with varying recycle rates in the bottom section of the column.

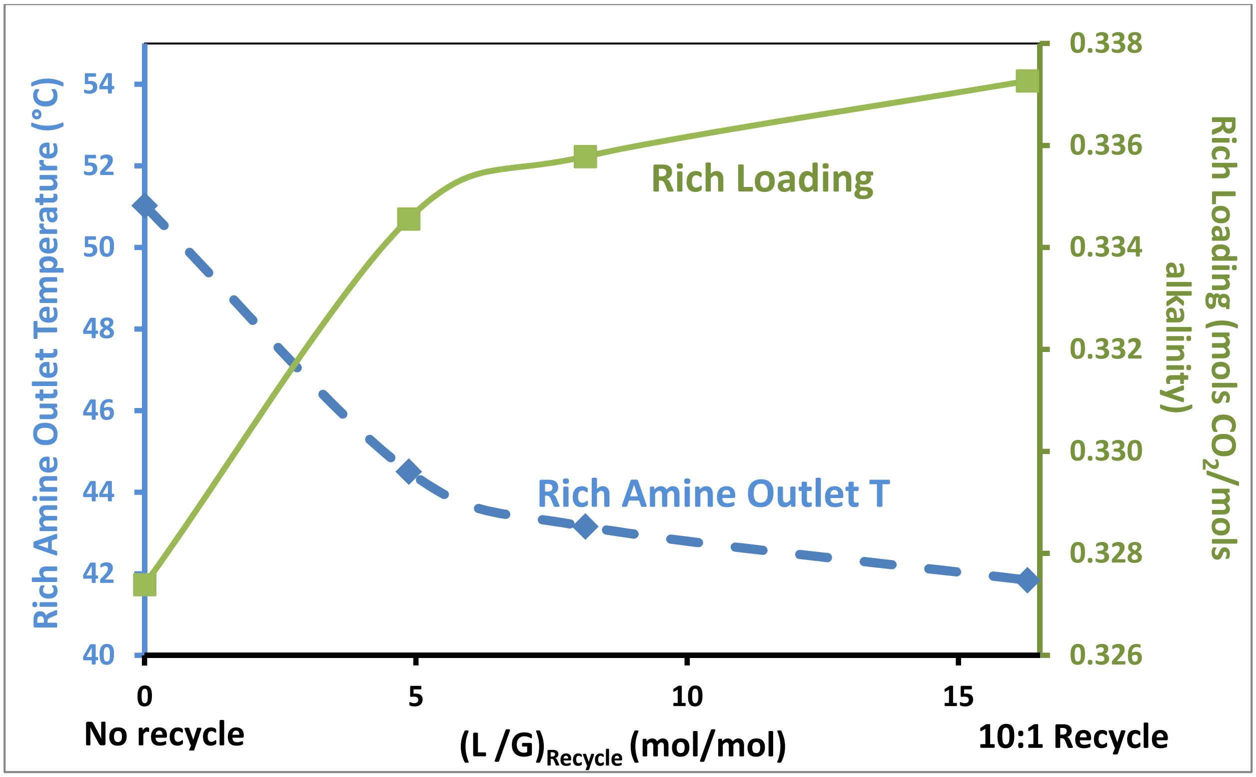

Figure 14: Benefit of increased recycle rate in gas cooling section of the column. Lean loading = 0.27 mols CO_2/mols alkalinity, lean amine T = 40 °C, rich gas T = 121 °C.

As expected, higher recycle rates in the bottom section of the column result in a colder rich amine stream leaving the absorber; this also leads to a richer solvent. It is interesting to note the change in slope around an L/G of 5; beyond this point, the return in rich loading improvement for increased liquid rate is reduced. This may be a point of future optimization. Figure 15 provides the temperature and mass transfer profiles in the column for a base case design with the parameters from Table 4 and with a recycle rate of 10:1 in the bottom section of the column.

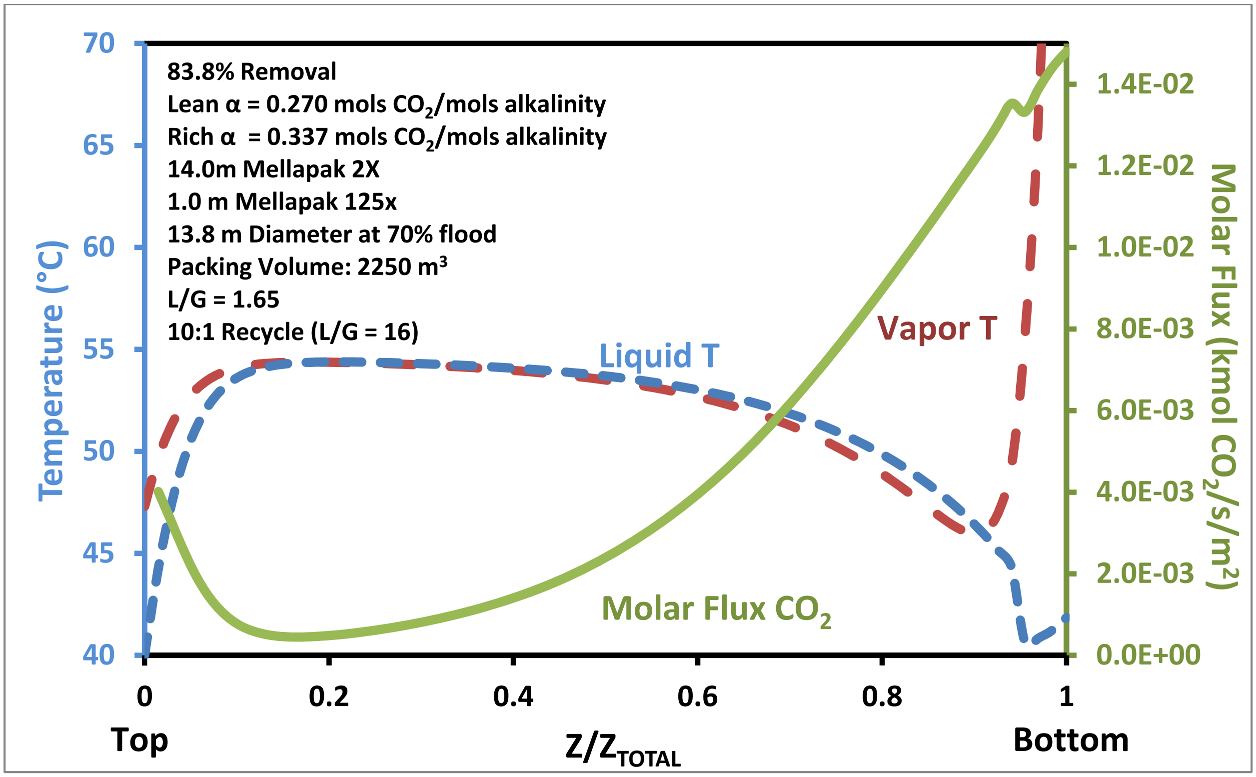

Figure 15: Temperature and Mass Transfer Profiles for base case design. See Tables 3 and 4 for general design parameters.

The case in Figure 15 only achieves 84% removal despite 15 meters of total packed height in the column. The low liquid rate used in the case provided a higher rich loading than previous cases, but the case needs optimization to reflect a realistic design case. As the plot shows, the gas temperature is cooled to 47 °C in the bottom section of the column and never exceeds 55 °C in the rest of the column. In addition, the majority of mass transfer occurs in the bottom of the column. The driving forces over the length of the column were evaluated in Figure 16.

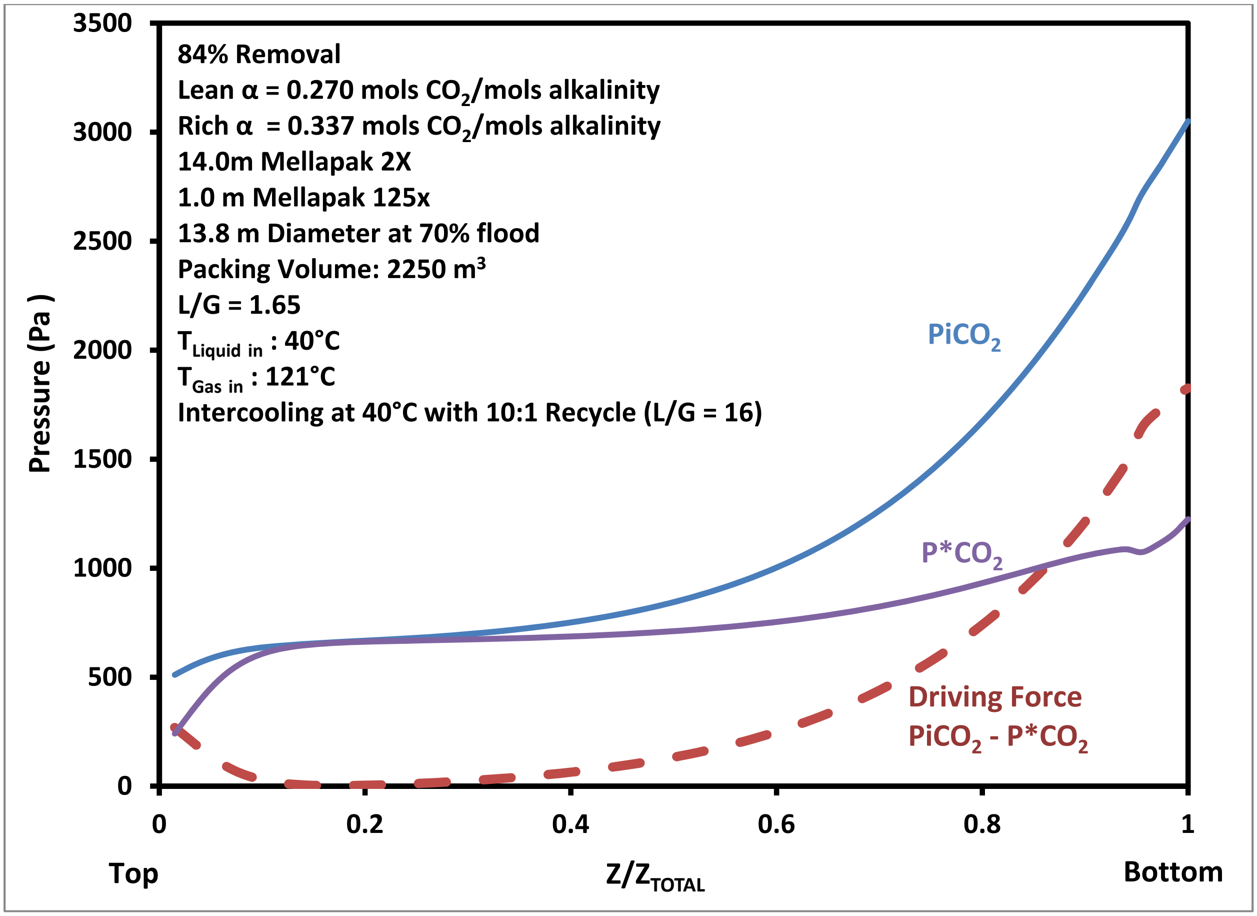

Figure 16: Partial pressure driving force through the absorber column for the base case design. $PiCO_2$ is the gas liquid interface partial pressure and P^*CO_2 is the equilibrium partial pressure of CO_2 for the bulk liquid composition.

Figure 16 reveals a lean end pinch that is a constraint on the column performance. This issue will initially be addressed by evaluating lower lean loadings. Stripper design evaluation has indicated minimal energy penalty for a drop in lean loading from the current case. In addition, the lean end pinch coincides with the temperature bulge in Figure 15; this indicates that an alternative intercooling scheme might be required for optimal performance in the gas-fired system.

Discussion

The preliminary absorber design for the natural gas application has demonstrated benefits of cooling the gas in the column by improved rich loading leaving the column while cooling the gas to 47 °C in 1 meter of packing. The initial design, however, requires 15 meters of total packed height and does not appear to be an optimal design. Driving force analysis has shown the need for lower lean loadings to increase driving forces in the top of the column in addition to an alternate intercooling design to address the temperature bulge at the top of the column.

Final Absorber Design for Coal-Fired Economic Analysis

In the final quarter of 2011, preliminary results were detailed for absorber designs developed for economic evaluation of CO_2 capture from coal-fired power plant flue gas using 8 m PZ. The designs were developed using the 5deMayo framework. During the past quarter, the absorber designs were finalized for the four design scenarios summarized in Table 5.

Table 5: Absorber Design Parameters and Column Sizing Results (All cases designed for 90% CO_2 Removal)

	Case 1	Case 2	Case 3	Case 4
Lean Amine Feed				
T (°C)	**40**	**40**	**30**	**30**
Mass Flow Rate (kg/s)	1.21	1.53	1.13	1.37
Flow Rate Relative to Minimum Required	1.1	1.1	1.2	1.2
Volumetric Flow Rate (m^3/s)	1.09E-03	1.37E-03	1.02E-03	1.22E-03
Loading (mols CO_2/mols alkalinity)	**0.27**	**0.30**	**0.27**	**0.30**
Gas In				
T(°C)	40	40	30	30
Molar Flow Rate (kmol/s)	8.83E-03	8.83E-03	8.56E-03	8.56E-03
Volumetric Flow Rate (m^3/s)	0.209	0.209	0.196	0.196
Gas In, Mole Fractions				
CO_2	0.149	0.149	0.153	0.153
H_2O	0.068	0.068	0.039	0.039
N_2 (includes All Inerts)	0.757	0.757	0.781	0.781
O_2	0.026	0.026	0.027	0.027
Intercooling				
Location (Z/Z_{Total})	0.5	0.5	0.5	0.5
Temperature (°C)	40	40	30	30
Performance Results				
CO_2 Removal	90%	90%	90%	90%
Rich Loading (mols CO_2/mols alkalinity)	0.385	0.392	0.392	0.402
Column Sizing				
Column Diameter (m)	0.38	0.39	0.37	0.38
Capacity (%Flood)	70%	70%	70%	70%
Packing Height (m)	9.00	9.34	6.99	7.90
Volume (m^3)	1.02	1.13	0.74	0.88
Volume per CO_2 removed (m^3/kmol/s)	863	958	646	771

The four cases cover two lean loading choices (0.27 and 0.3 mols CO_2/mols alkalinity) and two absorber operating temperatures (40 °C and 30 °C). All cases included intercooling at the midpoint of the column. The "cold" absorber cases are constrained by the temperature of cooling water available. The 30 °C absorber cases were designed at 1.2 times the minimum required flow rate, compared to 1.1 times the minimum at 40 °C; this is consistent with previous work by Frailie that indicated a shift in the trade-off between packing height and liquid flow rate at lower absorber temperatures to fully leverage the higher capacity of the solvent (Rochelle et al., 2011). Thus, the guideline of 1.1 times the minimum flow rate at the standard design of 40 °C was no longer an appropriate choice for operation at 30 °C.

The results confirm the potential economic benefits of low temperature operations; at both lean loadings, the total packing volume required is reduced by 20% or more than the corresponding case at 40 °C. In addition, despite the higher flow rates relative to the minimum required flow rate, the lower temperature designs have a lower absolute solvent circulation rate at the same lean loading. Additionally, the rich loadings for the low temperature cases are higher than the comparable 40 °C cases, yielding potential energy benefits for stripper operation.

Finally, it is important to note that the flow rates used in the analysis correspond to pilot scale flow rates similar to those used at PRC; however, the sizing results can be scaled based on the appropriate gas rate and CO_2 removal based on the final row of Table 5. This result normalizes the packing volume to the CO_2 removed to make the results independent of scale assumptions used in the design.

Conclusions

Pilot plant data analysis yielded the following key observations:

- Manual titration closed the mass balance for 6 of 7 runs with a relative standard error (RSE) of 7.5% while auto titration closed the balance for 5 of 7 runs with an RSE of 11.7%. The results validate the use of manual titration over auto titration.
- Gas side removal calculations revealed statistically significant (95% confidence interval) improvement in CO_2 removal for two of three spray nozzle trials (5% and 8% increase in CO_2 removal relative to runs without the nozzle operating).
- PZ mass balance revealed potential systematic bias in auto titration measurements and discrepancy in rich side flow measurements.
- Preliminary absorber design for gas combustion capture applications demonstrated the benefit of gas cooling in the column but is limited by a lean end pinch corresponding to a temperature bulge at the top of the column.
- Optimized absorber design for economic analysis confirmed the potential benefit of low temperature absorber design (30 °C) relative to standard design conditions (40 °C) by reducing packing volume by as much as 25% and absolute solvent circulation rate by as much as 10% for holding all other design conditions constant.

Future Work

Future work related to pilot plant activities includes absorber model validation using data from the October 2011 campaign at PRC, evaluation of additional analytical measurements in mass balance calculations (e.g., density), and detailed modeling and evaluation of the spray nozzle.

The gas combustion capture case will be optimized, and two additional gas combustion cases with different inlet flue gas rates and compositions will be developed.

References

Plaza JM. *Modeling of Carbon Dioxide Absorption using Aqueous Monoethanolamine, Piperazine, and Promoted Potassium Carbonate.* The University of Texas at Austin. Ph.D. Dissertation. 2012.

Rochelle GT et al. "CO_2 Capture by Aqueous Absorption, Third Quarterly Progress Report 2010." Luminant Carbon Management Program. The University of Texas at Austin. 2010.

Rochelle GT et al. "CO_2 Capture by Aqueous Absorption, Fourth Quarterly Progress Report 2010." Luminant Carbon Management Program. The University of Texas at Austin. 2011.

Measurement of Packing Effective Area and Mass Transfer Coefficients

Quarterly Report for January 1 – March 31, 2012

by Chao Wang

Supported by the Luminant Carbon Management Program,

and Process Science and Technology Center

Department of Chemical Engineering

The University of Texas at Austin

April 20, 2012

Abstract

In this quarter, significant effort has been made troubleshooting the outlet SO_2 sampling system. The mass transfer characteristics of gas-film control systems and their physical properties make the solute gas very easy to remove. The high mass transfer efficiency of this system makes the outlet SO_2 concentration very low (ppb levels) after counter-contacting the solvent in just a few feet of packing. Thus, it is difficult to obtain a reliable outlet SO_2 reading.

Several methods have been tried to obtain a reasonable SO_2 outlet reading. To eliminate the water condensation in the outlet sample line, a Micro-GASS^{TM} Gas Analysis Sampling System from PERMA PURE LLC has been installed based on recommendations of SO_2 analytical experts. The sample conditioner uses the hot exhaust gas from the analyzer as the drying gas. The sample gas and purge gas is contacted indirectly in a Nafion® Membrane Dryer. Water vapor is then transferred from the wet sample gas through the membrane to the counter-current dry purge.

The outlet SO_2 analyzer was sent to the manufacturer to repair a hydrocarbon knockout component. Upon its return, the analyzer was carefully re-calibrated to ensure its accuracy.

The upper and lower end effects were measured this quarter during the SO_2 outlet troubleshooting. The upper end effect was measured by obtaining samples directly above the packing section and at the traditional outlet sample point above the Trutna tray de-entrainer. The NTU for the top end effect is approximately 0.5. The lower end effect was measured by obtaining samples at the traditional air inlet piping and immediately below the packing. The NTU_{bottom} was determined to be around 1.1–1.3.

In the course of systematically checking the outlet sampling system section, a leak was found associated with the membrane filter. The leak only occurred when the inlet of the membrane filter was under vacuum. No leak was present if the inlet was under positive pressure. This made the leak difficult to find and was a characteristic of the fitting assembly used. The fitting was changed and the vacuum leak stopped. The membrane filter is installed just before the SO_2 analyzer to make sure no liquid gets into the analyzer. After changing the fitting on the membrane filter, the outlet SO_2 analyzer responded more quickly and reliably.

The gas film mass transfer coefficient for Mellapak 250Y has been measured this quarter. MP250Y is a standard structured packing with a total area of 250 m^2/m^3 and corrugation angle of 45 degrees. It can be used as a baseline for our structured packing comparison. k_G for this packing is a function of liquid velocity and independent of gas velocity. The exponent of k_G over u_G for this packing is 0.61 compared with values of 0.73 to 1 in previous result. The exponent after SO_2 sampling troubleshooting is lower than before, which suggests previous results should be explored further.

Introduction

Packing is widely used in distillation, stripping, and gas-scrubbing processes because of its relatively low pressure drop, good mass transfer efficiency, and ease of installation. Packing is being investigated for post-combustion carbon capture for these reasons. In the CO_2 capture process, absorber performance depends on the effective mass transfer area of the packing (a_e), stripper performance depends on liquid film mass transfer coefficient (k_L), and the gas cooler and water wash performance depends on gas film mass transfer coefficient (k_G). This research is focused on the measurement of these important fundamental parameters and construction of mechanistic design models.

In this quarter, work has been focused on troubleshooting and collecting k_G measurements. The gas phase mass transfer coefficient is measured by absorption of SO_2 using 0.1 gmol/L NaOH solution, which is a gas-film control system. The characteristic of gas-film control systems makes the solute gas very reactive and very soluble in water. The high mass transfer efficiency of this system makes the outlet SO_2 concentration very low (ppb levels). Thus, it is difficult to get a reliable outlet SO_2 reading. Efforts have been made troubleshooting the SO_2 sampling system.

Experimental work

SO_2 sampling troubleshooting

At the beginning of this work, the measured SO_2 outlet concentration was below 10 ppb independent of packing height. Also, when the gas flow rate or the liquid flow rate changed, the outlet SO_2 reading did not change dramatically. There were several possibilities that could cause this:

1. Water condensing in the outlet sample line.
2. The outlet analyzer was not calibrated accurately in the ppb level region.
3. The end effect mass transfer above and below the packing could be large enough to absorb all the remaining SO_2.
4. There could be air intrusion between the outlet sample point and the SO_2 analyzer.
5. The caustic solution could be entrained into the sample line which will absorb most of the SO_2 before reaching the analyzer.

Several trouble-shooting methods were attempted.

1. To eliminate the water condensation in the outlet sample line, a Micro-GASS^{TM} Gas Analysis Sampling System from PERMA PURE LLC was installed. The sample conditioner is connected at the end of the outlet sample line upstream from the analyzer. The sample conditioner is self-regenerating. It uses the exhaust gas from the analyzer as the drying gas. The exhaust gas passes a needle valve and expands, causing a reduction in vapor pressure. It then re-enters the dryer to be used as a purge gas. The sample gas and purge gas are contacted indirectly in the Nafion$^{®}$ Membrane Dryer. Water vapor is then transferred from the wet sample gas through the

membrane to the counter-current dry purge. The driving force for this process is the difference in partial vapor pressure of water between the sample and purge gas flows. The sample inlet portion of the dryer is also heated to accelerate the drying process. However after installation, questionable outlet SO_2 values were still observed.

2. To obtain an accurate reading from the outlet SO_2 analyzer, the Thermo 43i Trace Level SO_2 analyzer was sent back to Thermo Scientific. The manufacturer fixed some components and calibrated it. A calibration report of this analyzer from Thermo Scientific ensures its accuracy. Moreover, a known concentration of SO_2 is also used to test the reliability of the outlet SO_2 analyzer in SRP. The reading from the analyzer matches the concentration of the gas. Unfortunately, the questionable outlet SO_2 values were still present.

3. The upper and lower end effects for the k_G measurement were measured. Because of the high efficiency of the SO_2/NaOH system, a short bed of packing must be used to get a measureable outlet SO_2 concentration. Thus, there will be an eight-foot gap between the packing and the original outlet sample point compared with the 3-4-inche gap for the area and k_L measurement. The upper end effect for k_G measurement is not negligible. To measure the upper end effect, a sample line is attached to the distributor; the sample point is right above the packing. This trouble-shooting endeavor will eventually lead to an improved sampling method and eliminating and correcting the end effects for the k_G measurements. Nevertheless, this trouble-shooting task did not correct the questionable outlet SO_2 readings.

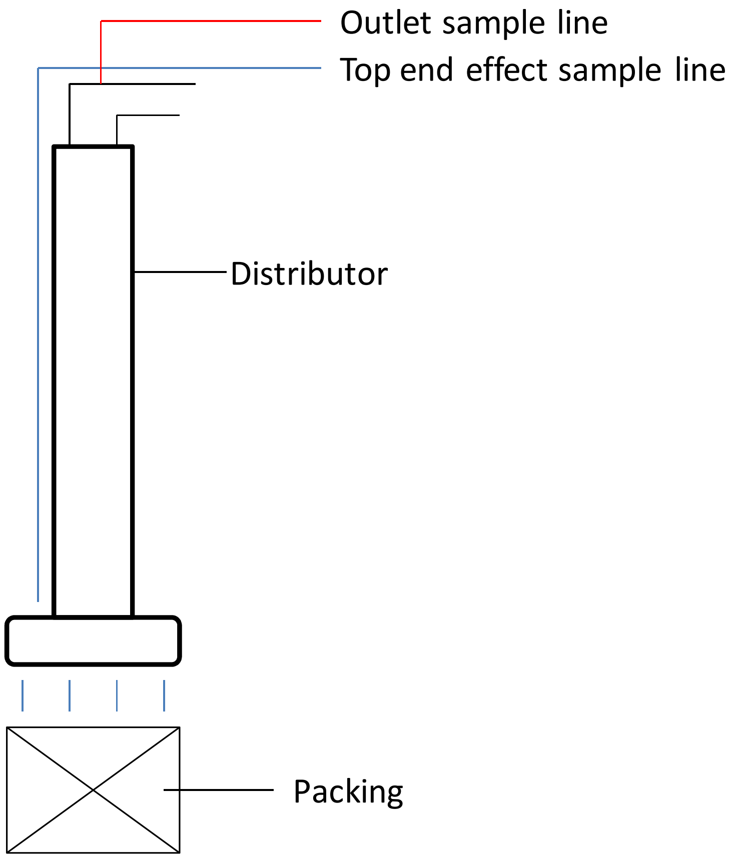

Figure 1: Upper End Effect Measurement

Figure 1 shows the upper end effect measurement. Data are taken from the outlet sample line and upper end effect sample line to obtain the number of transfer units (NTU) from the top. The NTU for the upper end effect is calculated to be approximately 0.5.

The lower end effect measurements are shown in Figure 2. There is approximately 8 feet spacing between the bottom of the packing and the sump liquid at the bottom of the column. Thus liquid films flowing down from the bottom of the packing to the sump liquid could result in additional mass transfer. If only 3 feet of packing is used, the lower end effect is not negligible relative to the total k_G measurement. The lower end effect is measured by sampling the traditional inlet air and sampling just below the packing. There is a lower end effect measurement sample line just below the packing as shown in Figure 2. The measured number of mass transfer units in the bottom section, NTU_{lower}, was at 1.1–1.3. The NTU_{lower} varies somewhat with gas and liquid flow rate.

The total of upper and lower end effects is approximately 1.6–1.8 transfer units. The mass transfer associated with the end effects is not large enough to absorb all of the SO_2 being fed to the column.

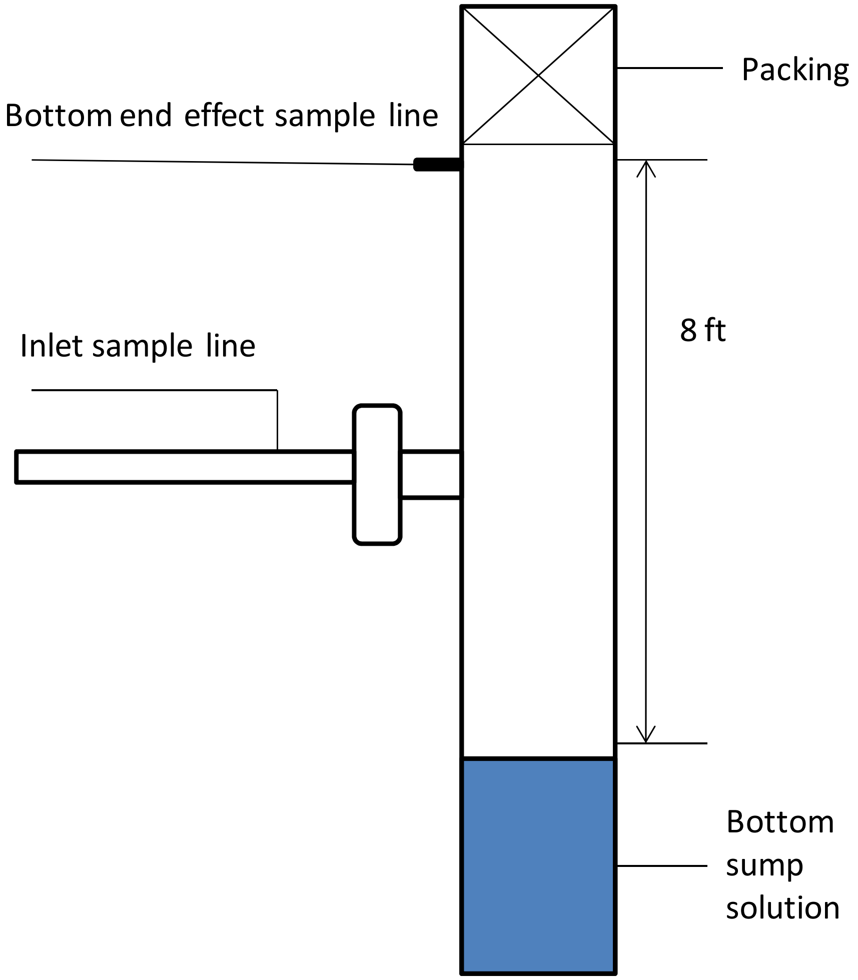

Figure 2: Lower End Effect Measurement

4. A systematic check of the outlet piping to the analyzer was performed. In this case, small segments of piping were checked using a low pressure air sample containing SO_2. This eventually led to the determination of the problem, a leaky fitting to the membrane filter which had been checked numerous times when under pressure. However the fitting allowed ambient air to contaminate the sample when under vacuum. The membrane filter is installed just before the SO_2 analyzer to ensure no liquid enters the analyzer. After replacing the fitting, the outlet SO_2 analyzer behaved normally, changing with flow rates and varying inlet SO_2 concentrations as was expected.

Gas film mass transfer coefficient (k_G) measurement for MP250Y

After SO_2 sampling troubleshooting and repairing the leak in the membrane filter, k_G measurement was performed for Mellapak 250Y(MP250Y). MP250Y is a typical structured packing with a total area of 250 m^2/m^3 and corrugation angle of 45 degrees. Since it is a standard structured packing, it is used as a baseline for our structured packing comparison. Because of the high mass transfer efficiency of the SO_2/NaOH system, a short packing bed is used (Z = 0.841m) to get a measurable outlet SO_2 reading. The lower end effect is measured at two different conditions. The results show that the lower end effect does not change much with gas and liquid flow rate. The $NTU_{end\ effect}$ = 1.64. The k_G results for MP250Y are shown in Figure 3.

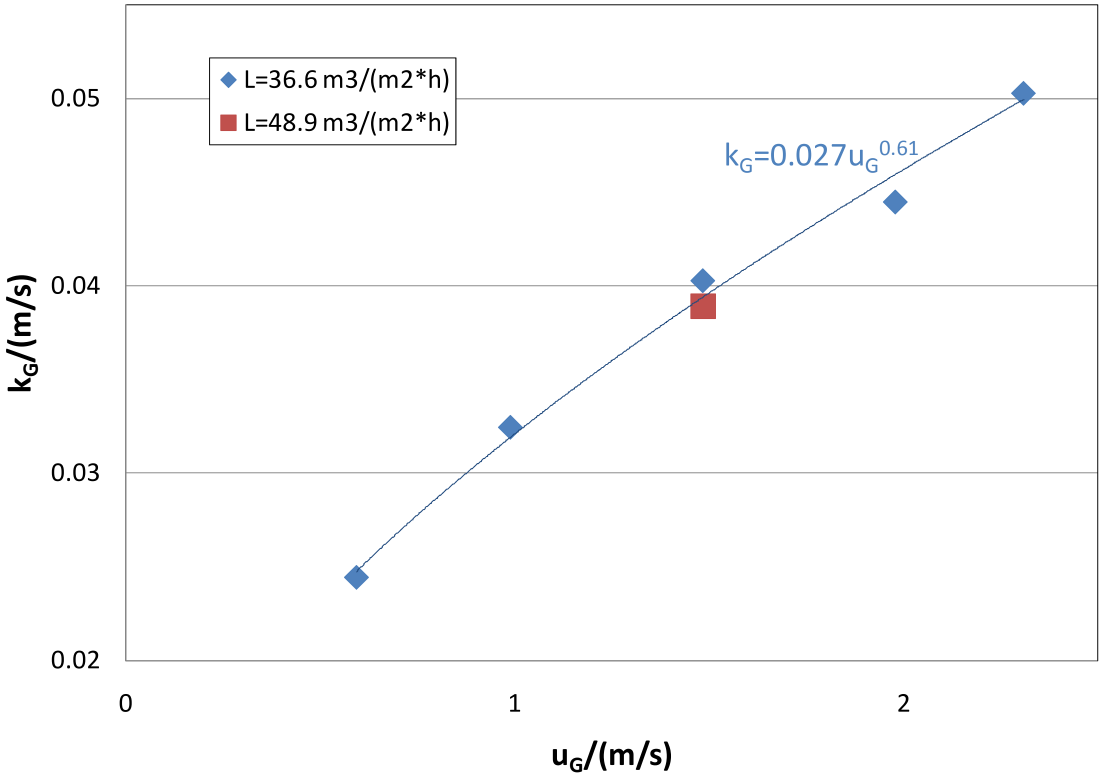

Figure 3: k_G measurement for MP250Y

According to Figure 3, k_G is a function of liquid velocity and independent of gas velocity, which concurs with previous results. However, the exponent of k_G over u_G for this packing is 0.61, which is lower than the exponent from previous experiments (typically from 0.73 to 1). Results from k_G measurement for other packings after SO_2 sampling trouble shooting also show that the exponent of k_G over u_G should be around 0.4–0.6, which means the exponents from previous measurements need to be explored more.

Lab safety issues

Sulfur dioxide is used to measure the gas film mass transfer coefficient. It is a poisonous gas with a pungent, irritating smell. Inhaling sulfur dioxide is associated with increased respiratory symptoms and disease, difficulty in breathing, and premature death. To minimize SO_2 inventory, it is supplied from a standard gas cylinder with less than 2% SO_2 in nitrogen. For safety reasons, the inlet SO_2 concentration is controlled to less than 100 ppm. Before SO_2 runs, the leakage of the pipelines of the system is carefully checked. A gas mask is worn when changing the SO_2 cylinder. In the absorption process, the NaOH solution is in excess so no SO_2 or only ppb levels of SO_2 are exiting the system.

Conclusions

In this quarter, work has been focused on troubleshooting the SO_2 sampling system. Efforts have been made to obtain accurate SO_2 outlet readings.

1. A Micro-GASS^{TM} Gas Analysis Sampling System effectively prevents water condensation in the sample line.
2. The outlet SO_2 analyzer was sent back to the manufacturer and was repaired. Re-calibration was performed to guarantee its accuracy.
3. The upper and lower end effects were measured. The NTU_{top} is approximately 0.5 while NTU_{bottom} is around 1.1–1.3.
4. The outlet SO_2 analyzer reading was corrected after fixing the leak in the membrane filter upstream from the analyzer.
5. The exponent of k_G over u_G is 0.61 for MP250Y, which is lower than exponents from previous experiments.
6. The k_G and SO_2 measurements should be repeated for other packings studied prior to this work.

Future Work

Next quarter, we will re-measure the gas film mass transfer coefficient for some of the previous packings: GTC GT-Pak^{TM} 350Z and 1” Plastic Pall Ring.

We have an interest in measuring structured packing with high surface area and large corrugation angle, such as GTC GT-Pak^{TM} 500Z. The packing should have a relatively low pressure drop and high mass transfer efficiency. We also have interest in measuring GTC GT-Pak^{TM} 350Y to explore how corrugation angle can influence mass transfer efficiency.

Modeling and simulation of complex stripping configurations

Quarterly Report for January 1 – March 31, 2012

by Tarun Madan

Supported by the Luminant Carbon Management Program
and by the PSTC Project on CO_2 Capture from Natural Gas Combustion (funded by TOTAL)

Department of Chemical Engineering
The University of Texas at Austin

April 30, 2012

Abstract

Stripper complexity is an important area of research to minimize the energy penalty of CO_2 capture process from amine scrubbing of post combustion gases. Configurations such as the interheated stripper, multistage flash with cold rich bypass, and adiabatic lean flash have shown promising results in decreasing the overall energy requirement of the process. These results depend on the design specifications used in the process, especially the design specification for the cross-exchanger. The problem becomes more complex when multiple heat exchangers are used in the system. Practical design specifications that can be applied across the heat exchanger network must be identified.

An overall log mean temperature difference (LMTD) of 5 °C across the cross exchanger(s) was investigated and identified as a reasonable design specification. This specification allows us to compare configurations developed by splitting a single cross exchanger with LMTD of 5 °C into two or more cross exchangers with an overall LMTD across all the exchangers of 5 °C. Such a configuration was investigated with a single-stage flash and warm rich bypass to identify the optimum operating condition for 8 m PZ operating at 150 °C stripping. The effect of splitting the exchanger to multiple exchangers was studied for minimum equivalent work. A minimum equivalent work value of 29.2 kJ/mol CO_2 was achieved using this specification, corresponding to the operating condition of a single cross exchanger (or coldest possible temperature of bypass) and 0.33 lean loading (0.4 rich loading).

The complex configuration of a LP flash followed by a HP flash was optimized with an overall LMTD of 5 ^oC.

Amine scrubbing is being investigated for CO_2 removal from flue gas of natural gas fired power plants using 8 m PZ. Preliminary results for the interheated stripper configuration give an equivalent work of 39 kJ/mol CO_2 at the optimum lean loading for 0.33 rich loading.

Pilot plant reconciliation was continued from last quarter. On the stripper side, Aspen Plus® models were modified and shifted to adjust rich loading to close the mass balance. Energy balances were also closed out with this adjusted model. A single more rigorous model based on modeling of individual units of the pilot plant will be prepared in next quarter.

Introduction

Stripper complexity and advanced stripper configurations have been studied in the past to minimize the energy requirement of amine scrubbing for post combustion carbon capture. Increasing the reversibility of the process using advanced configurations improves the energy performance. This complexity can be increased by using recycles, better heat recovery, splits, multiple pressure stages, and other features (Leites et al., 2003). For post-combustion CO_2 capture with 8 m PZ, Van Wagener (2011) has evaluated advanced configurations including multi-stage flash, cold-rich bypass, interheated stripper. These configurations were investigated using Aspen Plus® with thermodynamic models developed using experimental data. For 8 m PZ, the solvent currently being researched, values in the range of 30.5–35.3 kJ/mol CO_2 have been reported for configurations ranging from single-stage flash to interheated stripper.

It is important when comparing configurations to ensure consistent design specifications. Important specifications include:

1. 150 °C reboiler temperature: Typically, the stripper reboiler/steam heater is modeled for operation at 150 °C, corresponding to the temperature up to which 8 m PZ is known to be thermally stable (Voice, 2012). PZ has also been demonstrated to resist thermal degradation at pilot scale for temperatures up to 150 °C (Rochelle, 2012).
2. 5 °C approach temperature/LMTD for cross exchanger: This is a typical design specification often used as a trade-off between capital cost and operating cost. LMTD for a heat exchanger is defined as:

$$LMTD = \frac{\Delta T_h - \Delta T_c}{\ln\left(\frac{\Delta T_h}{\Delta T_c}\right)}$$

$$\Delta T_h = T_{Lh} - T_{Rh}$$
$$\Delta T_c = T_{Lc} - T_{Rc}$$

   where:

   T_{Lh} = hot side T of lean amine
   T_{Rh} = hot side T of rich amine
   T_{Lc} = cold side T of lean amine
   T_{Rc} = cold side T of rich amine

   Variation in this specification would usually cause significant changes in the resulting equivalent work as any heat that is not recovered in the heat exchanger results in extra heat duty required in the reboiler/steam heater. It becomes especially important where more than one cross exchanger is utilized in series (with or without unit operation in between). While a similar design specification of 5 °C LMTD can be utilized for both or all the exchangers, the resulting configuration may not be optimum since in practice, the two exchangers can be individually designed for a total LMTD of 5 °C, which will have different LMTD for the two exchangers, based on their individual size. This means that the individual exchangers can be varied in size for a specification of total LMTD of 5 ˚C.
3. Other typical specifications include rich loading (usually 0.4 for post-combustion CO_2 capture), and pump and compressor efficiencies (0.72)

The LMTD was investigated in this work for optimizing heat exchangers in configurations where more than one exchanger is used. The configuration used was a single-stage flash with warm rich bypass. Also examined was a LP flash followed by HP flash.

Methods and Discussion

Process Modeling

The configuration of two heat exchangers with bypass taken between the two exchangers was investigated. The flowsheet is given in Figure 1. Rich solvent from the absorber goes through a series of two cross exchangers. There is a provision for bypassing the second cross exchanger to divert flow directly to the flash vessel where stripping takes place. The rich solvent is heated to the desired temperature upstream from the flash vessel. Heat is recovered from the incoming lean solvent stream in the cross exchanger.

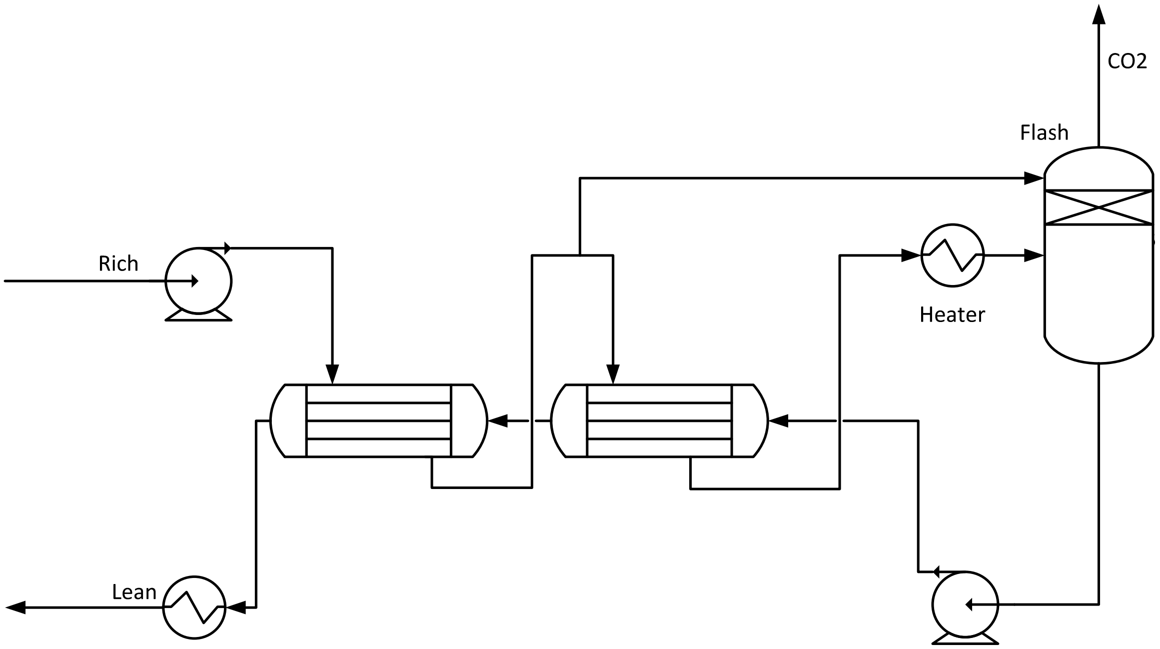

Figure 1: Split cross exchanger with single-stage flash

Process modeling details for this configuration are as follows:

1. Process Modeling Tool – Aspen Plus® v7.3
2. Solvent – 8 m piperazine (PZ)
3. Thermodynamic Model – Fawkes Model developed in-house
4. Rich Loading – 0.4
5. Pump efficiency – 0.72
6. Cross Exchangers – Total LMTD of 5 °C. Total LMTD can be defined as total Q divided by total UA, where total UA is the sum of individual UAs:

$$LMTD_T = \frac{Q_1 + Q_2}{UA_T} = 5$$

$$UA_T = UA_1 + UA_2 = \frac{Q_1}{LMTD_1} + \frac{Q_2}{LMTD_2}$$

Where:

$LMTD_T =$ Total LMTD
$UA_T =$ Total UA
$Q_1, LMTD_1 =$ Heat Duty and LMTD for exchanger 1
$Q_2, LMTD_2 =$ Heat Duty and LMTD for exchanger 2

This specification allows variation in the size of the exchangers to maintain a total LMTD of 5

7. Heater Temperature – 150 °C

A minimum value for overall equivalent work can be obtained by varying the following:

1. Lean loading (varied from 0.27 to 0.33)
2. Bypass (varied from 0 to 15%)
3. Relative size of exchangers.

Temperature of the stream between the two exchangers (split temperature) was varied from 46 °C to 105 °C, which determined the relative size of the exchangers.

Another configuration was studied using the same approach. The process for this is given in Figure 2. It consists of a network of three cross exchangers, an LP adiabatic column, and an HP flash. The first column operates at lower pressure and is heated by the returning lean stream.

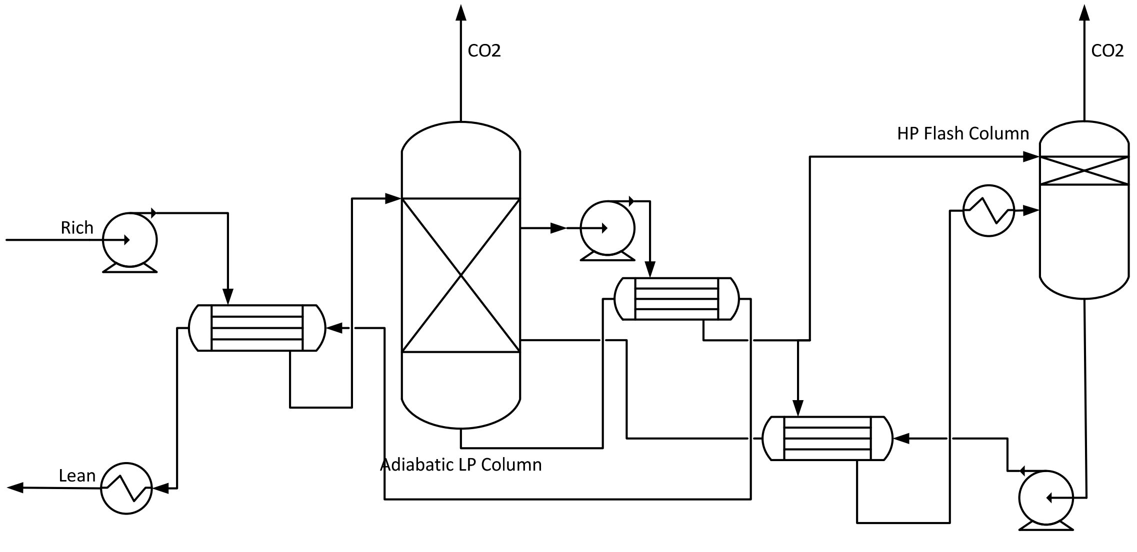

Figure 2: Adiabatic LP column with HP flash

This configuration offers multiple optimization possibilities by varying the following parameters:

1. Lean loading (varied from 0.27 to 0.33)
2. Bypass (%)
3. Pressure of LP column
4. Relative size of exchangers.

This quarter, a LMTD of 5 was used for individual exchangers, determining the relative size of exchangers and hence the spec no. 4 was not used for optimization. Effect of its variation on this configuration will be studied in the future.

CO_2 capture from natural gas fired power plants

Amine scrubbing using 8 m PZ is being investigated for CO_2 removal from flue gas of natural gas fired power plants. The major difference between the flue gas of coal fired and natural gas fired power plants is the CO_2 composition which is less in the case of natural gas. This results in lower values of rich loading for natural gas.

Preliminary investigation of absorption indicates rich loading values in the range of 0.3–0.36. Two cases of rich loading of 0.33 and 0.36 were investigated for energy consumption with the configuration of interheated stripper. Lean loading was optimized for these two cases of rich loading. Other specifications are as follows

1. 8 m PZ
2. 5 °C LMTD across cross exchanger
3. 150 °C Reboiler Temperature

This incremental effort is being funded by Total through the Process Science and Technology Center.

Pilot Plant Reconciliation

Reconciliation of pilot plant data from the previous campaign is ongoing. Aspen Plus® models were created for individual runs of the campaign in the previous quarter and adjusted for rich loading to close out mass balances.

The model was improved with incorporation of pressure drops in the system. Resulting models were again adjusted for rich loading. The resulting cases were used to close out the heat and mass balances.

Results and Discussion

Configuration of split cross exchangers with single-stage flash

88 cases were run by varying the values of optimization variables as identified above. Absolute values and detailed results of equivalent work obtained using these runs are given in Appendix A. Equivalent work was calculated using the following formula and assumptions.

$$W(eq) = 0.75\left(\frac{T_{reb} - T_{sink} + \Delta T}{T_{reb} + \Delta T}\right)Q_{reb} + Q_{pump} + Q_{comp}$$

Where:

$T_{reb} = \text{Reboiler T}$
$T_{sink} = \text{Sink T, assumed 40 °C}$
$\Delta T = \text{Approach T for steam heater, 5 °C}$
$Q_{reb} = \text{Heat duty of reboiler}$
$Q_{pump} = \text{Pump work}$
$Q_{comp} = \text{Compression work for 150 bar discharge P of CO2}$

Figures 3–6 compare the variation of equivalent work against lean loading for different values of other parameters. The minimum value of equivalent work observed was 29.2 kJ/mol for the following parameters:

1. 0.32 lean loading
2. 5% bypass
3. 46 °C temperature of stream between cross exchangers (i.e., coldest possible/no splitting of cross exchangers)

This was also found to be the overall minimum value of equivalent work when all the cases were analyzed.

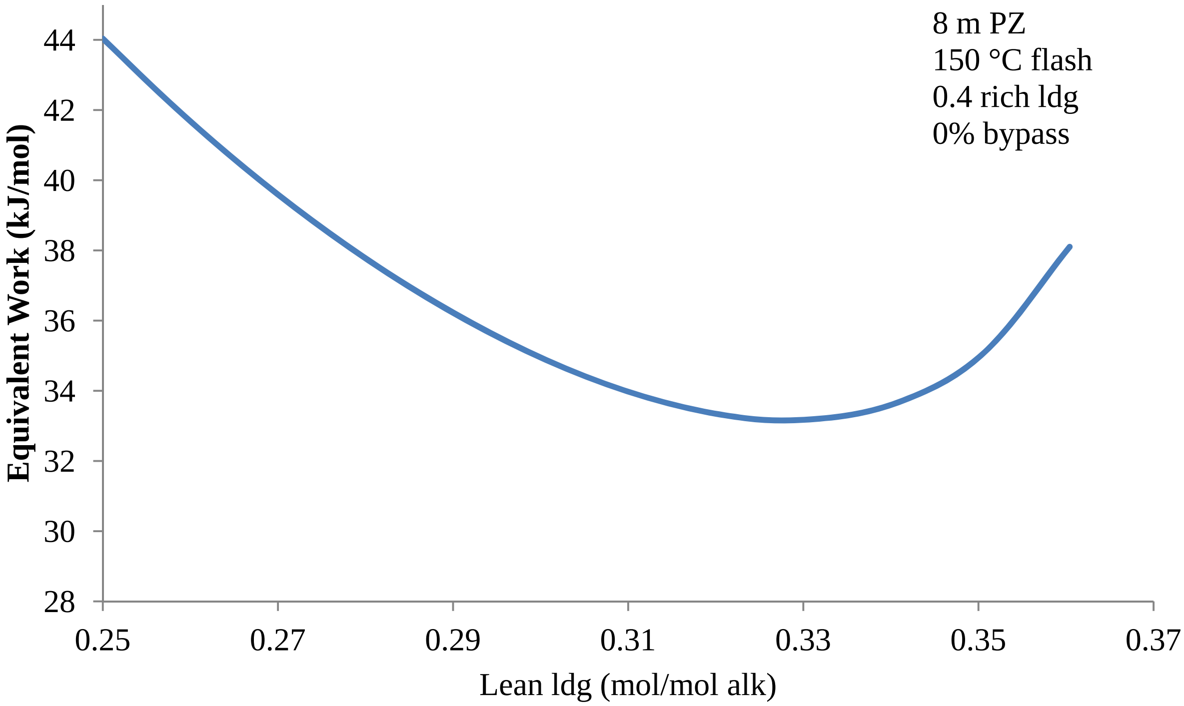

Figure 3: Energy performance of single stage flash with one cross-exchanger (base case, rich ldg 0.4, 0% bypass, variable lean ldg)

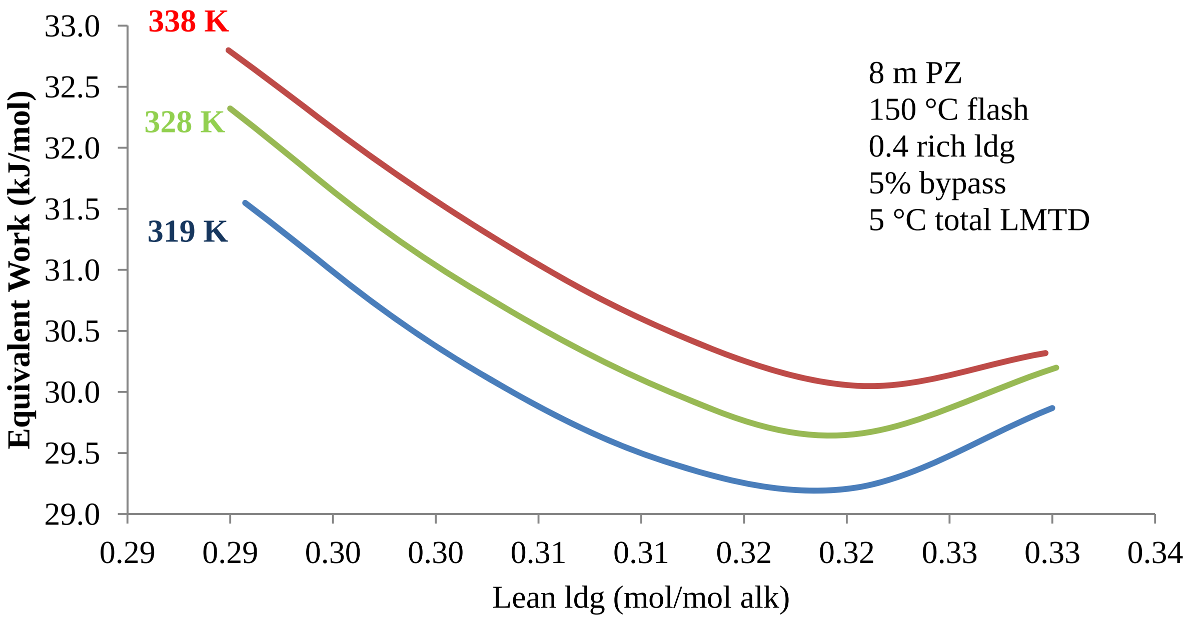

Figure 4: Energy performance of single stage flash with two cross-exchangers at different T of stream between exchangers (rich ldg 0.4, 5% bypass from stream after 1st exchanger, variable lean ldg)

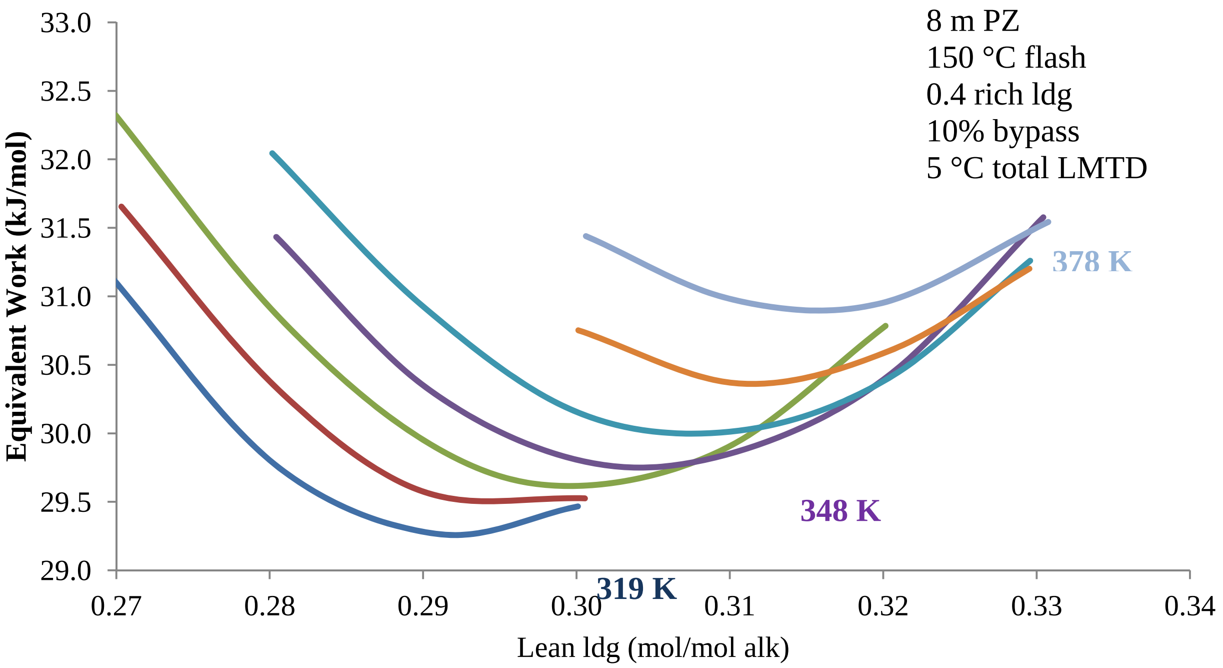

Figure 5: Energy performance of single stage flash with two cross-exchangers at different T of stream between exchangers (rich ldg 0.4, 10% bypass from stream after 1st exchanger, variable lean ldg)

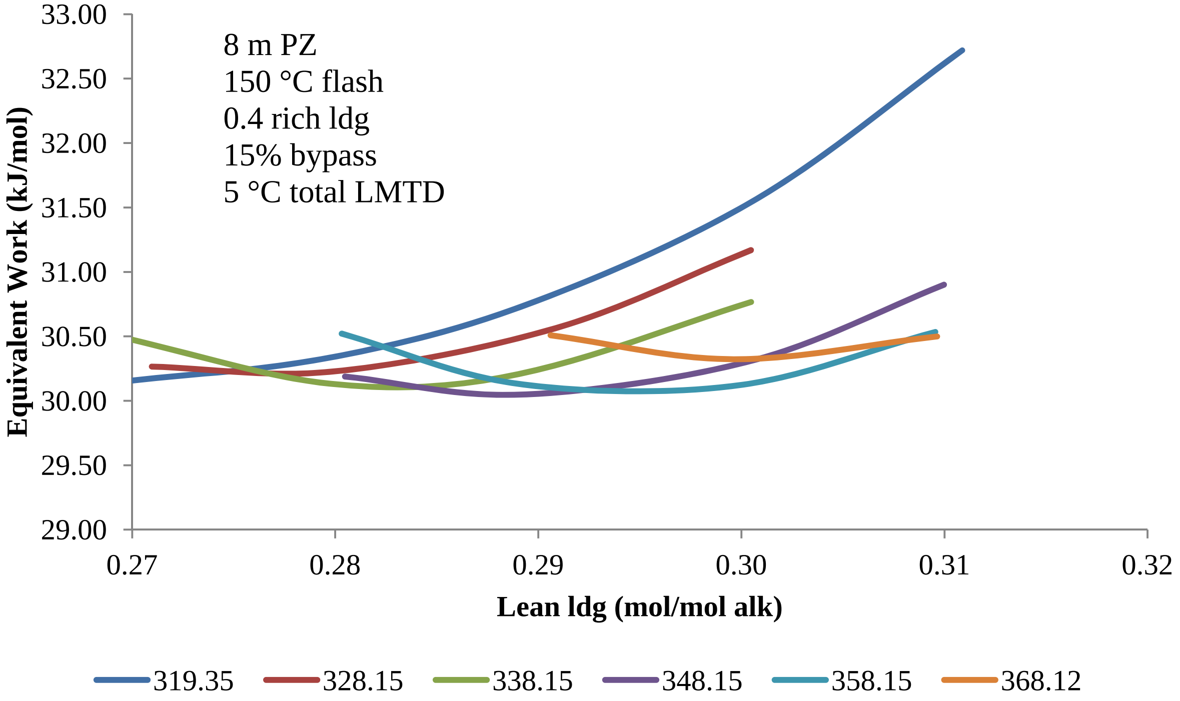

Figure 6: Energy performance of single stage flash with two cross-exchangers at different T of stream between exchangers (rich ldg 0.4, 15% bypass from stream after 1st exchanger, variable lean ldg)

Figures 7–9 compare the variation of equivalent work and temperature of stream between two cross exchangers. This analysis is useful for determining the sensitivity of equivalent work by varying the relative size of the cross exchanger.

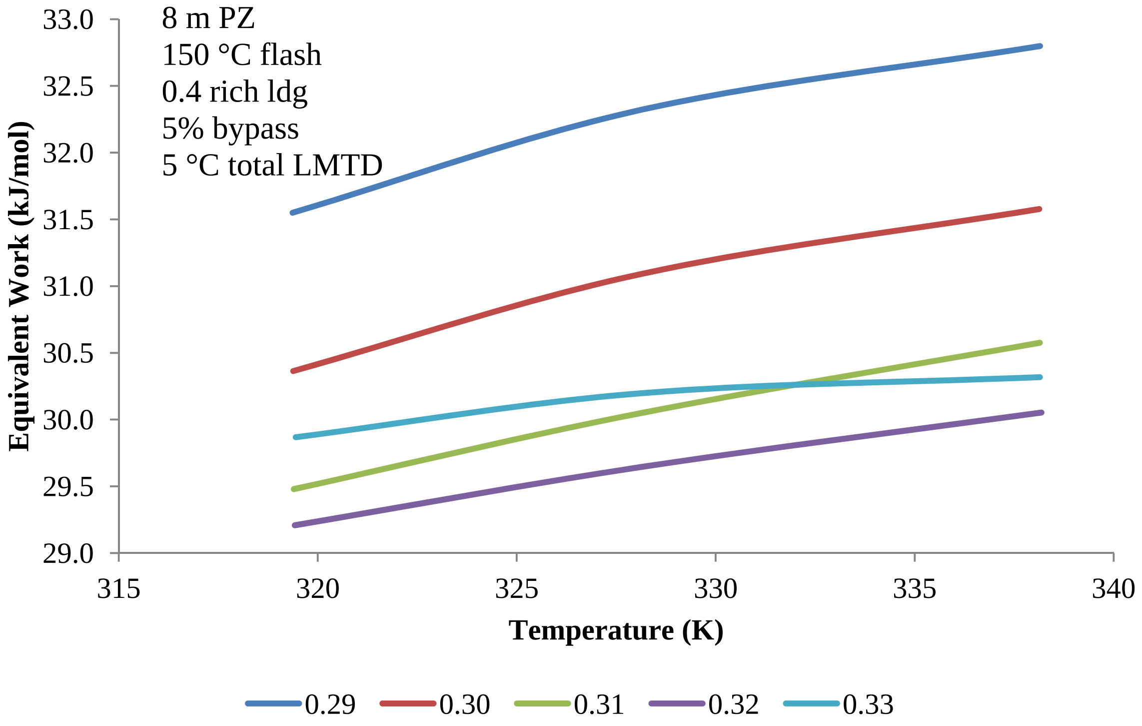

Figure 7: Energy performance of single stage flash with two cross-exchangers at different lean loadings (variable T of stream between two exchangers, rich ldg 0.4, 5% bypass from stream after 1st exchanger)

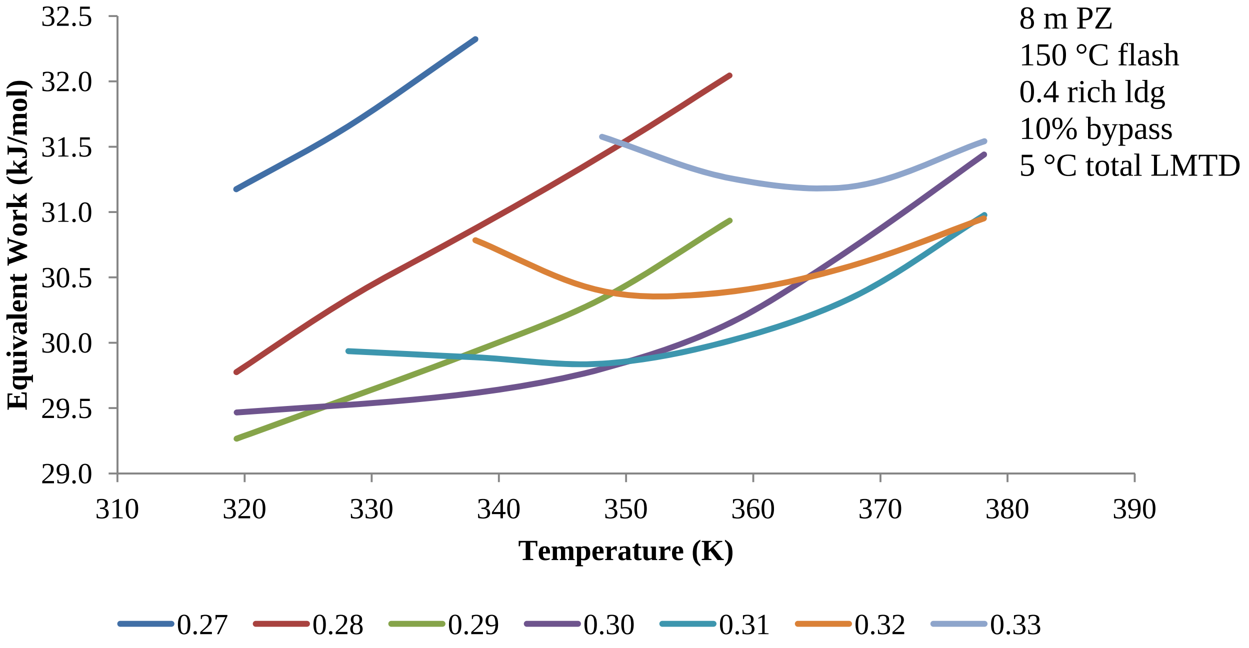

Figure 8: Energy performance of single stage flash with two cross-exchangers at different lean loadings (variable T of stream between two exchangers, rich ldg 0.4, 10% bypass from stream after 1st exchanger)

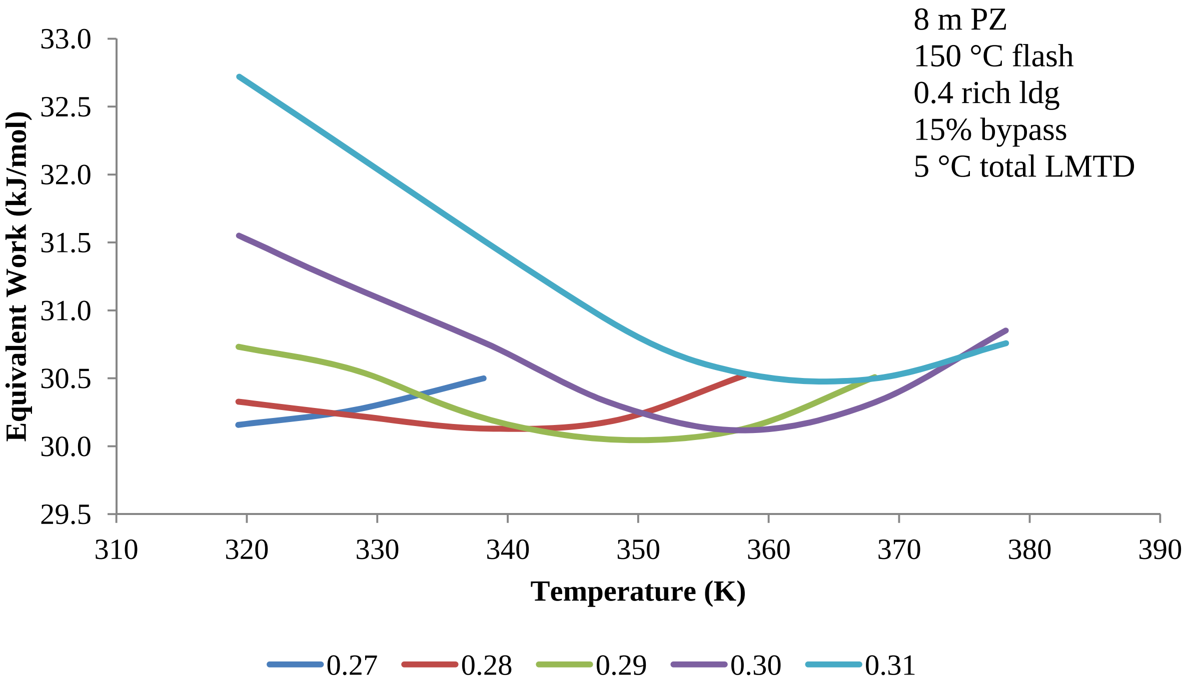

Figure 9: Energy performance of single stage flash with two cross-exchangers at different lean loadings (variable T of stream between two exchangers, rich ldg 0.4, 15% bypass from stream after 1st exchanger)

As can be seen from above figures, equivalent work monotonically decreased with decreasing temperature of stream between two cross exchangers for lower values of bypass. However, for higher values of bypass, there is a different optimum temperature with a corresponding value of equivalent work. The global minimum value among these variations was found at the coldest possible temperature of split stream.

Equivalent work was compared with the value calculated using the other common specification for cross exchanger design, i.e., 5 °C cold side temperature approach. The most stringent specification which this model was able to achieve was 7 °C hot side approach, which was limited by the cold side approach which approached 0 for any lower hot side approach. Table 1 provides the comparison of values obtained for these three cases. The configuration for this comparison is the base case of one cross exchanger, single-stage flash with no bypass, 0.4 rich loading, 0.33 lean loading (optimum lean loading for this configuration).

Table 1: Comparison of performance due to different design specifications on cross exchanger (Single stage flash with 0% bypass, 8 m PZ, 150 °C flash T, 0.4 rich ldg, 0.33 lean ldg)

S.no.	LMTD	Hot Side approach	Cold Side approach	Equivalent Work	Applied design specification on cross exchanger
		C	C	kJ/mol	
1	7.1	9.6	5.0	**35.8**	Cold side approach = 5 °C
2	5	8.3	2.7	**33.2**	LMTD = 5 °C
3	2.2	7.0	0.3	**30.5**	Hot side approach = 7 °C

As expected, energy performance was directly proportional to the hot side temperature approach achieved. However, the most stringent hot side temperature approach (and the best energy performance) leads to a LMTD of 2 °C for the exchanger which is not a practical design.

The same analysis can be useful for other advanced configurations, especially where CO_2 is stripped in two pressure stages, with the first stage pressure being another variable for optimization. This is the case in the second configuration studied in this work.

Configuration of LP column with HP flash

For this case, a design specification of individual LMTD of 5 was used on the exchangers. Results showed that again best performance was for cases with minimum draw-off from the LP vessel.

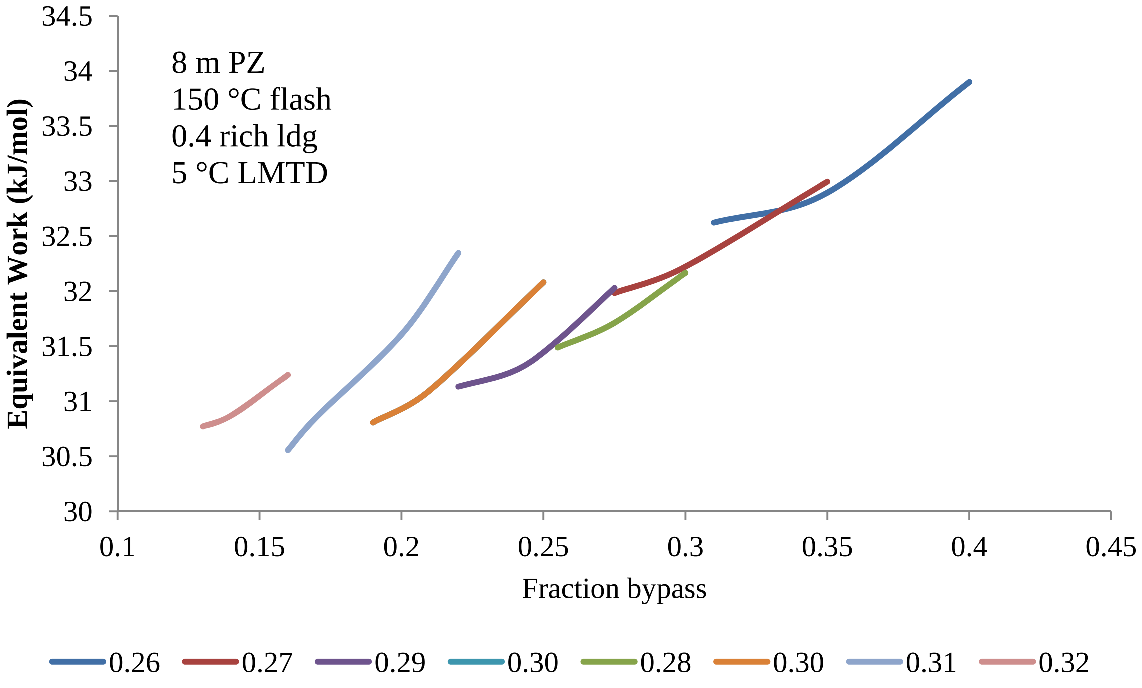

Figure 10: Energy performance of LP column with HP flash with three cross-exchangers at different lean loadings (variable bypass from stream between two exchangers, rich ldg 0.4)

CO_2 Capture from natural gas fired power plants (Total Project)

Two cases of rich loading 0.33 and 0.36 were investigated and optimized for equivalent work. Figure 11 compares the equivalent work with loading for these two cases. The minimum value obtained was 39 kJ/mol (corresponding to 0.24 lean ldg) for 0.33 rich ldg and 35.3 kJ/mol (corresponding to 0.25 lean ldg) for 0.36 rich ldg.

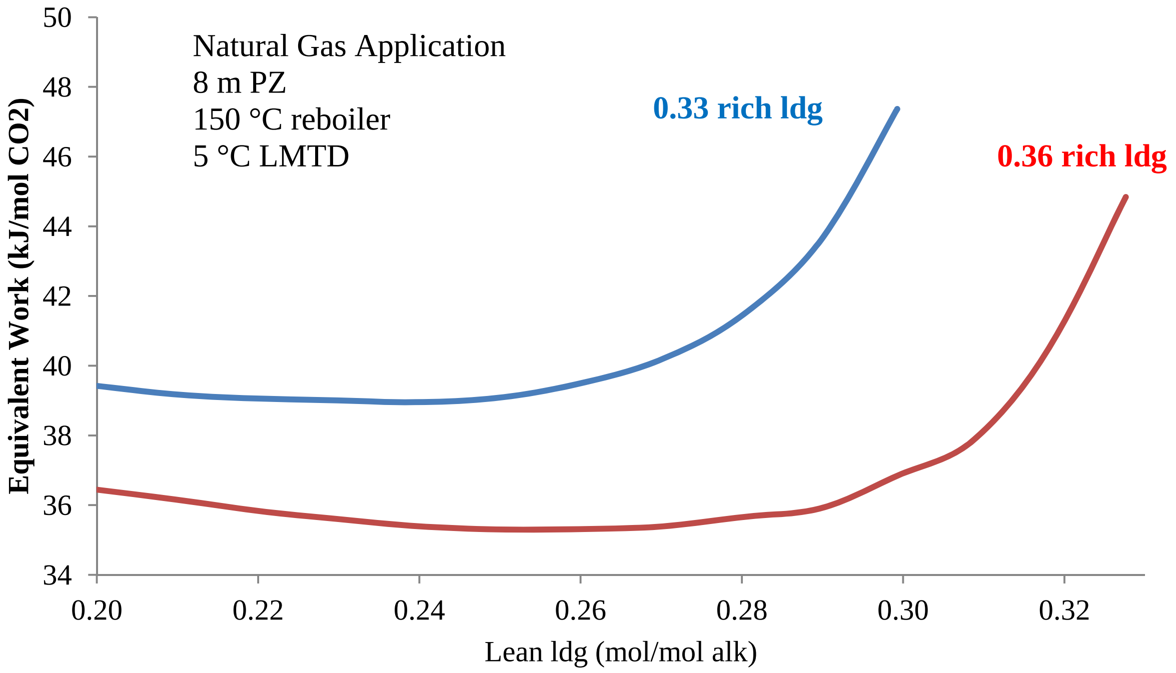

Figure 11: Energy performance of interheated stripper configuration for 0.33 and 0.36 rich loadings (0% bypass, 5 °C LMTD)

Pilot Plant reconciliation

Aspen Plus® models created in the previous quarter for pilot plant data reconciliation were improved upon by adding pressure drop data from the runs. Models adjusted for rich loading were used to predict the heat duty requirements in the two steam heaters of flash skid. Table 2 compares the values of modeled and reported values of heat duties and rich loadings.

Table 2: Comparison of modeled heat duties and adjusted rich loadings with corresponding values from the pilot plant measurements (rich ldg adjusted to close mass balance)

Run no.	**Rich ldg**		**HP Heater Duty**		**LP Heater Duty**		**Total Heat Duty**	
	mol/mol		MMBTU/h		MMBTU/h		MMBTU/h	
	Measured	Modeled	Reported	Modeled	Reported	Modeled	Reported[*]	Modeled
1	**0.343**	**0.378**	0.265	0.298	0.199	0.106	**0.409**	**0.405**
2	**0.334**	**0.372**	0.239	0.269	0.198	0.113	**0.385**	**0.382**
3	**0.345**	**0.392**	0.194	0.236	0.221	0.137	**0.365**	**0.373**
5	**0.339**	**0.378**	0.209	0.235	0.167	0.094	**0.331**	**0.329**
6	**0.351**	**0.386**	0.105	0.117	0.239	0.159	**0.284**	**0.276**
7	**0.338**	**0.369**	0.142	0.180	0.314	0.220	**0.413**	**0.400**
8	**0.369**	**0.376**	0.185	0.276	0.321	0.203	**0.453**	**0.478**
9	**0.344**	**0.377**	0.241	0.328	0.362	0.240	**0.549**	**0.568**
11	**0.350**	**0.383**	0.347	0.477	0.347	0.213	**0.645**	**0.690**

[*] Reported values are calculated based on Reported HP and Reported LP, less reported heat loss in each case.

As can be seen from Table 2, the model that was adjusted to close the mass balance also satisfies the overall heat balance for all the cases. In future work the individual unit operations and pressure drops will be modeled more rigorously to represent the pilot plant data in a single consistent model.

Conclusions

1. Design specification across the cross exchanger network is an important aspect of process modeling.
2. Typical design specification of total LMTD of 5 °C can be used across a network of cross exchangers. The relative size of the cross exchangers is another optimization parameter for minimization of equivalent work.
3. Equivalent work of 29.2 kJ/mol CO_2 was obtained for a configuration of split heat exchangers with single-stage flash and warm rich bypass.
4. Different optimum values of split temperature are obtained for higher values of bypass. For smaller values of bypass, it is optimum not to split the exchanger and use only one exchanger with a total LMTD specification of 5 °C.
5. An adiabatic LP column with HP flash gives an optimum equivalent work of 29 with specification of 5 °C LMTD on all cross exchangers.
6. Preliminary results for amine scrubbing for natural gas usage indicates energy performance in the range of 36–39 kJ/mol CO_2.

Future Work

The stripping configuration of adiabatic LP column with HP flash will be optimized with this specification. Other complex stripping configurations with multiple heat exchangers and multiple pressure stages will be investigated using these specifications. Sensitivity of these design specifications on complex configuration will be evaluated.

Investigation of amine scrubbing using 8 m PZ for natural gas fired power plants is an ongoing project. Stripping configurations for other values of rich loading will be investigated and optimized.

The Pilot Plant model will be updated to represent more rigorous models of unit operations and effects due to pressure drops.

References

Leites IL, et al. "The theory and practice of energy saving in the chemical industry: some methods for reducing the thermodynamic irreversibility in chemical technology processes." *Energy*, Volume 28, Issue 1, January 2003; 55–97.

Oyenekan B. *Modeling of Strippers for CO_2 Capture by Aqueous Amines*. The University of Texas at Austin. Ph.D. Dissertation. 2007.

Van Wagener DH. *Stripper Modeling for CO_2 Removal Using Monoethanolamine and Piperazine Solvents.* The University of Texas at Austin. Ph.D. Dissertation. 2011.

Rochelle GT et al. "CO_2 Capture by Aqueous Absorption, Fourth Quarterly Progress Report 2011." Luminant Carbon Management Program. The University of Texas at Austin. 2012.

Voice AK. "Degradation and Contamination in Amine Solutions for CO_2 Capture." Presented at *UTCCS-1*, Austin, TX. 2012.

Appendix A

Detailed data for all the runs executed for multiple heat exchanger configuration

S.no.	Lean Loading	Temperature Split	Fraction Bypass	Equivalent Work	LMTD – Heat Ex 1	LMTD – Heat Ex 2
	mol/mol	K		kJ/mol	°C	°C
1	0.33	348.11	0.1	31.58	5.44	4.86
2	0.33	358.13	0.1	31.26	5.13	5.01
3	0.33	368.13	0.1	31.20	4.89	5.17
4	0.33	378.17	0.1	31.54	4.82	5.40
5	0.32	338.15	0.1	30.78	5.46	5.02
6	0.32	348.15	0.1	30.40	4.98	4.98
7	0.32	358.17	0.1	30.39	4.80	5.18
8	0.32	368.19	0.1	30.60	4.71	5.43
9	0.32	378.14	0.1	30.95	4.61	5.72
10	0.31	328.17	0.1	29.94	5.17	4.98
11	0.31	338.13	0.1	29.89	4.89	5.01
12	0.31	348.15	0.1	29.84	4.63	5.14
13	0.31	358.14	0.1	30.02	4.52	5.37
14	0.31	368.13	0.1	30.36	4.45	5.65
15	0.31	378.17	0.1	30.98	4.47	6.04
16	0.30	319.38	0.1	29.47	-	5.03
17	0.30	328.13	0.1	29.53	4.75	4.98
18	0.30	338.15	0.1	29.62	4.48	5.09
19	0.30	348.14	0.1	29.80	4.36	5.28
20	0.30	358.17	0.1	30.15	4.25	5.55
21	0.30	368.19	0.1	30.75	4.27	5.95
22	0.30	378.15	0.1	31.44	4.35	6.35
23	0.29	319.37	0.1	29.27		4.99
24	0.29	328.15	0.1	29.58	4.35	5.03
25	0.29	338.15	0.1	29.93	4.23	5.20
26	0.29	348.15	0.1	30.34	4.08	5.44
27	0.29	358.15	0.1	30.93	4.07	5.83
28	0.28	319.36	0.1	29.77		4.97
29	0.28	328.15	0.1	30.34	4.06	5.12
30	0.28	338.15	0.1	30.87	3.94	5.32
31	0.28	348.15	0.1	31.43	3.90	5.66
32	0.28	358.14	0.1	32.04	3.84	6.04
33	0.27	319.34	0.1	31.17		5.01

34	0.27	328.14	0.1	31.66	3.67	5.15
35	0.27	338.15	0.1	32.32	3.61	5.42
36	0.31	319.41	0.15	32.72		4.97
37	0.31	348.15	0.15	30.90	5.73	4.76
38	0.31	358.17	0.15	30.53	5.20	4.91
39	0.31	368.19	0.15	30.50	4.87	5.17
40	0.31	378.19	0.15	30.76	4.65	5.51
41	0.30	319.39	0.15	31.55		4.98
42	0.30	328.17	0.15	31.17	6.61	4.87
43	0.30	338.15	0.15	30.77	5.96	4.87
44	0.30	348.15	0.15	30.31	5.30	4.86
45	0.30	358.13	0.15	30.12	4.83	5.05
46	0.30	368.13	0.15	30.32	4.61	5.41
47	0.30	378.18	0.15	30.85	4.59	5.86
48	0.29	319.37	0.15	30.73		5.00
49	0.29	328.15	0.15	30.56	6.07	4.90
50	0.29	338.18	0.15	30.21	5.37	4.91
51	0.29	348.16	0.15	30.05	4.91	5.03
52	0.29	358.16	0.15	30.13	4.55	5.27
53	0.29	368.12	0.15	30.51	4.44	5.64
54	0.28	319.36	0.15	30.33		5.01
55	0.28	328.15	0.15	30.23	5.57	4.95
56	0.28	338.18	0.15	30.13	5.05	5.00
57	0.28	348.15	0.15	30.19	4.67	5.17
58	0.28	358.15	0.15	30.52	4.38	5.47
59	0.27	319.35	0.15	30.16		4.96
60	0.27	328.15	0.15	30.27	5.22	4.99
61	0.27	338.15	0.15	30.50	4.64	5.05
62	0.33	319.45	0.05	29.87		5.00
63	0.33	328.15	0.05	30.20	4.60	5.05
64	0.33	338.15	0.05	30.32	4.46	5.09
65	0.32	319.42	0.05	29.21		5.01
66	0.32	328.15	0.05	29.65	4.13	5.07
67	0.32	338.19	0.05	30.05	4.13	5.20
68	0.31	319.40	0.05	29.48		5.03
69	0.31	328.15	0.05	30.05	3.84	5.17
70	0.31	338.15	0.05	30.58	3.87	5.36
71	0.30	319.38	0.05	30.36		4.98
72	0.30	328.15	0.05	31.09	3.44	5.22
73	0.30	338.13	0.05	31.58	3.59	5.50
74	0.29	319.37	0.05	31.55		4.97

75	0.29	328.15	0.05	32.32	3.17	5.30
76	0.29	338.15	0.05	32.80	3.29	5.59
77	0.25	319.34	0	44.03		5.01
78	0.26	319.34	0	41.90		5.00
79	0.27	319.36	0	39.68		5.00
80	0.28	319.37	0	37.79		5.00
81	0.29	319.38	0	36.23		5.00
82	0.30	319.40	0	34.97		4.99
83	0.31	319.42	0	34.01		5.00
84	0.32	319.44	0	33.36		5.00
85	0.33	319.47	0	33.17		5.01
86	0.34	319.50	0	33.60		5.00
87	0.35	319.54	0	35.03		5.00
88	0.36	319.58	0	38.11		5.01

2MPZ Heat Capacity, Speciation, and Process Modeling

Quarterly Report for January 1 – March 31, 2012

by Brent Sherman

Supported by the Luminant Carbon Management Program

Department of Chemical Engineering
The University of Texas at Austin

April 30, 2012

Abstract

Creating a process model of 2-methylpiperazine (2MPZ) will allow us to understand how reaction rate affects all aspects of the amine scrubbing process. The existing 2MPZ model is unsuitable for creating a process model, and so it will be re-regressed as it is blended with the Fawkes model. In order to improve the quality of this regression, heat capacity and additional speciation data were sought. However, the available differential scanning calorimeter (DSC) failed to replicate results. Changing the equilibration time, scan rate, and reference resulted in only minor improvement. At higher loadings, the 4 m 2MPZ/4 m PZ blend NMR had merged peaks at 40 °C. This means speciation cannot be determined. Running at a lower temperature will give more peak separation. Results from this are pending. Work next quarter will focus on creating a 2MPZ process model as well as obtaining accurate heat capacities.

Motivation

This quarter, work focused on 2-methylpiperazine (2MPZ). 2MPZ is analogous to piperazine (PZ) except for having approximately half the reaction rate. By developing a full process model of 2MPZ and comparing it to our existing model of PZ the results of changing reaction rate on all process aspects can be quantified. Isolating the effect of reaction rate is an essential step towards developing a generic amine model.

This work builds primarily on that done by Xi Chen by removing an assumption and modifying the existing thermodynamic and kinetic 2MPZ model (Chen, 2011). The current model assumes that the heat capacity of 2MPZ is equal to that of PZ. While this is a good assumption as their molecular structure differs only by a methyl group, differential scanning calorimetry (DSC) can determine the true heat capacity of 2MPZ. This will improve the accuracy of our model.

Gathering additional speciation data on the 2MPZ/PZ blend will help with the integration of the 2MPZ and Fawkes model. Having one model for a variety of amines makes comparisons easier and will allow us to model a blend of 2MPZ/PZ, which is a longer term goal.

Experimental Methods

DSC

Differential scanning calorimetry (DSC) works by measuring the heat flow difference between the reference and sample required to reach a set temperature. The reference and sample are placed in a furnace that is continually swept with a purge gas. A rough schematic is shown in Figure 1. Before each run, the calibration of the machine is checked by using an indium sample. Once the melting point and the heat of fusion are verified, a baseline is run. This baseline is the reference crucible and an empty crucible. Then, a standard is run. Finally, four samples of the same solution are run.

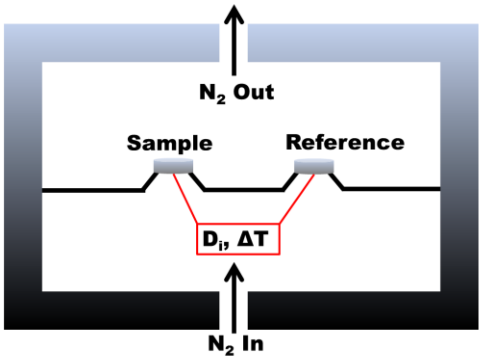

Figure 1: DSC diagram

Hilliard and Nguyen have measured the heat capacity of monoethanolamine (MEA), piperazine (PZ), and blends of monodiethanolamine and piperazine (MDEA/PZ) (Hilliard, 2004; Rochelle, 2011). Since the ASTM standard (E1269-05) that Hilliard based his method on was updated last year, the method was re-examined. The sample preparation remained the same, but the DSC steps were altered. In addition, the DSC used by previous group members was unavailable. In order to test the accuracy of the alterations as well as the different DSC, the new method was benchmarked using water.

Large volume (60 μl^3) crucibles were used to measure heat capacity. Each crucible is comprised of a pan, lid, and O-ring. The pan and lid were made of 304 stainless steel while the O-ring was made of rubber (Perkin Elmer, #0319-0218). Each component was weighed separately, then the sample was added to the pan, and finally the whole thing was crimped and reweighed (Perkin Elmer, #0990-8467). Once crimped, the crucibles can withstand an internal pressure of 150 bar, which is necessary as vaporization occurs at higher temperatures.

The modifications to the DSC steps consisted of varying the rate of heating and the standards. Three different standards were tried: 129 mg of Al_2O_3, 60 mg of Al_2O_3, and 60 mg of H_2O. The procedure followed was to allow the samples to equilibrate for 10 minutes at 15 °C and then heat to 125 °C at either a rate of 5 °C/min or 20 °C/min. All samples were run in a Perkin Elmer DSC 6000, which is owned and maintained by another research group in Chemical Engineering

The sample heat capacity $C_p(s)$ is calculated as follows:

$$C_p(s) = \frac{60E \cdot D_s}{W_s \cdot b} - \frac{\Delta W C_p(c)}{W_s} \tag{1}$$

$$E = \frac{b}{60D_{st}}\left[W_{st}C_p(st) + \Delta W C_p(c)\right] \tag{2}$$

Here E is the cell constant; D_s is the difference in heat flow between the sample and reference; W_s is the weight of the sample; $C_p(c)$ is the heat capacity of the crucible holding the sample; D_{st} is the difference in heat flow between the sample and the standard.

NMR

The sample was prepared using the method described in §3.3.2 of Chen's dissertation (2011). The sample tube was sealed and submitted to Steve Sorey of the Department of Chemistry and Biochemistry in the University of Texas at Austin. He used a VARIAN INOVA 500, 500 MHz NMR spectrometer to acquire qualitative ^{13}C, ^{1}H, and COSY spectra.

Modeling

The goal was to create a full 2MPZ process model. A simple absorber model was created as a base case and testing began. Problems quickly arose, and it was found that 90% removal could only be achieved for an unreasonably low lean loading. Efforts to troubleshoot the model were unsuccessful, and so focus shifted to integration of the existing 2MPZ model into the Fawkes model. To integrate the 2MPZ model, a re-regression is required to bring it in line with the standards used in the Fawkes model. During this re-regression, the 2MPZ model will be fully understood. This understanding should remove any impediments to a process model.

Safety

There are only small hazards posed by making samples and running them in the DSC. A razor blade is used to cut the indium to size, and so care must be taken with the sharp edge. The indium is extremely small, so safety goggles are worn to prevent flecks from bouncing into the eyes. After heating the samples in the DSC, adequate time must be allowed for the furnace to cool down before the sample can be removed.

When preparing samples for NMR, there are additional hazards posed by the chemicals themselves. Amines are handled according to standard lab protocol, but 1,4-dioxane poses an additional hazard as it is toxic and flammable. As we have a 1.5 L jug of it, it is only taken out for the moment it is needed. It is then promptly restored in the flammable cabinet. Loading the solutions is done with pressurized gas, and so caution is exercised to ensure that all connections are secure.

Materials

MEA (99%, Acros), PZ (anhydrous, 99%, Sigma-Aldrich), 2MPZ (98%, Acros), distilled deionized water (Millipore, Direct-Q), Al_2O_3 (40 mesh, 99.999%, Acros), Indium (99.999%, Perkin Elmer), $^{13}CO_2$ (99.9%, Cambridge Isotope Laboratories, Inc.), 1,4-Dioxane (99%, Acros), D_2O (99.9%, Cambridge Isotope Laboratories, Inc.) were used as received.

Results and Discussion

DSC

The current 2MPZ model assumes that the heat capacity of 2MPZ is equal to that of PZ. While this is a good assumption as their molecular structure differs only by a methyl group, differential scanning calorimetry (DSC) can determine the true heat capacity of 2MPZ. This will improve the accuracy of our model, particularly in sizing the heat exchanger.

At first, the ASTM procedure was followed. The high heating rate of 20 °C/min gave unsatisfactory results, so the heating rate was changed to 5 °C/min. While this gave better results, they were still far from the accuracy achieved by Hilliard and Nguyen. The heat capacity increased too rapidly with temperature and tended to underestimate the true value. It was hypothesized that matching the weight of the reference to the sample would give better results based on the ASTM standard. This was found to not be the case, as the heat capacity was now drastically overestimated.

In conducting the testing, using water as a standard decreased the dependence of heat capacity on temperature. Due to this desirable characteristic, water was chosen as an internal standard. To prove its validity, it was benchmarked against prior MEA results (Figure 2).

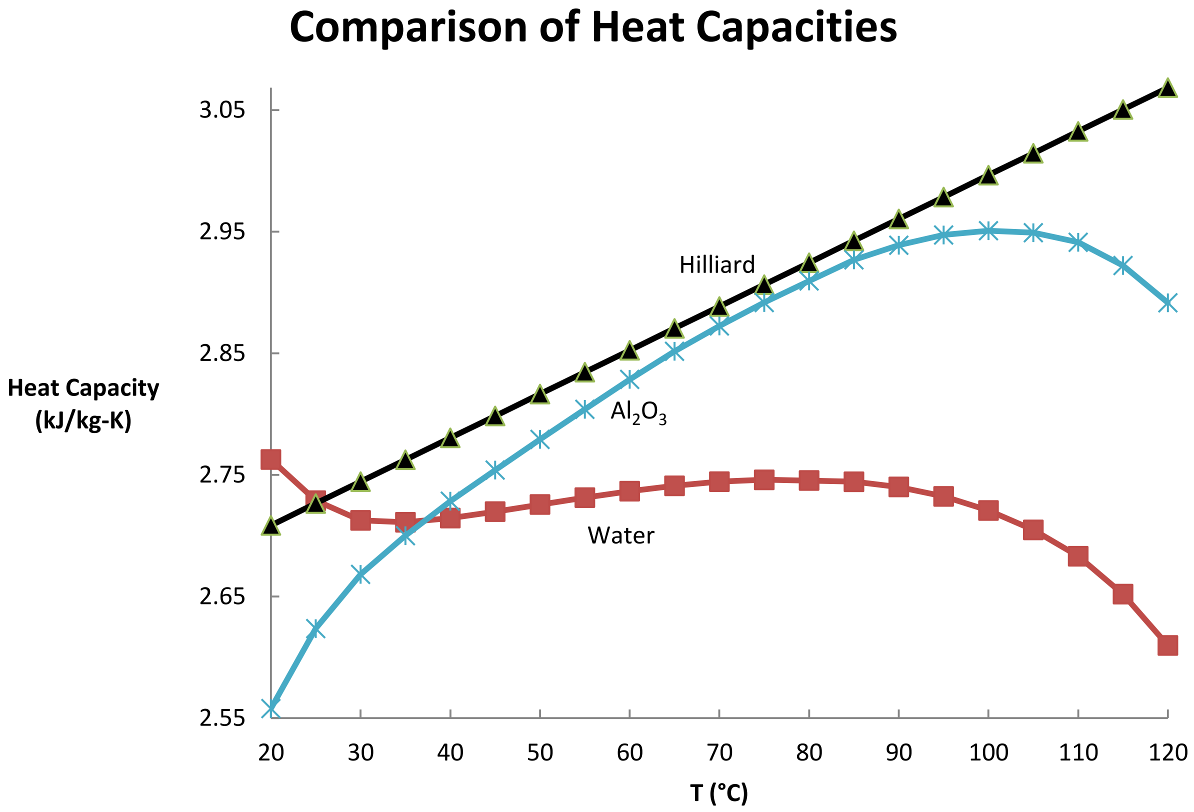

Figure 2: Heat capacity of MEA using Al_2O_3 and water as a standard compared to prior results (Hilliard, 2004), heating rate = 5 °C/min, Perkin Elmer DSC 6000.

Heat capacity should linearly increase with increasing temperature. The bend at temperatures below 30 °C may be due to initial transient effects, but the 10 minute equilibration time should negate those. The bend at temperatures above 80 °C cannot be explained. One reason heat capacity might appear to decrease would be a loss of mass. Another may be due to the vaporization of our water standard above 80 °C, but Al_2O_3 does not change phase within our temperature range. The samples were found to have the same weight before and after the runs.

Due to this odd behavior and the lack of agreement with prior results, the same DSC used by previous group members, a TA Instruments DSC-Q100, will be used.

NMR

Accurate speciation is needed for the kinetic model reactions for 2MPZ/PZ. The species expected in a loaded 2MPZ/PZ solution are shown in Table 1 below. Each carbon is numbered and a prime is used to denote PZ rather than 2MPZ.

Table 1: NMR speciation guide. Reproduced from Chen, 2011.

Name	Molecular Structure
2MPZ/2MPZH$^+$	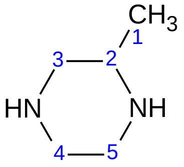 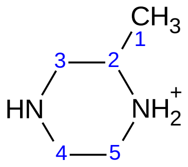
2MPZCOO$^-$/H2MPZCOO	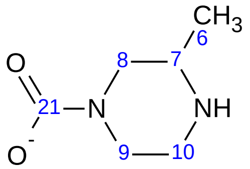 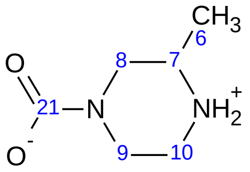
$^-$OOC2MPZ/OOC2MPZH	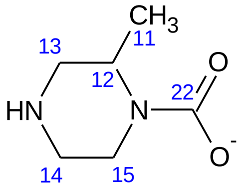 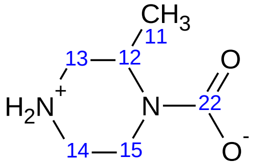
2MPZ(COO$^-$)$_2$	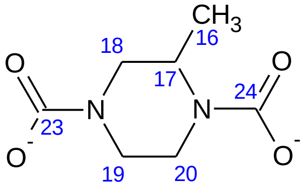
PZ/PZH$^+$	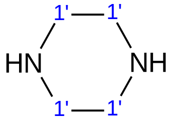 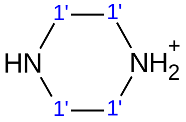
PZCOO$^-$/HPZCOO	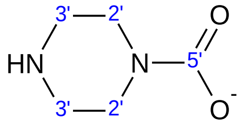 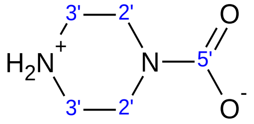
PZ(COO$^-$)$_2$	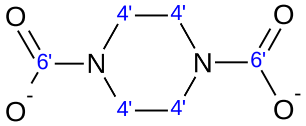

Species cannot be quantified if their spectra peaks cannot be isolated. At 40 °C and α = 0.44, many of the peaks overlap, as shown below in Figures 2 through 4.

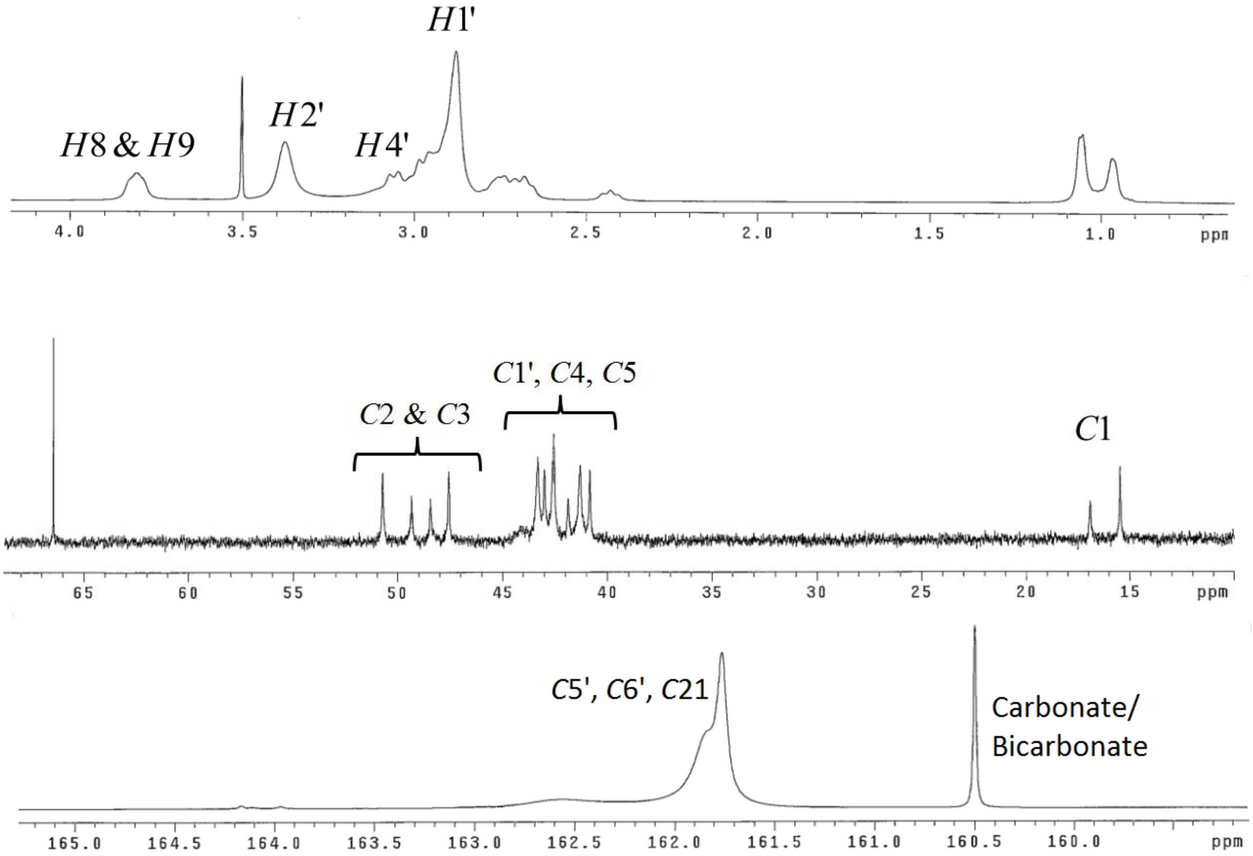

Figures 3, 4, and 5, numbered top down. All spectra are 4 m 2MPZ/4 m PZ for α = 0.440 at 40 °C. Modified from Chen, 2011.

In Figure 3, the $PZ(COO^-)_2$ and PZ/PZH^+ peaks overlap (H4' and H1'). In Figure 4, $2MPZ/2MPZH^+$ and PZ/PZH^+ overlap (C1', C4, and C5). In Figure 5, $PZCOO^-/HPZCOO$, $PZ(COO^-)_2$, and $2MPZCOO^-/H2MPZCOO$ all overlap. In an effort to separate these peaks, the original sample was resubmitted for analysis at room temperature instead of 40 °C. However, the technician was unable to lock onto the D_2O signal, and so the sample had to be remade and resubmitted. Results are pending.

Modeling

As a first step towards creating a full process model for 2MPZ, an absorber column was modeled. While the model converged assuming equilibrium, the model refused to converge with kinetics enabled except for an extremely lean loading of 0.0088. This is unrealistic, and a clear indication that something is amiss with the reaction set. After trying to troubleshoot the process model, it was found that the error had to lie in the regression. Thus, attention shifted towards the goal of integrating the 2MPZ model with the Fawkes model. In order to do this, MPZ must be re-regressed to bring it in line with the standards used in Fawkes. During this process, the error will be found and eliminated.

Conclusions

1. The heat capacity results using the Perkin Elmer DSC-6000 were unsatisfactory and so the TA Instruments DSC-Q100 will be used.
2. The existing 2MPZ kinetic model is not a suitable basis for a process model due to its reaction set.

Future Work

1. If the peaks separate at room temperature, the 4 m 2MPZ/4 m PZ sample will be rerun quantitatively for speciation.
2. The heat capacity of unloaded and loaded 2MPZ will be determined.
3. The 2MPZ model will be re-regressed and blended into the Fawkes model.

References

Chen X. *Carbon Dioxide Thermodynamics, Kinetics, and Mass Transfer in Aqueous Piperazine Derivatives and Other Amines.* The University of Texas at Austin. Ph.D. Dissertation. 2011.

Hilliard MD. *A Predictive Thermodynamic Model for an Aqueous Blend of Potassium Carbonate, Piperazine, and Monoethanolamine for Carbon Dioxide Capture from Flue Gas.* The University of Texas at Austin. Ph.D. Dissertation. 2008.

Rochelle GT et al. "CO_2 Capture by Aqueous Absorption, Second Quarterly Progress Report 2011." Luminant Carbon Management Program. The University of Texas at Austin. 2011.

First-Principles Dynamic Model for a Flash Tank

Quarterly Report for January 1 – March 31, 2012

by Matthew Walters

Supported by the Luminant Carbon Management Program

Department of Chemical Engineering
The University of Texas at Austin

April 30, 2012

Abstract

A set of dynamic model equations has been developed for a flash tank, which represents the high pressure flash at the PRC pilot plant. Seven dynamic variables have been identified as defining the state of the flash tank system: total liquid molar hold-up, total vapor molar hold-up, mole fraction of CO_2 in the semi-rich liquid, mole fraction of PZ in the semi-rich liquid, mole fraction of CO_2 in the overhead vapor, temperature of the liquid hold-up, and temperature of the vapor hold-up. Additionally, this system has seven input variables associated with the material and energy streams: molar flow rate of the rich liquid feed, vapor overhead, and semi-rich liquid, mole fraction of CO_2 and PZ in the rich liquid feed, feed temperature, and heat duty. This seven input, seven output system will be used for modeling and control of a flash tank.

Introduction

The development of an accurate model is important for understanding system dynamics and synthesizing process control strategies. Model predictive control, which is widely used in the chemical and petroleum industries, requires a model that can adequately predict the behavior of the system so future control moves can be predicted. While there are several literature examples of dynamic stripper models for solvent regeneration in amine scrubbing, there has been little work done on dynamic modeling of a 2-stage flash configuration (Rochelle et al., 2012). The model developed here is for a single flash tank, which will represent the high pressure flash at the PRC pilot plant.

Dynamic Model Development for a Flash Tank

A first principles model for a single flash tank was developed for the rate-based, ternary system of piperazine (PZ), CO_2, and H_2O shown in Figure 1. Several assumptions were made in formulating the model equations:

- Ideal gas law is valid in the vapor phase.
- Raoult's law is valid (ideal liquid) for H_2O.
- Each phase is well mixed with a unique composition and temperature.
- Temperature is high enough that reaction equilibrium is attained.
- A liquid stream enters the tank, and heat is applied to the entire liquid inventory.
- Vapor fraction entering the tank is 0.

- PZ is non-volatile.
- A unique pressure is defined for the tank (mechanical equilibrium).
- Material and energy is exchanged through a gas-liquid interface according to a rate-based mechanism.

The model developed here draws ideas from the model of a packed stripper with MEA, CO_2, and H_2O by Ziaii (2009) and the model of a single-stage flash with cyclohexane and heptane by Lextrait (2003).

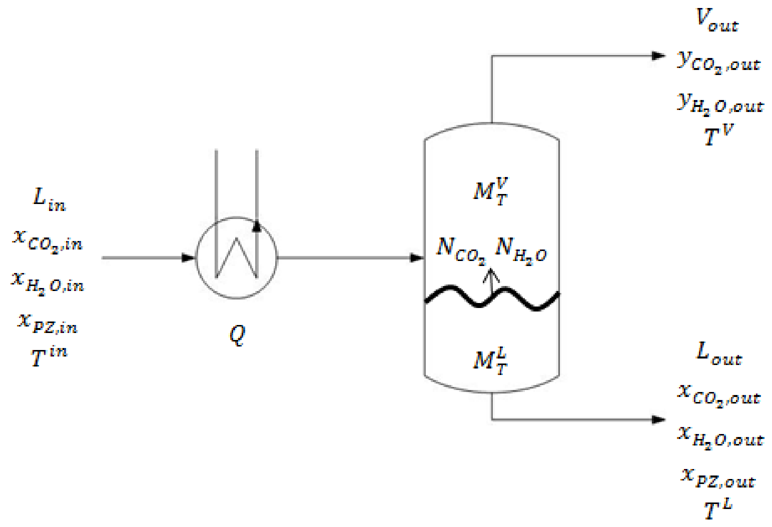

Figure 1: Flowsheet for flash tank model

Material Balances and Related Equations

In the liquid phase, molar balances for total moles, CO_2, H_2O, and PZ are given by Equations 1–4. Only three of these four equations are independent, so Equation 3 will be excluded from the model. The most convenient representation includes a total molar balance, and since loading is given in terms of PZ and CO_2 mole fractions, Equation 3 seems to be the best choice to eliminate.

$$\frac{dM_T^L}{dt} = L_{out} - L_{in} + a\left(N_{CO_2} + N_{H_2O}\right) \tag{1}$$

$$\frac{dM_{CO_2}^L}{dt} = L_{out}x_{CO_2,out} - L_{in}x_{CO_2,in} + aN_{CO_2} \tag{2}$$

$$\frac{dM_{H_2O}^L}{dt} = L_{out}x_{H_2O,out} - L_{in}x_{H_2O,in} + aN_{H_2O} \tag{3}$$

$$\frac{dM_{PZ}^L}{dt} = L_{out}x_{PZ,out} - L_{in}x_{PZ,in} \tag{4}$$

A similar set of equations can be written for the vapor phase (Equations 5–7). Again, since one of the equations is not independent, the molar balance on water is excluded (Equation 7).

$$\frac{dM_T^V}{dt} = V_{out} - a\left(N_{CO_2} + N_{H_2O}\right) \tag{5}$$

$$\frac{dM_{CO_2}^V}{dt} = V_{out}y_{CO_2,out} - aN_{CO_2} \tag{6}$$

$$\frac{dM^V_{H_2O}}{dt} = V_{out}y_{H_2O,out} - aN_{H_2O} \tag{7}$$

The molar hold-ups (M) are defined in the liquid phase by Equations 8–11 and in the vapor phase by Equations 12–14.

$$0 = M^L_T - M^L_{CO_2} - M^L_{H_2O} - M^L_{PZ} \tag{8}$$

$$0 = M^L_{CO_2} - x_{CO_2,out}M^L_T \tag{9}$$

$$0 = M^L_{H_2O} - x_{H_2O,out}M^L_T \tag{10}$$

$$0 = M^L_{PZ} - x_{PZ,out}M^L_T \tag{11}$$

$$0 = M^V_T - M^V_{CO_2} - M^V_{H_2O} \tag{12}$$

$$0 = M^V_{CO_2} - y_{CO_2,out}M^V_T \tag{13}$$

$$0 = M^V_{H_2O} - y_{H_2O,out}M^V_T \tag{14}$$

The liquid film controlled flux of CO_2 from the liquid phase to the vapor phase is driven by a difference between the equilibrium partial pressure and the partial pressure in the bulk gas (Equation 15). A similar equation can be written for the flux of water (Equation 16).

$$0 = N_{CO_2} - k^L_{CO_2}\left(P^*_{CO_2} - P^b_{CO_2}\right) \tag{15}$$

$$0 = N_{H_2O} - k^L_{H_2O}\left(P^*_{H_2O} - P^b_{H_2O}\right) \tag{16}$$

It is important that Equations 15 and 16 are not independent according to film theory. Equation 17 is written using film theory assuming both convective and diffusive flow, and can be solved to give Equation 18, where the gas film mass transfer coefficient, k^v, is defined as $D\rho^v/\delta$. However, since there are other factors driving mass transfer other than a partial pressure gradient such as boiling, it is possible that the mass transfer coefficient parameters in Equations 15–16 can be adjusted in a way that makes the equations independent, and film theory is not strictly true for the system being considered. Therefore, Equations 17–18 are not included in this model.

$$N_{CO_2} = -D\rho^v\frac{dy_{CO_2}}{dz} + y_{CO_2}\left(N_{CO_2} + N_{H_2O}\right) \tag{17}$$

$$N_{CO_2} + N_{H_2O} = k^v \ln\left[\frac{\frac{N_{CO_2}}{N_{CO_2}+N_{H_2O}} - y_{CO_2}}{\frac{N_{CO_2}}{N_{CO_2}+N_{H_2O}} - y^*_{CO_2}}\right] \tag{18}$$

The equilibrium partial pressure of CO_2 is given by an equation developed in-house (Xu, 2011) which depends on loading and temperature (Equation 19).

$$0 = \ln\left(P^*_{CO_2}\right) - 35.3 + 11054\frac{1}{T^l} + 18.9\left(\alpha_{out}\right)^2 - 4958\frac{\alpha_{out}}{T^l} - 10163\frac{\left(\alpha_{out}\right)^2}{T^l} \tag{19}$$

The loading in Equation 19 is defined by Equation 20.

$$\alpha_{out} = \frac{x_{CO_2,out}}{2x_{PZ,out}} \tag{20}$$

The equilibrium partial pressure of H_2O is found by first determining the vapor pressure of water using a correlation found in the DIPPR database (Equation 21) and then applying Raoult's Law assuming the solution is an ideal liquid (Equation 22)

$$0 = \ln\left(P^{vap}_{H_2O}\right) - 73.649 + \frac{7.2582 * 10^3}{T^L} + 7.3037\ln\left(T^L\right) - 4.1653 * 10^{-6}\left(T^L\right)^2 \tag{21}$$

$$0 = P^*_{H_2O} - P^{vap}_{H_2O}\, x_{H_2O,out} \tag{22}$$

The ideal gas law is assumed to be valid in the vapor phase (Equation 23) and a total volume balance is performed (Equation 24).

$$0 = Pv^V - M^V_T R T^V \tag{23}$$

$$0 = v - v^V - \frac{M^L_T}{\rho^L} \tag{24}$$

The partial pressures in the bulk gas are defined by Equations 25–26.

$$0 = P^b_{CO_2} - y_{CO_2,out} P \tag{25}$$

$$0 = P^b_{H_2O} - y_{H_2O,out} P \tag{26}$$

Energy Balances

An energy balance can be written for both the liquid and vapor phases in the flash tank (Equation 27–28).

$$\frac{dE^L}{dt} = L_{out} H^L_{out} - L_{in} H^L_{in} + a\left(N_{CO_2} H^L_{CO_2} + N_{H_2O} H^L_{H_2O} + h^V\left(T^L - T^V\right)\right) - Q \tag{27}$$

$$\frac{dE^V}{dt} = V_{out} H^V_{out} - a\left(N_{CO_2} H^V_{CO_2} + N_{H_2O} H^V_{H_2O} + h^V\left(T^L - T^V\right)\right) \tag{28}$$

Energy hold-ups (E) in the liquid and vapor are defined by Equations 29–30.

$$0 = E^L - H^L_{out} M^L_T \tag{29}$$

$$0 = E^V - H^V_{out} M^V_T \tag{30}$$

The enthalpy of the liquid relative to a reference state can be calculated for both the inlet and outlet liquid streams using Equations 31–32. Note that the ideal gas heats of formation, heat capacities, and enthalpies of vaporization are available in the DIPPR database.

$$0 = H^L_{in} - x_{CO_2,in}\left(H^{ig}_{CO_2}\left(T^{ref}\right) + \int_{T^{ref}}^{T^{in}} Cp^V_{CO_2}\, dT - \Delta H_{vap,CO_2}\left(T^{in}\right)\right) - x_{PZ,in}\left(H^{ig}_{PZ}\left(T^{ref}\right) + \int_{T^{ref}}^{T^{in}} Cp^V_{PZ}\, dT - \Delta H_{vap,PZ}\left(T^{in}\right)\right) - \left(1 - x_{CO_2,in} - x_{PZ,in}\right)\left(H^{ig}_{H_2O}\left(T^{ref}\right) + \int_{T^{ref}}^{T^{in}} Cp^V_{H_2O}\, dT - \Delta H_{vap,H_2O}\left(T^{in}\right)\right) \tag{31}$$

$$0 = H_{out}^{L} - x_{CO_2,out}\left(H_{CO_2}^{ig}(T^{ref}) + \int_{T^{ref}}^{T^L} Cp_{CO_2}^{V}\,dT - \Delta H_{vap,CO_2}(T^L)\right) - x_{PZ,out}\left(H_{PZ}^{ig}(T^{ref}) + \int_{T^{ref}}^{T^L} Cp_{PZ}^{V}\,dT - \Delta H_{vap,PZ}(T^L)\right) - (1 - x_{CO_2,out} - x_{PZ,out})\left(H_{H_2O}^{ig}(T^{ref}) + \int_{T^{ref}}^{T^L} Cp_{H_2O}^{V}\,dT - \Delta H_{vap,H_2O}(T^L)\right) \tag{32}$$

The enthalpy of the vapor outlet is similarly determined using Equation 33.

$$0 = H_{out}^{V} - y_{CO_2,out}\left(H_{CO_2}^{ig}(T^{ref}) + \int_{T^{ref}}^{T^V} Cp_{CO_2}^{V}\,dT\right) - (1 - y_{CO_2,out})\left(H_{H_2O}^{ig}(T^{ref}) + \int_{T^{ref}}^{T^V} Cp_{H_2O}^{V}\,dT\right) \tag{33}$$

Enthalpy is transferred as a result of molar flux of CO_2 and H_2O from the liquid phase to the vapor phase. The partial enthalpy of each component due to material flux is given by Equations 34–37. The heat of absorption is included in the liquid side partial enthalpy since the heat from the steam heater is being applied to the liquid phase.

$$0 = H_{CO_2}^{L} - (H_{CO_2}^{ig}(T^{ref}) + \int_{T^{ref}}^{T^L} Cp_{CO_2}^{V}\,dT - \Delta H_{vap,CO_2}(T^L)) + \Delta H_{abs,CO_2}(T^L) \tag{34}$$

$$0 = H_{CO_2}^{V} - (H_{CO_2}^{ig}(T^{ref}) + \int_{T^{ref}}^{T^L} Cp_{CO_2}^{V}\,dT) \tag{35}$$

$$0 = H_{H_2O}^{L} - (H_{H_2O}^{ig}(T^{ref}) + \int_{T^{ref}}^{T^L} Cp_{H_2O}^{V}\,dT - \Delta H_{vap,H_2O}(T^L)) - \Delta H_{vap,H_2O}(T^L) \tag{36}$$

$$0 = H_{H_2O}^{V} - (H_{H_2O}^{ig}(T^{ref}) + \int_{T^{ref}}^{T^L} Cp_{H_2O}^{V}\,dT) \tag{37}$$

Final Set of Dynamic Equations

Seven differential equations and twenty-six algebraic equations have been formulated to represent a single-stage heated flash with a ternary system. This set of equations contains seven inputs which arise from the heat and material streams physically connected to the system [L_{in}, L_{out}, V_{out}, $x_{CO_2,in}$, $x_{PZ,in}$, T^{in}, Q], seven dynamic material and energy hold-up variables [M_T^L, $M_{CO_2}^L$, M_{PZ}^L, M_T^V, $M_{CO_2}^V$, E^L, E^V], twenty-sex algebraic variables [L_{out}, V_{out}, $x_{CO_2,out}$, $x_{PZ,out}$, $y_{CO_2,out}$, $M_{H_2O}^L$, $M_{H_2O}^V$, N_{CO_2}, N_{H_2O}, v^V, P, $P_{CO_2}^{*}$, $P_{H_2O}^{*}$, $P_{CO_2}^{b}$, $P_{H_2O}^{b}$, $P_{H_2O}^{vap}$, α_{out}, H_{in}^L, H_{out}^L, H_{out}^V, $H_{CO_2}^L$, $H_{H_2O}^L$, $H_{CO_2}^V$, $H_{H_2O}^V$, T^L, T^V], and 15 parameters, some of which may be a known function of temperature [a, $k_{CO_2}^L$, $k_{H_2O}^L$, R, ρ^L, h^V, $H_{CO_2}^{ig}$, $Cp_{CO_2}^V$, $\Delta H_{vap,CO_2}$, H_{PZ}^{ig}, Cp_{PZ}^V, $\Delta H_{vap,PZ}$, $H_{H_2O}^{ig}$, $Cp_{H_2O}^V$, $\Delta H_{vap,H_2O}$].

Through tedious manipulation, this large set of differential and algebraic equations can be reduced to seven first-order, highly nonlinear differential equations (Equations 38–44) with the dynamic variables: [M_T^L, $x_{CO_2,out}$, $x_{PZ,out}$, M_T^V, $y_{CO_2,out}$, T^L, T^V]. For brevity, some algebraic variables were left in the differential equation in this report, but it is clearly seen that substitutions can be made to eliminate all of the algebraic variables. The algebraic variables that remain are: molar fluxes (given explicitly in Equations 45–46), enthalpy relations (previously defined in Equations 31–37), and a new variable **f** (Equations 47–48).

$$\frac{dM_T^L}{dt} = L_{out} - L_{in} + a\left(N_{CO_2} + N_{H_2O}\right) \tag{38}$$

$$\frac{dx_{CO_2,out}}{dt} = \frac{L_{in}}{M_T^L}\left(x_{CO_2,out} - x_{CO_2,in}\right) + \frac{a\left(1 - x_{CO_2,out}\right)N_{CO_2}}{M_T^L} - \frac{a x_{CO_2,out} N_{H_2O}}{M_T^L} \tag{39}$$

$$\frac{dx_{PZ,out}}{dt} = \frac{L_{in}}{M_T^L}\left(x_{PZ,out} - x_{PZ,in}\right) - \frac{a x_{PZ,out}}{M_T^L}\left(N_{CO_2} + N_{H_2O}\right) \tag{40}$$

$$\frac{dM_T^V}{dt} - V_{out} - a\left(N_{CO_2} + N_{H_2O}\right) \tag{41}$$

$$\frac{dy_{CO_2,out}}{dt} = \frac{\left(y_{CO_2,out} - 1\right) a N_{CO_2}}{M_T^V} + \frac{y_{CO_2,out}\, a N_{H_2O}}{M_T^V} \tag{42}$$

$$\frac{dT^L}{dt} = \frac{L_{in}}{M_T^L f^L}\left(\bar{H}_{out}^L - \bar{H}_{in}^L\right) + \frac{a}{M_T^L f^L}\left(N_{CO_2}\left(\bar{H}_{CO_2}^L - \bar{H}_{out}^L\right) + N_{H_2O}\left(\bar{H}_{H_2O}^L - \bar{H}_{out}^L\right) + h^V\left(T^L - T^V\right)\right) - \frac{Q}{M_T^L f^L} \tag{43}$$

$$\frac{dT^V}{dt} = \frac{a}{M_T^V f^V}\left(N_{CO_2}\left(\bar{H}_{out}^V - \bar{H}_{CO_2}^V\right) + N_{H_2O}\left(\bar{H}_{out}^V - \bar{H}_{H_2O}^V\right) - h^V\left(T^L - T^V\right)\right) \tag{44}$$

$$N_{CO_2} = k_{CO_2}^L\left(e^{35.3 - 11054\frac{1}{T^L} - 18.9\left(\frac{x_{CO_2,out}}{2x_{PZ,out}}\right)^2 + 4958\frac{\frac{x_{CO_2,out}}{2x_{PZ,out}}}{T^L} + 10163\frac{\left(\frac{x_{CO_2,out}}{2x_{PZ,out}}\right)^2}{T^L}} - \frac{y_{CO_2,out} M_T^V R T^V}{v - \frac{M_T^L}{\rho^L}}\right) \tag{45}$$

$$N_{H_2O} = k_{H_2O}^L\left(x_{H_2O,out}\, e^{73.649 - \frac{7.2582 \times 10^3}{T^L} - 7.3037\ln\left(T^L\right) + 4.1653 \times 10^{-6}\left(T^L\right)^2} - \frac{y_{H_2O,out} M_T^V R T^V}{v - \frac{M_T^L}{\rho^L}}\right) \tag{46}$$

$$f^L = x_{CO_2,out}\left(Cp_{CO_2}^V - \frac{\partial \Delta \bar{H}_{vap,CO_2}}{\partial T^L}\right) + x_{PZ,out}\left(Cp_{PZ}^V - \frac{\partial \Delta \bar{H}_{vap,PZ}}{\partial T^L}\right) + \left(1 - x_{CO_2,out} - x_{PZ,out}\right)\left(Cp_{H_2O}^V - \frac{\partial \Delta \bar{H}_{vap,H_2O}}{\partial T^L}\right) \tag{47}$$

$$f^V = y_{CO_2,out} Cp_{CO_2}^V + \left(1 - y_{CO_2,out}\right) Cp_{H_2O}^V \tag{48}$$

Conclusions

- The state of a single-stage flash of a ternary mixture is determined by seven dynamic variables: liquid and vapor molar hold-ups, liquid mole fractions of CO_2 and PZ, vapor mole fraction of CO_2, and temperature of the liquid and vapor.
- The inputs to the system are molar flows of the liquid in, liquid out, and vapor out, composition and temperature of the feed, and heat duty.

- The first principles model describing the flash system is highly nonlinear, even with some simplifying assumptions.

Future Work

1. Determine the unknown model parameters using steady state pilot plant data.
2. Validate the model with dynamic pilot plant data.
3. Linearize the model to put it into a standard state-space form.
4. Apply model predictive control using the linearized form.

Notation

a	surface area at vapor-liquid interface (m^2)
C_p	specific heat capacity (kJ/(mol*K))
D	diffusion coefficient (m^2/s)
E	energy hold-up (kJ)
$\hat{H}$	specific enthalpy (kJ/mol)
$\bar{H}$	partial specific enthalpy (kJ/mol)
$\Delta\hat{H}$	specific enthalpy of phase change (kJ/mol)
h	convective heat transfer coefficient (kJ/(m^2*K))
k	mass transfer coefficient (mol/(m^2*s*bar))
L	liquid molar flow rate (mol/s)
M	molar hold-up (mol)
N	molar flux from liquid phase to vapor phase (mol/(m^2*s))
P	pressure (bar)
P_j	partial pressure of component j (bar)
Q	heat from steam heater (kJ)
T	temperature (°C)
t	time (s)
V	vapor molar flow rate (mol/s)
v	volume (m^3)
x_j	liquid mole fraction of component j
y_j	vapor mole fraction of component j
z	height of flash tank (m)

Greek

α	loading (mol CO_2/mol alkalinity)
ρ	molar density (mol/m^3)

Subscripts

abs	absorption
ig	ideal gas
In	inlet stream
Out	outlet stream
Vap	vaporization

Superscripts

b	bulk fluid
L	liquid phase

Electric Grid-Level Implications
of Flexible CO_2 Capture Operation

Quarterly Report for January 1 – March 31, 2012

by Stuart Cohen

Supported by the EPA STAR Fellowship Program and the
Luminant Carbon Management Program

Department of Chemical Engineering
The University of Texas at Austin

April 30, 2012

Abstract

Flexible post-combustion absorption/stripping that vents carbon dioxide (CO_2) or stores rich solvent at partial or zero load could add value to facilities with CO_2 capture by providing a facility with opportunities to perform electricity price arbitrage or provide grid reliability services (ancillary services, or AS). Work has continued this quarter on both the grid-level electricity dispatch model discussed in the Rochelle Group 3rd and 4th quarterly reports of 2011 and the single plant profit maximization model used in earlier work. The least-cost dispatch model uses performance parameters for each generation facility, electricity demand, wind-based electricity production, and AS requirements to determine the power plant operation that minimizes total dispatch costs. It is intended to determine whether flexible CO_2 capture increases AS revenues and improves grid reliability. The single plant model maximizes operating profits at a single facility with CO_2 capture in response to input electricity prices.

The following are key conclusions and accomplishments from this quarter.

- The grid-level least-cost dispatch model has been successfully tested with unit-specific data and demonstrates reasonable computation time under tested input conditions.
- A detailed description and scenario results from a single plant profit maximization model has been published in the *International Journal of Greenhouse Gas Control* under the title “Optimizing post-combustion CO_2 capture in response to volatile electricity prices.”
- A new procedure has been developed to adjust historical electricity prices for changes in market prices of fuel (coal, natural gas) and CO_2. This procedure will supply input data to the single plant profit maximization model.
- Adjusting electricity prices for CO_2 prices by adding the average CO_2 emissions cost of gas-fired facilities provides conservative estimates of any electricity price increase.
- Coal-based capacity will often supply marginal generation when gas prices are low, CO_2 prices are moderate, and net electricity demand (demand, or load, minus wind production) exceeds 40 gigawatts.

Introduction to Flexible CO_2 Capture

Flexible operation of a post-combustion amine absorption and stripping system entails varying the liquid and vapor flow rates in the stripping and/or absorption systems in order to choose the most economical CO_2 capture operating point for current electricity market conditions. During partial- or zero-load CO_2 capture, some or all of the steam being used for solvent regeneration is redirected back to the low pressure turbine in the power cycle to increase electrical output. The resulting decrease in CO_2 flow exiting the stripper also reduces energy requirements for CO_2 compression. Solvent flow to the absorber and stripper and flue gas flow to the absorber could also be modulated for efficient system operation.

Flexible CO_2 capture could allow the plant operator to increase power output when electricity prices are high if additional electricity sales offset any increase in CO_2 emissions costs under a CO_2 regulatory framework (Ziaii et al., 2008; Cohen et al. 2010a). In addition, operating CO_2 capture at zero load during annual peak electricity demand can eliminate the need to spend billions of dollars to replace generation capacity lost when CO_2 capture operates at full load (Cohen et al., 2010b). If the load on energy-intensive CO_2 capture components can be reduced quickly, CO_2 capture energy requirements could be offered as reserve capacity in ancillary service (AS) markets for grid reliability services. AS markets can be quite lucrative, and the demand for AS might grow with greater penetration of intermittent renewable electricity sources such as wind (Chalmers et al., 2009). At the grid level, flexible CO_2 capture provides another method to control power output and respond to expected or unexpected changes in electricity supply and demand.

There are two basic concepts for flexible CO_2 capture using amine scrubbing. One reduces the energy requirements of solvent stripping and CO_2 compression while allowing the CO_2 removal rate to fall. Figure 1 displays one way to implement such a configuration, where steam and rich solvent flow rates to the stripper are reduced equally and simultaneously during partial- or zero-load operation (Ziaii et al., 2008). At partial load, rich solvent diverted from the stripper is recycled to the absorber, so CO_2 removal rates in the absorber will decrease as solvent becomes saturated with CO_2. Zero load could involve recirculating all solvent through the absorber, or the CO_2 capture system could be bypassed completely. Assuming a retrofit application where the low pressure turbine and generator has been sized to operate without CO_2 capture, this design has negligible capital cost, but its primary disadvantage is any cost and environmental impact of increased CO_2 emissions.

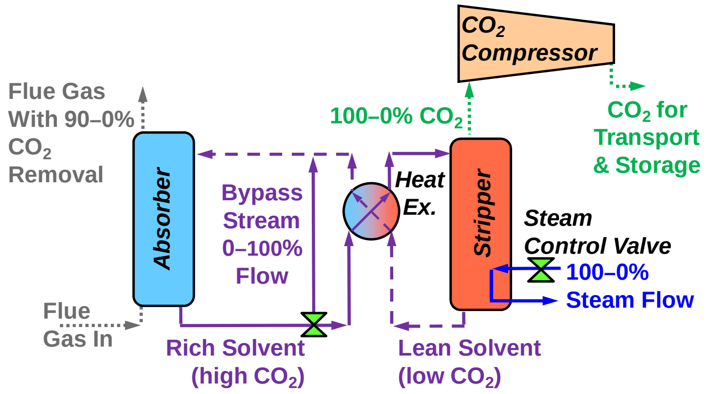

Figure 1: Simultaneously reducing steam and rich solvent flow to the stripper allows increased output but at the expense of additional CO_2 emissions.

Another flexible CO_2 capture concept uses auxiliary solvent storage tanks to maintain high CO_2 removal when stripping and compression systems operate at partial or zero load (Figure 2) (Chalmers and Gibbins, 2007; Rochelle et al., 2009). When electricity prices are high, the plant can reduce stripper and compressor load while maintaining full-load CO_2 absorption by feeding the absorber from a lean solvent storage tank and depositing rich solvent into another tank. When electricity prices are low, stripping and compression systems return to a higher load to treat the current process stream and the stored rich solvent. To treat both the current stream and stored solvent, stripping and compression systems must be larger and require more total energy than a CO_2 capture system without solvent storage. Maintaining high CO_2 removal keeps operating costs down while storing rich solvent, but any operating profit improvement must be weighed against the capital cost of solvent inventory, storage tanks, and larger stripping and compression equipment. A facility with solvent storage would likely also maintain the ability to vent CO_2 when economically desirable or necessary for maintenance.

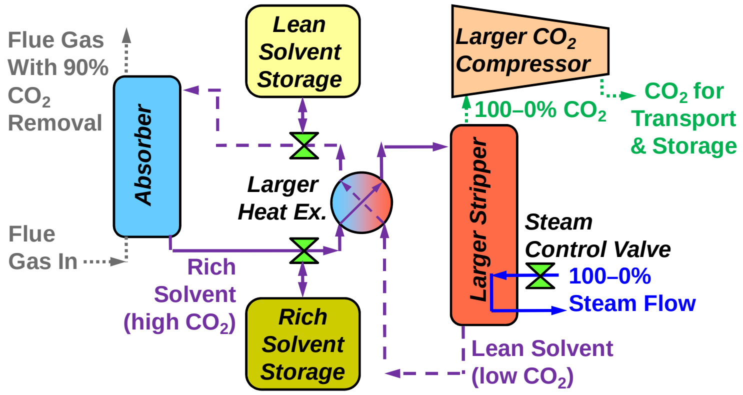

Figure 2: Including solvent storage incurs significant capital costs but allows continued high CO_2 removal at partial and zero load.

Grid-Level Least-Cost Dispatch Model

The grid-level least-cost dispatch model described in the 2011 3rd and 4th quarterly reports has undergone continued development and testing this quarter (Rochelle et al., 2011; 2012). Since the last quarter, a generating unit-specific input database has been readied, and the model has undergone testing with the unit-specific database under sample electricity system input conditions. This report will repeat a brief summary of model characteristics before discussing new activities in greater detail.

Description of the ERCOT Market

ERCOT comprises ~550 generating units across ~200 power generation facilities that supply 85% of electricity demand in Texas (ERCOT, 2010a; USEPA, 2010). Its total installed capacity at the end of 2010 was 84.2 gigawatts (GW) with an available capacity of 75.8 GW after derating the 9.3 GW of wind capacity for its average availability (ERCOT, 2010a).

ERCOT operates markets for electricity to meet consumer demand as well as ancillary services to ensure grid reliability. Based on electricity and ancillary service offers submitted to ERCOT, forecasted electricity demand, and ERCOT AS requirements, ERCOT co-optimizes electricity supply and ancillary service procurements for each hour in a day-ahead market. The day-ahead market determines which units will be online (committed) in each hour, then the real-time market determines electricity prices every 15 minutes by averaging shadow prices for electricity over each three successive 5-minute intervals.

There are four ancillary service markets in ERCOT. Regulation Up (RU) and Regulation Down (RD) services are procured to respond within 5 minutes to discrepancies between expected and actual load (ERCOT, 2011a). The RU and RD requirement varies by hour and month depending on current load uncertainty, historical Regulation deployments, and installed wind capacity (ERCOT, 2011a). Responsive Reserve Service (RRS), commonly called spinning reserves, must be supplied by online units capable of responding within 10 minutes (ERCOT, 2011a). Total RRS procurements must be able to alleviate the largest single outage possible within ERCOT, currently 2300 megawatts (MW), the maximum output of the South Texas Project nuclear facility (ERCOT, 2011a). Up to half the RRS requirement can be met by interruptible load facilities that are contracted to reduce demand if necessary to maintain grid reliability (ERCOT, 2011a). Non-Spinning Reserve Service (NSRS) can be provided by online or offline units as well as interruptible load and must be able to respond within 30 minutes. The quantity of NSRS required in each hour depends on the Regulation Up procurement and net load uncertainty (ERCOT, 2011a).

Model Description and Formulation

The model is implemented as a mixed-integer linear program created using GAMS software. It employs a two-stage optimization procedure for each day to mimic ERCOT operating procedures. A day-ahead optimization minimizes the cost of meeting electricity demand and AS requirements in each hour, and the optimal solution determines the commitment status (online or offline) of each facility as well as ancillary service procurements. Commitment status and AS procurements are fixed, and electrical output in 15-minute intervals is determined in a real-time market optimization. If the grid is assumed to contain energy storage systems, the quantity of stored energy in each time period is also determined by the real-time optimization. The solution from the current day informs initial conditions for the following day, and the process repeats for the desired number of days.

The model does not perform AS deployments, which are executed within ERCOT in response to discrepancies between planned and actual electricity demand, wind generation, and unplanned transmission and generation outages. Modeling the manner in which AS are deployed is outside the scope of this work. Instead, the model assesses a large cost penalty to any imbalances between electricity supply and demand, and the existence of these penalties indicates when AS deployments would likely be required.

The model can consider several power plant types: coal-fired, natural gas-fired combined-cycle (NGCC), open-cycle gas turbines (OCGT), gas-fired steam boilers (NGBLR), natural gas internal combustion (NGIC), oil-fired, nuclear, hydroelectric, wind, and biomass. Thermal generation facilities can also be designated as combined heat and power (CHP) facilities. CHP facilities are typically designed to meet near-constant heat loads, so these systems are assumed to operate continuously at their maximum output regardless of operating costs. Interruptible load systems are also included in the model but are allowed only to provide RRS and NSRS. Energy storage systems can also be modeled along with inflexible and flexible CO_2 capture facilities at coal-fired power plants.

Objective Function

The objective function sums operating costs over all plants and time periods in the day being optimized. Power plant operating costs include startup costs, shutdown costs, and operating costs not attributed to fuel or CO_2 emissions. All fossil-fueled facilities have fuel costs as well as CO_2 emissions costs that are assessed if a CO_2 price is assumed to exist due to an emissions reduction policy. There are no direct costs assessed for AS procurements, though there are indirect costs if an AS procurement requires more expensive facilities to be used for electricity supply.

For facilities with CO_2 capture, additional costs are assessed for the following: solvent makeup to offset degradation and volatility losses, caustic sodium hydroxide (NaOH) for thermal solvent reclaiming, reclaimer waste disposal, additional water use for CO_2 capture, CO_2 transport and storage, and ramping the capture system components up and down. CO_2 capture ramping costs are a proxy for costs associated with efficiency losses during transient CO_2 capture operation.

The model also assesses cost penalties for any electricity supply-demand imbalance using the same penalties as ERCOT. The real-time market penalty for oversupply is $250 per megawatt-hour (MWh), and the penalty for undersupply increases with the supply deficiency until reaching the market maximum electricity price of $3,000/MWh above 50 MW undersupply (ERCOT, 2010b).

Constraints

Constraints have not changed since the formulation discussed last quarter (Rochelle et al., 2012). Table 1 lists the constraint types included in the model formulation and the systems to which they apply.

Table 1: The model contains the following constraints on the systems indicated.

Constraint type	Systems applicable
Minimum and maximum load	Power output, absorber, stripper, power input (storage)
Ramp rate	Power output, absorber, stripper, power input (storage)
Minimum time online after startup and offline after shutdown	Power output, absorber, stripper, power input (storage)
Combined energy and AS must be within output limits	Power output
AS offer limitations by ramp rate and capacity fraction	Power output, absorber, stripper, power input (storage)
Maximum storage capacity	Energy storage, CO_2 capture solvent storage
Stored energy flow balance	Energy storage
CO_2 flow balance	Solvent storage
Electricity supply-demand balance	Electric grid
AS requirements	Electric grid
Limit on RRS provided by interruptible load	Electric grid

Unit-Specific Database Creation

To examine flexible CO_2 capture under realistic electricity system conditions, the model will be used with each generating unit in ERCOT represented individually. Doing so requires an input database containing performance specifications for each generating unit. The 2011 4th Quarterly Report described progress creating this database, which uses information supplied by ERCOT representatives and the U.S. Environmental Protection Agency (EPA) eGRID database (Rochelle et al., 2012; ERCOT, 2011b; USEPA, 2010).

The ERCOT database includes a list of available generating units in 2010 along with their maximum capacities (ERCOT, 2011b). Unit-specific performance parameters are proprietary, so the ERCOT database provides representative quantities for each unit type that are used to assign minimum capacity fraction, minimum up/down time, startup cost, and non-fuel/CO_2 variable operation and maintenance (VOM) cost (ERCOT, 2011b). These data are publicly available as part of a contract between ERCOT and the U.S. Department of Energy. Initially, ERCOT-provided ramp rates for each unit type will also be used. However, because these quantities are conservative relative to ramp rates quoted in other sources, the sensitivity of results to ramp rate specifications will be examined to assess how the value of capture flexibility might change with the flexibility of other power generation facilities.

ERCOT also provides typical heat rates and CO_2 emissions rates for each unit type; however, greater performance differentiation is achieved using the eGRID database, which provides these quantities for each generating facility. Performance differentiation between facilities of the same type prevents large segments of generating capacity from abruptly switching in dispatch order when market conditions such as fuel prices are varied. Though eGRID contains plant-specific rather than unit-specific data, more realistic dispatch is achieved using eGRID heat rates and CO_2 emissions rates whenever possible. The most recent eGRID database contains 2007 data, so facilities installed between 2007 and 2010 are assigned ERCOT unit-specific parameters as an approximation. Multi-unit facilities where all units are the same type use eGRID parameters when possible. For facilities that appear in both databases but have multiple unit types, eGRID parameters are used for units where the generic unit-specific parameter is within 10% of the eGRID value, and generic unit-specific parameters are used for other units. For a multi-unit type facility where ERCOT and eGRID performance specifications are not within 10% for any units, only ERCOT unit type-specific parameters are used.

Wind generation is subtracted from input electricity demand, so wind generating units are not included in the unit-specific database. As a result, the final database contains 311 generating units.

Testing with Unit-Specific Database

To ensure proper model functionality and reasonable computation time with the unit-specific database, the model was tested without any CO_2 capture systems with a near-sinusoidal electricity demand curve for a two day period. Volatile wind production is not implemented in these input data. To include some temporal AS variability, regulation up and down requirements are adjusted from 500 MW by factors recommended in a General Electric wind integration study commissioned by ERCOT, where 10,000 MW wind capacity is assumed (ERCOT, 2011a). For testing purposes net load uncertainty, which is used to determine non-spinning reserve requirements, is randomized between 1,000 MW and 1,500 MW. Responsive reserve requirements are always 2,300 MW as specified by ERCOT.

The test case assumes a \$1.54 per million British thermal unit (MMBTU) coal price, a \$4/MMBTU natural gas price, and a \$35 per metric ton of CO_2 (tCO_2) emissions cost.

Figure 3 displays electrical output from each of the 311 units across the two day period. In repeated model runs under these conditions, computation time on a desktop PC[1] was on the order of 15 minutes, which is considered acceptable for purposes of future analysis. Runtime will likely be longer when flexible CO_2 capture, energy storage, and wind variability are included, but initial testing provides confidence that these scenarios will have reasonable computation times.

---

[1] HP Compaq 8200 Elite SFF PC with an Intel Core i5-2500 CPU at 3.30 GHz and 8 GB RAM

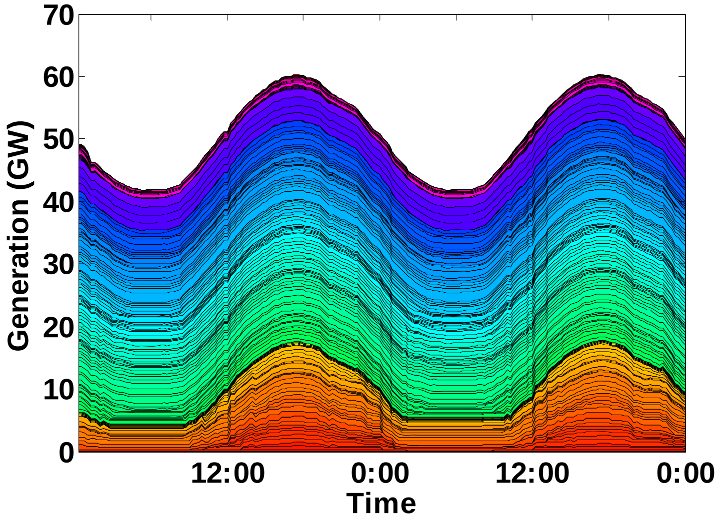

Figure 3: The model has been tested with unit-specific data (311 facilities, \$35/tCO$_2$, no CO$_2$ capture).

Unit-specific results offer limited opportunity for interpretation, so Figure 4 displays results when electrical output is aggregated by plant type. Nuclear facilities have low operating costs, so they operate continuously at base load. CHP facilities are required to operate continuously at maximum output, so NGCC and OCGT CHP facilities effectively provide base load and displace all other plant types. At \$35/tCO$_2$, a large portion of non-CHP NGCC capacity also displaces much of the coal-fired generation, especially with a relatively low \$4/MMBTU natural gas price. At times of higher electricity demand, coal-based and OCGT units are typically the marginal generating facilities.

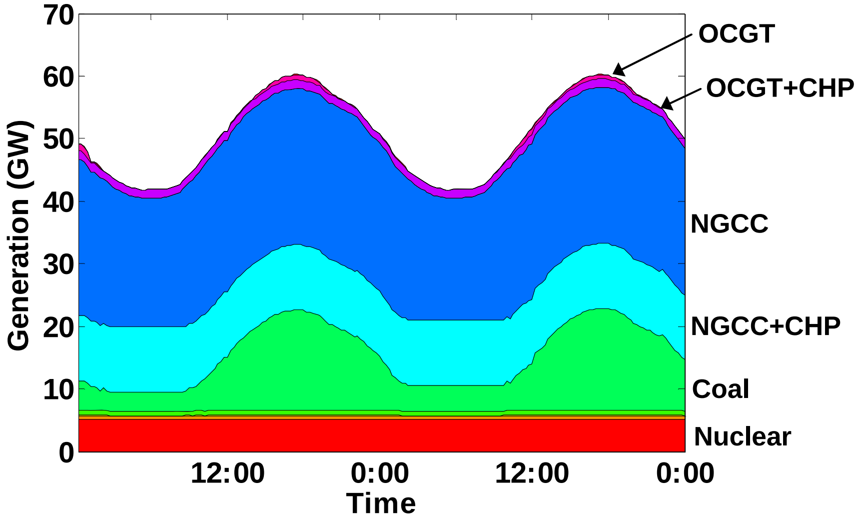

Figure 4: At \$35/tCO$_2$ and \$4/MMBTU natural gas, many NGCC units displace coal-based capacity.

Figure 5 displays model-calculated electricity prices in the real-time market along with a plot of net load. The model calculates electricity prices by determining the marginal cost of increasing demand in each time interval. Typically, electricity prices trend with demand because greater demand necessitates more expensive generating capacity. In this test case, there are also several price spikes during time periods when demand is increasing or decreasing. These price spikes occur because online units designated in the forward market have insufficient ramping capability to respond to demand changes in those intervals. The resulting imbalance in electricity supply and demand invokes a cost penalty, and the electricity price is determined by the ERCOT-specified relationship between the magnitude of this imbalance and the cost penalty. This behavior is expected to some degree and indicates the need to deploy AS in those intervals; however, observed price spikes are more frequent than is likely realistic. As a result, the frequency of price spikes will be monitored closely when examining the sensitivity to base plant ramp rates, and the forward market unit commitment optimization might be modified to help ensure enough units are online to meet ramping requirements.

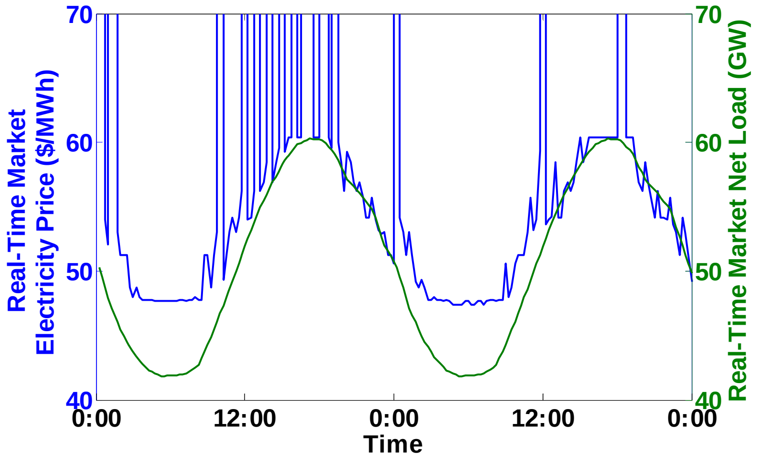

Figure 5: Electricity price results demonstrate the possibility for price spikes to occur due to inadequate ramping capability.

Single Plant Profit Maximization Model

This quarter, work continued on a previously developed model that maximizes profits at a single coal-fired facility with flexible CO_2 capture in response to input electricity prices. This model allows quantification of the value of flexible CO_2 capture in response to electricity prices with volatility that cannot be reproduced with the least-cost dispatch model described above. High electricity prices can occur due to several events such as transmission congestion, high demand during planned outages, and wind intermittency. Since these high prices offer excellent opportunities for flexible CO_2 capture systems to perform price arbitrage, the single plant profit maximization model provides additional insights into the value of flexible capture. A full description of the single plant profit maximization model and results from a CO_2 price path scenario analysis have recently been published in the *International Journal of Greenhouse Gas Control* and is attached to this report.

Assessing Value of Flexibility under Varying Market Conditions

In previous analysis using the single plant profit maximization model, the CO_2 price was the only independently varied electricity market condition. In this work, the impact of CO_2 price on electricity prices was approximated by uniformly increasing all electricity prices by the average CO_2 emissions cost of gas-fired facilities in ERCOT (Cohen et al., 2012). For example, the generation-weighted average CO_2 emissions rate for ERCOT gas-fired facilities in 2007 according to the EPA eGRID database is 0.43 tCO_2/MWh, so a CO_2 price of \$50/tCO_2 would raise electricity prices in each time interval by \$21.5/MWh (USEPA, 2010). This approximation is reasonable for ERCOT under moderate CO_2 prices and moderate to high natural gas prices because ERCOT is a gas-dominated market where gas-based capacity will typically be the marginal, or most expensive, generation. However, this approximation does not account for variability in the emissions costs of natural gas-based generators, and it breaks down further under market conditions where gas begins to replace coal as base load fuel, and coal-fired facilities serve more frequently as the marginal generator. With current natural gas prices below \$3/MMBTU, gas is already poised to largely displace coal as a base load fuel.

To confidently use the model to assess flexible CO_2 capture under a wider range of electricity market conditions or in other electricity systems, a more accurate method to approximate the effect of fuel and CO_2 prices on electricity prices is required. Such a method is described in the next section. Using this more rigorous procedure to adjust electricity prices for fuel and CO_2 prices allows the following research questions to be answered.

1. Under what combinations of coal, natural gas, and CO_2 price does flexible CO_2 capture have the most value?
2. What electricity price forecasting accuracy is required to derive significant value from a flexible CO_2 capture system?
3. What degree of electricity price volatility is necessary to derive significant value from a flexible CO_2 capture system?

Electricity Price Adjustment for Market Conditions

Changing fuel and CO_2 emissions prices will affect the relative dispatch order of generating facilities, so the characteristics of the power plant fleet must be considered when estimating the impact of changing market conditions on electricity prices. For instance, low natural gas prices and high CO_2 prices would increase the frequency with which coal-based facilities provide marginal generation, causing electricity prices to increase at roughly \$1/MWh per \$1/tCO_2 because coal-fired plants typically emit ~1 tCO_2/MWh. To account for the effect of fuel and CO_2 price changes on dispatch order while preserving historical electricity price volatility, the following procedure has been implemented in the MATLAB environment to adjust electricity prices for fuel and CO_2 prices. The steps are described in detail in the following sections.

1. Use a first-order electricity dispatch model to calculate electricity prices in each time interval under historical and adjusted fuel and CO_2 price conditions using historical electricity demand and power plant fleet characteristics.
2. Calculate the difference between first-order electricity prices under historical versus adjusted conditions for each time interval.
3. Add the calculated change in first-order prices to historical electricity prices in each time interval to produce an adjusted electricity price series that preserves historical volatility.

First-Order Electricity Price Calculation (Step 1)

The MATLAB program first imports a time series of net electricity load (demand, or load, minus wind production), generating unit characteristics, and time series of historical and adjusted fuel and CO_2 prices. Electricity demand data are retrieved from the ERCOT website in hourly intervals (ERCOT, 2012a). To enable calculated first-order electricity prices to be synchronized with historical electricity price data in 15-minute intervals, historical demand is up-sampled using a linear interpolation between each hourly demand data point. A spline or polynomial fit of the demand data could provide more accurate up-sampling results, but linear interpolation is assumed sufficient for a first-order calculation. The prices of coal, natural gas, oil, and CO_2 are imported for each day so that either constant or variable price data may be used. The first-order dispatch procedure does not account for detailed generating unit constraints such as minimum load, ramp rates, and minimum up/down time, so only the following characteristics are imported: unit name, unit type, maximum electrical output, heat rate, CO_2 emissions rate, base plant VOM costs, and whether or not the facility is designated for CHP.

After importing requisite data, the program iterates through each 15-minute time interval and calculates first-order electricity prices for each interval under historical and adjusted fuel and CO_2 price conditions. It does this by calculating marginal generating costs for each generating unit, placing units in cost order, choosing the least-expensive available capacity to meet current electricity demand, and setting the electricity price equal to the most expensive facility required to meet current demand. Costs at fossil-fueled and biomass-based facilities are the sum of fuel costs, base plant VOM costs, and CO_2 emissions costs, if applicable. Nuclear and hydroelectric facilities have assigned VOM costs, and wind facilities are not represented in the plant database because wind production is subtracted from the imported demand data. CHP facilities are forced to operate at their maximum capacity during dispatch calculations, which effectively displaces all other base load facilities. The MATLAB program also records information on which facility set electricity prices in each interval.

Creating Adjusted Electricity Prices with Volatility (Steps 2 and 3)

After determining first-order electricity prices for all time intervals under historical and adjusted fuel and CO_2 price conditions, the electricity price difference is taken at each time interval. This difference is then added to historical electricity prices in each interval that have been averaged across load zones[2] in the ERCOT grid. Historical electricity price data are retrieved from ERCOT archives of the market clearing prices of electricity to (generation) resources (MCPER) (ERCOT, 2012b). The resulting adjusted electricity price series preserve historical price volatility while approximating the effect of changes to fuel and CO_2 price.

Adjusted volatile electricity prices will be used to calculate profits for the facility represented in the single plant profit maximization model. However, optimizing plant operation in response to these prices implies perfect foreknowledge of price data for the duration of the study period. Perfect foreknowledge is unrealistic, so operation is instead optimized in response to a "pseudo-forecasted" electricity price series that approximates expected electricity prices given day-ahead forecasting ability. The "pseudo-forecasted" price series is calculated for each historical or adjusted volatile price series using a procedure discussed in earlier work where outlier prices are

---

[2] ERCOT switched to a nodal market on December 1, 2010, but historical price data used in this analysis are taken from before the nodal market switch.

first removed, and the outlier-free price series is smoothed until the resulting price series deviates from original prices by an amount typical of day-ahead forecasting models. This procedure is described in more detail in Cohen et al. (2012).

Sample Results

This section demonstrates the electricity price adjustment procedure for a sample set of input data. Historical electricity demand and prices from December 1, 2009 – November 30, 2010 are used as input (ERCOT, 2012a; ERCOT, 2012b). This date range represents the most recent available electricity price data before ERCOT switched from a zonal to a nodal market structure. Generating unit data are representative of the ERCOT electricity system in 2010 and are taken from the same unit-specific database described in the above sections on the least-cost dispatch model.

Though the model can utilize daily fuel and CO_2 price data, constant values are used are throughout the entire date range in this analysis. Table 2 lists historical annual average fuel and CO_2 prices in 2010 along with three sample adjusted price cases (USEIA, 2012). Adjustment 1 adds a \$50/tCO_2 emissions price, Adjustment 2 uses a \$25/tCO_2 price and reduces natural gas prices to \$3/MMBTU, and Adjustment 3 uses the historical natural gas price and a \$100/tCO_2 price.

Table 2: The following historical and adjusted fuel and CO_2 prices are used throughout the entire date range (USEIA, 2012).

Price set	*Coal price (\$/MMBTU)*	*Natural gas price (\$/MMBTU)*	*Oil price (\$/MMBTU)*	*CO_2 price (\$/tCO_2)*
Historical (2010)	2.25	5.14	12.34	0
Adjustment 1	2.25	5.14	12.34	50
Adjustment 2	2.25	3.00	12.34	25
Adjustment 3	2.25	5.14	12.34	100

Figure 6 plots electricity demand along with first-order electricity prices under historical and adjusted fuel and CO_2 price conditions for February 4 and 5, 2010, a moderate net load day. For the same dates, Figure 7 plots electricity demand with historical electricity prices and adjusted volatile electricity prices for each fuel and CO_2 price conditions. The ordinate axis range is larger for volatile price data so that all comparable figures (7, 9, and 11) can be plotted on the same scale. On Figure 6, a \$50/tCO_2 price increases electricity prices nearly uniformly by approximately \$30/tCO_2, which is greater than the \$21.5/MWh increase used in previous analysis. This discrepancy arises because marginal gas-fired facilities have higher CO_2 emissions rates than the previously used average emissions rate from all gas-fired facilities. Therefore, electricity prices, operating profits, and the value of flexible CO_2 capture calculated in earlier studies is likely to be conservative. At \$100/tCO_2, prices increase by roughly \$60/MWh, which implies that gas-fired facilities are still marginal under these market conditions. With \$25/tCO_2 and \$3/MMBTU natural gas, reduced fuel prices dampen the increase in electricity prices caused by CO_2 prices.

These first-order prices are used to adjust volatile historical electricity prices as shown in Figure 7. Actual prices are greater than the first-order prices shown in Figure 6 but follow a similar pattern of relative uniformity over the two-day duration. Prices calculated using the first-order approach will match poorly with historical data without highly accurate cost information, so using first-order prices for price changes only allows absolute price levels to remain realistic while accounting for the effects of changing electricity market conditions.

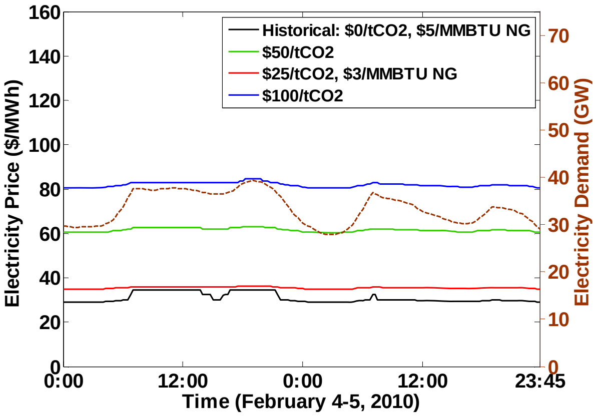

Figure 6: At moderate net load, changes to first-order electricity prices reflect CO_2 and fuel costs of marginal gas-fired facilities.

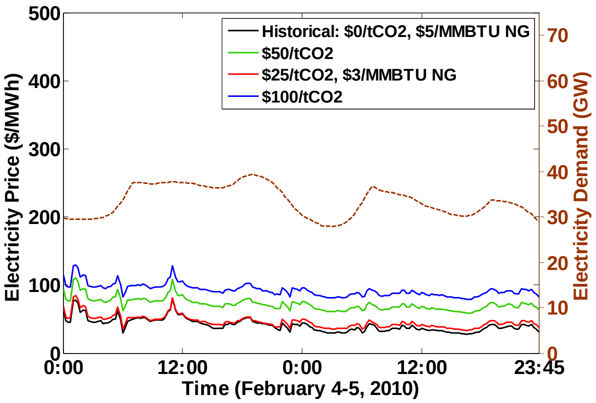

Figure 7: Historical and volatile adjusted prices are relatively steady but higher than first-order prices.

Figure 8 and Figure 9 display the same results for April 4 and 5, 2010, where net electricity demand is particularly low. First-order electricity price calculations typically find gas-fired facilities to be marginal generators; however, there is a short time period of low demand where first-order prices fall to $4/MWh, which is the operating cost for nuclear power plants in the database. At these demand levels, net electricity demand is met almost entirely by CHP capacity, so nuclear capacity is found to be marginal. While not necessarily realistic, it is likely that low carbon capacity would be marginal under these circumstances, so the resulting adjustment of $0/MWh is reasonable.

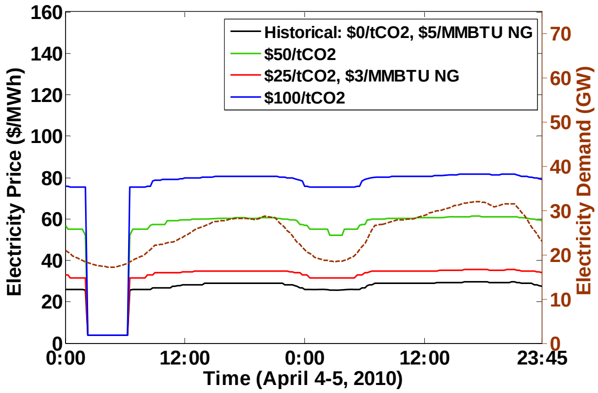

Figure 8: At low net load, first-order calculations find that CHP facilities supply enough electricity for nuclear capacity to be marginal at some times.

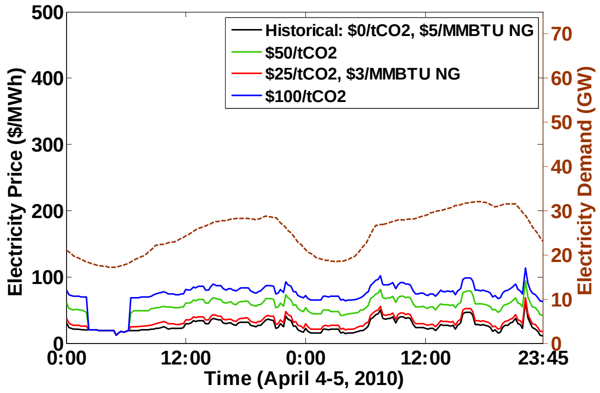

Figure 9: At low net load, historical and adjusted volatile prices are relatively stable.

Figure 10 and Figure 11 display the same data for the summer days of July 15 and 16, 2010, when demand was very high. Below ~40 GW of net load, gas-fired capacity is usually marginal, so the typical electricity price shift follows a similar pattern as previous results. However, coal-fired capacity is marginal at higher demand, so the electricity price shift more closely reflects the emissions cost of coal-fired generation, ~1 tCO_2/MWh. Figure 11 also illustrates the utility of preserving historical price volatility, as there are large electricity price spikes on July 15, 2010 and a reasonably long period of high prices on the same day that would not be captured with a first-order approach. These high prices could be very valuable for flexible CO_2 capture, so including them in the model is important.

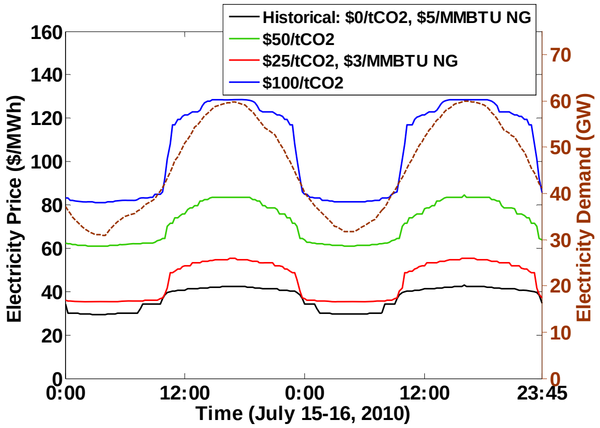

Figure 10: First-order dispatch calculations find coal-fired facilities to often be marginal above ~40 GW net load.

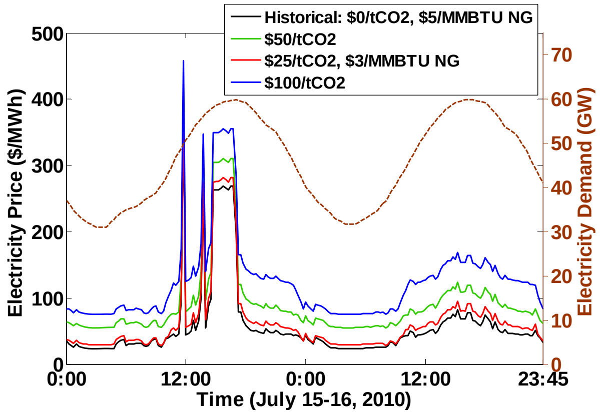

Figure 11: Periods of high prices occurring on this high demand day would not be reproduced by first-order modeling.

Figure 12 demonstrates the procedure that calculates pseudo-forecasted electricity prices from a given volatile electricity price series, in this case the actual historical prices on July 15 and 16, 2010. The original electricity prices are shown in black. The red price series has had outliers removed, where outliers are defined as prices more than two standard deviations outside a 1-

week moving average of electricity prices. Thus, the price spikes and peak price plateau on July 15 are largely removed, yielding the red curve. Then, a 4th order Savitzky-Golay polynomial smoothing procedure with a frame size of 21 time intervals produces the pseudo-forecast curve shown in blue. These smoothing parameters have been established previously to yield a price series with a realistic deviation from historical price data (Cohen et al., 2012).

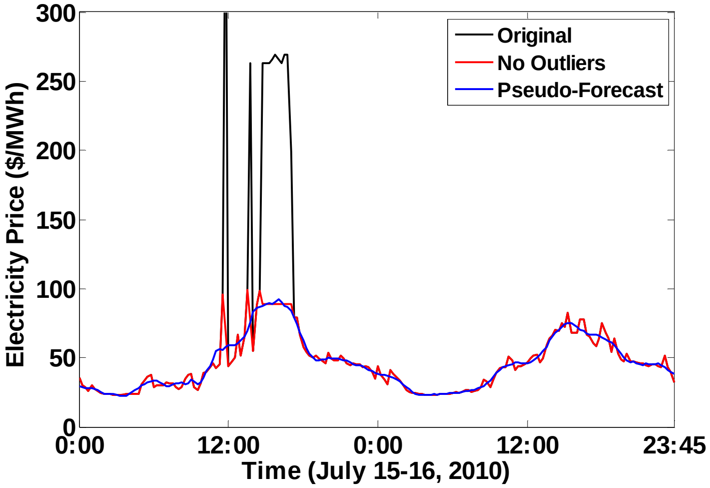

Figure 12: Outlier removal and smoothing of electricity price data produce a pseudo-forecasted electricity price series.

Conclusions

The following are key conclusions and accomplishments from this quarter.

- The grid-level least-cost dispatch model has been successfully tested with unit-specific data and demonstrates reasonable computation time under tested input conditions.
- A detailed description and scenario results from a single plant profit maximization model has been published in the *International Journal of Greenhouse Gas Control* under the title "Optimizing post-combustion CO_2 capture in response to volatile electricity prices."
- A new procedure has been developed to adjust historical electricity prices for changes in market prices of fuel (coal, natural gas) and CO_2. This procedure will supply input data to the single plant profit maximization model.
- Adjusting electricity prices for CO_2 prices by adding the average CO_2 emissions cost of gas-fired facilities provides conservative estimates of any electricity price increase.
- Coal-based capacity will often supply marginal generation when gas prices are low, CO_2 prices are moderate, and net electricity load (demand, or load, minus wind production) exceeds 40 GW.

Future Work

After finalizing input data for net load and AS requirements, the least-cost dispatch model will be used to explore the impact of flexible CO_2 capture on AS provision for a wide range of market conditions and CO_2 capture performance specifications.

With the development of a more rigorous procedure to adjust electricity prices for market conditions, the single plant optimization model will now be used to study the sensitivity of results to market conditions such as fuel and electricity prices. The model will then be used for a detailed study of the solvent storage configuration that compares solvents and design operating points to test tradeoffs among solvent price, solvent capacity, and energy performance. Sensitivity to the capital cost of stripping and compression equipment will be explored, as well as the degree to which equipment is oversized for treating stored rich solvent.

Once analysis with the single plant and grid-level models is complete, results from both models will be used to inform investment analysis using traditional net present value calculations and more rigorous approaches to decision making under uncertainty.

References

Chalmers H, Gibbins J. "Initial evaluation of the impact of post-combustion capture of carbon dioxide on supercritical pulverised coal power plant part load performance." *Fuel.* 2007;86:2109–2123.

Chalmers H, Lucquiaud M, Gibbins J, Leach M. "Flexible Operation of Coal Fired Power Plants with Postcombustion Capture of Carbon Dioxide." *J Environ Engin*. 2009.

Cohen SM, Rochelle GT, Webber ME. "Optimal operation of flexible post-combustion CO_2 capture in response to volatile electricity prices." *GHGT-10*. Amsterdam, The Netherlands, 2010a.

Cohen SM, Rochelle GT, Webber ME. "Turning CO_2 Capture On & Off in Response to Electric Grid Demand: A Baseline Analysis of Emissions and Economics." *ASME J Energy Res Techy*. 2010b;132:021003-1–8.

Cohen SM, Rochelle GT, Webber ME. "Optimizing post-combustion CO_2 capture in response to volatile electricity prices." *Int J Greenhouse Gas Control*. 2012;8:180–194.

ERCOT. "2009 Annual Report." 2010a.

ERCOT. "Setting the Shadow Price Caps and Power Balance Penalties in Security Constrained Economic Dispatch." Taylor, TX, 2010b.

ERCOT. "ERCOT Methodologies for Determining Ancillary Service Requirements." 2011a.

ERCOT. *Generic_Database_Characteristics_REV_1.xls*. 2011b.

ERCOT. "Hourly Load Data Archives." 2012a.

ERCOT. "Balancing Energy Services Market Clearing Prices for Energy Annual Reports Archives." 2012b.

Rochelle GT, et al. "CO_2 Capture by Aqueous Absorption, Second Quarterly Progress Report 2009." Luminant Carbon Management Program. The University of Texas at Austin. 2009.

Rochelle GT, et al. "CO_2 Capture by Aqueous Absorption, Third Quarterly Progress Report 2011." Luminant Carbon Management Program. The University of Texas at Austin. 2011.

Rochelle GT, et al. "CO_2 Capture by Aqueous Absorption, Fourth Quarterly Progress Report 2011." Luminant Carbon Management Program. The University of Texas at Austin. 2012.

USEIA. "Annual Energy Outlook 2012 Early Release." 2012.

USEPA. Emissions & Generation Resource Integrated Database (eGRID). *eGRID2010_Version_1_1*. 2010.

Ziaii S, Cohen SM, Rochelle GT, Webber ME. "Dynamic operation of amine scrubbing in response to electricity demand and pricing." *GHGT-9*. Washington, DC, 2008.

ref	reference state
V	vapor phase
vap	vapor pressure
*	equilibrium

References

Lextrait S. *Packed Reactive Distillation Columns: Modeling, Simulation, and Control Analyses.* The University of Texas at Austin. Ph.D. Dissertation. 2003.

Rochelle GT et al. "CO_2 Capture by Aqueous Absorption, Fourth Quarterly Progress Report 2011." Luminant Carbon Management Program. The University of Texas at Austin. 2012.

Xu Q. *Thermodynamics of CO_2 Loaded Aqueous Amines.* The University of Texas at Austin. Ph.D. Dissertation. 2011.

Ziaii S, Rochelle GT, Edgar TF. “Dynamic modeling to minimize energy use for CO_2 capture in power plants by aqueous monoethanolamine.” *Ind Eng Chem Res.* 2009;48:6105–6111.

Synthesis of Aminoethylpiperazine via Monoethanolamine and Piperazine at Stripper Conditions

Quarterly Report for January 1 – March 31, 2012

by Omkar Namjoshi

Supported by the Luminant Carbon Management Program

Department of Chemical Engineering
The University of Texas at Austin

April 30, 2012

Abstract

The selective production of aminoethylpiperazine (AEP) has been investigated this quarter. AEP can be blended with PZ to widen the solid solubility window while maintaining competitive CO_2 absorption rates, capacities, and degradation characteristics compared to 8 m PZ. AEP can be produced in the stripping column of the amine plant by reaction between the monoethanolamine (MEA) oxazolidinone, and piperazine (PZ). Another major synthesis product is diaminoethylpiperazine, or DAEP.

The synthesis of AEP was studied at 150 ^{o}C with an initial loading of 0.3 mol CO_2 / mol alkalinity with two blends: 7 m PZ/2 m MEA and 6 m PZ/4 m MEA. A combined AEP/DAEP yield of 68% was obtained with 89% of the total alkalinity present as PZ, AEP, or DAEP over 840 hours for the 7 m PZ/2 m MEA system. A combined AEP/DAEP yield of 52% was obtained with 77% of the total alkalinity present as PZ, AEP, or DAEP for the 6 m PZ/4 m MEA system. Ureas appear to be the greatest contributor to alkalinity loss. MEA degradation products and formates do not appear to significantly contribute to alkalinity loss.

Introduction

In this quarter, a novel method for synthesizing triamines and tetramines in the stripper was investigated. This process uses piperazine (PZ) or a PZ derivative and an amine whose initial degradation product is an oxazolidinone. Examples of these amines include monoethanolamine (MEA), propanolamine (MPA), methylisopropanolamine (MIPA), aminomethylpropanol (AMP), and methylaminoethanol (MAE). Examples of PZ derivatives include 1-methylpiperazine (1MPZ) and 2-methylpiperazine (2MPZ).

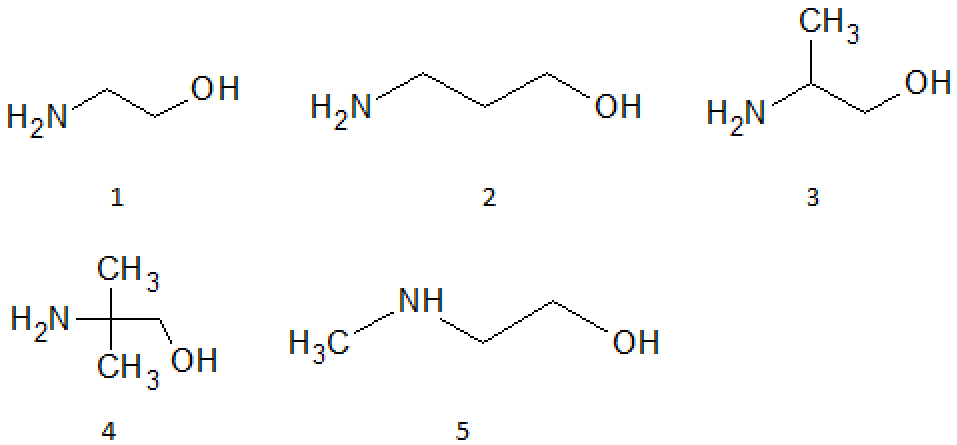

Figure 1: Structures of amines whose initial degradation product is an oxazolidinone. Component 1 is MEA, 2 is MPA, 3 is MIPA, 4 is AMP, and 5 is MAE.

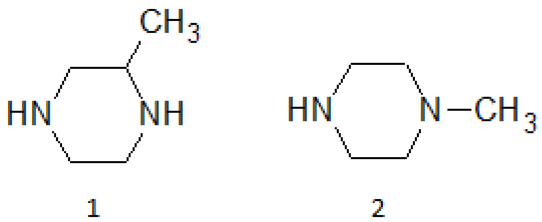

Figure 2: PZ derivatives. Component 1 is 2MPZ and component 2 is 1MPZ.

One of the secondary nitrogens in the PZ ring can react with the MEA oxazolidinone to form aminoethylpiperazine (AEP) and, to a lesser extent, 1,4-diaminoethylpiperazine (DAEP). The reaction scheme (for the reaction between PZ and the MEA oxazolidinone) follows below (Davis, 2009):

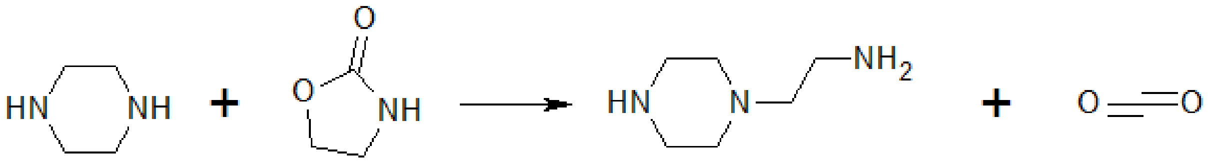

Figure 3: AEP formation via PZ and MEA oxazolidinone

The secondary amino group in AEP can react with the MEA oxazolidinone to make diaminoethylpiperazine (DAEP), a tetramine.

AEP has been studied as a potential capture solvent by Chen (Chen, 2011) and Du (Rochelle, 2012). 6 m AEP and 5 m PZ/2.3 m AEP both have lower working capacities than 8 m PZ but have competitive rates, slightly higher heats of absorption and, in the case of 5 m PZ/2.3 m AEP, comparable oxidative and thermal degradation to 8 m PZ. AEP, when blended with PZ, has better solid solubility characteristics than straight PZ. AEP (and other triamines and tetramines) are less volatile than PZ, so with proper equipment design volatile emissions from the absorber/water wash can be reduced.

Although AEP is commercially available, analogues of AEP, such as the substituted aminoisopropylpiperazine (AIPPZ), formed by the reaction of the MIPA oxazolidinone and PZ, and amino-tert-butylpiperazine (ATBPZ), formed by the reaction of the AMP oxazolidinone and PZ, are not readily available. These molecules have, in the case of AIPPZ, slightly hindered primary amino groups and, in the case of ATBPZ, severely hindered primary amino groups; these could work to increase working capacity of the solvent system while still maintaining competitive rates of CO_2 absorption and solid solubility characteristics as well as acceptable degradation characteristics.

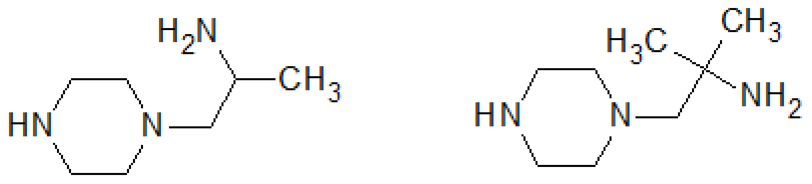

1 2

Figure 4: AEP derivatives. Component 1 is AIPPZ and component 2 is ATBPZ.

Experimental Methods

Samples were prepared gravimetrically. CO_2 was sparged into the solution and measured gravimetrically. Anion chromatography was used to analyze for free formate. Cation chromatography was used to analyze for parent amine concentrations and synthesis product concentrations. Acid titration was used to estimate the loss of alkalinity and estimate the concentration of nitrogen in ureas. Lastly, high performance liquid chromatography (HPLC) was used to estimate the concentration of hydroxyethylimidazolidone (HEIA), the principal degradation product of MEA.

The anion, cation, and total alkalinity experimental apparatuses, methods, and programs are described in previous reports and dissertations (Freeman, 2011) and will not be described in this report.

The HPLC method used to detect HEIA is similar to the method used to detect mononitrosopiperazine (MNPZ) but with a different UV wavelength. A Dionex Polar Advantage II column is used with a total eluent flow of 1 ml/min and a UV wavelength of 210 nm; the method takes 15 minutes to complete and with the flow conditions has a column dead time of 2 minutes. From 0–5 minutes, the eluent flow consists of 0.95 ml/min of 10 mM ammonium carbonate in DDI water and 0.05 ml/min of acetonitrile. From 5–10 minutes, the ammonium carbonate flow is ramped down linearly to 0.5 ml/min while the acetonitrile flow is ramped up linearly to 0.5 ml/min. From 10–15 minutes the eluent flow consists of 0.5 ml/min of

10 mM ammonium carbonate in DDI water and 0.5 ml/min of acetonitrile. HEIA elutes at approximately 4 minutes into the run.

Samples were placed in stainless steel Swagelok cylinders, which were then sealed and placed in a convection oven held at 150 °C. Cylinders were removed periodically and samples were analyzed.

Safety Aspects

A standard operating procedure (SOP) has been developed for experiments making use of the sealed Swagelok cylinders and has been attached to this report.

Results and Discussion

Calibration of DAEP

Unlike MEA, PZ, and AEP, standards could not be prepared for DAEP due to the unavailability of the molecule. However, its concentration can be estimated by using the PZ and AEP calibration data and converting the calibration data from a mass basis to a mole basis. Davis used this technique to estimate the concentrations of amines in the MEA polymerization family (e.g., HEEDA) (Davis, 2009). Figure 5 plots of the calibration of AEP and PZ on a mole basis.

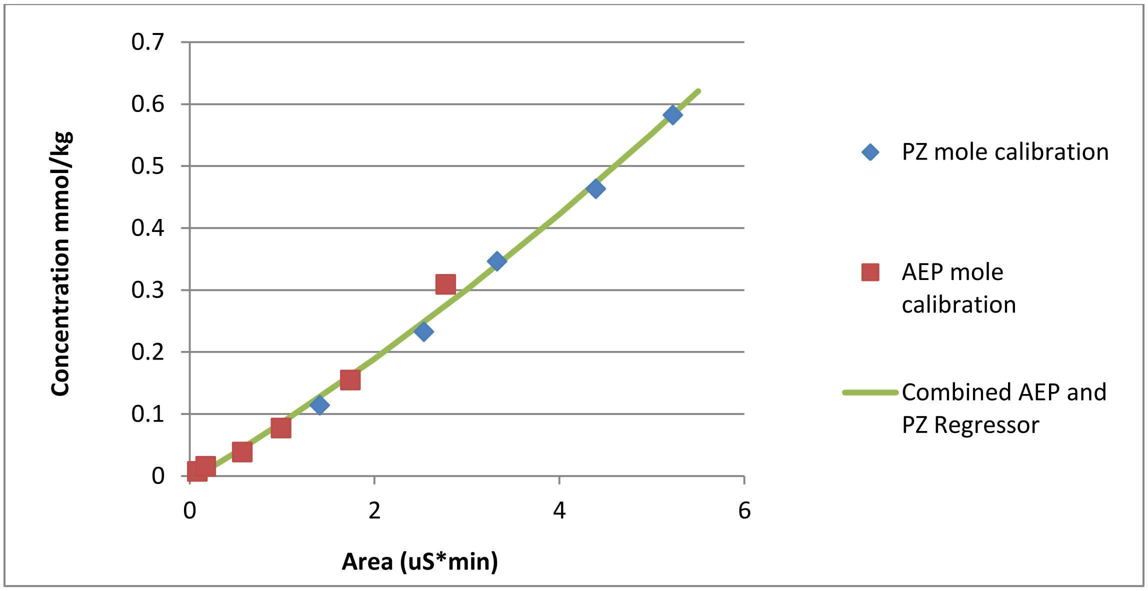

Figure 5: Calibration of DAEP

The data indicate that the calibration curves of both AEP and PZ overlap and that a combined calibration curve using points from AEP and PZ calibrations can be used to estimate the calibration of DAEP.

7 m PZ/2 m MEA, initial loading 0.3 mol CO_2/mol alk, 150 ^oC

Figure 6 shows the concentration of the parent amines as well as the primary synthesis products as a function of time. Series 1 and series 2 denote replicate experiments.

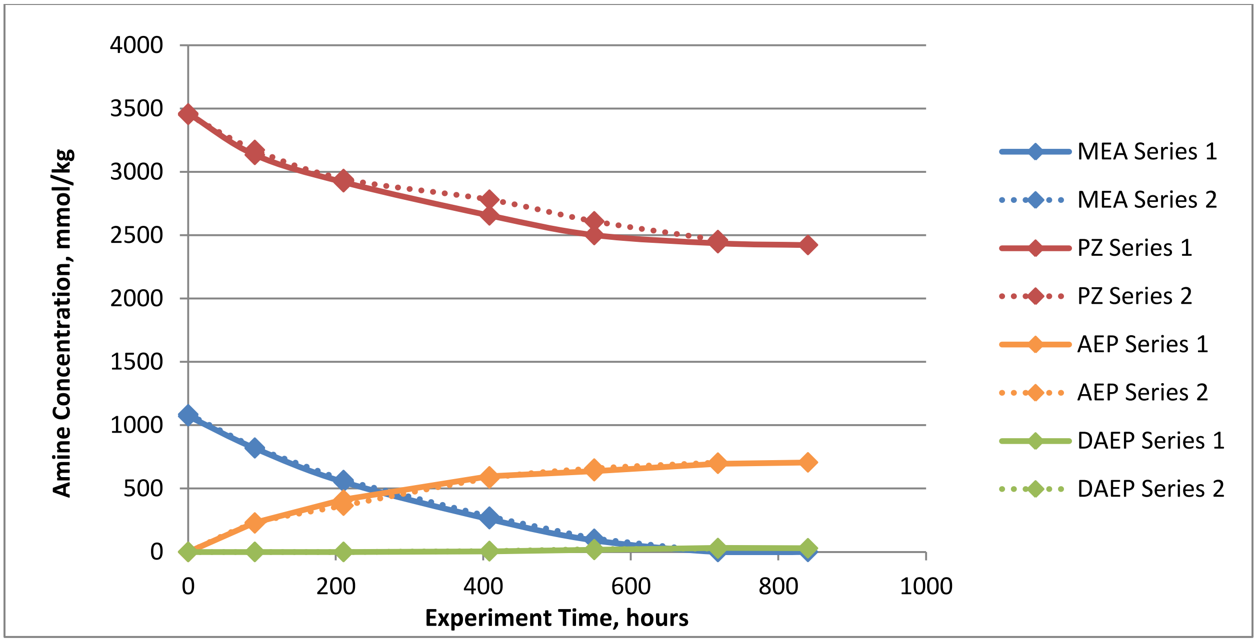

Figure 6: Formation of AEP and DAEP (7 m PZ/2 m MEA, T = 150 ^{o}C, alfa = 0.3)

The replicated points show generally good agreement with one another.

About 68% of the MEA is converted to AEP or DAEP; the remainder consists of other degradation byproducts. The amount of PZ loss (on an absolute, numerical basis) is about the same as the amount of MEA loss throughout the course of the experiment (1026 mmol/kg PZ loss compared to 1086 mmol/kg MEA loss).

Figure 7 shows the same data, except that the concentration is shown on a logarithmic scale. From these data it seems as if PZ degradation follows first-order kinetics; the same cannot be said about MEA. The formation of AEP and DAEP is confounded by the formation reactions as well as known degradation mechanisms (arm switching, or the primary amine group of AEP/DAEP attacking the MEA oxazolidinone).

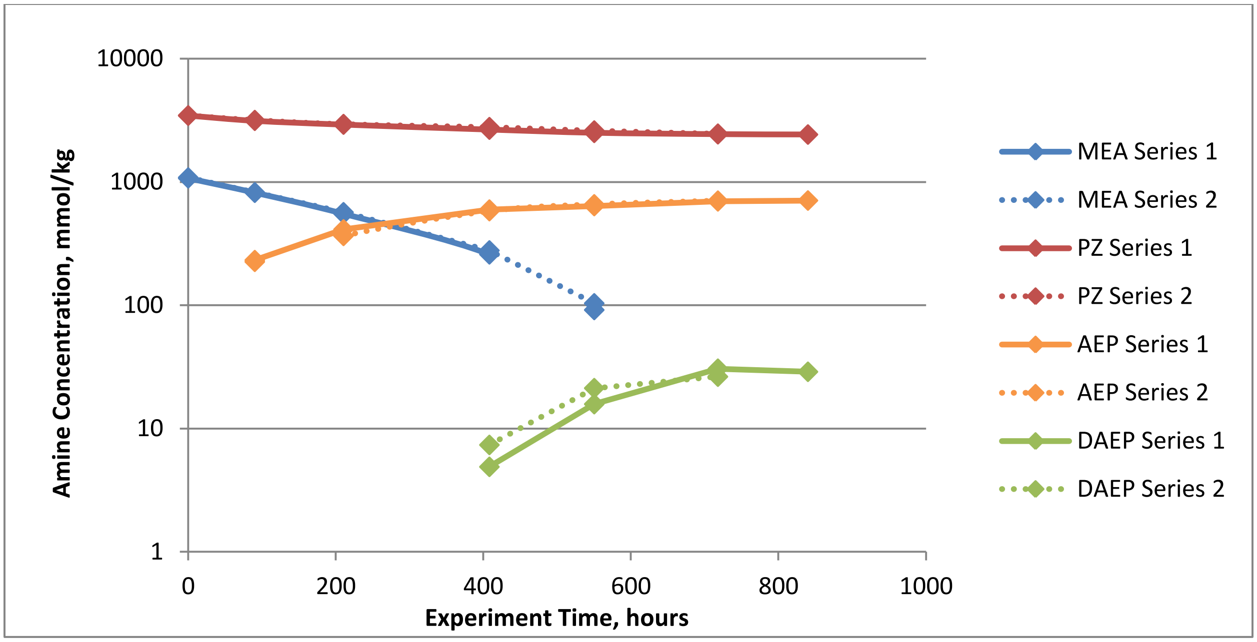

Figure 7: Formation of AEP and DAEP (7 m PZ/2 m MEA, T = 150 ^{o}C, alfa = 0.3) (log scale)

The concentrations of AEP, DAEP, and PZ are almost identical from the last two data points. Three reasons are suggested for this:

1. MEA is already completely consumed at this stage, so there is no further reaction of PZ to AEP or AEP to DAEP.
2. PZ and AEP can react to form PZ and DAEP (and undergo arm switching, much like what happens between PZ and 1MPZ). This arm-switching reaction might have reached equilibrium (or be close to it) at these concentrations and conditions.
3. The arm switching degradation mechanisms are sufficiently slow that the time difference between the last two points (5 days) is not enough to show any appreciable change in concentration.

Figure 8 shows the total nitrogen balance assuming that all of the nitrogen comes from either the desired synthesis products or from the parent amines.

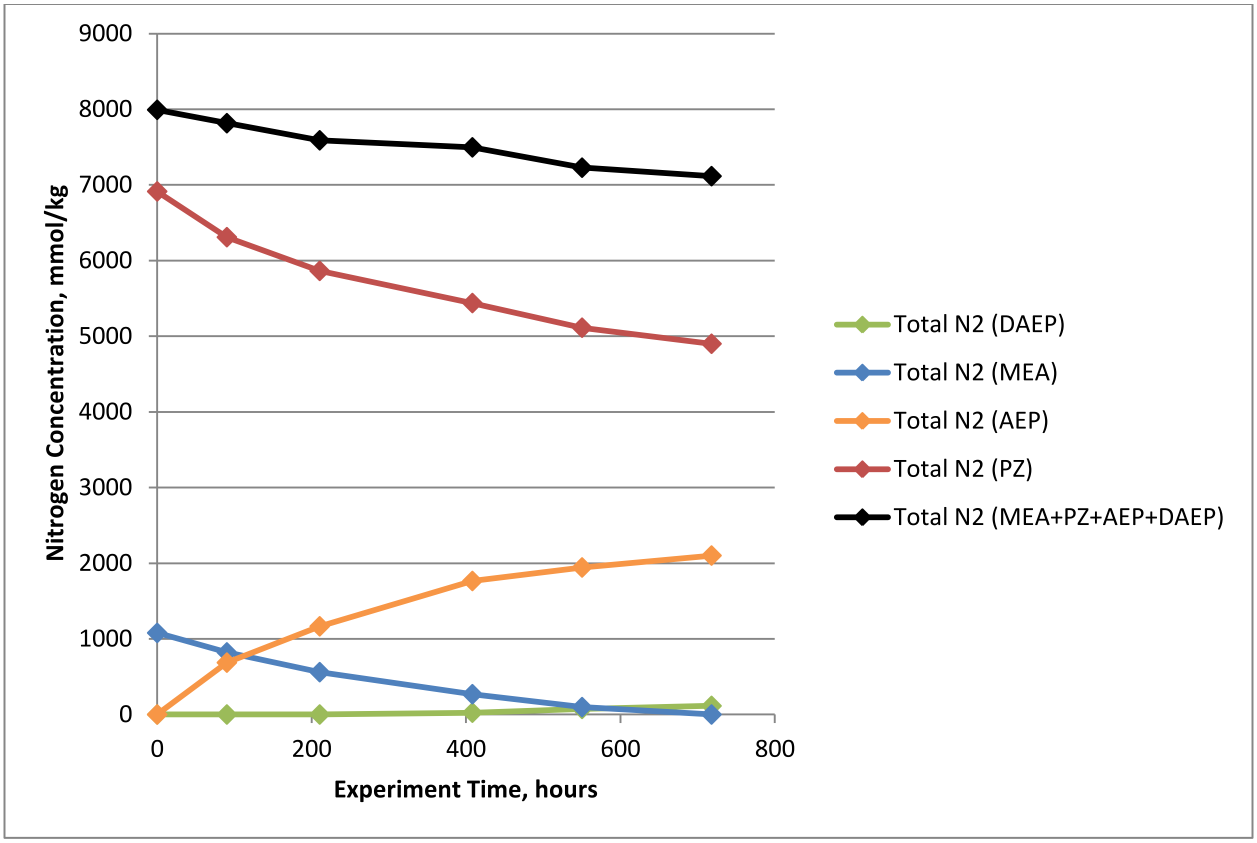

Figure 8: Nitrogen Balance (7 m PZ/2 m MEA, T = 150 ^{o}C, alfa = 0.3)

About 89% of the alkalinity is retained after about 30 days as PZ, AEP, and DAEP; 30% of the alkalinity is comprised of AEP.

Acid titration was used to estimate the total alkalinity of the sample. Due to air entrainment in the acid injection syringe the volume of acid used to titrate the sample also includes the volume of the entrained air and, as such, the total alkalinity as measured by the instrument is overstated. Important qualitative conclusions concerning byproduct selectivity to ureas can still be drawn from this analysis as ureas cannot accept protons and therefore represent a potential loss of alkalinity. Table 1 shows the total alkalinity for the last two samples taken.

Table 1: Alkalinity measured using titration and cation chromatography

(note that cation chromatography only accounts for MEA, PZ, AEP, and DAEP as products contributing to alkalinity)

Sample ID / measurement	Total Alkalinity, mmol/kg
T = 840 hours / Titration	7600
T = 840 hours / Cation	7083
T = 718 hours / Titration	7400
T = 718 hours / Cation	7086

A scheme for urea formation is presented in Figure 9. In addition to the MEA degradation pathways (via HEEDA) to make HEIA, AEP could react with the MEA oxazolidinone and degrade to a cyclic urea:

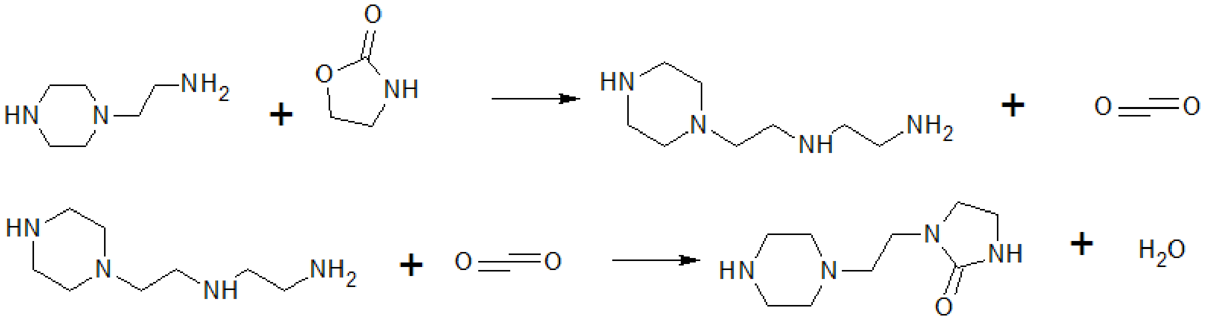

Figure 9: Production of an AEP urea via attack of MEA oxazolidinone

Other byproducts, such as long-chain polyamines formed as a result of attack of the MEA oxazolidinone by the primary amine in the polyamine chain attached to the PZ, could also be present. This could explain why the titrator measured slightly higher alkalinity compared to alkalinity calculated from concentrations of only PZ, MEA, AEP, and DAEP. (It is also important that these polyamines can undergo cyclic urea formation.)

Free formate concentrations are presented in Figure 10.

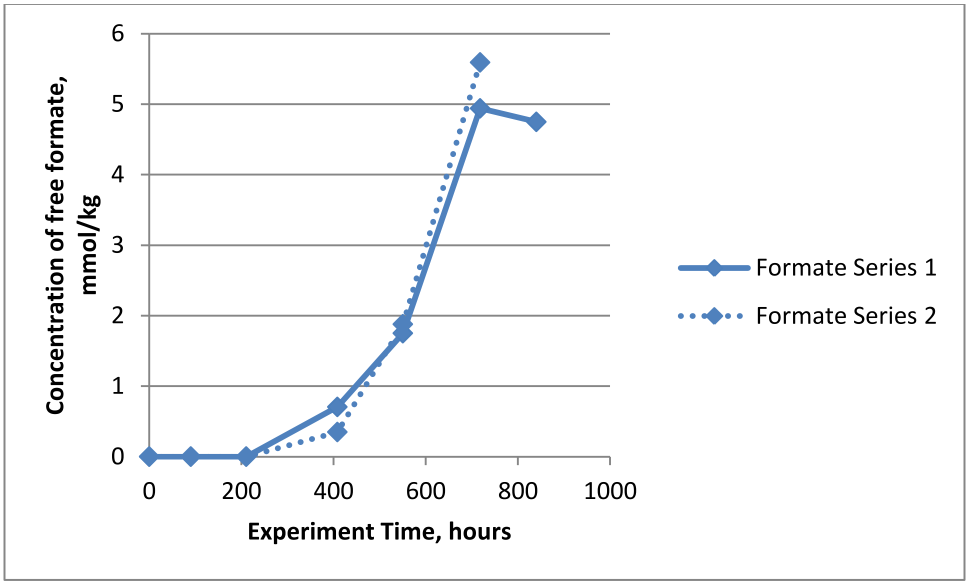

Figure 10: concentration of free formate as a function of time

The concentration of free formate is relatively low; this seems to suggest that formate is not a major byproduct of the system and cannot completely account for the alkalinity loss.

6 m PZ/4 m MEA, initial loading 0.3 mol CO_2/mol alk, 150 ^oC

Figure 11 shows the concentration of the parent amines as well as the primary synthesis products as a function of time. Series 1 and series 2 denote replicate experiments.

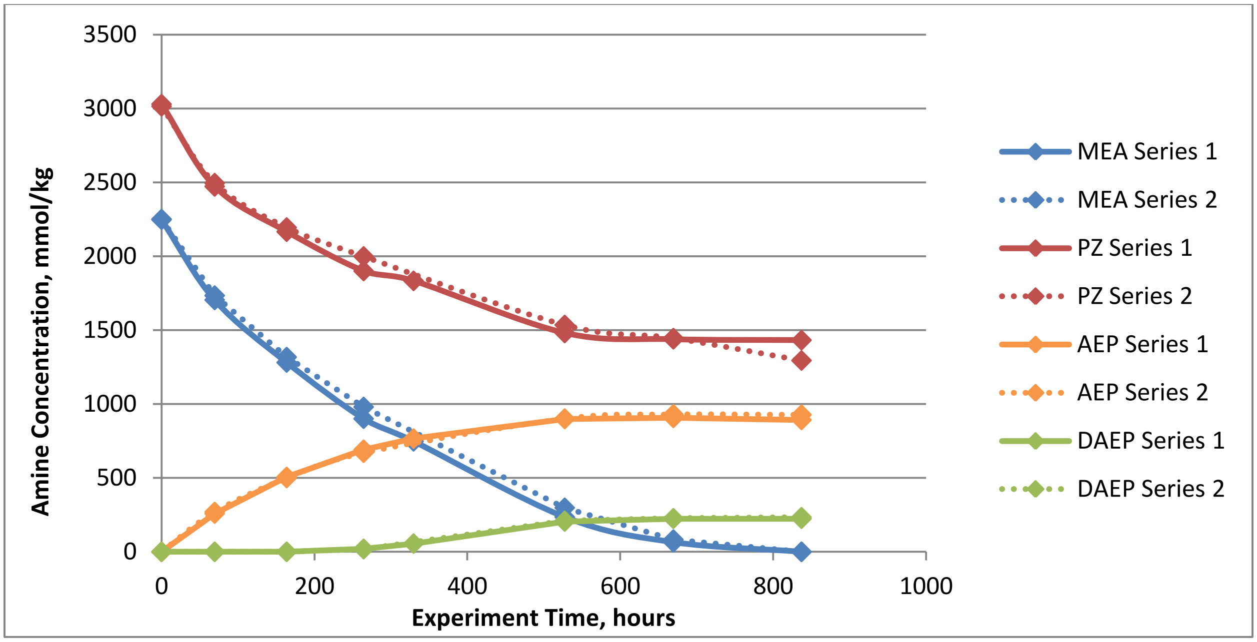

Figure 11: Formation of AEP (6 m PZ/4 m MEA, T = 150 ^{o}C, alfa = 0.3)

The general behavior of 6 m PZ/4 m MEA is similar to that of 7 m PZ/2 m MEA: DAEP, AEP, and PZ all appear to stabilize once the MEA is mostly consumed, suggesting that either the arm-switching reaction is slow or, at these conditions, the reaction has reached equilibrium. About 10 times as much DAEP is produced at the end of this experiment which results from the increased amount of MEA used at the start.

About 52% of the MEA is converted to AEP or DAEP. The amount of PZ loss (on an absolute, numerical basis) is equal to 73% of the loss of MEA throughout the course of the experiment (1653 mmol/kg PZ loss compared to 2251 mmol/kg MEA loss).

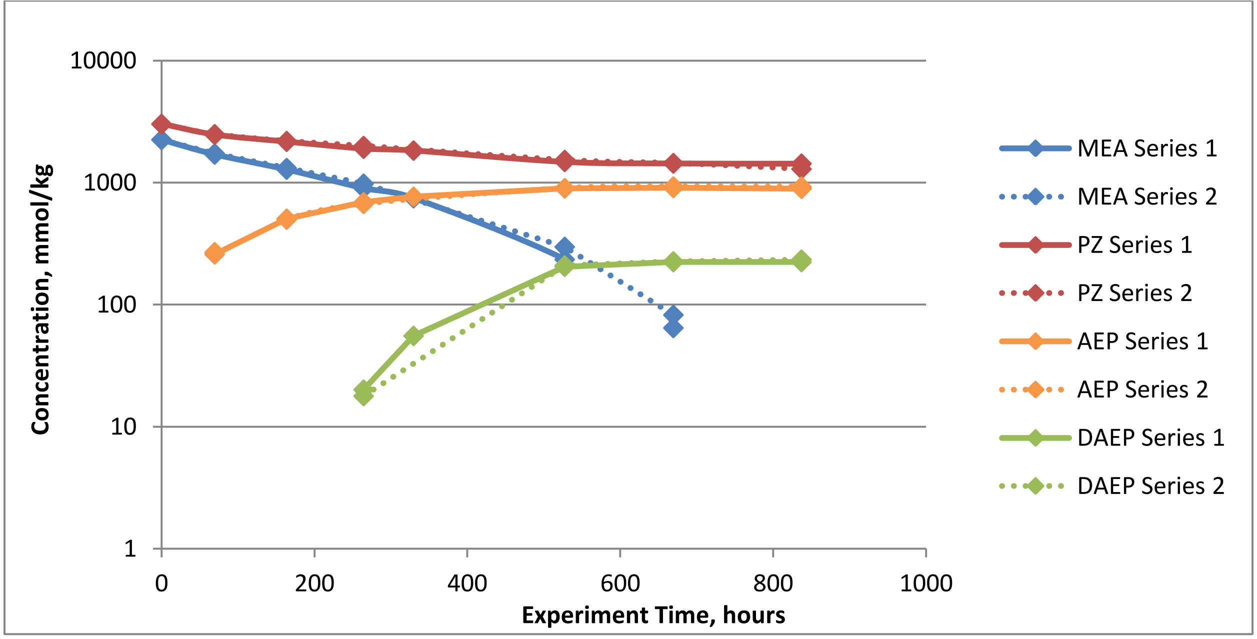

Figure 12: Formation of AEP (6 m PZ/4 m MEA, T = 150 ^{o}C, alfa = 0.3), concentration in log scale.

Figure 12 suggests that the kinetics of the formation of AEP and DAEP are confounded by formation (via PZ or AEP) and degradation (via attacking the MEA oxazolidinone).

Figure 13 shows the total nitrogen balance assuming that all of the nitrogen comes from either the desired synthesis products or from the parent amines.

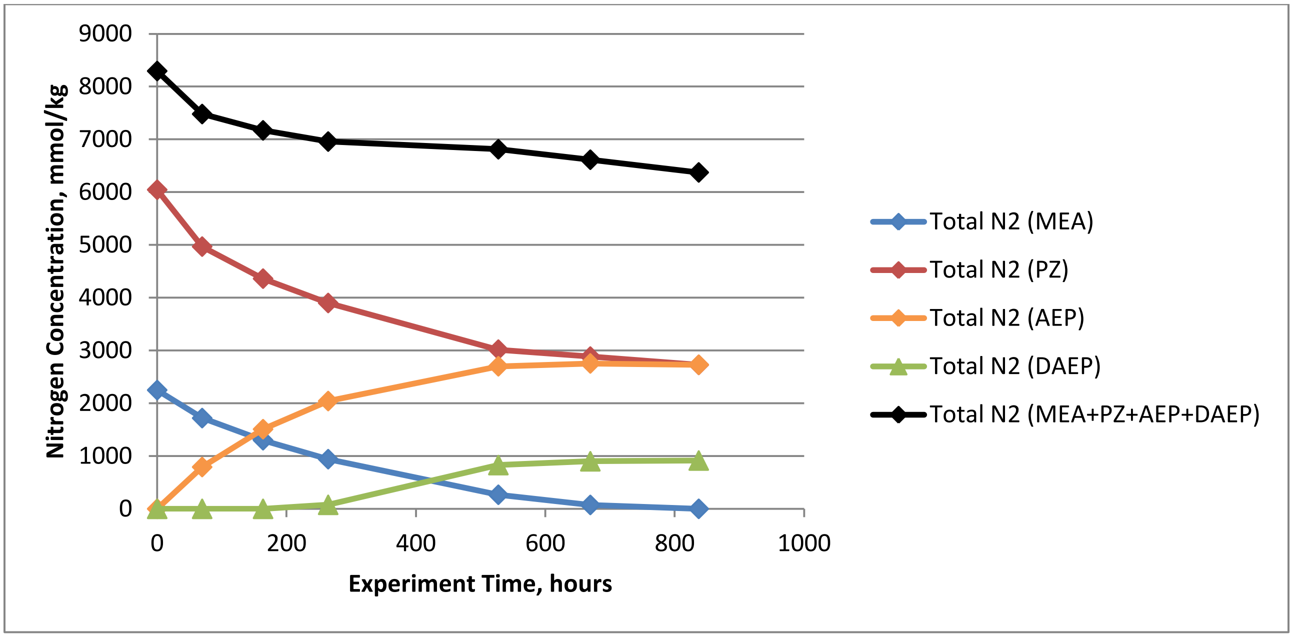

Figure 13: Nitrogen Balance (6 m PZ/4 m MEA, T = 150 ^{o}C, alfa = 0.3)

About 77% of the total alkalinity is retained as MEA, PZ, AEP, or DAEP.

As in the previous experiment acid titration was used to measure alkalinity (subject to the same air entrainment issues). Table 2 compares the alkalinity of the samples. There is not much consistency between the data points but they do suggest that the bulk of the alkalinity is bound with the remaining PZ, AEP, and DAEP. As in the previous experiment it appears as if the bulk of the alkalinity loss is via urea formation.

Table 2: Alkalinity measured using titration and cation chromatography

(note that cation chromatography only accounts for MEA, PZ, AEP, and DAEP as products contributing to alkalinity)

Sample ID / measurement	Total Alkalinity, mmol/kg
T = 837 hours / Titration	6300
T = 837 hours / Cation	6373
T = 670 hours / Titration	6500
T = 670 hours / Cation	6614

The concentrations of free formates are presented in Figure 14. The concentrations of free formates are low and do not account for the loss of alkalinity.

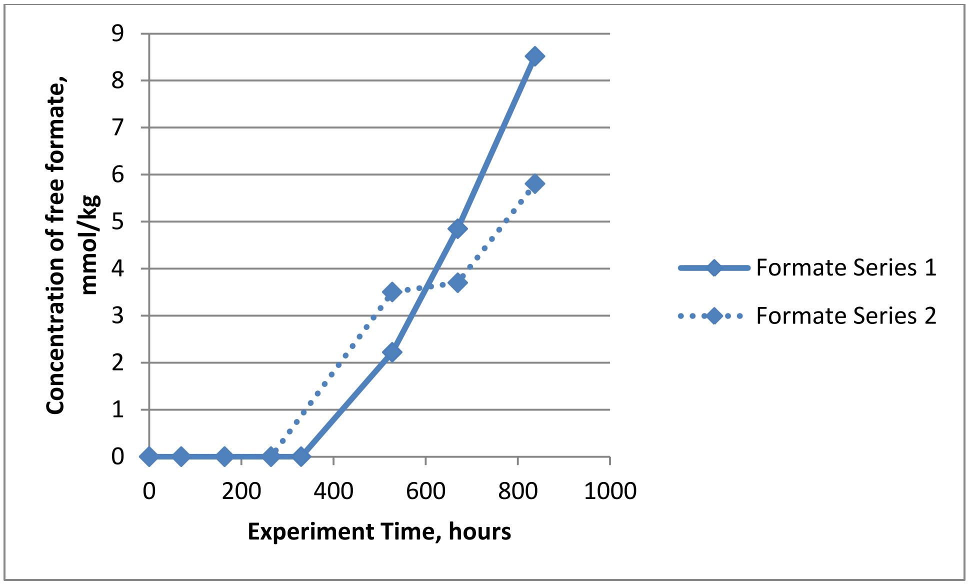

Figure 14: Concentration of free formate as a function of time

The last sample in this experimental series was analyzed for HEIA content as HEIA is the dominant product of MEA degradation. The data from the HPLC suggested that less than 500 ppmw of HEIA is present in the sample. This data point seems to suggest that MEA degradation products are not significant in this experiment and also cannot account for the alkalinity loss.

Conclusions

1. At 150 °C and 0.3 CO_2 loading, MEA reacts in 600 hours with PZ to produce aminoethylpiperazine and diaminoethylpiperazine with a yield of 53 to 68%. No other significant products appeared in the available analytical methods.
2. The conversion of MEA to AEP and DAEP was 68% for the experiment with initial concentrations of 7 m PZ/2 m MEA at the end of 840 hours. 89% of the alkalinity was retained as PZ, DAEP, or AEP after this timeframe. The raw PZ loss was almost the same as the raw MEA loss over this time. Temperature was 150 °C and initial loading was 0.3 mol CO_2/mol alkalinity.
3. The conversion of MEA to AEP and DAEP was 52% for the experiment with initial concentrations of 6 m PZ/4 m MEA at the end of 837 hours. 77% of the alkalinity was retained as PZ, DAEP, or AEP after this timeframe. MEA loss was 36% greater than PZ loss over this time. Temperature was 150 °C and initial loading was 0.3 mol CO_2/mol alkalinity.
4. Total alkalinity estimates seem to suggest that the bulk of the alkalinity is retained as PZ, DAEP, or AEP.
5. The concentrations of free formate are low and cannot account for the alkalinity loss.
6. The concentration of HEIA, the dominant MEA degradation product, is present at less than 500 ppmw at the end of the run for the experiment with an initial concentration of 6 m PZ/4 m MEA. MEA degradation products do not appear to contribute to the total alkalinity loss.
7. Urea formation represents the bulk of the alkalinity loss.

Future Work

Future work will focus on the fundamentals behind the reaction of PZ with the oxazolidinone. MEA derivatives, such as AMP, MIPA, MPA, and MAE will be blended with PZ and analyzed for synthesis products at 135 ^{o}C and 150 ^{o}C with initial loadings of 0.3 mol CO_2/mol alkalinity. A kinetic model and fundamental relationships between oxazolidinone structure and rate constants will be developed.

References

Chen X. *Carbon Dioxide Thermodynamics, Kinetics, and Mass Transfer in Piperazine Derivatives and Other Amines.* The University of Texas at Austin. Ph.D. Dissertation. 2011.

Davis JD. *Thermal Degradation of Aqueous Amines Used for Carbon Dioxide Capture.* The University of Texas at Austin. Ph.D. Dissertation. 2009.

Freeman SA. *Thermal Degradation and Oxidation of Aqueous Piperazine for Carbon Dioxide Capture.* The University of Texas at Austin. Ph.D. Dissertation. 2011.

Rochelle GT et al. "CO_2 Capture by Aqueous Absorption, Fourth Quarterly Progress Report 2011." Luminant Carbon Management Program. The University of Texas at Austin. 2012.

Aqueous piperazine/aminoethylpiperazine for CO_2 Capture

Quarterly Report for January 1 – March 31, 2012

by Yang Du

Supported by the Luminant Carbon Management Program

Department of Chemical Engineering
The University of Texas at Austin

April 30, 2012

Abstract

Thermal degradation of piperazine (PZ)/aminoethylpiperazine (AEP) was investigated in this quarter. Degradation products were identified using cation and anion chromatography and mass spectrometry, and degradation pathways were inferred.

NH_4^+ and formate were the two most abundant products for PZ/AEP thermal degradation, and consistently increased in thermal degradation experiments. PEP was the next most abundant product and reached equilibrium in first week. The production of FPZ, AEAEPZ Urea, DMPZ, and HEP showed a fast phase in the first week, followed by a slow process within the following 4 weeks. A certain penta-amine and an unknown product (retention time of 17.7) also showed a similar process. The concentration of AEAEPZ reached its maximum after around 1 to 3 weeks and then decreased during the rest time of the 5 weeks degradation experiment. DAEP and EPZ were only positively identified by IC after 3 weeks degradation.

At 175 °C, the degradation of both PZ and AEP in this blend showed a fast phase in the first week, followed by a slow process in the following 4 weeks. Generally, reversible SN_2 reactions account for the fast degradation process in first week, and elimination reactions of AEP and the reaction between PZ and degradation products (such as AEAEPZ) contribute the further slow degradation of PZ/AEP in the following 4 weeks. At 150 °C, this blend showed a consistently slow degradation within 5 weeks, in terms of both PZ and AEP components, due to the fact that at lower temperature, reactions take more time to reach equilibrium. Degradation kinetics was modeled using a 2-stage first order model at 175 °C and a single-stage first order model at 150 °C.

The apparent first order rate constant (k_1) representing the PZ degradation rate in 5 m PZ/2 m AEP is similar to that of pure PZ at 175 °C for the first 5 weeks, but faster at 150 °C. The AEP degradation rate in 5 m PZ/2 m AEP should be slower than that of pure AEP. When compared to MEA and 6 m PZ/4 m AMP blend, 5 m PZ/2 m AEP is obviously more thermally stable at 150 °C in terms of k_1. The different degradation performance of PZ or AEP in blend system and pure system at 150 °C is expected to be the result of synergism/inhibition effect of these two components.

Introduction

Concentrated piperazine (PZ) has been proposed as a possible alternative to the standard 30 wt % MEA for CO_2 capture from coal-fired flue gas (Freeman, 2011). While PZ has a higher CO_2 absorption rate, higher CO_2 capacity, and higher resistance to degradation than 30 wt % MEA, the application of concentrated PZ in industry may be limited by solid precipitation at both lean and rich CO_2 loading as well as by high viscosity (Freeman, 2011).

Last quarter, 5 m PZ/2 m AEP was proposed as a possible alternative to pure concentrated PZ for CO_2 capture from coal-fired flue gas, based on solvent solubility and viscosity measurements. Solubility measurements indicated that PZ/AEP has a higher solubility than pure PZ with equal alkalinity. The highest CO_2 loading obtained at room temperature and 1 atm is 0.39 mol/mol alkalinity for 5 m PZ/2 m AEP, 0.38 mol/mol alkalinity for 4 m PZ/2.67 m AEP, and 0.38 mol/mol alkalinity for 3 m PZ/3.33 m AEP. No precipitate was observed at high CO_2 loading. Viscosity measurements suggested that the viscosity of 5 m PZ/2 m AEP is comparable to that of pure 8 m PZ.

In this quarter, thermal degradation of 5 m PZ/2 m AEP was investigated. Degradation products were identified and degradation pathways were inferred. Degradation kinetics was investigated using common kinetic models.

Experimental Methods

Thermal degradation

Thermal degradation experiments are being conducted for 5 m PZ/2 m AEP. Experimental apparatus, procedure, and analytical methods were described in detail by Davis (2009). 5 m PZ/2 m AEP was sealed in 10 mL stainless steel bombs. The bombs are placed in forced convection ovens at 150 °C and 175 °C for extended periods of time and removed for analysis.

The experimental protocol is as follows:

1. Record the dry weight of each clean cylinder with both endcaps.
2. Charge 10 mL cylinders with 7 mL of sample solvent.
3. Seal cylinders and record the total weight.
4. Place cylinders in ovens at target temperatures.
5. Remove sample cylinder periodically and record weight again.
6. Open cylinder at room T and transfer solvent to sample vials.
7. Store samples in freezer for analysis (IC, IC/MS, HPLC, MS).

Analytical Methods

Degraded samples are analyzed for a number of chemical parameters including: (1) total inorganic carbon (TIC) for CO_2 loading; (2) cation and anion chromatography for degradation product quantification and qualification; (3) mass spectrometry (MS) for degradation products qualification. The apparatus and procedures are identical to those used by Freeman (2011).

Results and discussion

Thermal degradation kinetics

The experiment tested the degradation of 5 m PZ/2 m AEP with a CO_2 loading of 0.3 mol/mol alkalinity at 150 °C and 175 °C (Figure 1). After 5 weeks at 150 °C the loss of PZ is about 10% and the loss of AEP is no more than 20%; however, at 175 °C the loss of PZ and AEP is about 50% and 70% respectively, which indicates 5 m PZ/2 m AEP is thermally stable up to 150 °C but not 175 °C.

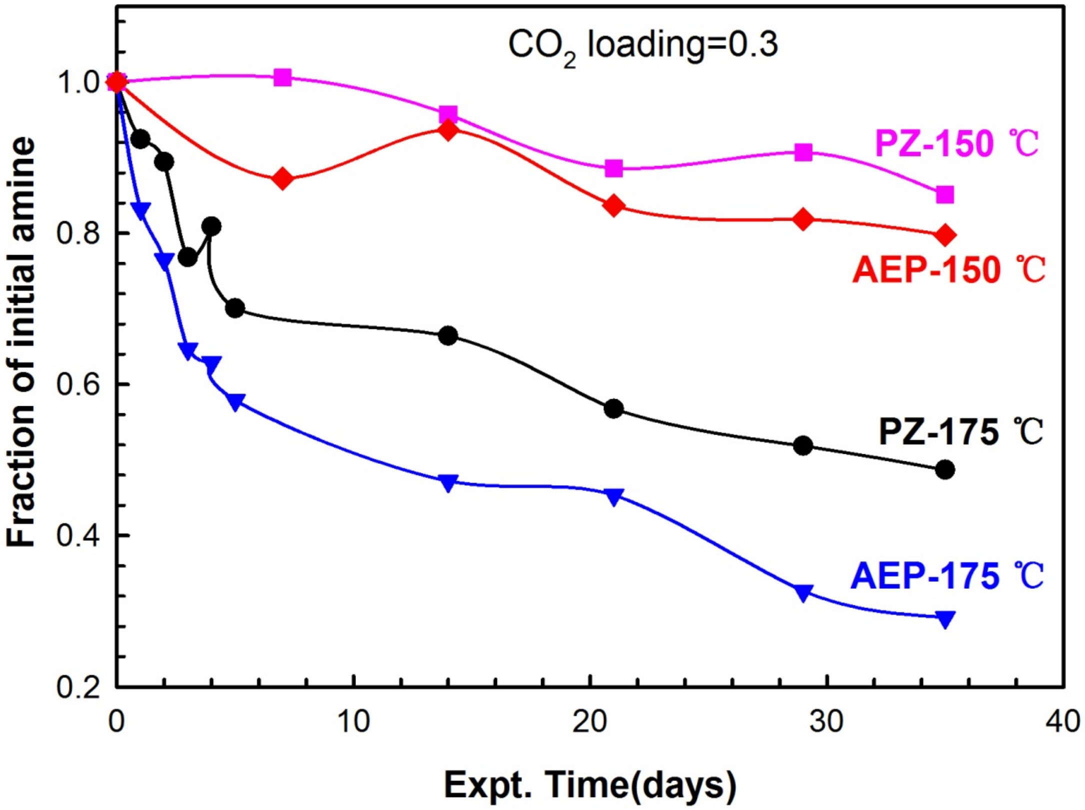

Figure 1: Thermal degradation of 5 m PZ/2 m AEP with 0.3 mol CO_2/mol alkalinity

At 175 °C, the degradation of both PZ and AEP in this blend show a fast phase in the first week, followed by a slow process within the following 4 weeks. At 150 °C, this blend shows a consistently slow degradation within 5 weeks, for both PZ and AEP. This whole process at 175 °C can be better characterized by a 2-stage first order kinetic model than by using other common models, such as 1-stage first order and second order kinetic models (Figure 2). Different reaction mechanisms are postulated as the reason for the distinct degradation rates in different stages, as discussed later. With the limited data at 150 °C, the thermal degradation of PZ and AEP is described by a single-stage first order kinetic model in order to compare with other solvents in terms of first order rate constants, k_1 (Figure 3).

The calculation of k_1 is shown by the following rate equation where C_{Amine} is the concentration of PZ or AEP in any appropriate units (Equation 1).

$$-\frac{dC_{Amine}}{dt} = k_1 * C_{Amine} \qquad (1)$$

This assumed form of a rate expression is a differential equation that can be solved for F_{Amine} (fraction of PZ or AEP) at any time point (Equation 2).

$$F_{Amine} = \frac{C_{Amine}}{C_{Amine,0}} = \exp(-k_1 * t) \qquad (2)$$

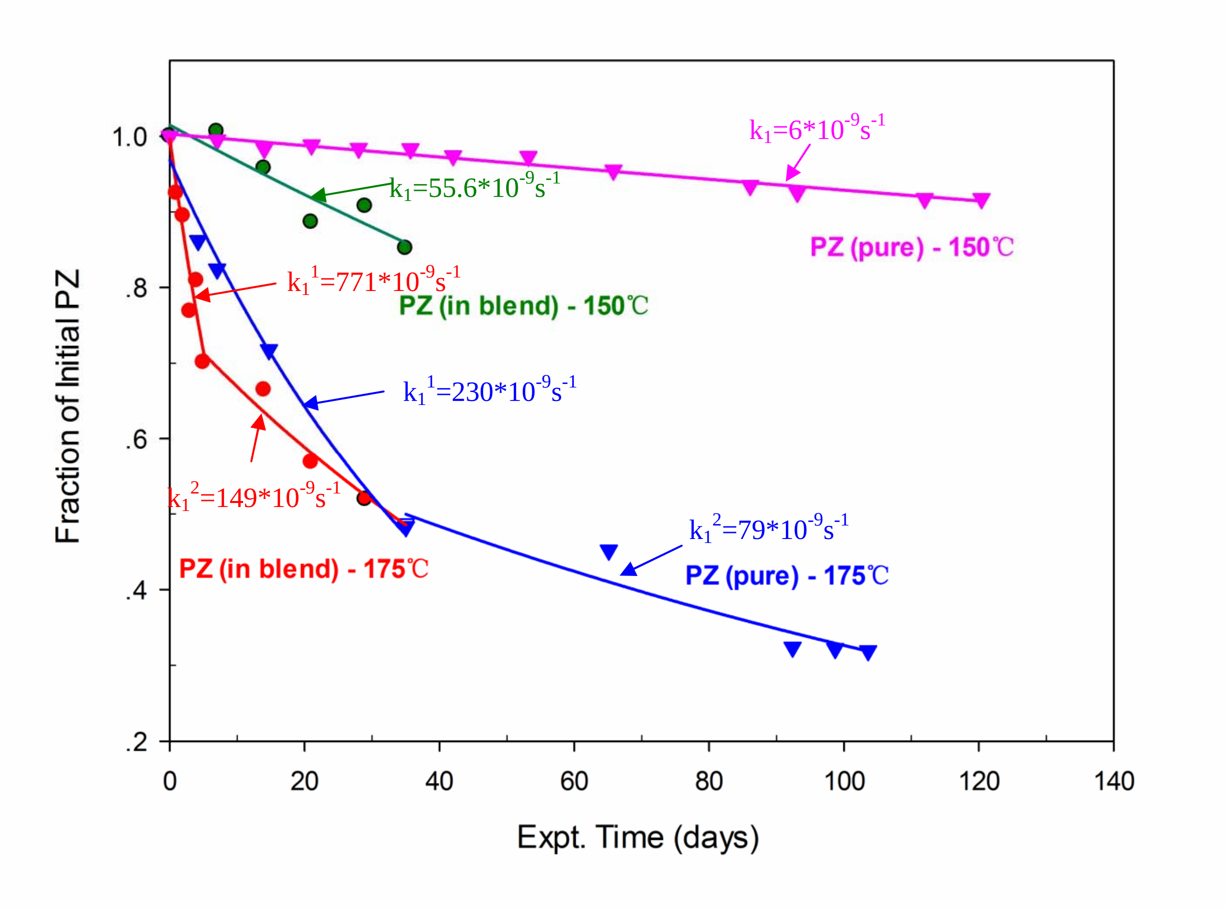

Figure 2: Comparison of PZ degradation kinetics in blend solution and that of 8 m pure PZ (from Freeman, 2011) at 150 and 175 °C.

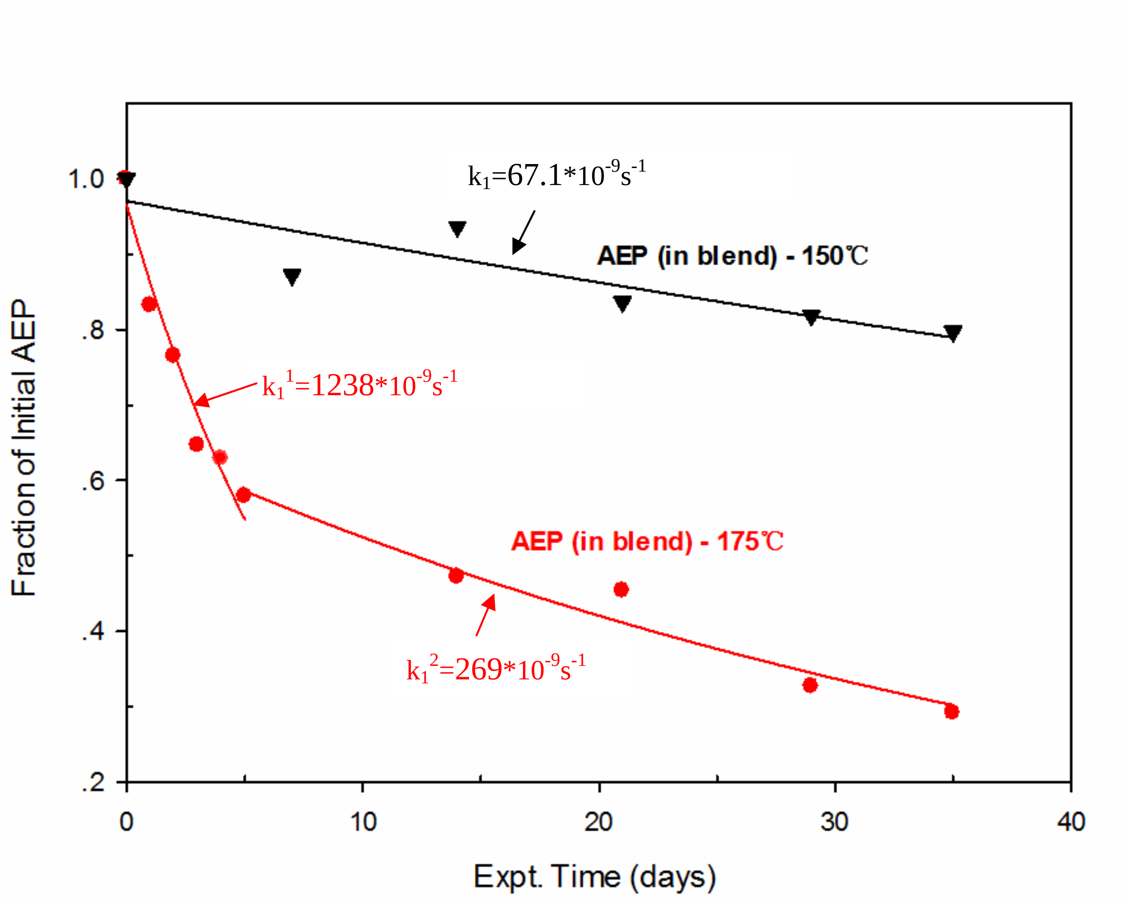

Figure 3: AEP degradation kinetics in blend solution at 150 and 175 °C

The apparent first order rate constant (k_1) for thermal degradation of 5 m PZ/2 m AEP is given in Table 1 in comparison with other common solvents. The table shows that for the first 5 weeks, the PZ degradation rate in 5 m PZ/2 m AEP is similar to that of pure PZ at 175 °C, but faster than at 150 °C. The AEP degradation rate in 5 m PZ/2 m AEP should be slower than that of pure AEP as the enhancement effect of CO_2 loading from 0.3 to 0.4 mol/mol alk is expected to be smaller than the enhancement effect of temperature from 135 to 150°C. When compared to MEA and 6 m PZ/4 m AMP, 5 m PZ/2 m AEP is obviously more thermally stable at 150 °C in terms of k_1. The different degradation performance of PZ or AEP in a blend and a pure system at 150 °C is expected to be the result of the synergism/inhibition effect of these two components.

Table 1: Apparent first order rate constant (k_1) for thermal degradation of PZ/AEP and some other common solvents

Amine	Components	Loading mol/mol alk	$k_1 \times 10^{-9}$ (s^{-1})		Ref. *
			150 °C	175 °C	
PZ	5 m PZ/2 m AEP	0.3	55.6	215.5※	
AEP	5 m PZ/2 m AEP	0.3	67.1	344※	
PZ	8 m PZ	0.3	6	230※	D

AEP	2.33 m AEP	0.4	191 (135 °C)		D
MEA	7 m MEA	0.4	828	——	D
AMP	7 m AMP	0.4	86	——	D
PZ	6 m PZ/4 m AMP	0.4	92	——	D
AMP	6 m PZ/4 m AMP	0.4	249	——	D

* If not specified, from this work; D = (Davis, 2009).

※ The single-stage first order rate constant for first 5w.

Thermal degradation products

Degradation products of 5 m PZ/2 m AEP were identified using cation and anion chromatography (with and without NaOH treatment) and mass spectrometry. The loss of CO_2 during degradation was measured by TIC.

Table 2: Glossary of Degradation Products

Chemical Name	**Abbreviation**	**Structure**	**CAS Number**	**MW (g/mol)**
1,4-Dimethylpiperazine	1,4-DMPZ	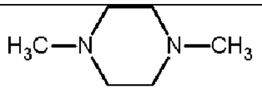	106-58-1	114.2
1-Ethylpiperazine	1-EPZ	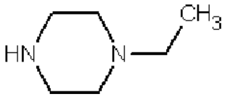	5308-25-8	114.2
1-[2-[(2-Aminoethyl)amino] ethyl] piperazine	AEAEPZ	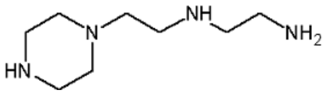	24028-46-4	172.27
1-[2-(Piperazinyl)ethyl]-2-imidazolidinone	AEAEPZ Urea	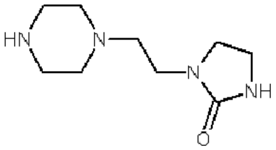	104087-61-8	198.27
1-(2-Aminoethyl)piperazine	AEP	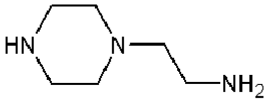	140-31-8	129.2
Acetate	CH3COO	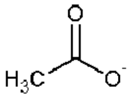	NA	59.1
Formate	CHO_2	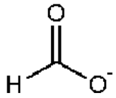	NA	45.0
1,4-di(2-aminoethyl) piperazine	DAEP	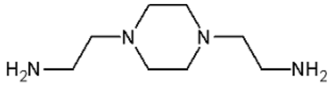	6531-38-0	172.2736
1-Formylpiperazine	FPZ	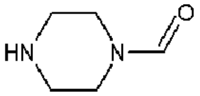	7755-92-2	114.2

1-(2-Hydroxyethyl)piperazine	HEP	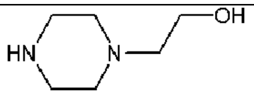	103-76-4	130.19
1,1'-(1,2-Ethanediyl)bis-piperazine	PEP	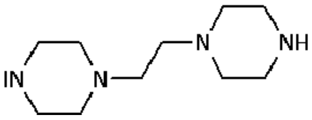	19479-83-5	198.3085
Triethylenediamine	TEDA	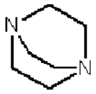	280-57-9	112.17

The chromatogram for the sample after 5 weeks of thermal degradation is shown in Figure 4. There were 3 major peaks at retention times of 10.8, 17.7, and 47.6 minutes that have yet to be positively identified and quantified. A comparison of the cation IC chromatograms for the original and NaOH treated final sample is made in Figure 5. The peak for N-formyl PZ is the only peak to disappear between the chromatograms indicating that none of the major unidentified peaks are also amides.

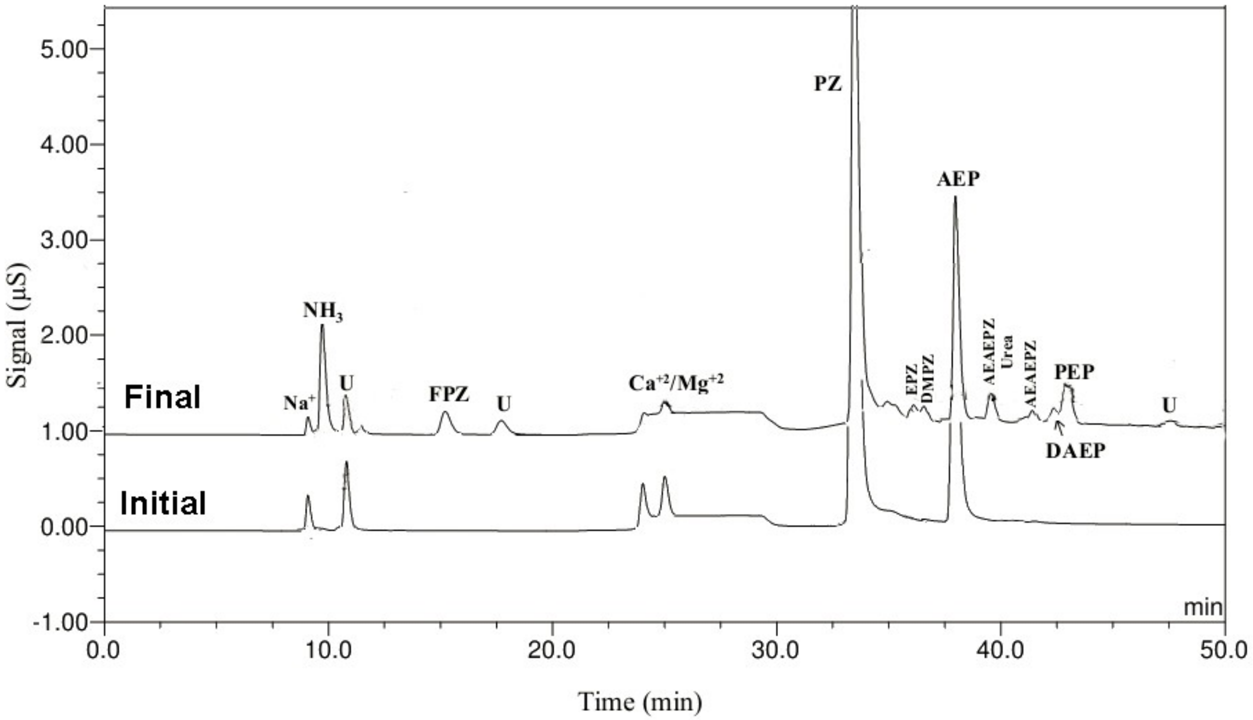

Figure 4: Cation IC chromatogram of the initial and final sample of 5 m PZ/2 m AEP at 175 °C.

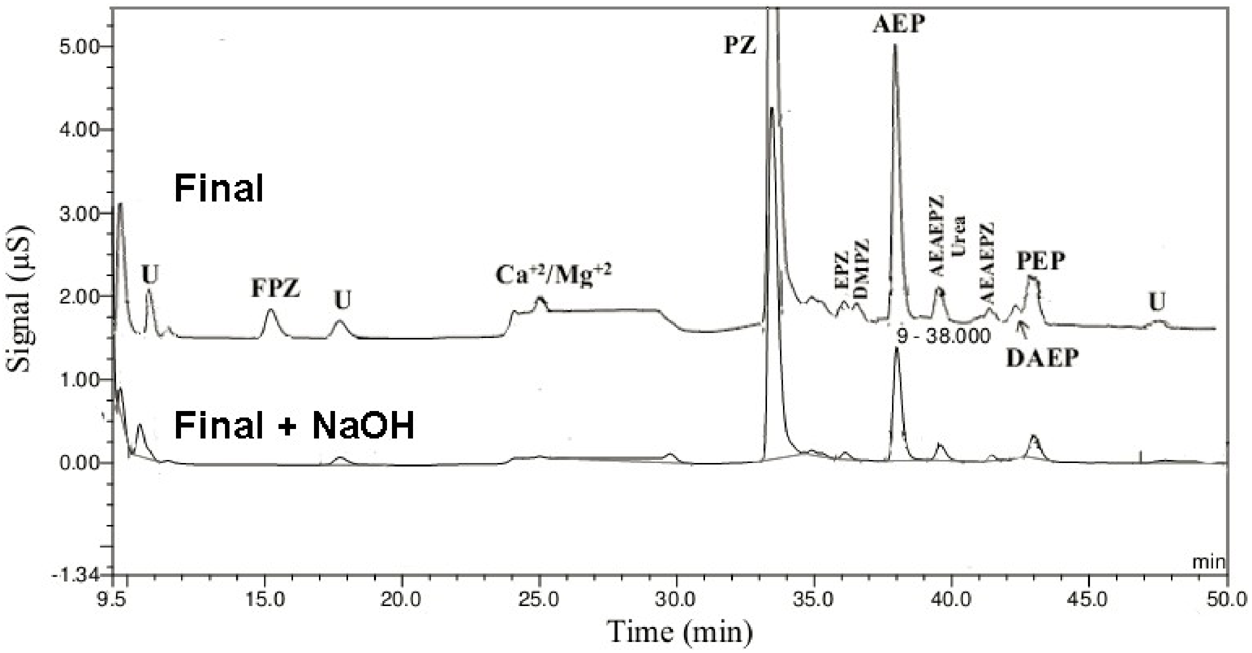

Figure 5: Cation IC chromatogram of original and NaOH treated final sample of 5 m PZ/2 m AEP at 175 °C

The relative amount profiles for amine products (except for AEP and PZ) of thermal degradation positively identified and quantified using cation IC are shown in Figure 6a. A magnified view of the same figure is shown in Figure 6b. NH_4^+ was found to have one of the largest amounts and consistently increased in thermal degradation experiments. PEP was the next most abundant product and reached equilibrium in the first week. The production of FPZ, AEAEPZ Urea, DMPZ, and HEP showed a fast phase in the first week, followed by a slow process within the following 4 weeks. A certain penta-amine and an unknown product (retention time of 17.7) also showed a similar process. The concentration of AEAEPZ reached its maximum after 1 to 3 weeks and then decreased during the rest time of the 5 weeks degradation experiment. DAEP and EPZ were only positively identified by IC after 3 weeks degradation.

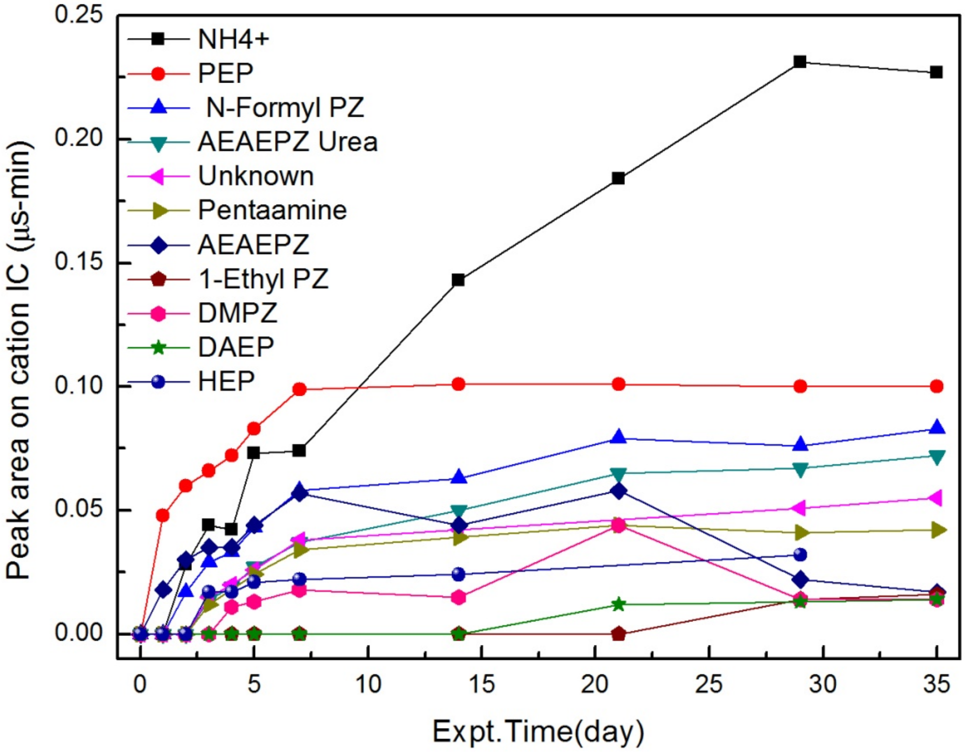

Figure 6a: Production of amine degradation products during thermal degradation of 5 m PZ/2 m AEP at 175 °C

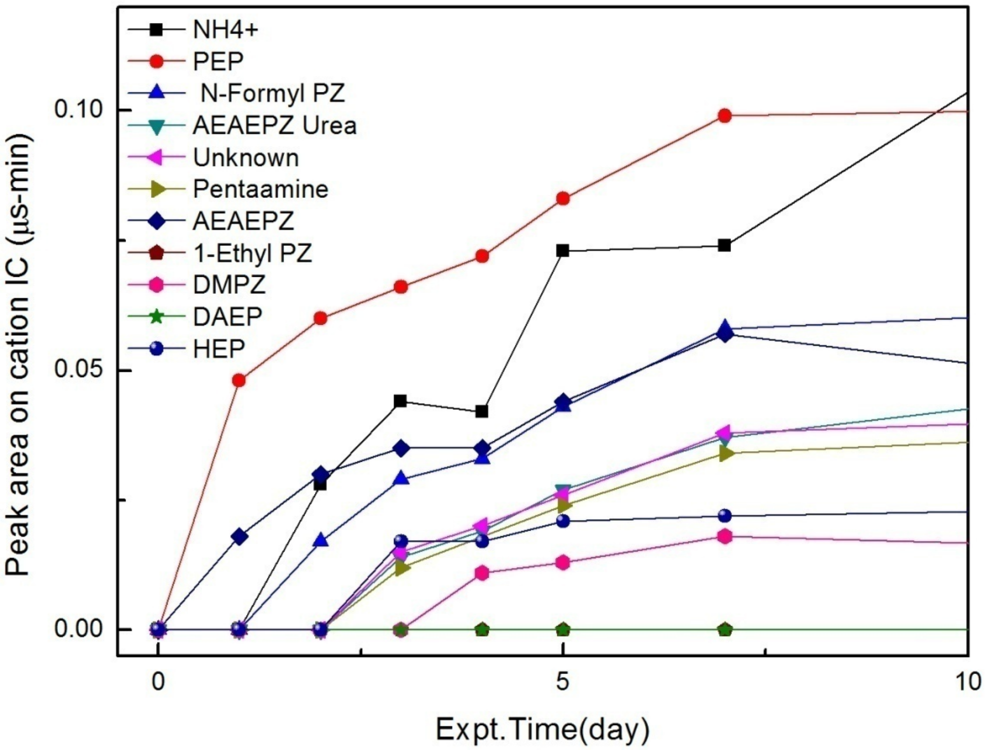

Figure 6b: A magnified view of the production of amine degradation products during thermal degradation of 5 m PZ/2 m AEP at 175 °C.

Carboxylate ions, known as heat stable salts, are also commonly produced in thermal degradation experiments and are quantified using anion IC. The carboxylate ions produced in 5 m PZ/2 m AEP degradation are shown in Figure 7. The concentrations of the two most abundant carboxylate ions (acetate and formate) identified by anion IC are shown in this figure along with their concentrations after NaOH treatment. This value, labeled "Total anion," represents the sum of all ion peaks identified by anion IC. "With NaOH" means the original ion and the concentration increase that may have resulted from the reversal of any amide formation. The difference between the original value and NaOH treatment value would represent the concentration of amides of that carboxylate ion. As shown in Figure 7, formate was the dominant carboxylate ion produced in the degradation of PZ/AEP at 175 °C and the treatment of NaOH only led to about 10 % increase of carboxylate ions. The loss of PZ/AEP and CO_2 during thermal degradation is compared to the production of main degradation products (NH_4^+ and formate) at 175 °C (Figure 8). The rate of PZ/AEP decrease is much faster than the rate of NH_4^+ increase in the first week, indicating some degradation pathways that do not produce NH_4^+ may also account for the fast degradation of PZ/AEP in the first week.

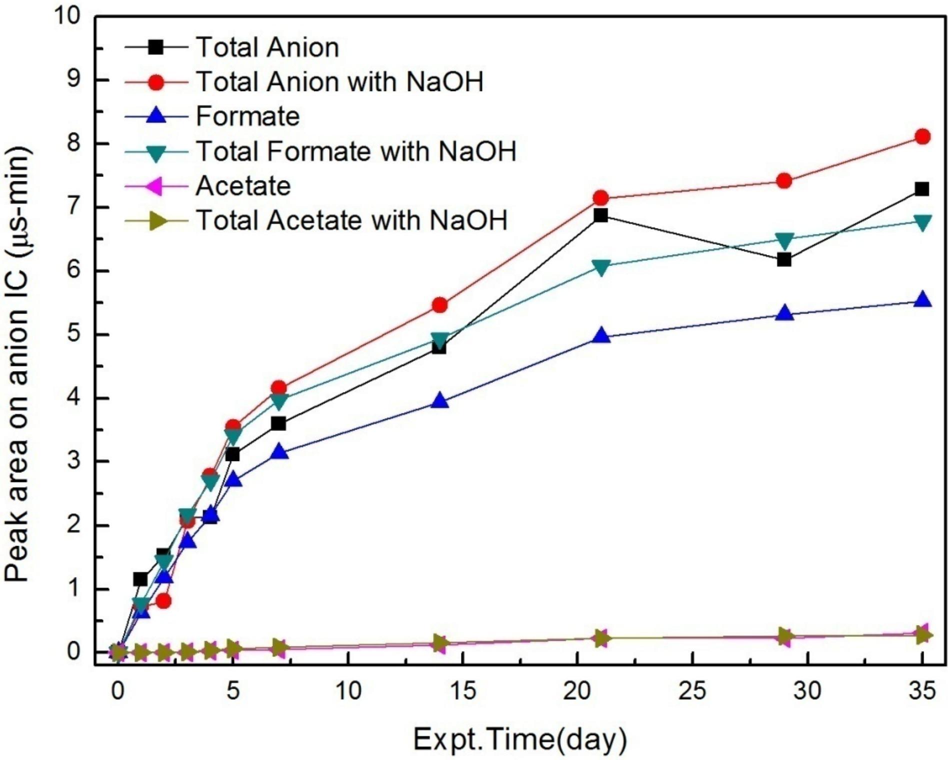

Figure 7: Production of carboxylate ions during thermal degradation of 5 m PZ/2 m AEP at 175 °C

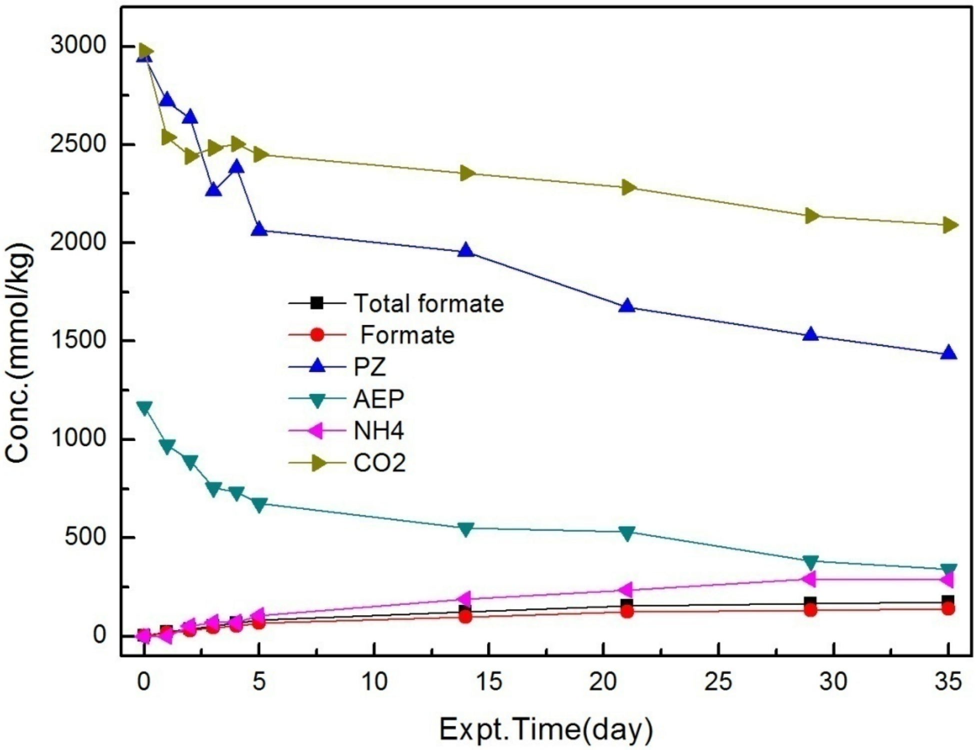

Figure 8: Comparison of loss of PZ/AEP and CO_2 and production of main degradation products (NH_4 and formate) at 175 °C

In order to further verify the identity of the degradation products, mass spectroscopy was used on the sample of PZ/AEP held at 150 °C for 5 weeks. The mass spectrum for the sample is shown in Figure 9. The main degradation products of PZ/AEP identified by cation IC can be verified by MS, such as PZ (m/z 87.1), AEP (m/z 129.9), AEAEPZ/DAEP (m/z 172.9), and AEAEPZ urea/PEP (m/z 199.0). The peak at 241.88 may correspond to a penta-amine.

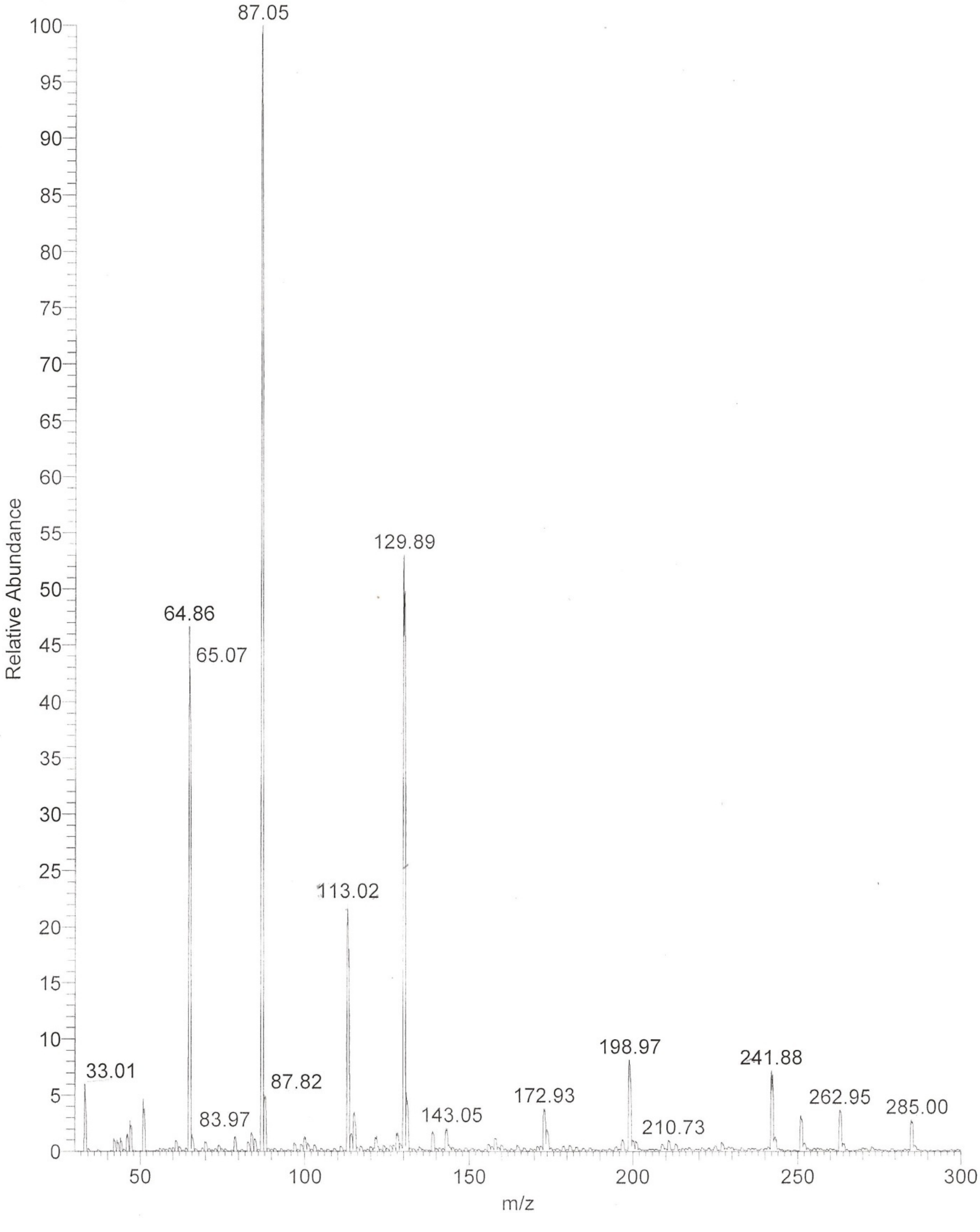

Figure 9: Mass spectrum for PZ/AEP degradation at 150 °C for 5 weeks.

At 175 °C the peak height of some degradation products increased significantly (Figure 10), such as m/z 99.93 (unknown), m/z 112.95 (TEDA/1-ethylenyl-piperazine), m/z 114.91 (NPZ/EPZ/DMPZ), m/z 121.7 (unknown), m/z 143.05 (which can result from loss of two NH_2

from DAEP), m/z 155.94 (which can be a derivative of TEDA/1-ethylenyl-piperazine), and m/z 158.22 (which can be the chemical result from loss of one NH_2 from AEAEPZ/DAEP).

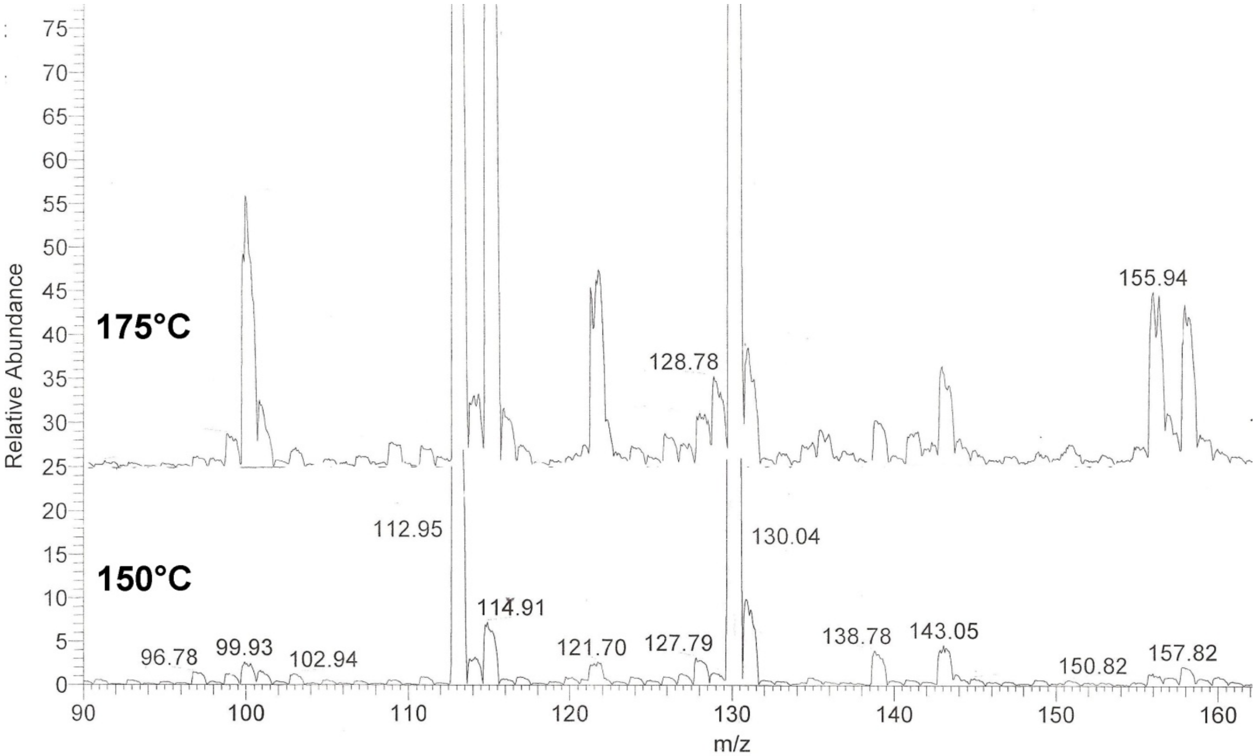

Figure 10: Comparison of Mass spectrum for PZ/AEP degradation at 150 °C and 175 °C for 5 weeks.

Proposed Thermal Degradation Pathways of PZ/AEP

Thermal degradation of PZ/AEP produces a wide variety of molecules as degradation products as discussed above. The chemical mechanisms involved in producing each known product are not yet clear, but an overall set of pathways was developed that involves typical reactions and can describe the generation of the major products. This proposed set of pathways is meant for illustrative purposes and is not known at this time to be correct with complete confidence. The purpose is to suggest the types of reactions believed to be occurring. Further research into specific reaction pathways may disprove any portion of the mechanism.

Similar to pure PZ, the thermal degradation of PZ/AEP can be described as proceeding with four types of reactions: secondary SN_2 type substitution reactions, elimination reactions, urea generation, and formate generation from CO_2-containing molecules. As mentioned early, the degradation of PZ/AEP at 175 °C shows a two-stage process, indicating different reactions involved in different stages. In the fast stage (within the first week), the following reactions may contribute significantly to the degradation:

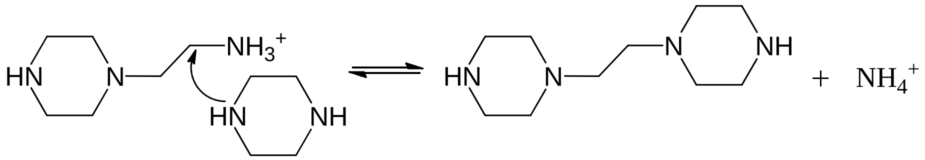

(AEP) **(PZ)** **(DAEP)**

(1)

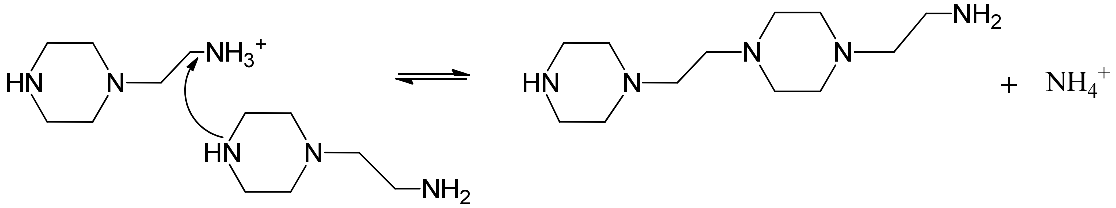

(AEP) **(Pentaamine)**

(2)

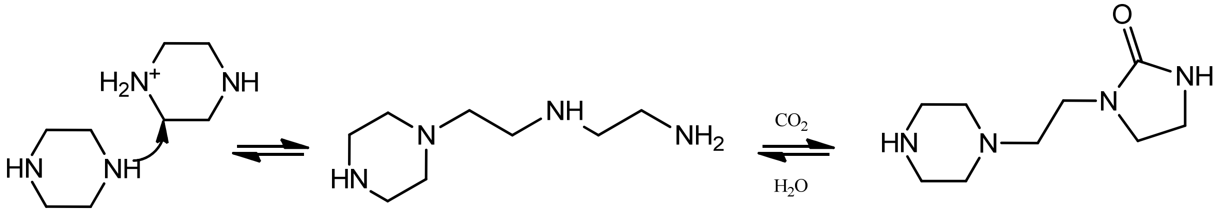

(PZ) **(AEAEPZ)** **(AEAEPZ Urea)**

(3)

As shown in Figures 6a and 6b, the production of PEP, penta-amine, and AEAEPZ Urea show a fast increase in the first week, followed by a quasi-steady state or very slow increase process in the next 4 weeks, indicating PEP, penta-amine and AEAEPZ Urea reach quasi-equilibrium with PZ and AEP in the first week through the above reversible mechanisms.

The following five reactions may contribute to the continuing slow degradation of PZ/AEP. Reactions 4, 5, 7, and 8 can explain the further decrease of PZ/AEP after one week of fast degradation. Reactions 6 and 7 can explain the decrease of AEAEPZ. Reactions 6 and 8 can explain the production of EPZ and DAEP, both of which were only identified by IC after 3 weeks degradation. The consistent increase of NH_4^+ in the slow stage may result from elimination reactions of PZ derivatives, such as AEP and AEAEPZ.

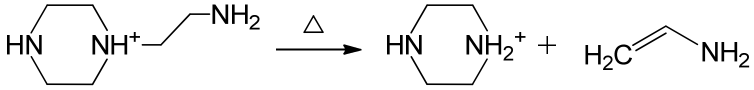

(AEP) **(PZ)** (4)

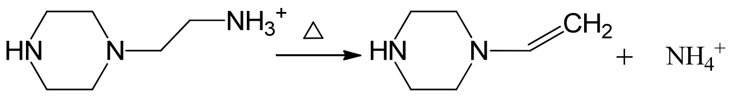

(AEP) **(1-ethylenyl-piperazine)**

(5)

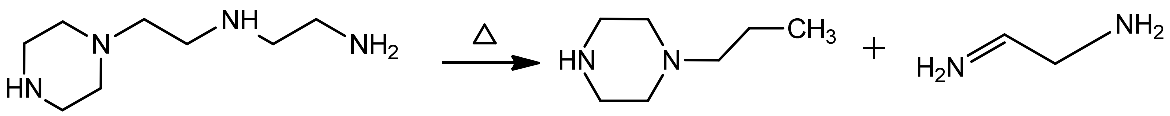

(AEAEPZ) **(EPZ)**

(6)

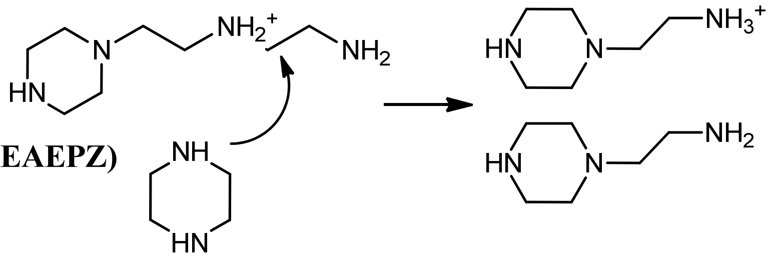

(AEAEPZ) **(PZ)** **(AEP)**

(7)

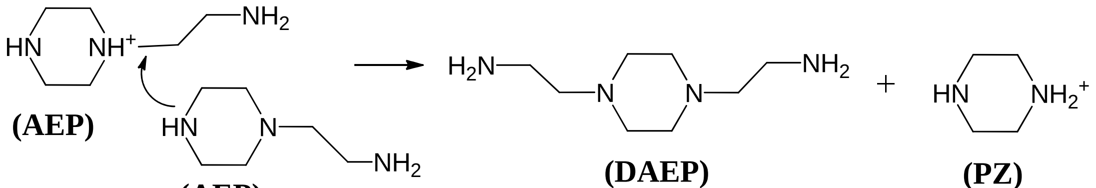

(AEP) **(AEP)** **(DAEP)** **(PZ)**

(8)

The formate and formyl amide (such as NPZ), which are also important degradation products, should result from CO_2 or CO_2-containing molecules. Formate and formyl amide establish equilibrium once they are present in solution but it was not clear yet which was produced first and how it is generated from CO_2 or CO_2-containing molecules.

Conclusions

1. 5 m PZ/2 m AEP is thermally stable up to 150 °C but not 175 °C.
2. The amount of products after 5-week thermal degradation were basically in the following rank order: NH_4^+ > formate > PEP > NPZ, AEAEPZ Urea, an unknown product (retention time of 17.7), penta-amine, HEP > DMPZ, AEAEPZ, DAEP, EPZ
3. NH_4^+ and formate consistently increased during 5-week thermal degradation.
4. PEP, FPZ, AEAEPZ Urea, DMPZ, HEP, penta-amine and an unknown product showed a fast phase in the first week of degradation, followed by a slow or equilibrium process within the following 4 weeks.
5. The concentration of AEAEPZ reached its maximum after 1 to 3 weeks and then decreased during the rest time of the 5-week degradation experiment.
6. DAEP and EPZ were only positively identified by IC after 3 weeks degradation.
7. At 175 °C, the degradation of both PZ and AEP in this blend showed a fast phase in the first week, followed by a slow process in the following 4 weeks. Reversible SN_2 reactions may account for the fast degradation process in first week, and elimination

reactions of AEP and the reaction between PZ and degradation products (such as AEAEPZ) contribute the further slow degradation of PZ/AEP in the following 4 weeks.

8. PZ degradation rate in 5 m PZ/2 m AEP is similar to that of pure PZ at 175 °C for the first 5 weeks, but faster at 150 °C. However, The AEP degradation rate in 5 m PZ/2 m AEP should be slower than that of pure AEP. The different degradation performance of PZ or AEP in blend system and pure system at 150 °C is expected to be the result of synergism/inhibition effect of these two components.

Future Work

The 20–30-week thermal degradation experiment that is ongoing will be completed in the next quarter and longer time point samples will be analyzed. Oxidative degradation experiments and high temperature VLE measurement of this blend will also be performed. A separate effort will be made to further investigate or model the degradation mechanism of PZ/AEP.

Lab safety

Thermal degradation is a high temperature/pressure experiment. In a minor incident, a hot (175 °C) sample cylinder was on a plastic cloth and burned a hole through it. Hot cylinders should not be placed on flammable or temperature sensitive objects. Hot cylinders are always handled with appropriate gloves.

References.

Davis JD. *Thermal Degradation of Aqueous Amines Used for Carbon Dioxide Capture.* The University of Texas at Austin. Ph.D. Dissertation. 2009.

Freeman SA. *Thermal Degradation and Oxidation of Aqueous Piperazine for Carbon Dioxide Capture.* The University of Texas at Austin. Ph.D. Dissertation. 2011.

Amine Degradation in CO_2 Capture

Quarterly Report for January 1 – March 31, 2012

by Alexander Voice

Supported by the Luminant Carbon Management Program

Department of Chemical Engineering

The University of Texas at Austin

April 30, 2012

Abstract

N-nitroso-piperazine (MNPZ) was produced at a net rate of 3.5 µMol/kg/hr in 8 m piperazine (PZ) in the integrated solvent degradation apparatus (ISDA). MNPZ formation was due to production of nitrite from degradation of PZ.

Addition of 7.2 mMol/kg of sodium nitrite to the solution resulted in an equimolar amount of MNPZ formed in less than 24 hours. The MNPZ then degraded over the course of the experiment.

The first-order thermal degradation rate constant of MNPZ at 120 °C was 0.599 day^{-1}, compared with a rate constant of 0.299 day^{-1} in batch cylinders (Rochelle, 2011). The difference is likely due to errors in correctly estimating the temperature and residence time of the amine in various parts of the ISDA. The thermal degradation rate of MNPZ was not affected by the presence of dissolved oxygen.

Geometry of the bubble removal vessel in the ISDA did not affect total formate production. Total formate was not produced in the absence of oxygen.

The presence of manganese increased the oxidation rate of monoethanolamine (MEA) by more than a factor of two. Normalized MEA loss was the same for three solutions with initial MEA concentration from 2.9 to 5.3 mol/kg MEA. No significant difference in MEA loss or total formate production was observed between solutions containing Mn(II), Mn(III), or Mn(IV). In all cases with manganese present, MEA loss leveled out at 70% after six days.

Introduction

Solvent management in amine scrubbing processes for CO_2 capture involves several elements, among others solvent degradation, reclaiming, corrosion, and emissions. This work focuses on two distinct aspects of this problem: (1) oxidation of the solvent by molecular oxygen and (2) formation and destruction of nitrosamines in the solvent.

Nitrosation

Nitrosation of amine solutions occurs as a result of reaction of $NO_2\bullet$ in flue gas to form nitrite ion in the liquid phase, followed by reaction with a secondary amine to form the nitrosamine. Formation of nitramines has also been reported in amine solutions in contact with NO_x.

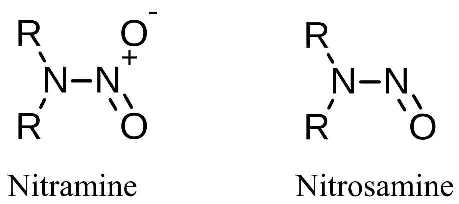

Figure 1: General structures of nitrosamines and nitramines

Nitrosamines via degradation of amine solutions to nitrite and subsequent reaction with a secondary amine to form nitrosamines. Heating degraded MEA solutions containing nitrite to higher temperatures (100 – 150 °C) results in disappearance of nitrite ion in solution, presumably as a result of nitrosamine formation.

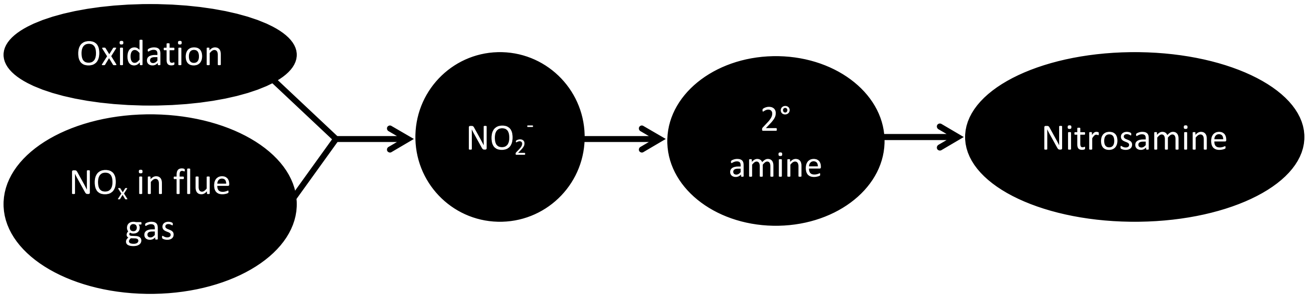

Figure 2: General pathway for nitrosamine production in CO_2 capture

In CO_2 capture solvents containing a secondary amine, such as piperazine, diethanolamine, morpholine, etc., as well as blends containing these, the most likely nitrosamine to be formed is from reaction of nitrite with the solvent. In solutions where the major components are primary or tertiary amines (MEA, methyl-diethanolamine, 2-amino-2-methyl-1-propanol, etc.), the nitrosamine formed will be from reaction of nitrite with one or more degradation products.

Table 1: Nitrosamines expected from various amines for CO_2 capture

Amine	Order	Most likely nitrosamine (s)
Monoethanolamine	1°	n-nitroso-(2-hydroxyethyl)-glycine; n-nitroso-(2-hydroxyethyl)-ethylenediamine; n-nitroso-1-(2-hydroxyethyl)-piperazin-2-one
Diethanolamine	2°	n-nitroso-diethanolamine
Piperazine	2°	n-nitroso-piperazine
Methyl-diethanolamine	3°	n-nitroso-diethanolamine
1-(2-aminoethyl)-piperazine	2°/3°	n-nitroso-piperazine

Previous work has also studied the formation and degradation of MNPZ in PZ solutions at various conditions (Rochelle, 2011). The goal of this work is to determine:

- Rate of formation of MNPZ in a neat 8 m PZ solution in a cycling apparatus;
- Yield of MNPZ from spiking with nitrite in a cycling apparatus;
- Effect of dissolved oxygen on thermal degradation of MNPZ;
- Reaction order of MNPZ in thermal degradation in MNPZ.

Oxidation

Oxidation of MEA occurs by reaction of MEA radical with oxygen to form semi-stable organic hydroperoxides. The decomposition of these peroxides controls the rate of oxidation in MEA solutions. These peroxides can undergo many reactions, including homolytic decomposition, heterolytic decomposition, and metal-catalyzed cyclic homolytic decomposition. Homolytic decomposition of organic hydroperoxides typically has a higher activation energy than heterolytic cleavage; thus heterolytic decomposition is relatively more favorable at low temperature than at high temperature. Heterolytic decomposition is desirable because this halts the oxidation process.

In the metal-catalyzed degradation pathway, the reacting metal species is likely the MEA-metal or MEA carbamate-metal complex, rather than the free metal ion. Complexing agents change the reactivity of metal ions towards peroxides and can change the relative rates of heterolytic and homolytic decomposition.

MEA Hydroperoxide Formation

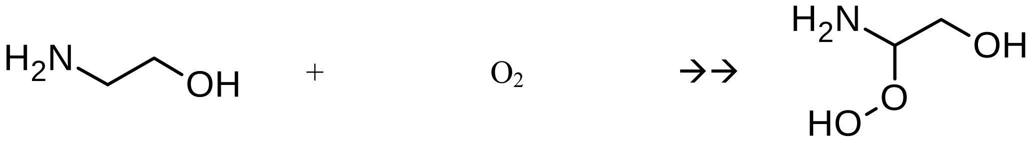

Heterolytic Hydroperoxide Decomposition

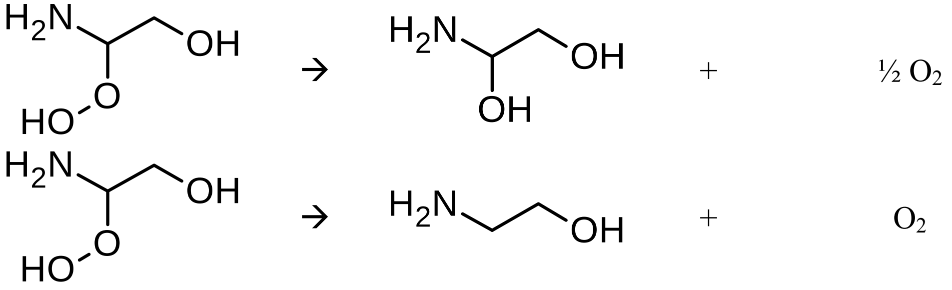

Homolytic Hydroperoxide Decomposition

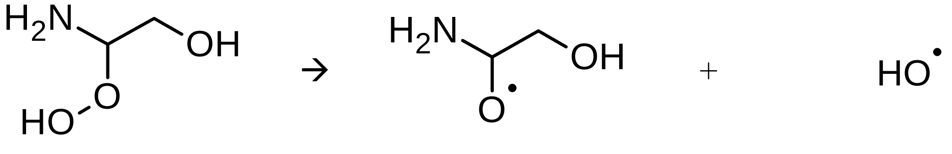

Metal-catalyzed Cyclic Heterolytic Hydroperoxide Decomposition

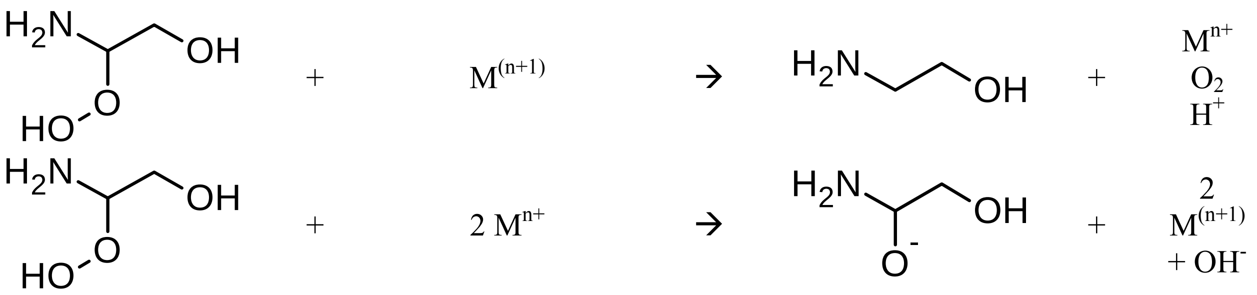

Metal-catalyzed Cyclic Homolytic Hydroperoxide Decomposition

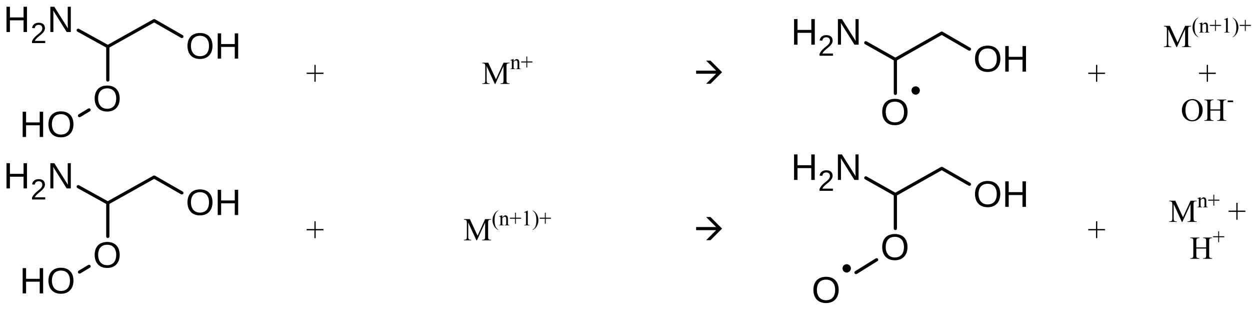

Figure 3: Peroxide decomposition pathways in MEA oxidation

Previous work showed that used MEA received from the SRP pilot plant oxidized more rapidly than a solution of fresh MEA, on the basis of higher rates of MEA loss and formate production in the presence of oxygen (Figures 4 and 5). The enhanced oxidation was potentially due to a variety of factors, including:

- MEA concentration (9 m vs. 7 m MEA);
- Presence of thermal degradation products;
- Presence of metal catalysts from corrosion or other contamination.

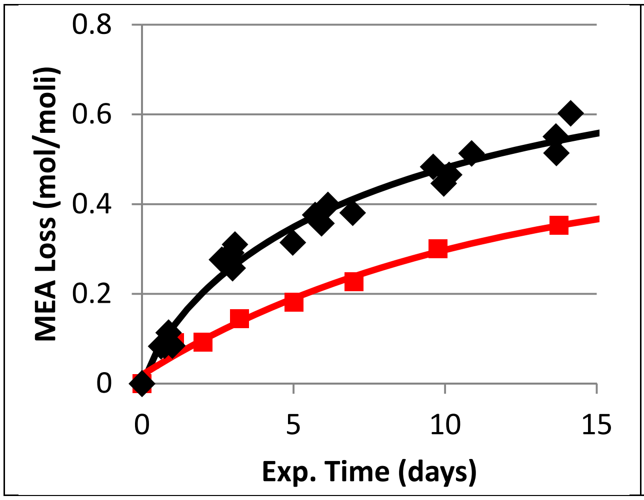

Figure 4: Comparison of MEA loss in fresh and used MEA solutions. Conditions: LGF, 98% O_2, 2% CO_2, 55 °C. 9 m MEA with 0.5 mM Fe as received from SRP (black); 7

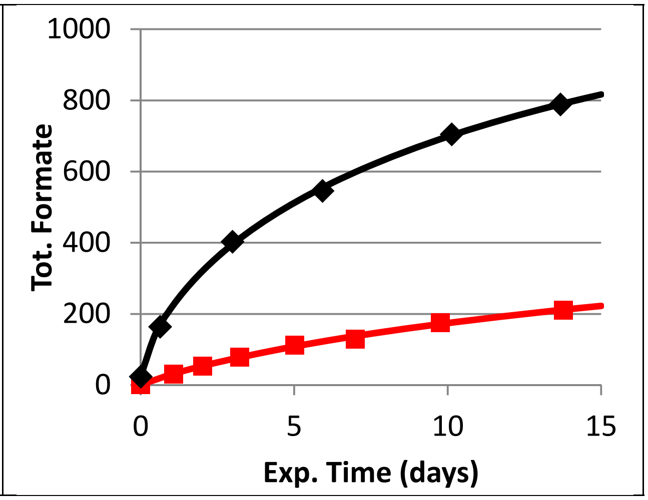

Figure 5: Comparison of formate production in fresh and used MEA solutions. Conditions: LGF, 98% O_2, 2% CO_2, 55 °C. 9 m MEA with 0.5 mM Fe as

m MEA with 0.4 mM Fe^{2+}, 0.1 mM Ni^{2+}, 0.05 mM Cr^{3+} added (red).

received from SRP (black); 7 m MEA with 0.4 mM Fe^{2+}, 0.1 mM Ni^{2+}, 0.05 mM Cr^{3+} added (red).

Both solutions contained similar amounts of iron, however the possibility existed for the presence of undetectable amounts of manganese in the pilot plant sample due to corrosion of type 304 stainless steel (contains 2% Mn).

Previous work indicated the potential for manganese to be a potent catalyst of MEA oxidation at low concentration on the basis of substantial increased rates of ammonia production upon addition of $MnSO_4$ to the reactor (Figure 6).

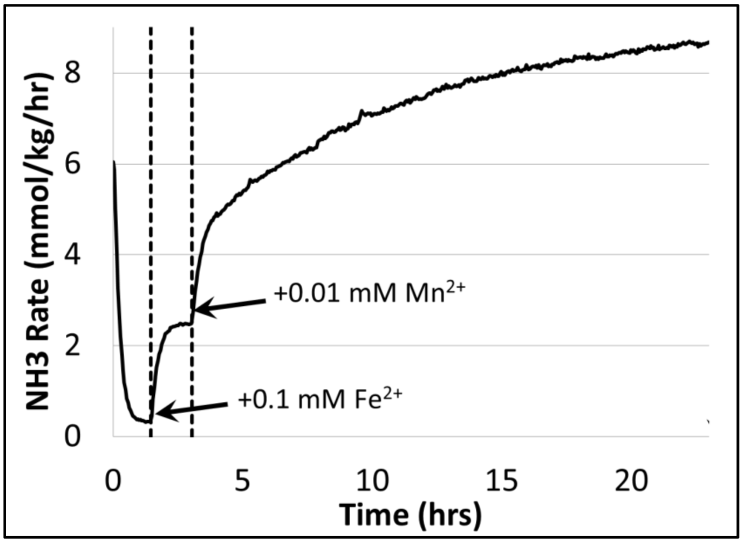

Metals	*NH_3 Rate*
None added	0.33
0.1 mM Fe	2.5
0.1 mM Fe^{2+} + 0.01 mM Mn^{2+}	8.6
0.1 mM Fe^{2+} + 0.25 mM Mn^{2+}	9.7
0.1 mM Fe^{2+} + 0. 50 mM Mn^{2+}	11.6
0.1 mM Fe^{2+} + 1.00 mM Mn^{2+}	12.6
1.0 mM Fe^{2+} + 1.00 mM Cu^{2+}	6.6
1.0 mM Fe^{2+} + 1.00 mM Mn^{2+} + 1.00 mM Cu^{2+}	11.6

Figure 6: NH_3 rates from 7 m MEA oxidized with 98% air and 2% CO_2 in the high gas-flow apparatus at 70 °C in the presence of added iron and manganese salts

The purpose of this work is to:

- Verify that manganese is a catalyst of MEA oxidation with a long-term oxidation experiment (in the LGF apparatus);
- Assess the catalytic potency of various oxidation states of manganese (II, III, IV);
- Determine the effect of initial MEA concentration on the MEA oxidation rate.

Experimental Methods

Experimental methods are unchanged from those described in previous work.

Experimental results discussed in this report used the following apparatuses:

- Low gas-flow (LGF) oxidation reactor (55–70 °C; 98% O_2, 2% CO_2) (Freeman, 2011);

- Integrated solvent degradation apparatus (ISDA) (55 °C/120 °C; 98% O_2, 2% CO_2) (Closmann, 2011).

Analytical methods employed in this work have also been previously described in detail. These include:

- Cation chromatography (amine concentration) (Freeman, 2011);
- Anion chromatography (formate concentration, total formate amide concentration) (Freeman, 2011);
- Reverse-phase HPLC with UV detection (nitrosamine concentration) (Rochelle, 2011).

Results

Results are presented for two types of experiments: (1) nitrosamine formation and destruction in the ISDA, and (2) oxidative degradation of MEA in the LGF.

Nitrosamine Formation and Destruction in the ISDA

Nitrosamine formation and destruction in the ISDA was studied for neat 8 m PZ, and with addition of potassium nitrite (Figure 8). Nitrosamine formation in the neat solution occurred at a net rate of 3.5 μmol/kg/hr. Nitrosamine formation in the neat solution was due to production of nitrite via oxidation of PZ, followed by reaction of nitrite with PZ at high temperature to form nitrosamine.

Addition of 15.1 mMol/kg of potassium nitrite to the solution resulted in rapid conversion to MNPZ. The yield was 59%, which is the yield observed in previous similar experiments (in a different apparatus). Thermal degradation of MNPZ followed first order kinetics with a kinetic rate constant of 5.99 day^{-1}, assuming thermal degradation only occurred in the high temperature reactor (at 120 °C), which was 6.5% of the total system inventory. The degradation rate was not affected by the presence of dissolved oxygen in the system.

This rate constant is different than the rate constant reported for batch systems (3.99 day^{-1}) reported previously (Rochelle, 2011). The discrepancy is likely due to errors in accurately estimating the temperature/residence time profile of the ISDA. In other words, the discrepancy could be due to:

- Greater than 6.5% of the inventory in the high-temperature reactor;
- Temperature gradient (hot spots) in the high-temperature reactor or pre-heater;
- Thermal degradation occurring in the pre-heater and cross-exchanger.

Total formate production in the ISDA with the new bubble removal vessel exactly matched formate production in previous work (Figure 7). The new bubble removal vessel was 1.5" OD x 11.5" tall (20 in^3) whereas the old one was 4.0" OD x 2.5" tall (30 in^3) (Figure 2).

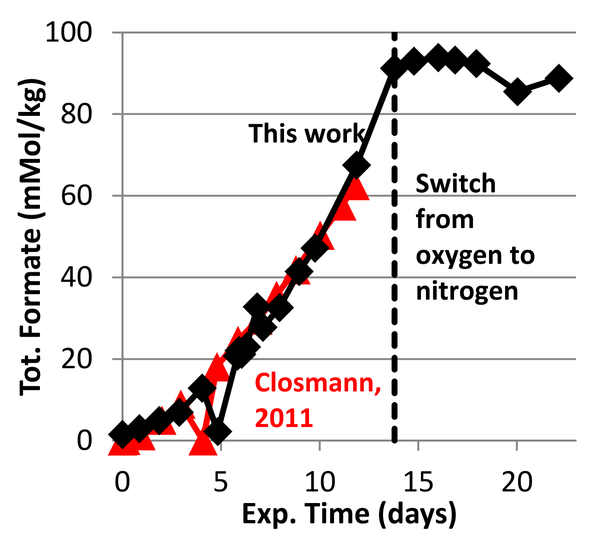

Figure 7: Formate detected after sodium hydroxide treatment in samples from the ISDA. Conditions: 8 m PZ cycled with 98% O_2 + 2% CO_2 from 55 °C to 120 °C at 200mL/min, 130 mL holdup at 120 °C. Black: This work, inventory=2.0 L. Red: reported by Closmann (2011), inventory=2.4 L. Dashed line: nitrogen instead of oxygen flow to the oxidative reactor.

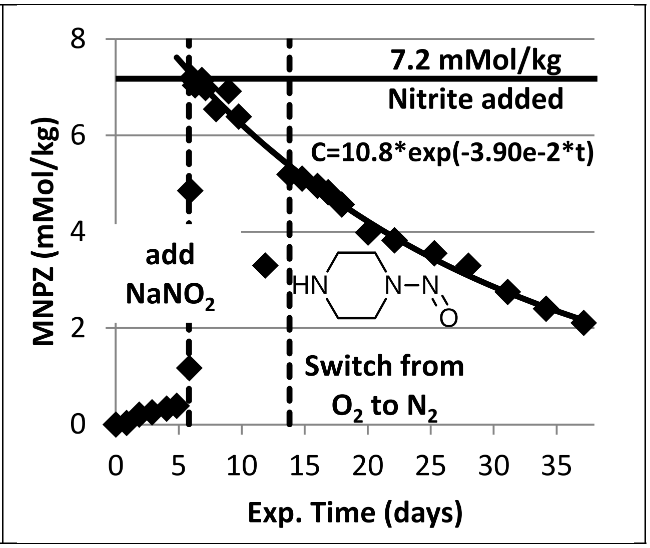

Figure 8: MNPZ formation and destruction in 8 m PZ in the ISDA, before and after addition of potassium nitrite. Conditions: 8 m PZ cycled with 98% O_2 + 2% CO_2 from 55 °C to 120 °C, 6.5% holdup at 120 °C, 200 mL/min circulation rate, 2.0 L inventory, 130 mL holdup at 120 °C (6.5%). First order MNPZ degradation rate constant k = -0.599 day^{-1}.

Table 2: Raw data from nitrosation of 8 m PZ in the ISDA with $NaNO_2$. Conditions: 8 m PZ cycled with 98% O_2 + 2% CO_2 from 55 °C to 120 °C, 6.5% holdup at 120 °C, 200 mL/min circulation rate, 2.0 L inventory, 130 mL holdup at 120 °C (6.5%). First order MNPZ degradation rate constant k = -0.599 day^{-1}.

Time	**MNPZ (mMol/kg)**	**Total Formate (mMol/kg)**
0.00	0.00	1.54
0.86	0.03	2.97
1.86	0.21	4.95
2.88	0.25	6.97
4.04	0.33	12.89
4.83	0.39	2.26
5.83	1.17	20.75
5.91	4.86	22.09

6.04	7.19	21.19
6.29	7.04	23.00
6.83	7.15	32.81
7.12	6.98	27.82
7.96	6.55	32.63
8.96	6.92	41.47
9.76	6.39	47.20
11.87	3.30	67.52
13.79	5.19	91.24
14.78	5.10	92.99
16.01	4.95	93.87
16.86	4.82	93.26
17.94	4.57	92.39
20.03	3.98	85.51
22.13	3.83	88.79
22.13	3.83	
25.28	3.55	
28.00	3.30	
31.11	2.75	
34.16	2.40	
37.15	2.11	

Oxidative Degradation of MEA in the LGF

Oxidative degradation was studied in the LGF in the presence of additives, including manganese, iron, and formic acid. Oxidation was most rapid in the presence of 0.5 mM Mn^{2+} (added as $MnSO_4$) (Figure 9 and 10). Mn(III) and Mn(IV) (added as MnF_3 and MnO_2, respectively) also catalyzed oxidation, although neither was fully soluble at 0.5 mM (Figures 11 and 12). Three concentrations of MEA were tested between 2.9 and 5.3 mol/kg to determine the effect of initial MEA concentration (Figure 13). MEA loss as a percent of initial concentration was independent of initial MEA concentration, indicating first order behavior (Figure 14). All MEA solutions oxidized in the presence of manganese leveled out at 70% MEA loss (Figures 14 and 11).

MEA loss was inhibited by 2.5 mol/kg formic acid added at the start of the experiment (Figure 14). The effect was not due to a change in the MEA concentration or the pH of the solution (measured as 9.1–9.3) for solutions with and without formic acid. The inhibiting effect is likely due a change in the ionic strength of the solution, a change in the redox potential of the metal ion from complexing with the formate ion, or, relatedly, a change in the CO_2 loading (Figure 15).

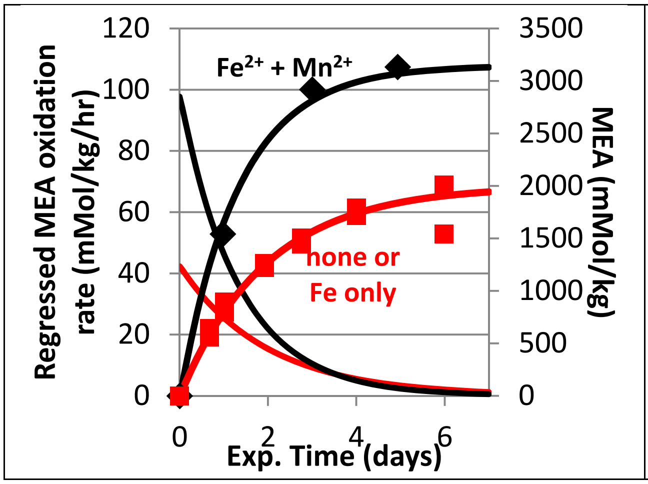

Figure 9: Comparison of MEA loss and oxidation rate in the low gas flow apparatus for two solutions at 70 °C with 98% O_2 and 2% CO_2 in the presence of 0.5 mM Mn^{2+} and 0.1 mM Fe^{2+} (black) and 0.1 mM Fe^{2+} or no added metal (red).

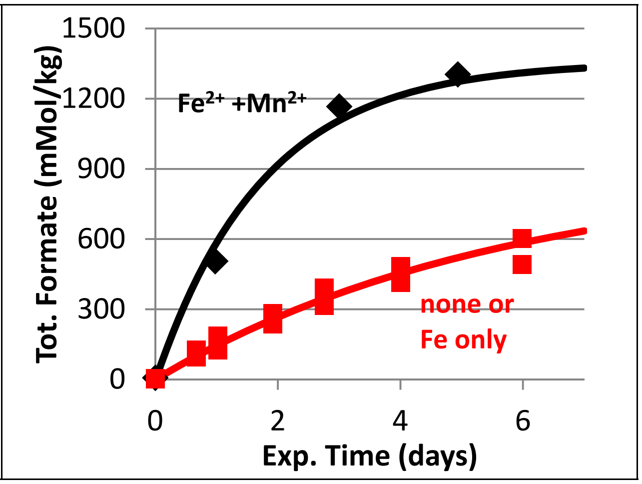

Figure 10: Comparison of total formate production in the low gas flow apparatus for two solutions at 70 °C with 98% O_2 and 2% CO_2 in the presence of 0.5 mM Mn^{2+} and 0.1 mM Fe^{2+} (black) and 0.1 mM Fe^{2+} or no added metal (red).

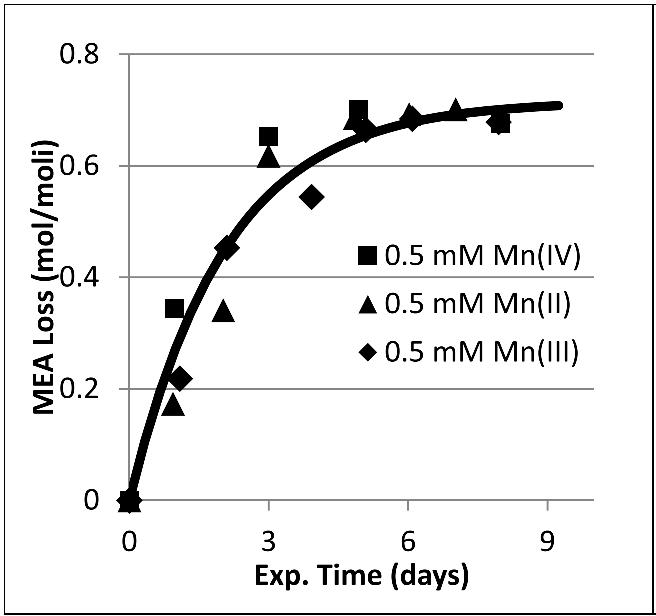

Figure 11: Fractional MEA loss in the low gas flow apparatus at 70 °C with 98% O_2 and 2% CO_2 in the presence of 0.1 Fe and 0.5 mM Mn^{2+}, Mn^{3+}, or Mn^{4+}.

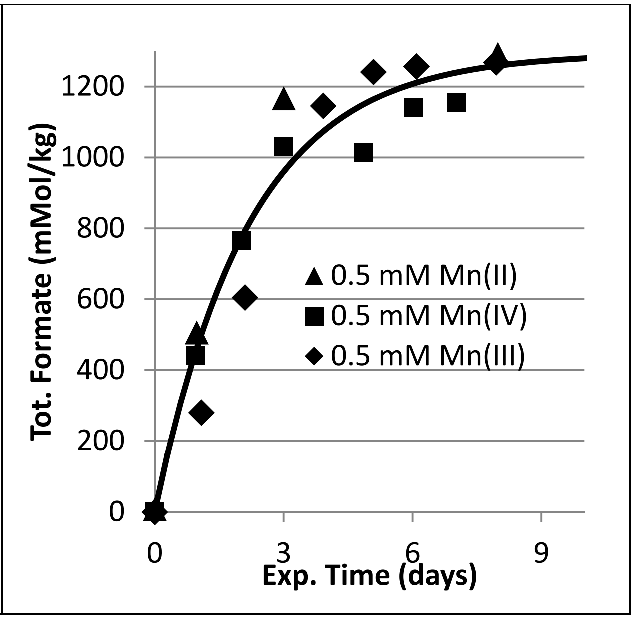

Figure 12: Total formate production in the low gas flow apparatus at 70 °C with 98% O_2 and 2% CO_2 in the presence of 0.1 Fe and 0.5 mM Mn^{2+}, Mn^{3+}, or Mn^{4+}.

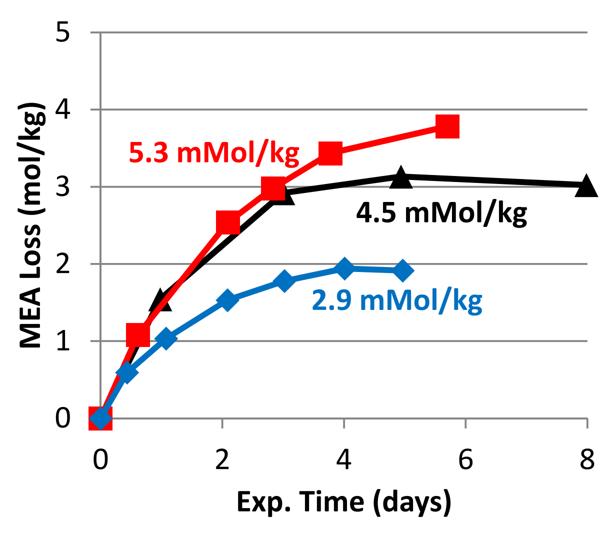

Figure 13: MEA loss in the low gas flow apparatus at 70 °C with 98 % O_2 and 2% CO_2 in the presence of 0.5 mM Mn^{2+} and 0.1 mM Fe^{2+} at three different initial concentrations of MEA.

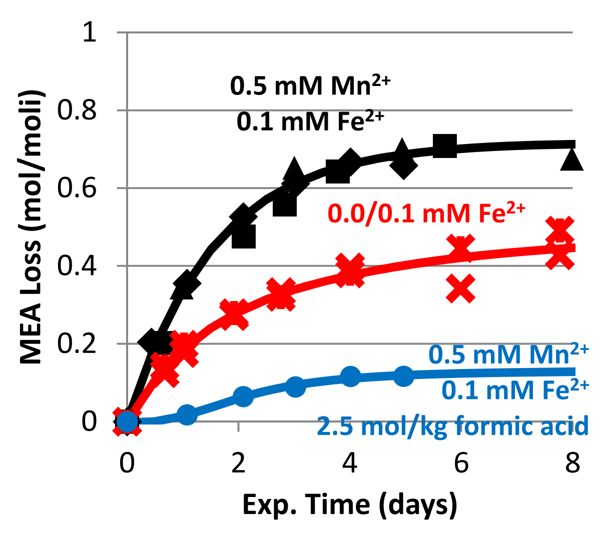

Figure 14: Fractional MEA loss in the low gas flow apparatus at 70 °C with 98 % O_2 and 2% CO_2. In the presence of Fe^{2+} and Mn^{2+}, Fe^{2+} only, no metal ions added, or Fe^{2+}, Mn^{2+}, and formic acid

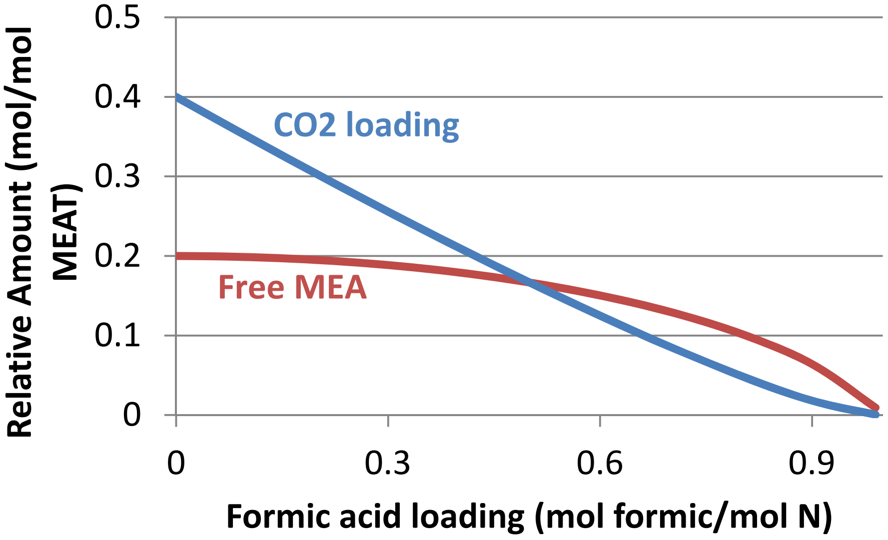

Figure 15: CO_2 loading and free MEA as a function of formic acid loading in equilibrium with 2 kPa CO_2 at 55 °C

Table 3: Raw data from oxidation of MEA in the low gas flow with various additives. Conditions: 70 °C with 98 % O_2 and 2% CO_2, initially 7 m MEA at 0.4 loading (4.5 mol/kg) except where noted.

No metals added			0.1 mM $FeSO_4$			0.1 mM $FeSO_4$, 0.5 mM $MnSO_4$, 2.6 mol/kg formic acid		
Time (days)	MEA (mol/kg)	Total Formate (mMol/kg)	Time (days)	MEA (mol/kg)	Total Formate (mMol/kg)	Time (days)	MEA (mol/kg)	Total Formate (mMol/kg)
0.00	4.5	4.7	0.00	4.5	3.3	0.00	4.7	2530
0.67	3.9	97.1	0.67	4.0	126.1	0.43	4.7	2735
1.02	3.6	126.1	1.02	3.7	187.7	1.08	4.6	2629
1.92	3.3	239.1	1.92	3.3	283.0	2.09	4.4	3715
2.76	3.1	316.1	2.76	3.0	392.1	3.02	4.2	2653
4.00	2.8	415.2	4.00	2.7	483.6	4.01	4.1	2600
5.99	2.5	491.0	5.99	3.0	602.9	4.96	4.1	2586
7.77	2.3	705.5	7.77	2.6	679.5	0.00	4.7	2530

0.1 mM $FeSO_4$, 0.5 mM $MnSO_4$,			0.1 mM $FeSO_4$ + 0.5 mM MnF_3			0.1 mM $FeSO_4$ + 0.5 mM MnO_2		
Time (days)	MEA (mol/kg)	Total Formate (mMol/kg)	Time (days)	MEA (mol/kg)	Total Formate (mMol/kg)	Time (days)	MEA (mol/kg)	Total Formate (mMol/kg)
0.00	4.5	8	0.00	4.5	0	0.00	4.5	0
0.98	2.9	506	1.08	3.5	280	0.94	3.7	442
3.00	1.6	1167	2.10	2.5	605	2.02	3.0	765
4.94	1.3	1304	3.92	2.1	1145	3.00	1.7	1031
7.98	1.4	1292	5.09	1.5	1241	4.85	1.4	1014
10.98	1.2	1181	6.09	1.4	1257	6.02	1.4	1140
14.00	1.6	1492	7.95	1.5	1268	7.02	1.4	1156

0.1 mM $FeSO_4$, 0.5 mM $MnSO_4$, 5.3 mol/kg MEA			0.1 mM $FeSO_4$, 0.5 mM $MnSO_4$, 2.9 mol/kg MEA		
Time (days)	MEA (mol/kg)	Total Formate (mMol/kg)	Time (days)	MEA (mol/kg)	Total Formate (mMol/kg)
0.00	5.3	4.7	0.00	2.9	4.3

0.67	4.3	97.1	1.08	2.3	220
1.02	2.8	126.1	2.10	1.9	343
1.92	2.4	239.1	3.92	1.4	493
2.76	1.9	316.1	5.09	1.1	588
4.00	1.6	415.2	6.09	1.0	612
5.99	5.3	491.0	7.95	1.0	632
7.77	4.3	705.5			

Conclusions

- The rate of formation of MNPZ in 8 m PZ in the presence of 100% oxygen was 3.5 µmol/kg/hr.
- The rate constant for thermal degradation of MNPZ at 120 °C in the ISDA was 0.599day^{-1}.
- The initial rate of MEA oxidation was increased by 230% by the presence of manganese over iron alone in the low gas flow apparatus.
- MEA loss in the presence of manganese in the low gas flow apparatus was first order in MEA concentration.
- Mn(II), Mn(III), and Mn(IV) were all potent catalysts of MEA oxidation and did not exhibit substantively different behavior as oxidation catalysts.
- Formic acid inhibited MEA oxidation in the low gas flow apparatus at high (2.5 mol/kg) concentrations.

References

Closmann F. *Oxidation and thermal degradation of methyldiethanolamine/piperazine in CO_2 capture*. The University of Texas at Austin. Ph.D. Dissertation. 2011.

Freeman SA. *Thermal degradation and oxidation of aqueous piperazine for CO_2 capture*. The University of Texas at Austin. Ph.D. Dissertation. 2011.

Rochelle GT et al. “CO_2 Capture by Aqueous Absorption, Fourth Quarterly Progress Report 2011.” Luminant Carbon Management Program. The University of Texas at Austin. 2012.

Aerosol and Volatile Emission Control in CO_2 Capture

Quarterly Report for January 1 – March 31, 2012

by Steven Fulk

Supported by the Luminant Carbon Management Program

Department of Chemical Engineering
The University of Texas at Austin

April 30, 2012

Abstract

In this quarter, an aerosol growth model was developed in Microsoft® Excel to gain a semi-quantitative understanding of aerosol size behavior throughout an absorber with a water wash section. Heat and mass transfer to aerosol particles was assumed to have negligible impact on the bulk gas and liquid mass and energy balances. Gas-phase properties for integration were calculated from Aspen Plus® simulations using a modified version of the Fawkes model developed in the Rochelle group. Mass, heat, and momentum balances for aerosol particles were modeled assuming homogeneous spheres traveling through an infinite, quiescent gas.

H_2O and piperazine (PZ) mass transfer were assumed to be gas-film controlled; however, CO_2 mass transfer was found to be liquid-film controlled for particle sizes down to 5 μm and initial PZ concentrations greater than 1 molal. Particles less than 0.1 μm are in equilibrium to CO_2 for any starting PZ concentration.

Aerosol size is driven by water mass transfer since gas phase concentrations of PZ are very low and CO_2 quickly reaches equilibrium upon entering the absorber or further upstream where nucleation sites first become available. Water mass transfer dominates the all latent effects in the aerosol such that the heat flux to the droplet equals the latent heat of condensation or evaporation. The aerosol is at the wet bulb temperature of the gas.

Goals for next quarter include coding a steady-state mass and heat transfer model into Matlab® with a long term goal of including sulfuric acid into rigorous speciation calculations.

Introduction

Volatile emissions are a primary concern for CO_2 capture plants using amine scrubbers. Emissions constitute increased economic expense through solvent loss as well as being a source of potentially hazardous environmental pollutants. Compounds found in treated flue gas include contaminants from thermal degradation and oxidation as well as combustion byproducts. Degradation and reaction products have a wide range of toxicity and biodegradation characteristics which potentially represent unacceptable emissions; as a result, recent work has focused on estimating volatile losses and assessing their toxicological impact.

Volatile emissions can be reduced through the use of an absorber column using recycled water as a solvent, called a water wash. Design considerations for water wash systems include liquid distribution methods to adequately wet packing with small liquid rates, and balancing water in the absorber/stripper system by adjusting the total volatile concentration in the wash water. Water wash columns have relatively flat efficiency profiles, meaning the removal efficiency is not a strong function of either the gas or liquid flow rates or the operating temperature. Water wash columns are usually a small fraction of the absorber height and have low pump-around rates so capital expenditure is not likely an issue.

Recent pilot plant studies have shown that even properly designed water wash systems can significantly underperform. The drop in performance has been linked to amine absorption into aerosols that leave with the scrubbed flue gas.

Emissions with Aerosols

A presentation by Mitsubishi Heavy Industries (MHI) and a joint presentation from SINTEF and Netherlands Organization for Applied Scientific Research (TNO) both pointed to pilot plant campaigns in which amine emissions were higher than predicted. In both instances, aerosol formation was the cause of excessive amine loss.

MHI analyzed gas leaving the wash section for amine emissions while varying the inlet SO_3 concentration. Collected data for cases run with KS-1^{TM} and monoethanolamine (MEA) solvents showed that amine emissions were proportional to inlet SO_3 concentration. White "smoke," most likely sulfuric acid mist, was observed in clear piping at the exit of the wash section. The study recommends stricter SO_3 control to minimize acid aerosol formation. Table 1 provides abbreviated emissions data from MHI campaigns leading to the conclusion of the impact of SO_3 on volatile amine loss.

Table 1: MHI pilot plant results of the influence of SO_3 on amine emissions

	Amine Concentration at Wash Outlet	
Inlet SO_3 (ppm)	KS-1^{TM} (ppm)	MEA (ppm)
0	0.4	0.8
1	9.1	29.8
3	23.2	67.5

Joint work from TNO and SINTEF on the Maasvlakte CO_2 capture pilot plant found that quality of the flue gas and characteristics of the temperature bulge in the absorber influenced the growth of aerosols on heterogeneous nuclei. A Brownian demister was added downstream from the water wash and showed a significant decrease in amine emissions at the expense of roughly doubling the pressure drop in the absorber/water wash section.

Both studies illustrate the need to qualitatively and quantitatively understand how flue gas and CO_2 capture system design parameters can influence the creation and growth of aerosols so proper mitigation techniques can be employed.

Work Goals

It is the initial goal of this work to develop a basic understanding of how conditions in the absorber and water wash column directly lead to aerosol growth or shrinkage due to condensation and evaporation using combined heat and mass transfer modeling.

Though water wash systems cannot capture small aerosols directly, they may be useful for growing aerosols to sizes more suitable for removal. Design of the water wash may ultimately be linked to providing residence time for aerosol growth since the required packing height to remove compounds not partitioned to aerosols is far less.

Work in this quarter includes initial efforts to model changes in aerosols as they travel through both the absorber and water wash columns. The first version of an aerosol growth model was created in Microsoft® Excel using visual basic (VBA) to perform an Euler-type integration of a homogeneous particle traveling through a pre-specified gas-phase taken from Aspen Plus® simulations. Basic model structure will be presented in this work.

Aerosol Sources

Nucleation sites for aerosols can be created in a variety of ways from combustion. Damle et al. (1982) reviewed possible mechanisms for aerosol formation in coal combustion in an attempt to explain experimentally observed data on composition and size distribution of nucleation sites. Experimental size distributions of particulate matter from coal combustion show bimodal characteristics. The "fine" mode (mean diameter ~ 0.1 μm) consists of homogeneous sulfuric acid droplets and heterogeneous, hard-centered particulate matter. The "coarse" mode (mean diameter ~ 1 μm) is primarily heterogeneous fly-ash particles and cenospheres.

Post-combustion processing can effectively remove most potential aerosol sources by impaction or electrostatic removal; however, finite nucleation is still present. In some cases, removal of other pollutants can result in more aerosol formation potential. For instance, selective-catalytic-reduction increases gaseous SO_3 which leads to more sulfuric acid aerosol.

Once flue gas reaches the direct contact cooler before the CO_2 absorber, particulate matter will be between 0.1 and 5 μm. Possible nucleation sites include residual acid aerosol, heterogeneous ash, and nucleated water droplets. It is unclear at this point to what extent nucleation takes place in the absorber or water wash. Large temperature gradients can lead to homogenous nucleation of water or amine. Anecdotal evidence from pilot plant campaigns as well as laboratory measurements indicates possible aerosol formation, though the mechanism is unclear.

Aerosol Model Development

Reference Frame

The choice of reference frame for mass and heat transfer calculations can change a problem from a transient balance to one of steady-state. For instance, a sphere traveling through a gas can be modeled as a fixed-position sphere in a varying gas stream (Lagrangian reference frame), or droplets and gas moving concurrently through a fixed volume (Eulerian reference frame). The former case is a transient balance over a particle as a moving gas transfers heat and mass over time. The latter case represents a steady-state balance over finite sections in a two-phase transfer process.

Transient balances are useful for providing insight into transfer resistances and equilibrium assumptions. Initial calculations on transfer rates can determine the time required to reach equilibrium. If the time to approach equilibrium is significantly less than the overall system residence time, separation calculations can be performed using equilibrium stages rather than rate-based calculations. However, transfer calculations for multiple particle sizes as they appear and disappear in systems can be quite cumbersome. The steady-state formulation of aerosol distributions moving with a gas phase simplifies balances to summations of transfer rates to many discrete liquid phases of varying sizes.

Both formulations of the transfer problem reduce to sets of differential-algebraic equations which vary with column position and/or time. The Microsoft ® Excel model developed in this work is a transient model of a fixed aerosol in a varying gas phase. The steady-state form of the model is currently under development in Matlab®.

Differential Balances

Momentum

Transport properties including mass and heat transfer coefficients as well as particle acceleration are all dependent on the relative velocity of the droplet to the bulk gas phase. A force balance (momentum) on a particle is used to determine the acceleration, and subsequently, the velocity of the droplet as it grows and shrinks in a system.

Gravity acts to pull the particle downward, whereas drag and buoyancy cause the aerosol to move upwards. The drag force on the particle is calculated using a drag coefficient as shown in Equation 1, and Equation 2 shows the effective gravitational force. The balance of these forces yields the net force, and when divided by the particle mass, gives the droplet's acceleration, as shown in Equation 3.

$$F_D = \frac{1}{2}\,\rho_G\,v_{Rel}^{\,2}\,C_D\,A_{Proj} \tag{1}$$

$$F_w = m_{Drop}\left[1 - \frac{\rho_G}{\rho_L}\right] g \tag{2}$$

$$a_{Drop} = \frac{3\,C_D\,v_{Rel}^{\,2}}{4\,d_{Drop}}\,\frac{\rho_G}{\rho_L} - \left[1 - \frac{\rho_G}{\rho_L}\right] g \tag{3}$$

The drag coefficient is a function of the Reynold's number. The drag coefficient tends to decrease as the Reynold's number increases in the laminar region. As the fluid transitions to the turbulent region, there is a sharp decrease in the drag coefficient.

The area of interest for particle calculations is for small Reynold's numbers (Re < 100). Under these conditions the Navier-Stokes equations can be solved neglecting inertial terms. The analytical solution is termed Stokes, or creeping flow. The drag on a sphere under these circumstances has been shown to be 24/Re. As particles increase in size or for high gas velocities, corrections to the Stokes drag coefficient must be made. A simple corrective factor can be included, as shown in Equation 4, which extends confidence in drag coefficient calculations up to about Re = 1000. Figure 1 shows the fit of Equation 4 to experimentally determined drag coefficient of a smooth sphere. The dashed line represents the Stokes drag coefficient.

$$C_D = \left(\frac{24}{Re^G}\right)\left(1 + 0.15\left[Re^G\right]^{0.687}\right) \tag{4}$$

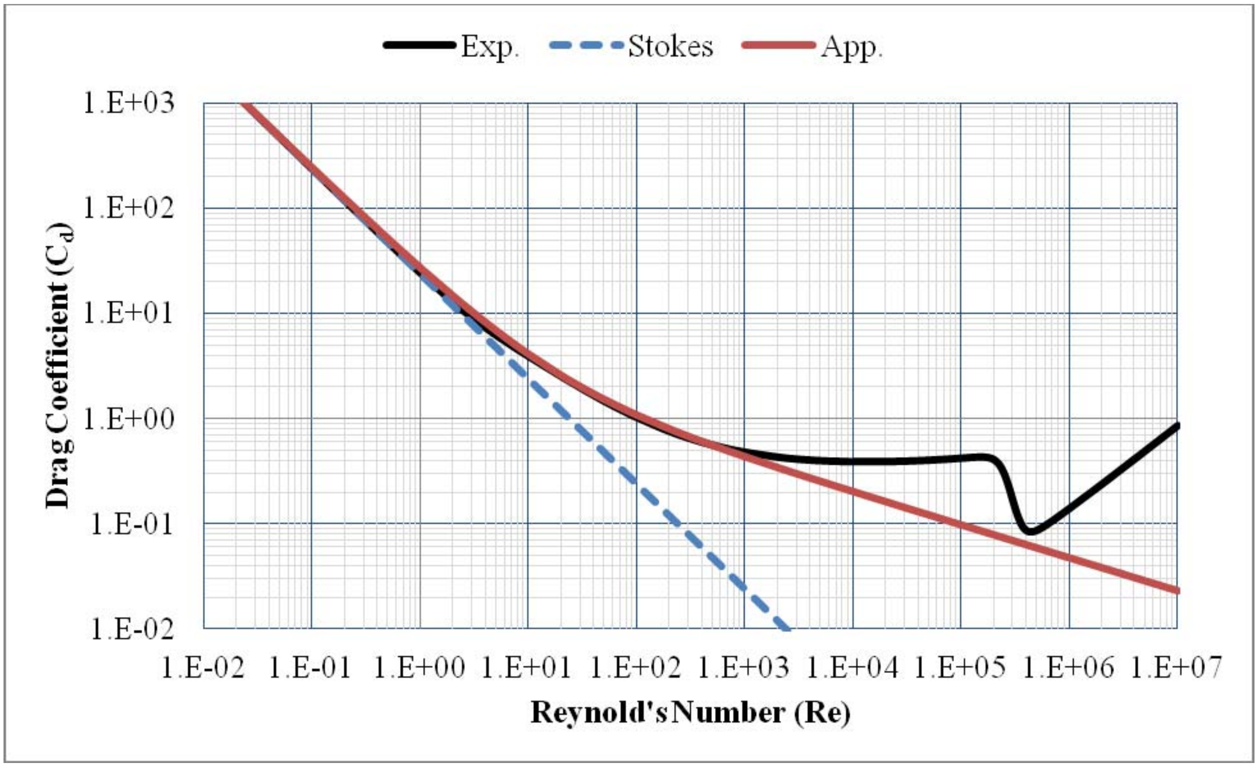

Figure 1: Smooth sphere drag coefficient variation with Reynold's number.

The Stokes form of the drag coefficient is advantageous because the momentum balance becomes a closed-form equation which can be solved directly for the relative velocity of the particle without requiring iteration. The initial velocity of a particle used in calculations assumes Stokes flow such that no iteration is required to initialize calculations. For small particles (< 20 μm) any error introduced by this assumption is negligible.

At each calculation step in the growth model, the acceleration is multiplied by the time step to determine the updated particle velocity. The particle velocity is subtracted from the gas-phase velocity to calculate the relative velocity used to update the Reynold's number, and subsequently the drag coefficient.

Mass

Mass transfer to and from the particle is calculated using mass transfer correlations developed for external flow around hard, perfect spheres. The classic formulation of mass transfer to a sphere for Re < 100 was developed by Frössling (1938). The analytical solution for the Sherwood number under low Reynold's number conditions is 2. Frössling proposed simple corrections to the Sherwood number by including Reynold's and Schmidt terms as shown in Equation 5.

$$Sh_i^G = 2 + 0.6\left(Re^G\right)^{\frac{1}{2}}\left(Sc_i^G\right)^{\frac{1}{3}} \qquad (5)$$

Mass transfer coefficients for gas-film controlled components (H_2O and PZ) are calculated using the corrected Sherwood number correlation.

CO_2 transfer rates using the Frössling (gas-film controlled) approach are significantly higher than those calculated using liquid-film resistance; however, for low amine concentrations and small particle sizes, the transfer rate of CO_2 is essentially instantaneous.

CO_2 solubility correlations are used to calculate equilibrium partial pressures of CO_2 as a function of temperature and loading. The equilibrium loading correlation can be rearranged and solved in terms of an equilibrium loading for a given CO_2 partial pressure using the quadratic equation. Equation 6 is the CO_2 solubility correlation and Equation 7 shows the solution for equilibrium loading for a given a gas-phase partial pressure of CO_2. If the total moles of amine are known, the total amount of CO_2 required to reach equilibrium can be directly calculated. There is always one positive and negative root for the quadratic loading equation; therefore, no selection criteria must be employed.

$$P^{*}_{CO_2} = \exp\left[A + \frac{B}{T_L} + C\,\alpha^2 + D\,\frac{\alpha}{T_L} + E\,\frac{\alpha^2}{T_L}\right] \qquad (6)$$

$$\alpha = \frac{-\left[\frac{D}{T_L}\right] \pm \sqrt{\left[\frac{D}{T_L}\right]^2 - 4\left[C + \frac{E}{T_L}\right]\left[A + \frac{B}{T_L} - \ln\left[P^{g}_{CO_2}\right]\right]}}{2\left[C + \frac{E}{T_L}\right]} \qquad (7)$$

Energy

The Lewis number provides insight into the ratio of heat to mass transfer for convective processes. If the Lewis number is unity, which occurs for low Reynold's number conditions, then the ratio of the Nusselt to Sherwood number is also unity. Therefore, the same correlation used to calculate mass transfer coefficients can be used to calculate heat transfer coefficients. Since aerosols meet many of these criteria, the Frössling correlation is used to calculate the Nusselt number which is used to get the heat transfer coefficient of the gas to the droplet. However, the Schmidt number, which is the ratio of momentum to mass diffusivity, was replaced by its thermal diffusivity counterpart, the Prandtl number, as detailed in Equation 8.

$$Nu^{G} = 2 + 0.6\,(Re^{G})^{\frac{1}{2}}(Pr^{G})^{\frac{1}{3}} \qquad (8)$$

The total heat transferred to and from the gas phase includes conduction due to the temperature difference between the bulk phases, and convection due to mass transfer. When the conductive heat transfer is balanced with latent heat transfer (convection), the "wet bulb" temperature of the gas is reached. The temperature of the liquid droplet will approach the wet bulb temperature of the gas for nearly any condition since reaction rates are not considerable for transfer into droplets.

Model Formulation/Assumptions

All bulk gas properties are copied from converged Aspen Plus® simulations and are inserted directly into Microsoft® Excel. Gas-phase properties are linearly interpolated between calculation points.

Liquid-phase properties are calculated using correlations developed in the Rochelle group and from the DIPPR® database. Physical properties are calculated using the same correlations as Aspen Plus® where applicable. Liquid-mixture heat capacity was regressed for calculation convenience using a simple quadratic mixing rule to calculate excess enthalpy. Property correlations are all based on apparent component mole or mass fractions and therefore do not require speciation calculations. As a consequence, equilibrium agreement between rigorous Aspen Plus® calculations and the developed aerosol model are limited by experimental uncertainty contained in empirical correlations. The models most closely agree for the range of experimental data; there may be significant differences in extrapolation.

The initial conditions for the particle input to the model include the following:

- Diameter
- Temperature
- Amine concentration
- CO_2 loading
- All absorber/water wash column and gas-phase information

The initial velocity of the particle is calculated using Stokes drag coefficient of $C_D = 24/Re$ and assuming zero initial acceleration. It is assumed that the particle has reached its settling velocity with the gas entering the column.

The resulting model formulation consists of differential and algebraic equations. All algebraic equations are solved from differential balance variables: moles of each species, temperature, and velocity. Each calculation step involves feeding all algebraic properties to the differential balances, numerically integrating over a small finite time step, and returning the variables into the algebraic function loop. The Microsoft® Excel model performs the integration using a first-order (Euler) integration method with a fixed time step.

The full set of equations, both algebraic and differential, as well as a table of all correlation parameters, variable definitions, and required units can be found in the appendices.

Results

CO_2 Equilibrium Assumption

The first part of this study into aerosol growth included determining the dominant film resistance for CO_2 transfer to a small particle. Assuming gas-phase resistance implies that the relationship between transfer rates of components is entirely dependent on the gas-phase diffusion coefficient. The liquid film, under a majority of realistic conditions, dominates CO_2 mass transfer resistance. However, particles are so small that even liquid-side mass transfer rates for CO_2 may be large enough to assume that equilibrium is achieved in very short time scales.

Figures 2 and 3 show the calculated time to approach 99.9% of equilibrium in CO_2 using a rough gas-phase resistance for a droplet that is essentially water ($1x10^{-4}$ m PZ), and a droplet approaching equilibrium to amine (1 m PZ).

It is clear from these figures that even under conditions where appreciable CO_2 must transfer to reach equilibrium, CO_2 transfer is essentially instantaneous.

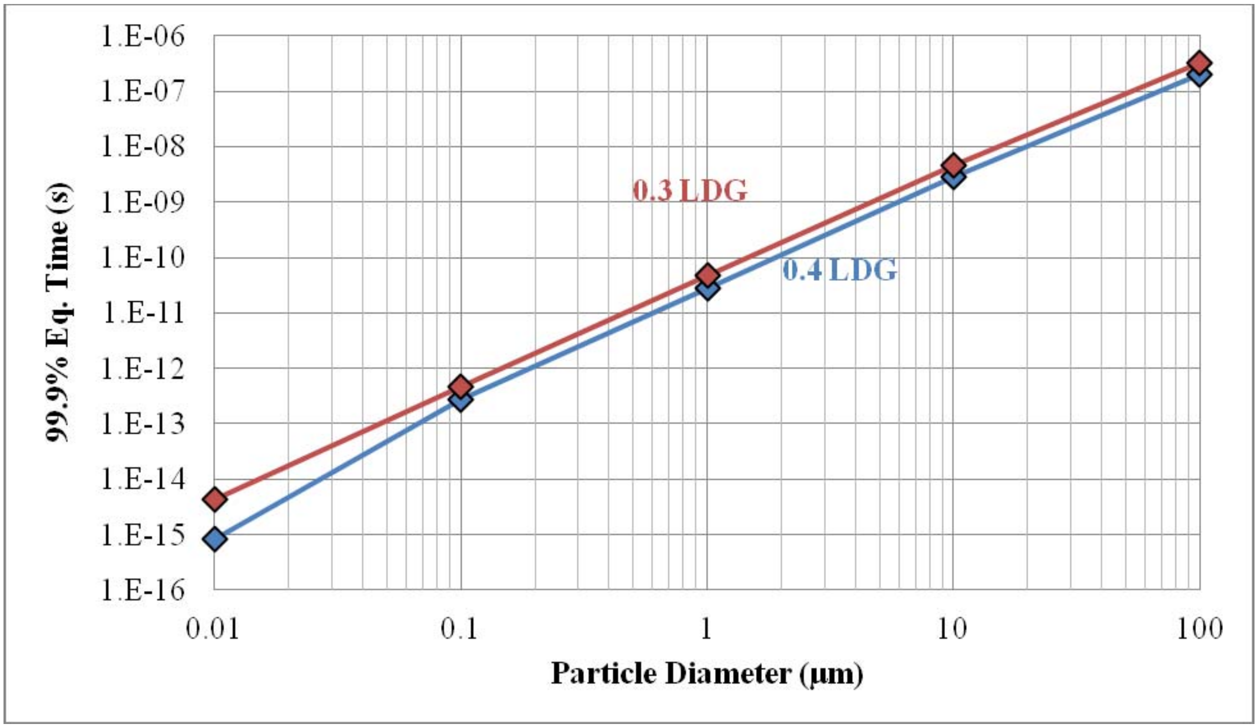

Figure 2: Time to reach 99.9% of equilibrium in CO_2 for $1x10^{-4}$ m PZ for two different initial loading conditions (0.3 and 0.4 mol CO_2/mol alk.) T = 40 °C. P_{CO2} = 1.2 kPa. Gas-film dominated mass transfer.

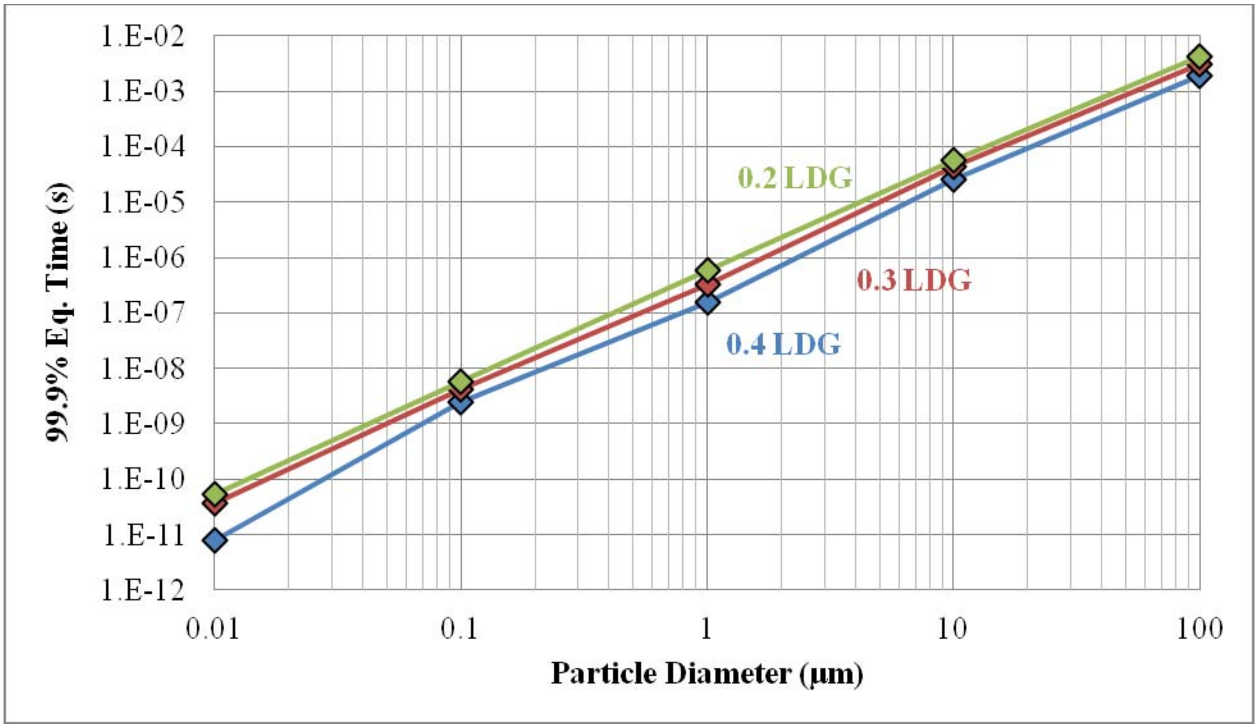

Figure 3: Time to reach 99.9% of equilibrium in CO_2 for 1 m PZ for different initial loading conditions (0.2, 0.3, and 0.4 mol CO_2/mol alk.) T = 40 °C. P_{CO2} = 1.2 kPa. Gas-film dominated mass transfer.

Total liquid-phase mass transfer coefficients, or kg', are about 5 orders of magnitude larger than gas-phase mass transfer coefficients. Therefore, mass transfer of CO_2 should occur 10^{-5} slower. Under liquid-film controlling assumptions, the time to approach CO_2 equilibrium becomes significant for most cases. Still, small particles (< 10 μm) that begin as water can still be considered in equilibrium with CO_2 without significant calculation error. As aerosols pick up amine, mass transfer rates of CO_2 must be considered.

Microsoft® Excel Model Stability

The Microsoft® Excel model suffers stability problems for particles under 5 μm. First-order numerical integration of the set of differential-algebraic equations requires very small times steps to prevent instability. Particles under 10 μm require about 1,000 time steps for every absorber segment. Calculations become especially unstable around absorber nodes from Aspen Plus®. Linear interpolation creates a discontinuity in the derivative of gas-phase profiles which causes stiffness in calculation.

Higher order numerical integration techniques with dynamic step algorithms will be used in Matlab® to improve model stability.

Conclusions

- Aerosols increase volatile amine loss.
- Water wash systems do not remove small aerosols.
- CO_2 transfer to aerosols is liquid-film controlled.
- Particles less than 0.1 μm are in equilibrium to CO_2 for any starting PZ concentration.
- Droplet temperature will be approximately the wet bulb temperature of the gas.

Future Work

Goals for next quarter include completing an aerosol growth model in Matlab® assuming a fixed section reference frame. The model will employ a more sophisticated numerical integration algorithm such that particle sizes below 5 μm can be simulated.

References

Damle AS, Ensor DS, and Ranade MB. "Coal Combustion Aerosol Formation Mechanisms: A Review." *Aerosol Science and Technology.* 1982;1:119–133.

DIPPR, 1998-Provo, UT: BYU DIPPR, Thermophysical Properties Laboratory, 1998-Version 13.0.

Frössling, N. "Evaporation of Falling Drops." *Gerlands Beitr. Geophys.* 1938;52:170.

Hilliard MD. *A Predictive Thermodynamic Model for an Aqueous Blend of Potassium Carbonate, Piperazine, and Monoethanolamine for Carbon Dioxide Capture from Flue Gas.* The University of Texas at Austin. Ph.D. Dissertation. 2008.

Mitsubishi Heavy Industries. (August 16, 2011). "Amine Emission Control Technology of KM CDR Process™." Presented at the Amine Workshop in Palo Alto, California.

Netherlands Organization for Applied Scientific Research. (January 25, 2012). “Emission Reducing Technologies Aerosols.” Presented at the University of Texas at Austin Research Review Meeting.

Rochelle GT et al. "CO_2 Capture by Aqueous Absorption, Fourth Quarterly Progress Report 2010." Luminant Carbon Management Program. The University of Texas at Austin. 2010.

Rochelle GT et al. "CO_2 Capture by Aqueous Absorption, Second Quarterly Progress Report 2011." Luminant Carbon Management Program. The University of Texas at Austin. 2011.

SINTEF. (January 25, 2012). “Emission Studies at the Maasvlakte CO_2 Capture Pilot Plant.” Presented at the University of Texas at Austin Research Review Meeting.

Sirignano, WA. *Fluid Dynamics and Transport of Droplets and Sprays.* Cambridge, United Kingdom: Press Syndicate of the University of Cambridge; 1999.

Appendix A – Nomenclature

Variable:	**Description:**	**Units:**
a_{Drop}	Droplet acceleration	m/s^2
A_{Drop}	Droplet surface area	m^2
A_{Proj}	Droplet projected area perpendicular to gas flow	m^2
C_C	Cunningham slip correction factor	--
C_D	Droplet drag coefficient	--
$\overline{Cp}^G$	Gas-phase molar heat capacity	J/kmol·K
$\overline{Cp}_i^L$	Pure component liquid-phase molar heat capacity of species i	J/kmol·K
$\overline{Cp}_{mix}^L$	Mixture liquid-phase molar heat capacity	J/kmol·K
$\overline{Cp}^{L,Ex}$	Excess liquid-phase molar heat capacity	J/kmol·K
d_{Col}	Water wash/Absorber diameter	m^2
d_{Drop}	Droplet diameter	m^2
$D_{i,mix}^G$	Mixture gas-phase diffusion coefficient of species i	m^2/s
$D_{Drop}^{G,KT}$	Kinetic theory gas-phase diffusion coefficient for a particle	m^2/s
$D_{Drop}^{G,STK}$	Stokes flow gas-phase diffusion coefficient for a particle	m^2/s
$D_{i,j}^L$	Liquid-phase diffusion coefficient of species i in j	m^2/s
g	Acceleration due to gravity	m/s^2
G	Volumetric gas flow rate	m^3/s
h_{Col}	Water wash/Absorber column height	m
h^G	Gas-phase heat transfer coefficient	$J/m^2 \cdot K \cdot s$
H_{CO_2,H_2O}	Henry's constant for CO_2 in H_2O	Pa

H_i^G	Gas-phase partial molar enthalpy	J/mol
H_i^L	Liquid-phase partial molar enthalpy	J/mol
ΔH_i^{Vap}	Enthalpy of vaporization of species i	J/mol
ΔH_i^{Abs}	Enthalpy of absorption of species i	J/mol
k_2	Kinetic reaction constant for CO_2 absorption in PZ	m3/mol·s
k_B	Boltzmann constant	m^2·kg/K·s^2
$k_{g,i}$	Gas-phase mass transfer coefficient	m/s
k_g'	Liquid-phase effective mass transfer coefficient	mol/Pa·m^2·s
m_{Drop}	Droplet mass	kg
m_{molec}	Molecule mass	kg
MW_i	Molecular weight of species i	kg/k-mol
MW_{Avg}	Average molecular weight	kg/k-mol
n_i	Moles of species i	mol
n_{Tot}	Total moles in droplet	mol
N_{AV}	Avogadro's number	molec/mol
Nc	Number of components	--
$Nseg_{Col}$	Water wash/Absorber calculation segments	--
$Nseg_{int}$	Calculation segments between water wash/absorber segments	--
NTU	Number of transfer units	--
Nu^G	Gas-phase Nusselt number	--
P_i^*	Equilibrium partial pressure of species i over bulk liquid solution	Pa
P_i^{int}	Partial pressure of species i at the gas-liquid interface	Pa
P_i^G	Partial pressure of species i in the bulk gas	Pa

Pr^G	Gas-phase Prandtl number	--
q	Total heat transfer due to conduction	J
Re^G	Gas-phase Reynold's number	--
Sc_i^G	Gas-phase Schmidt number for species i	--
Sh_i^G	Gas-phase Sherwood number for species i	--
$T_{C,i}$	Critical temperature for species i	K
T_G	Bulk gas temperature	K
T_L	Bulk liquid temperature	K
$T_{R,i}$	Reduced temperature for species i	--
v_{Drop}	Droplet velocity	m/s
v_G	Gas velocity	m/s
v_{Rel}	Velocity of the gas relative to the droplet	m/s
V_{Drop}	Droplet volume	m^3
wt_i^{App}	Apparent weight fraction of species i	--
x_i^{App}	Apparent mole fraction of species i	--
x_i^{True}	True mole fraction of species i	--

Greek Letters

Variable:	**Description:**	**Units:**
α	Loading: Moles of CO_2 per mole alkalinity	mol/mol
κ^G	Gas-phase thermal conductivity	J/m·s·K
λ^G_{molec}	Mean-free path of a gas molecule	m
μ_G	Gas-phase viscosity	Pa·s
μ_i^L	Pure component liquid-phase viscosity of species i	Pa·s

$\mu^L_{sol'n}$	Mixture liquid-phase viscosity	Pa·s
ρ_G	Gas-phase mass density	kg/m^3
ρ_L	Liquid-phase mass density	kg/m^3
$\bar{\rho}_G$	Gas-phase molar density	$mole/m^3$
σ_i	Surface tension of species i	N/m
σ_{mix}	Mixture surface tension	N/m
υ^L_i	Liquid-phase molar volume of species i	$kmol/m^3$
$[PZ]$	PZ molality	mol/kg H_2O
$[PZ]_{Free}$	Free PZ concentration	mol/m^3

Appendix - B

Table B.1 shows the required inputs for a single-sized droplet used in the Microsoft® Excel aerosol growth model. Gas-phase profiles are created via simulations using Aspen Plus®.

Table B.1: Droplet inputs required to calculate all required initial conditions for aerosol growth model integration.

Parameter	**Description**	**Units**
d_{Drop}	Diameter	μm
T_L	Liquid temperature	K
[PZ]	PZ concentration	mol/kg H_2O
LDG	CO_2 loading	mol/mol alk

Initial Conditions

Initial conditions for integration require the particle velocity (momentum), temperature (energy), and moles of each species (mass). Mass and energy conditions can be solved directly from given inputs and a liquid density correlation. The initial particle velocity is solved using Stoke's Law to calculate the drag coefficient and the initial gas-phase velocity and Reynold's number. The momentum balance is a closed-form equation such that the initial velocity can be solved for directly by assuming the initial axial acceleration of zero.

$$x_{H_2O}^{App} = \frac{[1000/MW_{H_2O}]}{\{[1000/MW_{H_2O}] + 2\,[PZ]\,\alpha + [PZ]\}} \tag{B.1}$$

$$x_{CO_2}^{App} = \frac{2\,[PZ]\,\alpha}{\{[1000/MW_{H_2O}] + 2\,[PZ]\,\alpha + [PZ]\}} \tag{B.2}$$

$$x_{PZ}^{App} = \frac{[PZ]}{\{[1000/MW_{H_2O}] + 2\,[PZ]\,\alpha + [PZ]\}} \tag{B.3}$$

$$MW_{AVG} = \sum_{i}^{Nc} x_i^{App}\,MW_i \tag{B.4}$$

$$\rho_L = 1000\,[E + F\,T_L]\,\ln\left[A\,x_{CO_2}^{App} + B\,x_{PZ}^{App} + C\,\alpha + D\right] \tag{B.5}$$

$$V_{Drop} = \frac{4}{3}\pi\left(\frac{d_{Drop}}{2}\right)^2 \tag{B.6}$$

$$n_i = \frac{1000\, x_i^{App}\, V_{Drop}\, \rho_L}{MW_{AVG}} \tag{B.7}$$

$$v_G = \frac{4\, G}{\pi\, d_{Col}^{\ 2}} \tag{B.8}$$

$$v_{Rel} = \frac{d_{Drop}^{\ 2}\, (\rho_L - \rho_G)}{18\, \mu_G} \tag{B.9}$$

$$v_{Drop} = v_G - v_{Rel} \tag{B.10}$$

Algebraic Equations

Physical properties, particle size information, transfer coefficients, and driving forces used for differential balances on momentum, mass, and energy are calculated using algebraic equations and correlations. All properties can be calculated using moles of each species, temperature, and droplet velocity.

The correlation parameters for the heat of absorption for CO_2 and PZ are the same as those used in the equilibrium partial pressure correlation for the same component. Heat of absorption correlations are calculated using the Gibbs-Helmholtz relationship.

$$\alpha = \frac{n_{CO_2}}{2\, n_{PZ}} \tag{B.11}$$

$$[PZ] = \frac{1000\, n_{PZ}}{n_{H_2O}\, MW_{H_2O}} \tag{B.12}$$

$$x_{H_2O}^{True} = \frac{n_{H_2O}}{n_{H_2O} + n_{PZ}} \tag{B.13}$$

$$x_i^{App} = \frac{n_i}{\sum_i^{Nc} n_i} \tag{B.14}$$

$$wt_i^{App} = \frac{n_i\, MW_i}{\sum_i^{Nc} n_i\, MW_i} \tag{B.15}$$

$$MW_{AVG} = \sum_i^{Nc} x_i^{App}\, MW_i \tag{B.16}$$

$$\rho_L = 1000\, [E + F\, T_L]\, \ln\left[A\, x_{CO_2}^{App} + B\, x_{PZ}^{App} + C\, \alpha + D\right] \tag{B.17}$$

$$\mu_{H_2O}^{L} = \exp\left[A + \frac{B}{T_L} + C \ln\left[T_L\right] + D\, T_L^{\ E}\right] \tag{B.18}$$

$$\frac{\mu^{soln}}{\mu_{H_2O}} = \exp\left\{\frac{\left[\left(A\,wt_{PZ}^{App}+B\right)T_L+\left(C\,wt_{PZ}^{App}+D\right)\right]\left[\alpha\left(E\,wt_{PZ}^{App}+F\,T_L+G\right)+1\right]wt_{PZ}^{App}}{T_L^{\,2}}\right\} \tag{B.19}$$

$$\upsilon_{H_2O}^{L} = \frac{1}{1000\,N_{Av}}\left[A+B\,T_L+C\,T_L^{\,2}+D\,T_L^{\,3}\right]^{-1} \tag{B.20}$$

$$\upsilon_{CO_2}^{L} = \frac{1}{1000\,N_{Av}}\left[\frac{A}{B^{\left[1+\left(1-\frac{304.21}{C}\right)^{D}\right]}}\right]^{-1} \tag{B.21}$$

$$\upsilon_{PZ}^{L} = \frac{1}{1000\,N_{Av}}\left[\frac{A}{B^{\left[1+\left(1-\frac{T_L}{C}\right)^{D}\right]}}\right]^{-1} \tag{B.22}$$

$$T_{R,i} = \frac{T_L}{T_{C,i}} \tag{B.23}$$

$$\sigma_{H_2O} = A\left[1-T_{R,H_2O}\right]^{\left(B+C\,T_{R,H_2O}+D\,T_{R,H_2O}^{\,2}\right)} \tag{B.24}$$

$$\sigma_{PZ} = A\left[1-T_{R,PZ}\right]^{B} \tag{B.25}$$

$$\sigma_{mix} = \sum_{i}^{N_c} x_i^{App}\,\sigma_i \tag{B.26}$$

$$P_{H_2O}^{*} = x_{H_2O}^{True}\,\exp\left[\frac{4\,\sigma_{mix}\,\upsilon_{H_2O}}{k_B\,T_L\,d_{Drop}}\right]\exp\left[A+\frac{B}{T_L}+C\ln(T_L)+D\,T_L^{\,E}\right] \tag{B.27}$$

$$P_{CO_2}^{*} = \exp\left[\frac{4\,\sigma_{mix}\,\upsilon_{CO_2}}{k_B\,T_L\,D_{Drop}}\right]\exp\left[A+\frac{B}{T_L}+C\,\alpha^2+D\,\frac{\alpha}{T_L}+E\,\frac{\alpha^2}{T_L}\right] \tag{B.28}$$

$$P_{PZ}^{*} = x_{PZ}^{App}\exp\left[\frac{4\,\sigma_{mix}\,\upsilon_{PZ}}{k_B\,T_L\,D_{Drop}}\right]\exp\left[A+B\ln(T_L)+C\,\alpha+D\,\frac{\alpha^2}{T_L}\right] \tag{B.29}$$

$$\Delta H_{H_2O}^{Vap} = \left(\frac{1}{1000}\right)A\left[1-T_{R,H_2O}\right]^{\left(B+C\,T_{R,H_2O}+D\,T_{R,H_2O}^{\,2}\right)} \tag{B.30}$$

$$\Delta H_{CO_2}^{Abs} = -R\left(B+D\,\alpha+E\,\alpha^2\right) \tag{B.31}$$

$$\Delta H_{PZ}^{Abs} = -R\left(B\,T_L+D\,\alpha^2\right) \tag{B.32}$$

$$\overline{Cp}^{L}_{H_2O} = A + B\,T_L + C\,T_L^{\,2} + D\,T_L^{\,3} \tag{B.33}$$

$$\overline{Cp}^{L}_{PZ} = A + B\,T_L \tag{B.34}$$

$$\overline{Cp}^{L,Ex}_{PZ\cdot CO_2} = x^{App}_{PZ}\,x^{App}_{CO_2}\left\{[A + B\,T_L] + [C + D\,T_L]\left(x^{App}_{PZ} - x^{App}_{CO_2}\right)\right\} \tag{B.35}$$

$$\overline{Cp}^{L,Ex}_{H_2O\cdot CO_2} = x^{App}_{H_2O}\,x^{App}_{CO_2}\left\{[A + B\,T_L] + [C + D\,T_L]\left(x^{App}_{H_2O} - x^{App}_{CO_2}\right)\right\} \tag{B.36}$$

$$\overline{Cp}^{L,Ex} = \sum_{i}^{Nc}\sum_{j}^{Nc} Cp^{L,Ex}_{i,j} \tag{B.37}$$

$$\overline{Cp}^{L}_{mix} = \sum_{i}^{Nc} x^{App}_{i}\,\overline{Cp}^{L}_{i} + \overline{Cp}^{L,Ex} \tag{B.38}$$

$$a_{Drop} = \frac{3\,C_D\,v_{Rel}^{\;2}}{4\,d_{Drop}}\frac{\rho_G}{\rho_L} - \left[1 - \frac{\rho_G}{\rho_L}\right]g \tag{B.39}$$

$$C_D = \left(\frac{24}{Re^G}\right)\left(1 + 0.15\,[Re^G]^{0.687}\right) \tag{B.40}$$

$$Re^G = \frac{\rho_G\,v_{Rel}\,d_{Drop}}{\mu_G} \tag{B.41}$$

$$Pr^G = \frac{\mu_G\,\overline{Cp}^{G}}{\kappa^G\,MW^G_{AVG}} \tag{B.42}$$

$$Sc^G_i = \frac{\mu_G}{\rho^G\,D^G_{i\text{-}mix}} \tag{B.43}$$

$$Nu^G = 2 + 0.6\,(Re^G)^{\frac{1}{2}}(Pr^G)^{\frac{1}{3}} \tag{B.44}$$

$$Sh^G_i = 2 + 0.6\,(Re^G)^{\frac{1}{2}}(Sc^G_i)^{\frac{1}{3}} \tag{B.45}$$

$$h^G = \frac{Nu^G\,\kappa^G}{d_{Drop}} \tag{B.46}$$

$$k_{g,i} = \frac{Sh^G_i\,D^G_{i,mix}}{d_{Drop}} \tag{B.47}$$

$$H_{CO_2 \cdot H_2O} = A \exp\left[\frac{B}{T_L}\right] \tag{B.48}$$

$$D^L_{CO_2 \cdot H_2O} = A \exp\left[\frac{B}{T_L}\right] \tag{B.49}$$

$$D^L_{CO_2 \cdot soln} = D^L_{CO_2 \cdot H_2O}\left(\frac{\mu_{H_2O}}{\mu_{soln}}\right)^{0.72} \tag{B.50}$$

$$k_2 = A \exp\left[\frac{B}{RT_L}\right] \tag{B.51}$$

$$[PZ]_{Free} = \frac{\left(n_{PZ} - n_{CO_2}\right)}{V_{Drop}} \tag{B.52}$$

$$k_g^{'} = \frac{\sqrt{k_2\ [PZ]_{Free}\ D^L_{CO_2 \cdot soln}}}{H_{CO_2 \cdot H_2O}} \tag{B.53}$$

$$V_{Drop}(t) = \frac{n_{Tot}\ MW_{Avg}}{1000\ \rho_L} \tag{B.54}$$

$$d_{Drop}(t) = \left(\frac{6\ V_{Drop}(t)}{\pi}\right)^{\frac{1}{3}} \tag{B.55}$$

$$A_{Drop}(t) = \pi\left[d_{Drop}(t)\right]^2 \tag{B.56}$$

Differential Equations

The differential equations below were numerically integrated using Euler's method with fixed space intervals. The amount of time spent in a given interval is calculated using the total height of the column, total calculation stages, and the particle velocity.

$$\frac{dn_i}{dt} = k_{g,i}\ A_{Drop}\ \frac{\left(P_i^G - P_i^{int}\right)}{RT_L} \approx k_{g,i}\ A_{Drop}\ \frac{\left(P_i^G - P_i^{*}\right)}{RT_L} \tag{B.57}$$

$$\frac{dn_{CO_2}}{dt} = k_g^{'}\ A_{Drop}\left(P^{int}_{CO_2} - P^{*}_{CO_2}\right) \approx k_g^{'}\ A_{Drop}\left(P^{G}_{CO_2} - P^{*}_{CO_2}\right) \tag{B.58}$$

$$n_{Tot}\overline{Cp}^L_{mix}\frac{dT_L}{dt} = h^G\ A_{Drop}\left(T_G - T_L\right) + \sum_i^{N_s}\frac{dn_i}{dt}\left(\bar{H}_i^{\,G} - \bar{H}_i^{\,L}\right) \tag{B.59}$$

$$\frac{dv_{Drop}}{dt} = a_{Drop} \tag{B.60}$$

$$\Delta t = \frac{h_{Col}}{Nseg_{Col}\ Nseg_{Int}\ v_{Drop}} \tag{B.61}$$

Appendix C – Correlation Parameters

Variable	Units	A	B	C	D	E	F	G
ρ_L	g/mL	2.676E+00	-3.098E-02	-7.262E-02	2.103E+00	1.549E+00	-5.728E-04	--
$\upsilon^L_{H_2O}$	kmol/m^3	-1.385E+01	6.404E-01	-1.912E-03	1.821E-06	--	--	--
$\upsilon^L_{CO_2}$	kmol/m^3	2.768E+00	2.621E-01	3.042E+02	2.908E-01	--	--	--
υ^L_{PZ}	kmol/m^3	1.043E+00	3.230E-01	6.380E+02	2.857E-01	--	--	--
$\mu^L_{H_2O}$	Pa·s	-5.284E+01	3.704E+03	5.866E+00	-5.879E-29	1.000E+01	--	--
$\mu^L_{sol'n}$	Pa·s	4.875E+02	1.389E+03	1.580E+00	4.500E+00	8.730E+00	-3.800E-03	-3.000E-01
σ_{H_2O}	N/m	1.777E-01	2.567E+00	-3.338E+00	1.970E+00	--	--	--
σ_{CO_2}	N/m	8.071E-02	1.266E+00	--	--	--	--	--
σ_{PZ}	N/m	2.485E-02	1.167E+00	--	--	--	--	--
$P^{vap}_{H_2O}$	Pa	7.365E+01	-7.258E+03	-7.304E+00	4.165E-06	2.000E+00	--	--
$P^*_{CO_2}$	Pa	3.550E+01	-1.108E+04	-2.250E+01	4.713E+03	1.172E+04	--	--
P^*_{PZ}	Pa	-1.230E+02	2.160E+01	1.990E+01	-1.803E+04	--	--	--
$\Delta H^{Vap}_{H_2O}$	J/kmol	5.155E+07	2.840E-01	-1.584E-01	2.375E-01	--	--	--
$\overline{Cp}^L_{H_2O}$	kJ/kmol·K	2.764E+05	-2.090E+03	8.125E+00	-1.412E-02	9.370E-06	--	--

Variable	**Units**	**A**	**B**	**C**	**D**	**E**	**F**	**G**
$\overline{Cp}_{PZ}^{L}$	kJ/kmol·K	4.669E+04	4.315E+02	--	--	--	--	--
$\overline{Cp}_{PZ\cdot CO_2}^{L,Ex}$	kJ/kmol·K	-8.722E+03	3.622E+01	4.076E+04	-1.734E+02	--	--	--
$\overline{Cp}_{H_2O\cdot CO_2}^{L,Ex}$	kJ/kmol·K	4.604E+03	-1.776E+01	-5.368E+03	2.038E+01	--	--	--
$H_{CO_2\cdot H_2O}$	atm·cm^3/mol	1.711E+07	-1.886E+03	--	--	--	--	--
$D_{CO_2\cdot H_2O}^{L}$	cm^2/s	2.400E-02	-2.122E+03	--	--	--	--	--
k_2	m^3/mol·s	6.570E+07	-3.410E+04	--	--	--	--	--
C_C	--	1.252E+00	3.990E-01	-1.100E+00	--	--	--	--

Piperazine Degradation in Pilot Plants

Quarterly Report for January 1 – March 31, 2012

by Paul T. Nielsen, III

Supported by the Luminant Carbon Management Program

Department of Chemical Engineering

The University of Texas at Austin

April 30, 2012

Abstract

This progress report discusses the findings made in the characterization of solvent degradation at the pilot-plant scale. Degraded 8 m piperazine (PZ) was analyzed from 2 pilot plant campaigns, one run at the Pickle Research Campus (PRC) in October 2011 and one run at "Pilot Plant 2" (PP2). The PRC campaign used synthetic flue gas consisting of air mixed with 12 kPa CO_2, while the PP2 campaign used a slip stream of real flue gas from a coal-fired power plant. Data from these campaigns can be used to determine the degradation rate of PZ and the formation of byproducts.

The major thermal degradation products detected in both pilot plant solvents included ethylenediamine, N-(aminoethyl)piperazine, and N-(hydroxyethyl)piperazine. Oxidative degradation products including formate, acetate, oxalate, and N-formlypiperazine were also detected. The formation of the oxidative degradation products was observed to be catalyzed by the accumulation of dissolved metal ions from corrosion in PP2.

N-nitrosopiperazine, a known carcinogen that forms when PZ reacts with nitrite absorbed from flue gas, was also observed in PP2 solvent at a steady state of 1 mmol/kg. The accumulation of MNPZ seems to be limited by its thermal degradation in the stripper.

Introduction

PZ has shown promise as a solvent for carbon dioxide capture, with greater capacity, adsorption rate, and stability than the baseline monoethanolamine solvent. PZ has been shown in bench-scale experiments to degrade into a wide variety of products through either thermal or oxidative degradation reactions. Only 10–25% of the degradation products have been quantified in these experiments. The most prevalent quantified degradation products are ethylenediamine (EDA), formate, and N-formyl-PZ (FPZ) (Closmann, 2011; Freeman, 2011).

PZ can also react with nitrite (NO_2^-) absorbed from the flue gas to form N-nitrosopiperazine (MNPZ), a known carcinogen. MNPZ degrades at high temperatures along a first-order pathway (Equation 1). Therefore, a model for the steady state concentration of MNPZ in a continuously-operated cyclic amine scrubbing plant has been proposed by Fine based on the flue gas nitrite composition and the temperature and residence time of the stripper sump. The model is shown below in Equation 2, where $C_{MNPZ,ss}$ is the steady-state MNPZ concentration, $C_{NO2,Flue}$ is the flue gas nitrite concentration, k_2 is the degradation rate constant (a function of temperature), and τ is the residence time of the solvent in the stripper sump (Rochelle, 2012).

(1)

(2)

Samples of PZ solvent were collected from pilot plants at the Separations Research Program (SRP) at the Pickle Research Campus (PRC) in Austin, Texas, and from "Pilot Plant 2." PRC ran a campaign using 8 m PZ with a two-stage flash stripping system in September and October 2011. A large sample of PZ was collected at the end of the run for extensive testing. PP2 included a test of a solvent reclaiming process and a water wash system to capture volatile degradation products. Samples of solvent were collected at least once a week from PP2 to observe solvent changes over time. Also, samples of water were collected from the water wash system installed on PP2.

Experimental Methods

HPLC

HPLC (Dionex ICS3000) was used to measure MNPZ and several other nonpolar degradation products in the solvent and wash samples. PZ solvent samples were diluted by a factor of 20X by weight and water wash samples were diluted 5X. A 0.01 M aqueous ammonium carbonate solution and acetonitrile were used as eluents. The ramp time for these solvents is shown below in Figure 1. The UV detector operated at a wavelength of 240 nm (Voice, 2011).

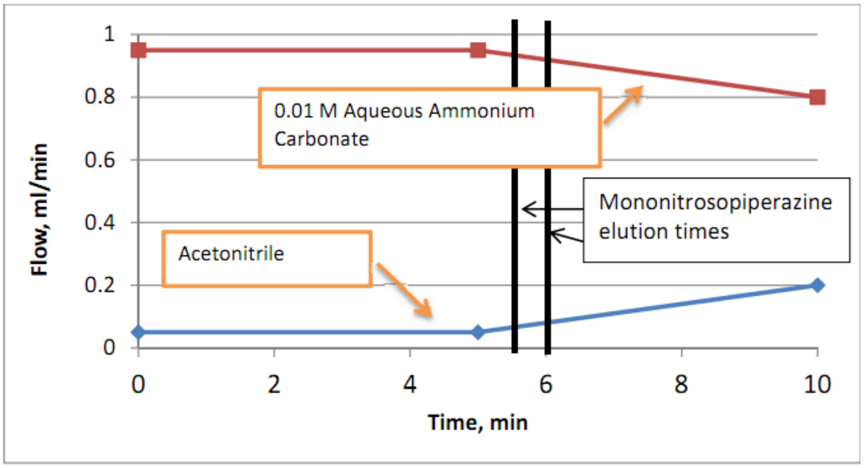

Figure 1: HPLC eluent flow as a function of time, adapted from Voice (2011)

MNPZ eluted at around 6 minutes. A quadratic calibration curve for MNPZ was developed from data collected by Fine in November 2011.

Cation IC

The concentration of PZ and other degradation products was measured using cation chromatography (Dionex ICS2100) at a dilution factor of 10,000X. Cation IC measures the concentration of positively charged cations. The eluent consisted of methanesulfonic acid (MSA) in deionized water. The method uses an eluent ramp starting at 5.5 mM MSA and increasing in concentration over the course of the run to 38.5 mM MSA. The run time per sample was 50 minutes. Flowing the sample and eluent between a cathode and anode separated by two membranes, the anions were removed from the sample, leaving only cations, as shown in Figure 2. The separation occurred in an IonPac GC 17 guard column and an IonPac CS 17 analytical column. Both columns contained ethylvinylbenzene cross-linked with 55% divinylbenzene resin as the primary separation medium. Changes in solution conductivity were then measured over time using a conductivity detector to create a chromatogram (Freeman, 2011).

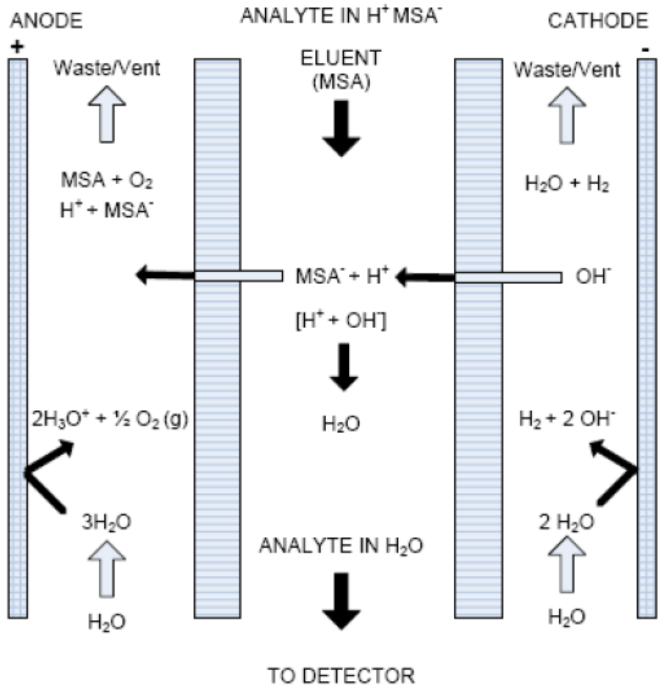

Figure 2: Schematic of CSRS 300 anion suppressor, adapted from Freeman (2011)

Table 1 shows the PZ degradation products that can be quantified using cation IC. For PZ quantification, all solvent samples were diluted to 10,000X by weight in DDI H_2O. For quantification of other degradation products, solvent samples were diluted to 1,000X.

Table 1: Species quantified by cation IC

Species	*Elution Time*
Piperazine (PZ)	33 min
Ammonium (NH_4^+)	10.1 min
N-formyl-PZ (FPZ)	15.4 min
Ethylenediamine (EDA)	30.2 min
N-(2-hydroxyethyl)-PZ (HEP)	35.2 min
N-(2-aminoethyl)-PZ (AEP)	38.2 min

Anion IC

Anion chromatography (Dionex ICS-3000) can be used to measure the concentration of carboxylic acids and other anions. The method uses a ramped eluent of KOH in water with an IonPac AS15 analytical column (4 x 250 mm) and a 4-mm Anionic Self-Regenerating Suppressor to remove cations. Table 2 lists the anions that can be quantified. Quadratic calibration curves were fitted for these anions.

Table 2: Species quantified by anion IC

Species	*Elution Time*
Glycolate	20.2 min
Acetate	20.7 min
Formate	21.2 min
Sulfate	28.3 min
Oxalate	28.8 min
Nitrate	32.4 min

Amide Hydrolyzation

Amides can be identified and quantified by hydrolyzing the solvent sample with NaOH. This was done by mixing 1 mL of filtered, undiluted solvent with 1 mL (~1.2 g) of 5 N NaOH and allowing the solution to react for 24 hours before diluting and analyzing by HPLC and IC. The NaOH hydrolyzes any amides into their constituent base amines and carboxylic acids. Therefore, any peaks on HPLC or cation IC that disappear when hydrolyzed can be identified as amides. The total amount of carboxylic acids (free heat-stable salts and amides combined) can be measured using anion IC.

Acid Titration: Total Alkalinity

Total alkalinity of the pilot plant solvents was measured by autotitration with 0.2 N H_2SO_4 using a Metrohm 835 Titrando autotitration system.

In order to determine the validity of the method, Total Alkalinity was compared to Cation Chromatography by analysis of loaded, undegraded 8 m PZ prepared from reagent chemicals. Six samples at various loadings were analyzed. Total alkalinity overestimated PZ concentration by 0.7% with a standard deviation of 1.1% compared to the value measured by cation IC. No statistically significant bias with respect to loading was observed.

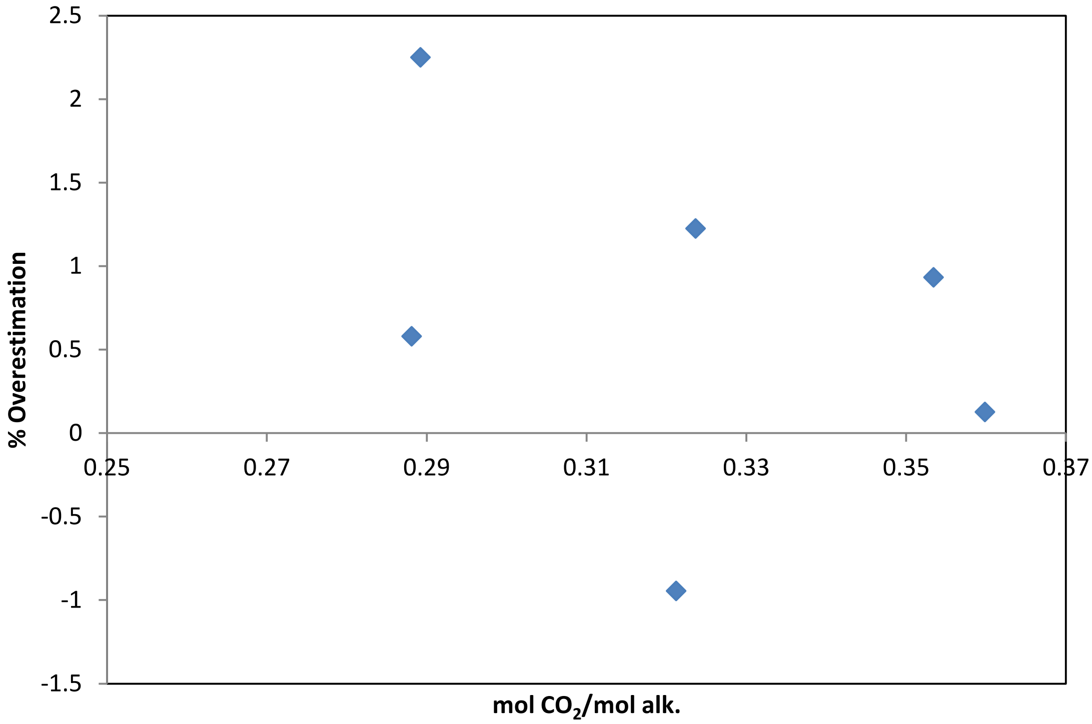

Figure 3: Overestimation of PZ by the total alkalinity method as compared to cation IC, using fresh loaded 8 m PZ made from 99% pure laboratory grade PZ

TIC

The Total Inorganic Carbon (TIC) method was used to determine CO_2 loading of the solvent samples. At a dilution of 100X, the samples were treated with 30 wt % phosphoric acid, which reacted with the PZ and released all the CO_2 as a vapor. The CO_2 could then be measured with an infrared CO_2 detector. Combined with titration to get total alkalinity, the CO_2 loading can be calculated.

Inductively-Coupled Plasma Optical Emission Spectroscopy (ICP-OES)

Quantification of dissolved metals in degraded solvent was performed using a Varian 710-ES Axial Inductively-Coupled Plasma Optical Emission Spectrometer. Samples were prepared by diluting to 25X through dilution with DDI H_2O and were acidified to 2% by mass of concentrated HNO_3. For the experiments conducted in this report, 6 M HNO_3 was used in place of concentrated (16 M) acid to acidify the samples. Therefore, the samples were acidified to 4.38 wt % of 6 M HNO_3. 10 mL of each sample and standard was prepared in a plastic centrifuge vial. Calibration curve standards were also prepared from Fischer Chemicals 2000 ppm atomic absorption reference standards for iron, chromium, and nickel.

Once injected into ICP-OES, samples are sent to a nebulizer to produce a fine aerosol before being atomized and ionized in an argon plasma flame at 7000 K. Atoms and ions inside the plasma flame transition from higher to lower transition states, emitting photons at very sharp characteristic wavelengths.

Four characteristic wavelengths were chosen for each element quantified. Only stainless steel metals (Fe, Cr, Ni) have been quantified. Table 3 shows metals quantified and their characteristic wavelengths. One wavelength was chosen to quantify the background emission intensity of argon. Calibration curves were prepared for each individual wavelength and were used to calculate an average concentration of each element measured. Because four different UV emission wavelengths are measured simultaneously for each species, this method produced very precise calibration curves, with an R^2 value in excess of 0.9999 for all curves created.

Table 3: Characteristic Wavelengths for ICP-OES Metal Quantification

Element Analyzed	*Measured Wavelengths (nm)*			
Argon (Ar)	737.12			
Iron (Fe)	234.350	238.204	239.563	259.540
Chromium (Cr)	205.560	206.158	206.550	267.716
Nickel (Ni)	216.555	221.648	230.299	231.604

Safety Considerations

All samples were stored in 15 to 100 mL vials that were kept sealed with screw caps and stored at room temperature in closed cabinets away from light to limit photolysis. Samples being used for MNPZ analysis were also stored in amber vials to prevent UV degradation of MNPZ. Gloves, safety glasses, and a lab coat were worn at all times in lab.

The large PRC sample was stored in a 5 gallon carboy that was kept sealed at all times except to withdraw smaller amounts (10 mL to 2 L) for analysis.

Results

Summary of Pilot Plant Solvent Degradation

Table 4 gives an overview of the quantified degradation products found in the PRC and PP2 degraded solvents. The table first compares the estimated piperazine concentration determined by titration and by cation IC at the beginning and end of the campaign. Fresh solvent from the beginning of the PP2 campaign had a discrepancy between the two methods of 0.7%, which is well within the experimental error of the two methods (see Experimental Methods). However, solvent collected at the end of the PRC campaign had 13.4% greater total alkalinity than could be accounted for in PZ concentration as measured by cation IC. The discrepancy at the end of the PP2 campaign was 15.5%. This difference can most readily be explained by the presence of additional degradation products in the solvent. This method can only quantify the presence of dissolved degradation products containing alkaline nitrogens. It does not account for volatile degradation products, and thus cannot be used to quantify the total amount of degradation that has occurred.

The rest of Table 4 lists the degradation products quantified in the degraded PRC and PP2 solvents collected at the end of the campaigns, organized by analytical method. Of the products quantified, ammonium (NH_4^+), N-formyl PZ (FPZ), ethylenediamine (EDA), and formate have the highest concentrations.

For both PRC and PP2 solvent, the total formate measured by anion IC on hydrolyzed samples is roughly equivalent to the sum of formate and FPZ measured in un-hydrolyzed samples. This indicates that FPZ is the only major formamide.

Table 4: Summary of Pilot Plant Solvent Degradation

	PRC *mmol/kg*	***PP2*** *mmol/kg*
Fresh Solvent PZ (Total alkalinity)	N/A	4150
Fresh Solvent PZ (Cation IC)	N/A	4121
Discrepancy	N/A	29 (0.7%)
Degraded Solvent PZ (Total alkalinity)	4073	4194
Degraded Solvent PZ (Cation IC)	3528	3546
Discrepancy	545 (13.4%)	648 (15.5%)
HPLC		
MNPZ	0.094	1.22
Cation		
NH_4^+	7.09	0.692±0.008
FPZ	1.29	38.0±0.62
EDA	25.2	9.33±0.074
HEP	3.91	2.64±0.22
AEP	5.68	2.94±0.27
Anion		
Glycolate	0.072±0.020	0.272±0.072
Acetate	0.174±0.11	11.2±0.3
Formate	1.43±0.37	38.6±9.3
Oxalate	0.383±0.053	8.62±0.51
Nitrate	0.146±0.029	4.82±0.28
Sulfate	0.442±0.32	7.07±1.0
Hydrolyzed:		
Total Acetate	0.286±0.11	14.6±0.73
Total Oxalate	0.374±0.036	17.0±0.43
Total Formate	2.97±0.28	72.7±1.4
ICP-OES Dissolved Metals		

	PRC *mmol/kg*	***PP2*** *mmol/kg*
Cr^{3+} (mg/L)	0.84±0.39	114.9±4.5
Fe^{2+} (mg/L)	1.29±0.50	63.09±0.83
Ni^{2+} (mg/L)	1.24±0.10	109.4±3.9

A few degradation products in PP2 reached a maximum concentration before the end of the campaign. Table 5 shows these values and the time in the campaign in which the maximum occurred relative to the total length of the campaign (t/t_{run}).

Table 5: Maximum values of degradation products in PP2

Species	*mmol/kg*	t/t_{run}
MNPZ	2.83±0.004	0.27
NH_4^+	22.9	0.11
EDA	30.8±0.57	0.52
Glycolate	0.306	0.94

PP2 Degradation

Samples were collected regularly over the course of the PP2 campaign. The following section illustrates the accumulation over time of the quantified degradation products. All concentrations have been normalized by dividing by the maximum measured concentration of that species (C/C_{max}) unless otherwise noted and plotted over the relative time of the campaign (t/t_{run}).

Oxidative Degradation and Corrosion

Figure 4 shows the accumulation of oxidative degradation products in PP2 solvent including carboxylic acids (formate, acetate, and glycolate) as well as the FPZ formamide. The concentrations of these products were relatively low until 44% of the way into the campaign, after which they accumulated rapidly. This trend may be linked to the accumulation of dissolved stainless steel metals due to corrosion, as shown in Figure 5. Both time series show similar trends. It has been hypothesized that oxidative degradation occurs by a free radical pathway that is catalyzed by the presence of metal ions (Freeman, 2011).

The ratios of dissolved metals observed in both PRC and PP2 solvents do not correlate with what would be expected from corrosion of stainless steel metal. Stainless steel consists of 72 wt % Fe, 18 wt % Cr, and 10 wt % Ni. However, PRC and early PP2 samples contain relatively equal concentrations of all three metals, and later samples from PP2 have less iron than either chromium or nickel. At least three possible explanations for this discrepancy can be hypothesized. First, there may be some sort of solubility issue that is affecting just iron. Second, the mechanism by which corrosion occurs may not be corroding the three elements equally, and the corrosion of iron is inhibited relative to the other two metals. Finally, iron may have precipitated out of the 2000 ppm standard used to prepare the calibration for iron, which has been sitting on a shelf for over a year before these experiments were conducted. If the latter hypothesis is correct, the measured values for iron concentration would be off by some constant factor. Given that the trends of all three metals appear correlated, the second and third hypotheses seem more likely than the first.

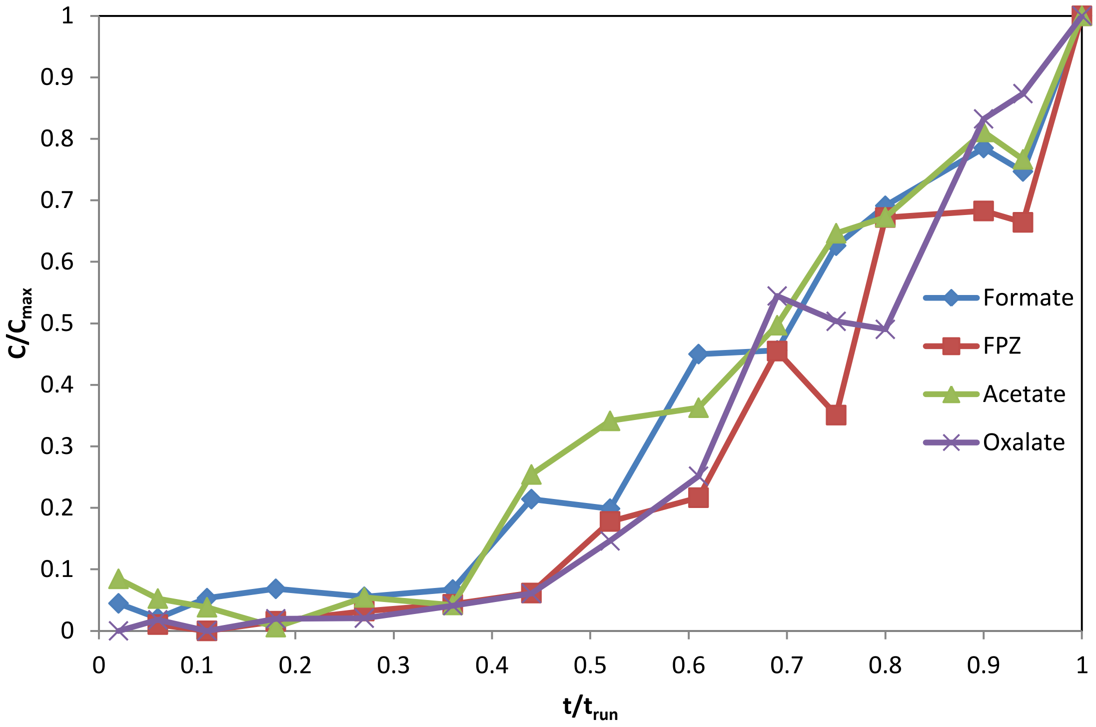

Figure 4: Accumulation of formate (C_{max} = 38.6 mmol/kg), N-formyl-PZ (FPZ, C_{max} = 38.0 mmol/kg), acetate (C_{max} = 11.2 mmol/kg), and oxalate (C_{max} = 8.62 mmol/kg) in PP2 solvent

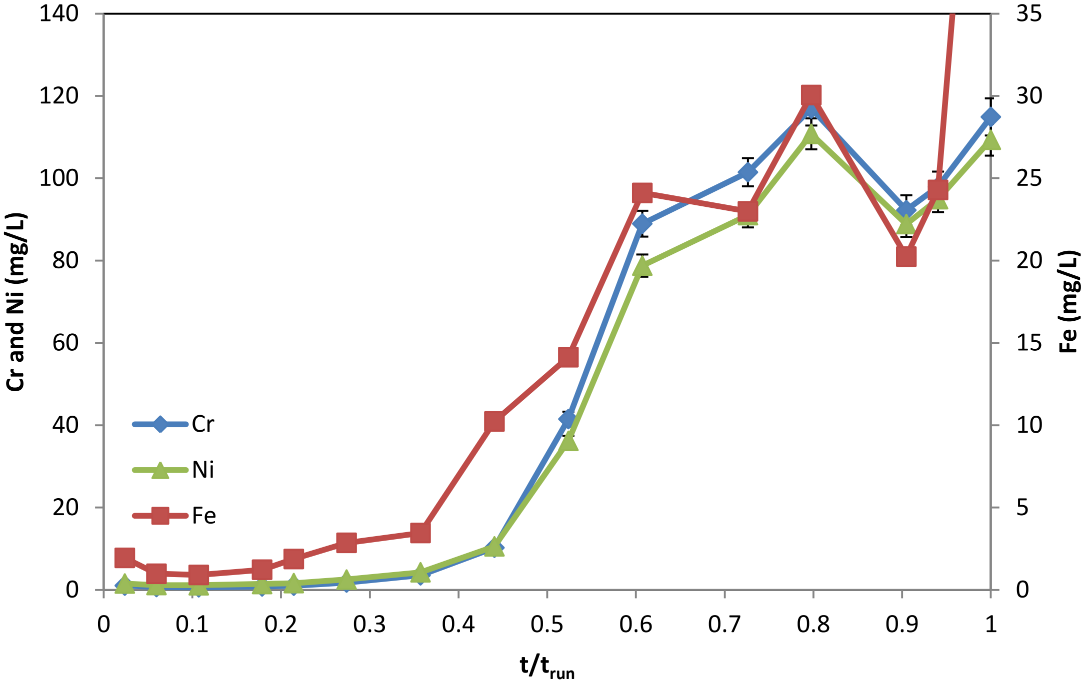

Figure 5: Accumulation of dissolved metal ions in PP2 solvent. Primary axis: Cr^{3+} and Ni^{2+}; secondary axis: Fe^{2+}.

Thermal Degradation

The major thermal degradation products quantified in PP2 were EDA, HEP, and AEP. As shown in Figure 6, all three species accumulated early in the campaign. Midway through the campaign, EDA and HEP reached their maximum measured concentrations and then began decreasing. Both species were most likely further degrading into other secondary degradation products. HEP, however, continued to accumulate throughout the length of the campaign. To better illustrate the matching trends of the three species early in the campaign, HEP has been normalized by its midpoint (1.35 mmol/kg) rather than its maximum value (2.64 mmol/kg).

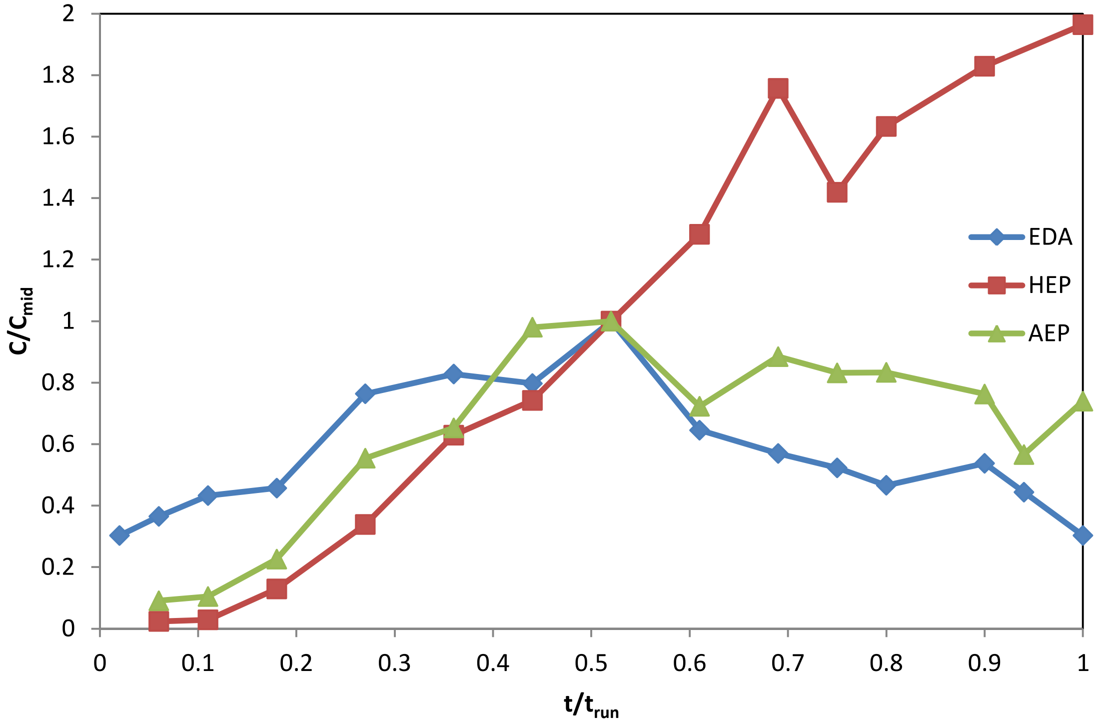

Figure 6: Accumulation of ethylenediamine (EDA, C_{max} = 30.8 mmol/kg), hydroxyethyl-PZ (HEP, C_{max} = 1.35 mmol/kg), and aminoethyl-PZ (AEP, C_{max} = 2.94 mmol/kg) in PP2 solvent.

Nitrate and Sulfate Accumulation and Nitrosation

Nitrates, sulfates, and nitrosamines can accumulate in the solvent due to the absorption of trace SO_x and NO_x present in the flue gas. N-nitrosopiperazine (MNPZ) forms from the reaction of nitrite (NO_2^-) with piperazine. Nitrate, sulfate, and MNPZ accumulation is plotted in Figure 7, with the relative concentration of MNPZ divided by 2 to illustrate similarities in the trends of all three early in the campaign.

Sulfate accumulated at a rate of 0.061 mmol/kg/day. Nitrate accumulated at a rate of 0.0416 mmol/kg/day. Both follow similar trends, and the rates are reasonable based on flue gas composition. Exact details of flue gas composition for PP2 cannot be divulged for proprietary reasons.

MNPZ accumulation trended along with nitrate early in the campaign, but after a quarter of the way through the campaign it settled to a steady state value of approximately 1 mmol/kg. This behavior concurs with the hypothesis that MNPZ will reach a steady state value in continuous operation due to the degradation of MNPZ in the high temperature stripper.

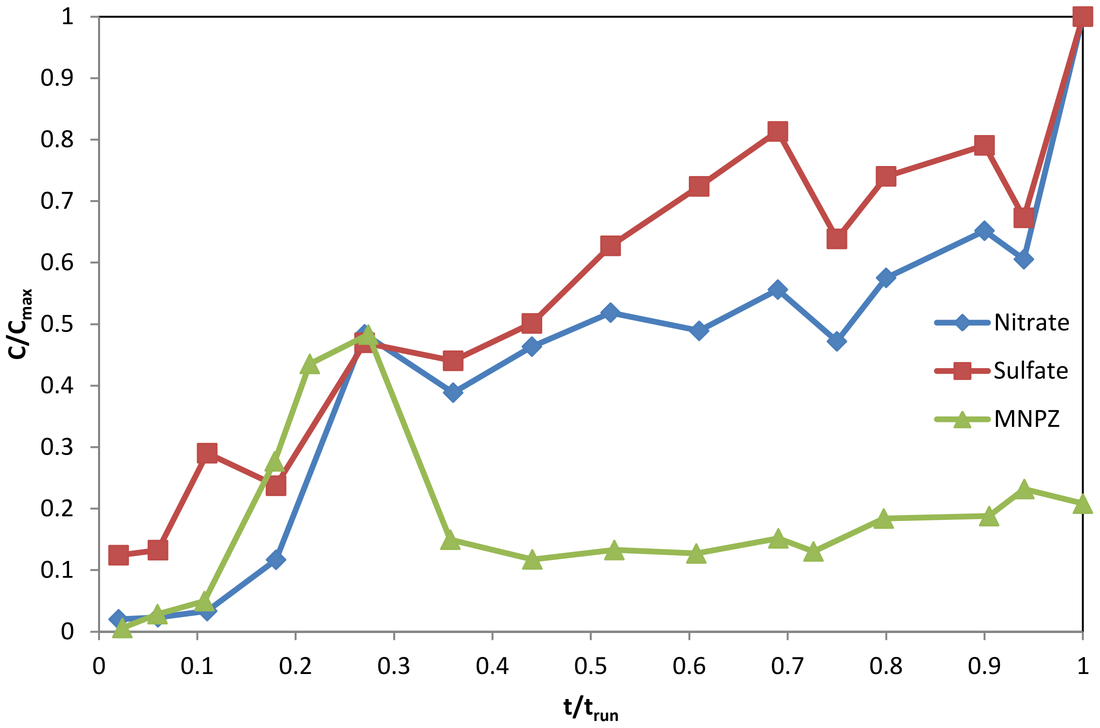

Figure 7: Accumulation of nitrate (C_{max} = 4.82 mmol/kg), sulfate (C_{max} = 7.07 mmol/kg), and N-nitrosopiperazine (MNPZ, C_{max} = 2.83 mmol/kg) in PP2 solvent

Figure 8 shows the concentrations of PZ and MNPZ measured in the water wash samples collected from PP2. MNPZ in the water wash correlated with PZ in water wash. The concentration of MNPZ in the water wash was about 1/1000th of the concentration of PZ. However, in the solvent the ratio of MNPZ to PZ was closer to 1/3500.

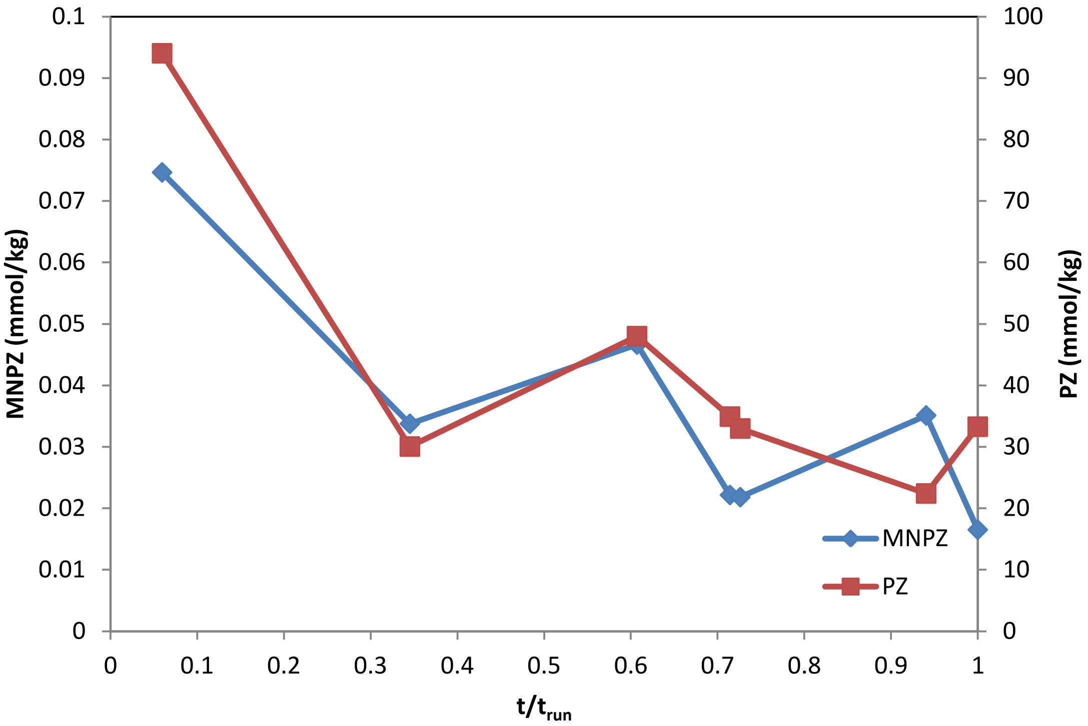

Figure 8: Accumulation of MNPZ and PZ in PP2 water wash

Unidentified Chromatogram Peaks in PP2 HPLC and IC Spectra

Many peaks in the HPLC and IC chromatograms of the degraded solvents remain unidentified at this time. In the following section, sample spectra of degraded solvent in HPLC and IC are shown. Fresh solvent and DDI H_2O blank spectra are also shown to illustrate the baseline of each system. All major degradation peaks are labeled with either their identified species or “U” for “unidentified.” “UA” indicates an unidentified amide, based on the peak’s reaction to hydrolyzation.

HPLC

Sample chromatograms and time series of major unidentified degradation peaks in the HPLC data from PP2 are shown below in Figure 9 and Figure 10. A large number of degradation products were only weakly retained by the column, resulting in a congregation of peaks early in the method. Only a few of these peaks could be dependably integrated due to the noise. The peaks at 4.7 and 8.9 minutes both follow similar trends. The change over time of the peak area at 4.7 minutes most closely resembles the accumulation of the thermal degradation product HEP, implying that this peak may also represent a thermal degradation product. The peak at 8.9 minutes could represent either an oxidative or thermal degradation product.

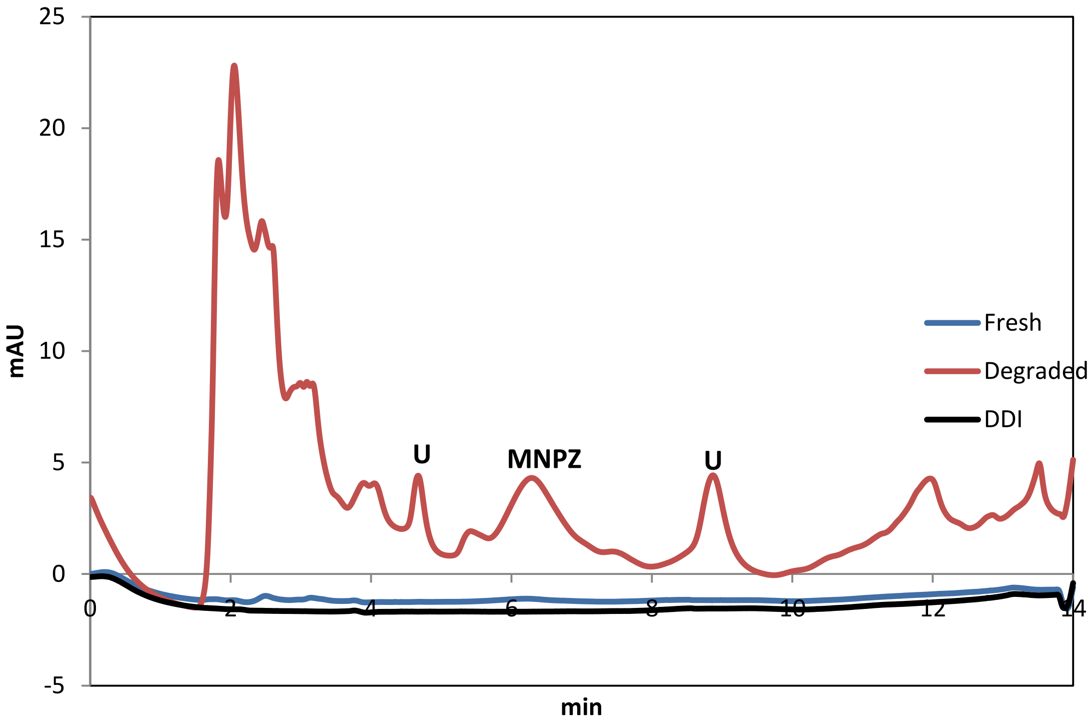

Figure 9: HPLC spectra of fresh and degraded PP2 solvent

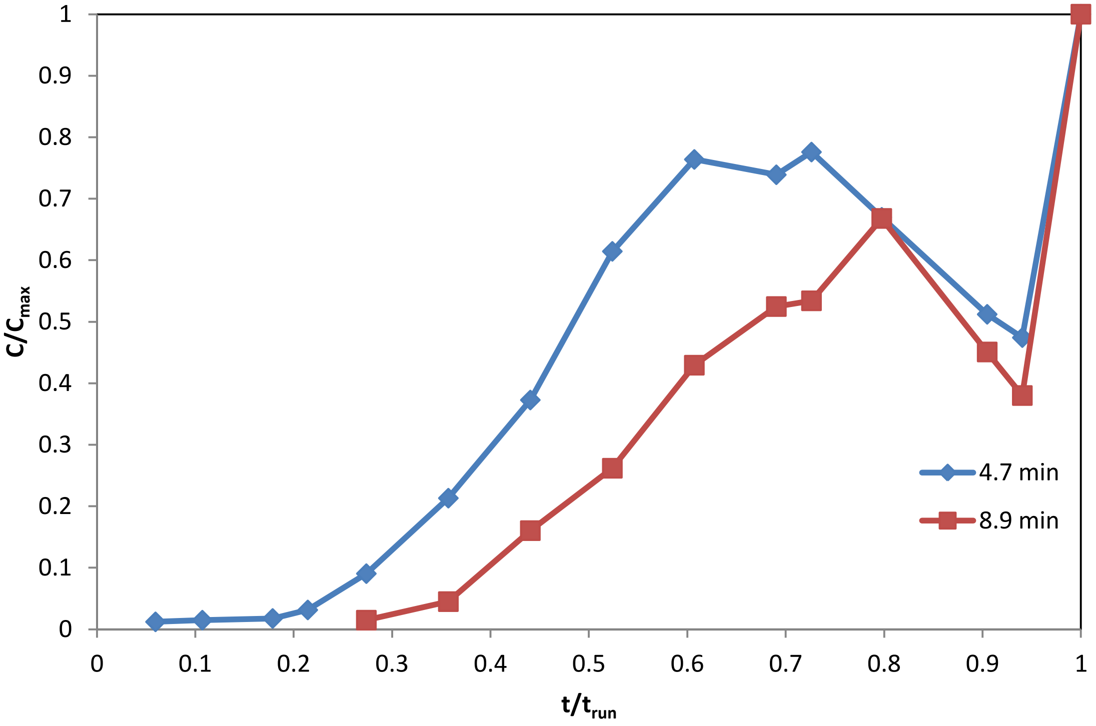

Figure 10: Growth of unidentified HPLC peaks in PP2 solvent

Cation IC

Figure 11 through Figure 13 show the spectra and accumulation of unidentified species in the cation IC data for PP2. Alkaline salts, ammonium, and smaller primary amines all generally elute in the 9- to 12-minute timeframe of the method, resulting in poor separation in this region. Potential unidentified degradation products eluted at 13 minutes, 17 minutes, 37 minutes, and 41.8 minutes. The species represented by the peak at 13 minutes appears to be a thermal degradation product. The species eluting at 17 minutes is almost certainly an amide as it disappears in the hydrolyzed spectra. The peaks at 37 and 41.8 minutes are most likely a substituted PZ compound, similar to HEP and AEP.

Other major unidentified peaks were observed at 24 and 25 minutes elution time. However, when plotted over time no discernible trend of accumulation could be seen in either peak, indicating that they may be sample contaminants. Both peaks disappeared when hydrolyzed.

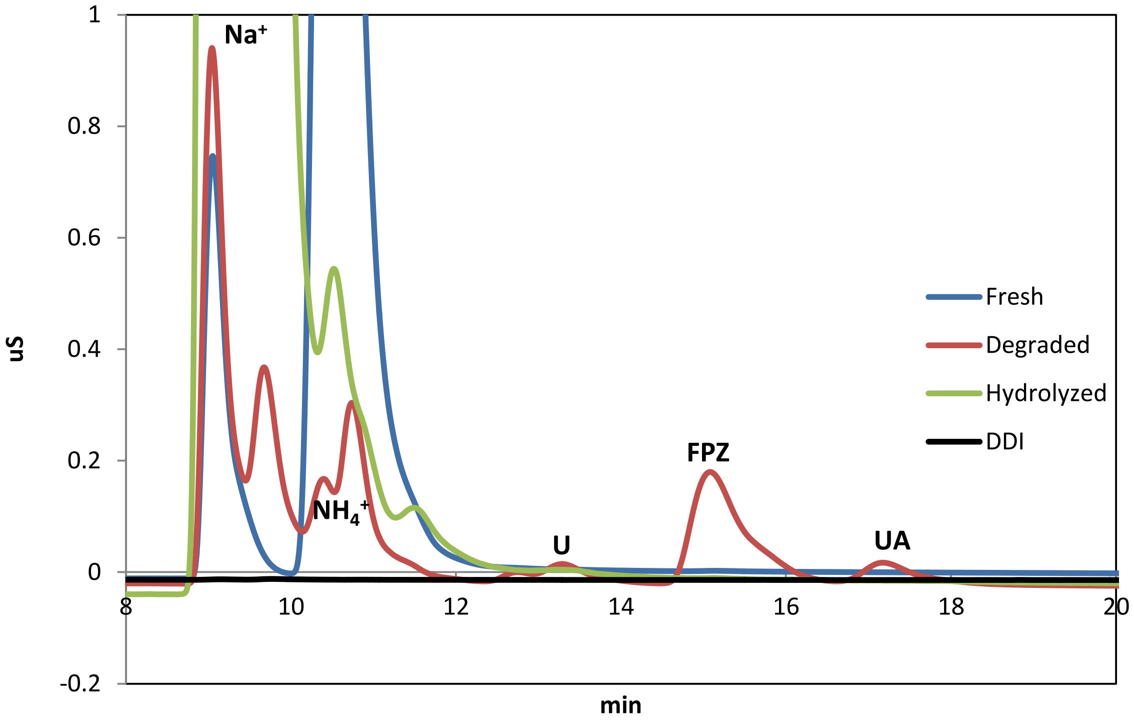

Figure 11: Cation IC spectra of fresh, degraded, and hydrolyzed PP2 solvent (8–20 minutes)

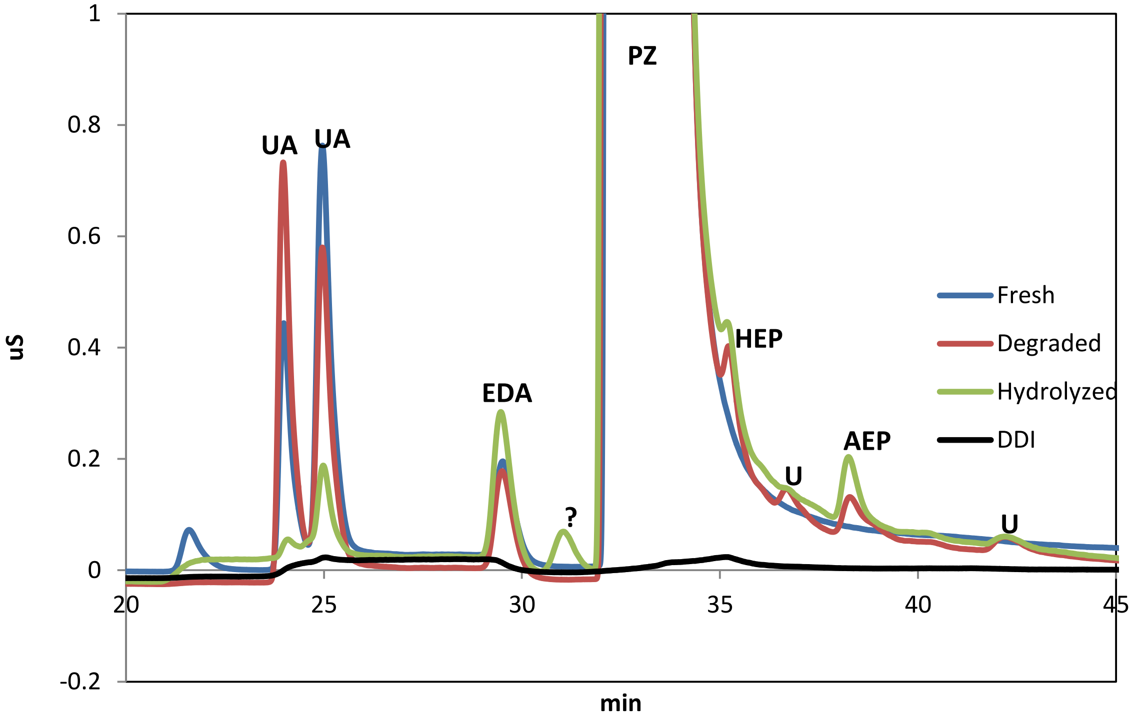

Figure 12: Cation IC spectra of fresh, degraded, and hydrolyzed PP2 solvent (20–45 minutes)

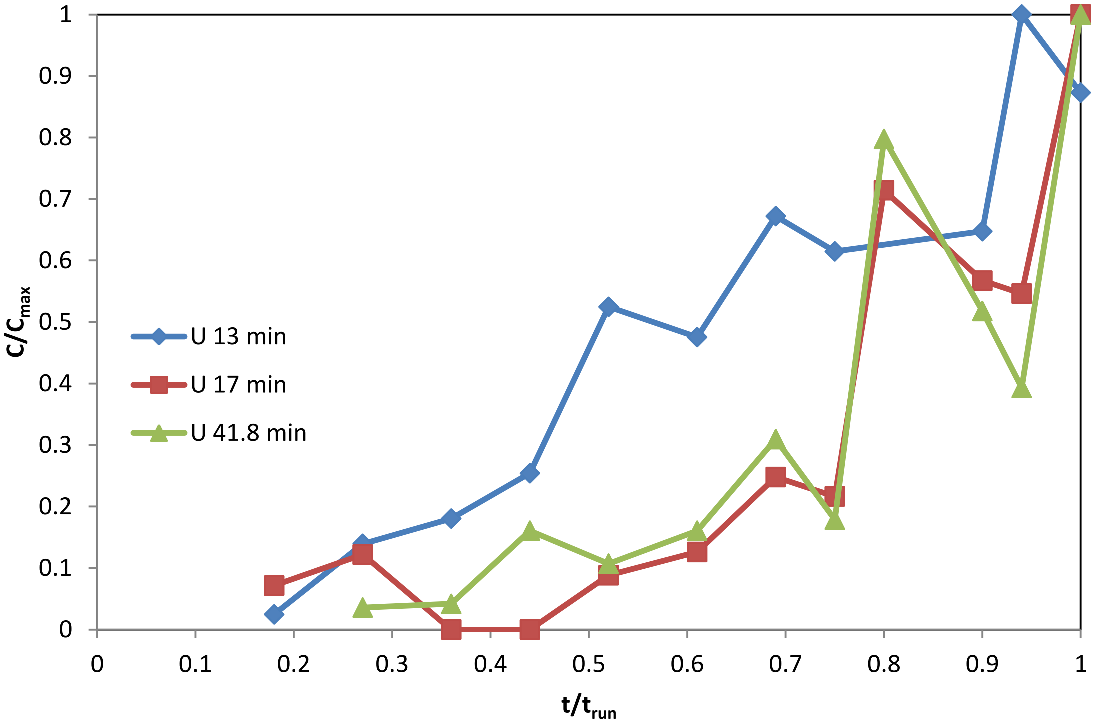

Figure 13: Growth of unidentified cation IC peaks in PP2 solvent

Anion IC

Unidentified peaks were observed at 22 minutes, 24 minutes, and 27 minutes in the anion IC spectra of PP2 solvent.

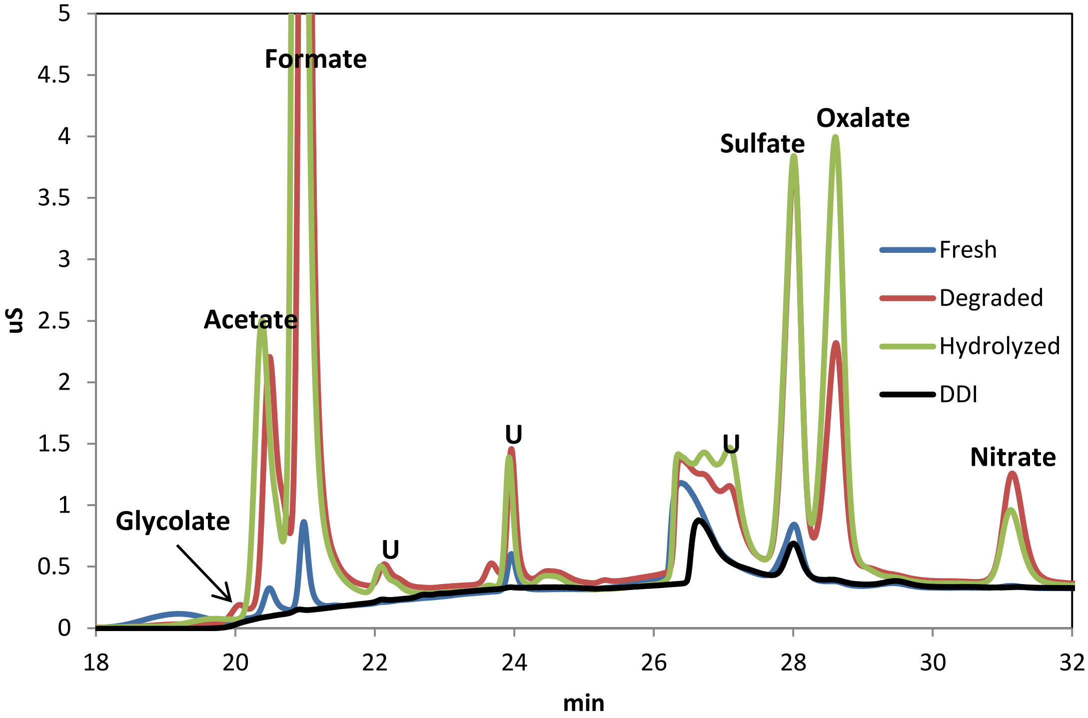

Figure 14: Anion IC spectra of fresh, degraded, and hydrolyzed PP2 solvent

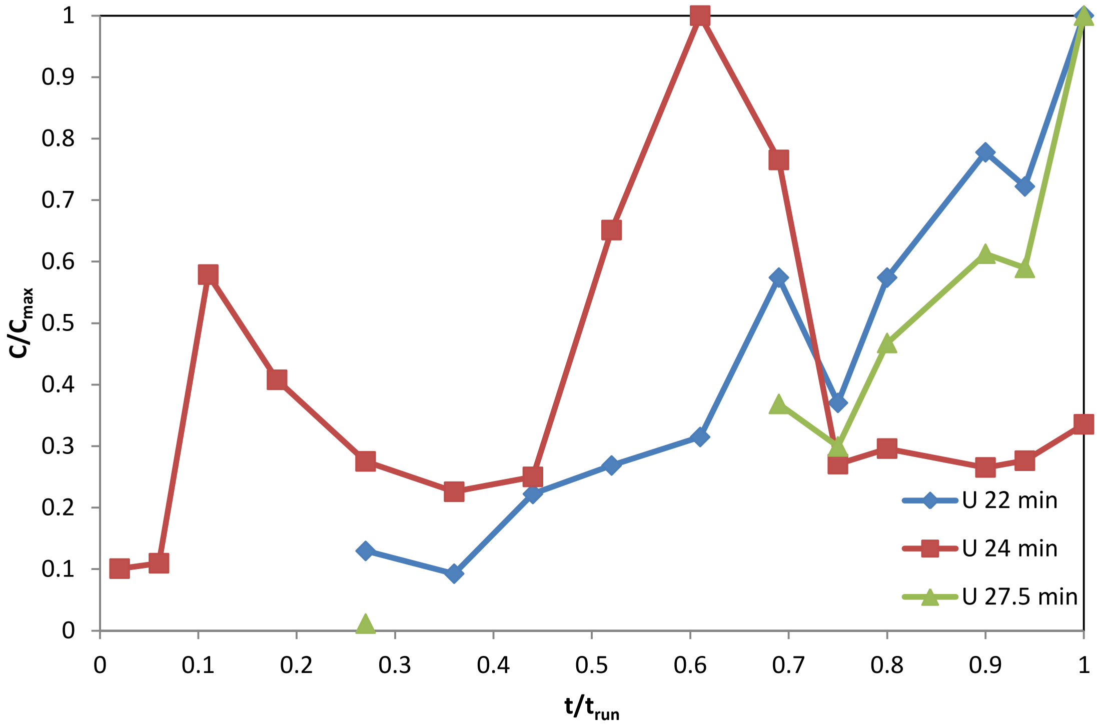

Figure 15: Growth of unidentified anion IC peaks in PP2 solvent

Conclusions

Both the PRC solvent and PP2 solvent had degraded significantly by the end of their respective campaigns. A greater amount of degradation products were observed in Pilot Plant 2. Formate, N-formylpiperazine, and ethylenediamine were the most prevalent degradation products measured. This agrees with previous lab-scale experiments.

In Pilot Plant 2, oxidative degradation products such as amides and carboxylic acids did not begin to accumulate in significant amounts until approximately halfway through the campaign. This strongly correlated with the accumulation of dissolved metals from corrosion, indicating that these metal ions help to catalyze the radical mechanism believed to be responsible for oxidative degradation. The PRC solvent had a much lower concentration of dissolved metals, and also had far less oxidative degradation products, even though the synthetic flue gas for contained approximately 18 kPa O_2, while the PP2 real flue gas was on the order of 5 kPa.

N-formlypiperazine was the only major formamide present in both pilot plant solvents, accounting for about 50% of the total formate present. The heat-stable salt form of formate accounted for the remaining formate present in the solvents.

The thermal degradation products ethylenediamine (EDA), N-(hydroxyethyl)piperazine (HEP), and N-(aminoethyl)piperazine (AEP) all accumulated at a relatively constant rate early in the PP2 campaign. HEP and other unidentified thermal degradation products continued to accumulate at this rate for the entire campaign. However, EDA and AEP in the solvent decreased over time later in the campaign, indicating that both are intermediate degradation products that will degrade further.

Accumulation of nitrate and sulfate in the PP2 solvent was most likely the result of absorption of trace levels (ppm) of SO_x and NO_x from the flue gas.

N-nitrosopiperazine (MNPZ) accumulation in PP2 solvent agreed with the model developed by Fine, reaching a steady state due to the balancing effects of PZ reacting with nitrite absorbed from the flue gas and thermal degradation of MNPZ in the stripper.

Several other important degradation products can be seen in the HPLC and IC spectra but have not yet been identified. Overall the degradation products quantified at this time can only account for 8% of the difference between the measured PZ concentration and the total alkalinity of the PRC solvent. 19% of this difference has been accounted for in the PP2 solvent.

Future Work

New Method Development

The HPLC and IC spectra will be further analyzed to determine the unidentified peaks. This will be done by running standards of suspected degradation products and by using LC-MS. New methods will be developed using LC-MS and IC-MS.

A major goal of the next quarter will be to determine methods to qualitatively measure degradation products that have been previously hypothesized but not positively identified in previous work, including 1-piperazineacetic acid (1-PA) and N-(2-aminoethyl)glycine (AEG). AEG is believed to form from 2-piperazinone and is likely a major product of oxidative degradation of PZ (Freeman, 2011). It will be determined whether these compounds will show up on HPLC if the buffer concentration (and thus pH) is changed. It has been hypothesized that AEG may be charge-balanced at a pH of between 7 and 8 and thus may be detectable with HPLC. A new method will be developed for HPLC in which the buffer and eluent ramp will be modified to better separate and detect AEG.

It has been suggested that the acidity added to the solvent by CO_2 loading may be causing a systematic error in the total alkalinity measurements. This issue will be explored in more depth and the validity of the autotitration method will be determined.

Suspected Degradation Products

Figure 16 and Figure 17 show some of the suspected thermal and oxidative degradation products that have not been quantified analytically (Freeman, 2011).

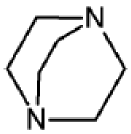

Triethylenediamine
MW: 112.17
(CAS: 280-57-9)

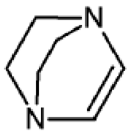

1,4-Diazabicyclo[2.2.2]oct-2-ene
(TEDA enamine)
MW: 110.16
(CAS: 122883-12-9)

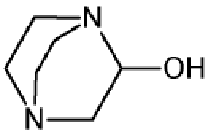

1,4-Diazabicyclo[2.2.2]octan-2-ol
(TEDA hemiaminal)
MW: 128.17
(CAS: 146562-84-7)

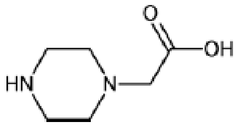

1-Piperazineacetic acid
(1-PA)
MW: 144.17
(CAS: 37478-58-3)

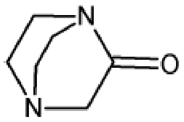

1,4-Diazabicyclo[2.2.2]octan-2-one (Amide of 1-PA)
MW: 126.16
(CAS: 146562-83-6)

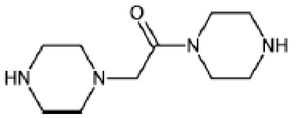

1-(1-Piperazinylacetyl)-piperazine
(Amide of 1-PZ)
MW: 212.29
(CAS: 69253-90-3)

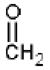

Formaldehyde
MW: 30.03
(CAS: 50-00-0)

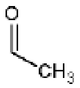

Acetaldehyde
MW: 44.05
(CAS: 75-07-0)

Hydroxyacetaldehyde
MW: 60.05
(CAS: 141-46-8)

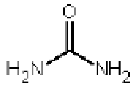

Urea
MW: 60.06
(CAS: 57-13-6)

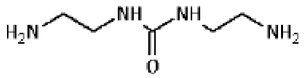

N,N'-bis(2-aminoethyl)-urea
(diEDA urea)
MW:146.19
(CAS: 940866-61-5)

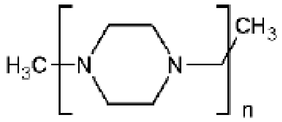

Poly(methylene)PZs

Figure 16: Suspected PZ thermal degradation products (Freeman, 2011)

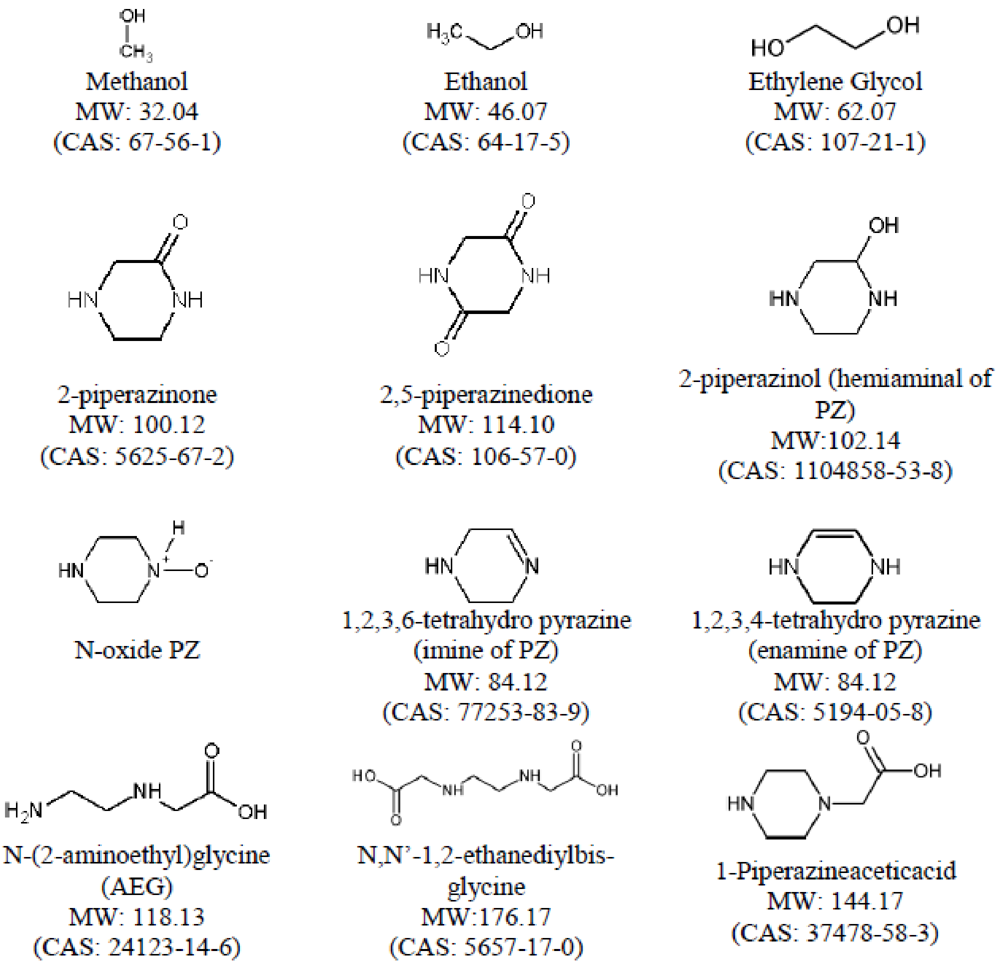

Methanol
MW: 32.04
(CAS: 67-56-1)

Ethanol
MW: 46.07
(CAS: 64-17-5)

Ethylene Glycol
MW: 62.07
(CAS: 107-21-1)

2-piperazinone
MW: 100.12
(CAS: 5625-67-2)

2,5-piperazinedione
MW: 114.10
(CAS: 106-57-0)

2-piperazinol (hemiaminal of PZ)
MW:102.14
(CAS: 1104858-53-8)

N-oxide PZ

1,2,3,6-tetrahydro pyrazine
(imine of PZ)
MW: 84.12
(CAS: 77253-83-9)

1,2,3,4-tetrahydro pyrazine
(enamine of PZ)
MW: 84.12
(CAS: 5194-05-8)

N-(2-aminoethyl)glycine
(AEG)
MW: 118.13
(CAS: 24123-14-6)

N,N'-1,2-ethanediylbis-glycine
MW:176.17
(CAS: 5657-17-0)

1-Piperazineaceticacid
MW: 144.17
(CAS: 37478-58-3)

Figure 17: Suspected PZ oxidative degradation products (Freeman, 2011)

References

Closmann FB. *Oxidation and thermal degradation of methyldiethanolamine/piperazine in CO_2 capture.* The University of Texas at Austin. Ph.D. Dissertation. 2011.

Freeman SA. *Thermal Degradation and Oxidation of Aqueous Piperazine for Carbon Dioxide Capture*. The University of Texas at Austin. Ph.D. Dissertation. 2011.

Rochelle GT et al. "CO_2 Capture by Aqueous Absorption, Fourth Quarterly Progress Report 2011." Luminant Carbon Management Program. The University of Texas at Austin. 2012.

Voice AK. *Production of MNPZ from reaction of aqueous nitrite with piperazine in 4 m 2-AMP + 6 m PZ for CO_2 Capture*. Unpublished Manuscript. 2011.

Appendix A: Comprehensive Data Tables

All data points with standard deviations (stdev) are averages over multiple runs.

Table 6: Anion IC Data, pilot plant 2

t/t$_{run}$	Glycolate		Acetate		Formate		U 22 min		U 24 min		U 27.5 min
	mmol/kg	stdev	mmol/kg	stdev	mmol/kg	stdev	uS*min	stdev	uS*min	stdev	uS*min
0.02			0.949		1.726				0.046		
0.06			0.589		0.791				0.05		
0.11			0.431		2.053				0.264		
0.18			0.067		2.640				0.186		
0.27	0.0937	0.036	0.610		2.141	0.226	0.007		0.1255	0.0064	0.005
0.36	0.0848		0.472		2.596		0.005		0.103		0
0.44	0.136		2.852		8.272		0.012		0.114		0
0.52	0.136	0.072	3.830	0.433	7.672	1.431	0.0145	0.0021	0.297	0.0269	0
0.61	0.0850		4.071		17.38		0.017		0.456		0
0.69	0.221		5.575		17.61		0.031		0.349		0.16
0.75	0.122	0.034	7.253	1.295	24.18	5.59	0.020	0.005	0.124	0.0461	0.13
0.8	0.204		7.546		26.69		0.031		0.135		0.203
0.9	0.306		9.101		30.32		0.042		0.121		0.266
0.94	0.306		8.600		28.82		0.039		0.126		0.256
1	0.272	0.072	11.22	0.29	38.62	9.25	0.054	0.010	0.153	0.0057	0.434

t/t$_{run}$	Sulfate		Oxalate		Nitrate	
	mmol/kg	stdev	mmol/kg	stdev	mmol/kg	stdev
0.02	0.879				0.097	
0.06	0.937		0.155		0.113	
0.11	2.052				0.162	
0.18	1.678		0.170		0.564	
0.27	3.321	0.609	0.177	0.163	2.332	0.068
0.36	3.114		0.353		1.874	

0.44	3.543		0.524		2.235	
0.52	4.436	0.020	1.260	0.282	2.502	0.045
0.61	5.119		2.168		2.359	
0.69	5.750		4.692		2.682	
0.75	4.515	1.033	4.337	0.927	2.276	0.557
0.8	5.234		4.225		2.774	
0.9	5.590		7.173		3.144	
0.94	4.758		7.527		2.920	
1	7.071	1.011	8.617	0.510	4.823	0.283

Table 7: Cation IC Data, pilot plant 2

t/t_{run}	NH4+		U 13 min		FPZ		U 17 min		EDA		HEP	
	mmol/kg	stdev	uS*min	Stdev	mmol/kg	Stdev	uS*min	Stdev	mmol/kg	Stdev	mmol/kg	stdev
0.02									9.323			
0.06	17.26				0.388				11.24		0.032	
0.11	22.87								13.32		0.039	
0.18	5.339		0.0003		0.593		0.0017		14.07		0.174	
0.27	5.864		0.0017		1.225	0.127	0.0029		23.52	1.58	0.456	0.231
0.36	4.047		0.0022		1.641				25.49		0.847	
0.44			0.0031		2.333				24.54		0.999	
0.52	2.494	0.023	0.0064	0.0047	6.754	1.919	0.0021	0.0013	30.79	0.57	1.346	0.574
0.61	2.423		0.0058		8.221		0.0030		19.87		1.726	
0.69	1.457		0.0082		17.27		0.0059		17.54		2.365	
0.75	1.346	0.089	0.0075	0.0031	13.32	2.36	0.0052	0.0019	16.10	0.04	1.910	0.627
0.8	0.714				25.51		0.0170		14.35		2.198	
0.9	0.781		0.0079		25.92		0.0135		16.55		2.462	
0.94	0.840		0.0122		25.22		0.0130		13.66			
1	0.691	0.008	0.0107	0.0005	37.96	0.62	0.0238	0.0006	9.326	0.074	2.644	0.223

t/t_{run}	U 36.7 min		AEP		U 41.8 min	
	uS*min	Stdev	mmol/kg	Stdev	uS*min	stdev
0.02						
0.06			0.361			
0.11	0.0020		0.415			
0.18			0.898			
0.27	0.0002		2.202	0.380	0.0006	
0.36			2.594		0.0007	
0.44	0.0017		3.895		0.0027	
0.52	0.0018	0.0001	3.973	0.247	0.0018	
0.61	0.0014		2.873		0.0027	
0.69	0.0057		3.515		0.0052	
0.75	0.0022	0.0004	3.304	0.122	0.0030	0.0008
0.8	0.0067		3.312		0.0134	
0.9	0.0029		3.031		0.0087	
0.94	0.0061		2.249		0.0066	
1	0.0176	0.0013	2.939	0.270	0.0168	0.0069

Table 8: HPLC Data (Solvent) pilot plant 2

t/t_{run}	MNPZ			U 4.7 min	U 8.9 min
	Peak Area	mmol/kg	stdev	Peak Area	Peak Area
0.00					
0.02	0.118	0.0351			
0.06	0.560	0.1669		0.013	
0.11	0.978	0.2909		0.016	
0.18	5.449	1.6200		0.019	
0.21	8.549	2.5469		0.034	
0.27	9.442	2.8257	0.0040	0.098	0.063
0.36	2.943	0.8749		0.231	0.192
0.44	2.306	0.6876		0.404	0.686

0.52	2.606	0.7766		0.666	1.12
0.61	2.505	0.7439		0.828	1.837
0.69	2.988	0.8874		0.801	2.245
0.73	2.474	0.7634		0.841	2.285
0.74	2.364	0.7042		0.49	1.567
0.75	2.468	0.7348		0.865	2.981
0.76	2.847	0.8489		0.833	2.915
0.77	2.149	0.6401		0.462	1.716
0.79	3.227	0.9603		0.654	2.519
0.80	3.618	1.0761		0.726	2.858
0.90	3.694	1.0993		0.555	1.929
0.94	4.557	1.3568		0.514	1.626
1.00	4.092	1.2177		1.084	4.279
0.06	1.004	0.0746			
0.35	0.454	0.0338			
0.61	0.523	0.0466			
0.71	0.248	0.0222			
0.73	0.241	0.0218			
0.94	0.472	0.0351			
1.00	0.222	0.0165			

Table 9: HPLC Data (Wash)

t/t_{run}	MNPZ	
	Peak Area	mmol/kg
0.06	1.004	0.0746
0.35	0.454	0.0338
0.61	0.523	0.0466
0.71	0.248	0.0222
0.73	0.241	0.0218
0.94	0.472	0.0351

1.00	0.222	0.0165

N-Nitrosopiperazine Kinetics in CO_2 Capture

Quarterly Report for January 1 – March 31, 2012

by Nathan Fine

Supported by the Luminant Carbon Management Program

Department of Chemical Engineering

The University of Texas at Austin

April 30, 2012

Abstract

This quarter, high temperature kinetics for the formation and decomposition of N-Nitrosopiperazine (MNPZ) were studied. MNPZ formation is first order with respect to nitrite, and MNPZ decomposition is first order with respect to MNPZ. Both reactions are irreversible. A temperature dependent model was determined for MNPZ decomposition from 120 °C to 150 °C. However, MNPZ formation was too fast to analyze at 135 °C and 150 °C using the current methodology. Stainless steel ions were found to have no effect on MNPZ decomposition. Piperazine carbamate ($PZCOO^-$) catalyzes MNPZ formation, but has no effect on MNPZ decomposition. Current data suggests that MNPZ decomposition is first order with respect to protonated piperazine (^+HPZ).

The MNPZ kinetics were used to calculate the transient and steady state MNPZ concentration in a carbon capture absorption-stripping unit. The steady state concentration can be lowered by decreasing the residence time in the stripping sump, decreasing the NO_2 concentration in the flue gas, or increasing the temperature in the sump. At a sump temperature of 150 °C and a total residence time 5 times the sump residence time, nitrosamine concentration should reach 90% of steady state after 5 days.

Introduction

PZ is currently considered a promising solvent for CO_2 capture in coal-fired power plants due to its high absorption rates, high working capacity, and resistance to thermal degradation. However, PZ readily undergoes nitrosation to form MNPZ, a relatively stable nitrosamine. MNPZ is carcinogenic with a TD50 of 8.7 mg/kg BW/day (Garcia, 1970). Thermal decomposition of N-Nitrosopiperazine (MNPZ) is a viable way to control MNPZ concentration in an amine scrubbing system that uses a PZ solvent. MNPZ management through thermal decomposition requires no additional equipment, no additional chemicals, and is possible at optimal conditions for running the stripper. This report attempts to characterize the kinetics for MNPZ formation and decomposition in order to predict and eventually manage MNPZ concentration through thermal decomposition.

Experimental Methods

Solvent Preparation

An 8 m PZ solvent was prepared gravimetrically and then loaded with 0.3 $\frac{\text{mol CO2}}{\text{mol alkilinity}}$. Iron, nickel, and chromium ions were also added volumetrically to the 120 °C and 150 °C experiments at concentrations of 0.4 mM, 0.1 mM, and 0.05 mM, respectively, to match the stainless steel conditions found in amine scrubbing. No stainless steel ions were added to the 135 °C in order to study the effects of stainless steel ions on MNPZ kinetics.

A separate solution of 8 m PZ was prepared with 98% pure sulfuric acid to match the concentration of protonated amine in a 0.3 CO_2 loaded solution. The sulfuric acid was added at a rate of approximately 5 mL/min because of the violent reaction between sulfuric acid and PZ. PZ hexahydrate precipitated out of the solution at room temperature, so the solution was heated to 50 °C to dissolve the solid. Stainless steel ions were also added into solution.

Sample Preparation

The solutions were spiked gravimetrically with 10 to 80 mmol/kg of sodium nitrite. The solution was well-mixed and then pipetted into 10 mL stainless steel thermal cylinders and placed in a convection oven operating between 120 °C and 150 °C. 2 mL of headspace was left in each cylinder to reduce the chance of cylinder failure due to overpressure. Samples were removed from the oven at semi-regular intervals until over 90% of the MNPZ had decomposed. Samples which leaked more than one gram were considered failures and not reported.

Lab Safety

Currently approximately 30% of the thermal cylinders fail in the high temperature ovens. This represents a serious risk since these cylinders contain MNPZ, a known carcinogen. Several measures have been taken to reduce the risk of exposure to these hazardous chemicals. First, a torque wrench has been purchased to standardize the cylinder tightening procedure and eliminate error due to fatigue and inexperience. Since every failed cylinder leaks at the fitting, the torque wrench should greatly reduce the number of failed cylinders. Second, nitrosamine experiments will be run in 3/8 inch diameter cylinders instead of 1/2 inch diameter cylinders. The smaller diameter will decrease total nitrosamine inventory and also give a better seal. If the cylinders do fail, the current method makes sure the contents are vented through the fume hood. The ovens are directly vented to the fume hood. When removing samples from the oven, the oven door is first cracked open. This creates suction for the oven vents to clear any gases in the oven.

Concentration Measurement

After 15 minutes of cooling, the thermal cylinders were opened and the samples were diluted in water to 20x and 5x for HPLC analysis or 100x and 20x for IC analysis. The MNPZ concentration was obtained by fitting the HPLC absorption curve results to the calibration curve prepared by Namjoshi. No IC nitrite data was obtained for any samples other than the initial sample because nitrite completely reacts within the first hour. The initial nitrite data from the IC was used to confirm the gravimetric measurements for nitrite concentration. A new MNPZ calibration curve was prepared; it showed no statistical difference from the curve prepared by Namjoshi, and both curves have a quantification limit around 5 ppm MNPZ.

Materials

N-Nitrosopiperazine (MNPZ) (98 wt % purity)	Supplied by Toronto Research Chemicals
Piperazine (PZ) (99 wt % purity)	Supplied by Sigma-Aldrich
Sodium Nitrite (98.5 wt % purity)	Supplied by Acros organics
Carbon Dioxide (99.99% purity)	Supplied by Matheson Tri-Gas
Sulfuric Acid (98% purity)	Supplied by Acros organics
Nickel Sulfate (0.2 M)	Prepared by Stephanie Freeman
Chromium Sulfate (0.2 M)	Prepared by Stephanie Freeman
Iron Sulfate (0.2 M)	Prepared by Stephanie Freeman

Results and Discussion

No Temperature Dependence

Previous research has suggested that the kinetics for MNPZ formation and decomposition are as follows:

$$NO_2^- \underset{k1-}{\overset{k1}{\overset{\rightarrow}{\longleftarrow}}} MNPZ \underset{k2}{\rightarrow} Byproducts \tag{1}$$

Since the loading and PZ concentration are constant throughout the batch process, all rate kinetics are assumed first order with respect to reactants:

$$\frac{dC_{NO_2}}{dt} = -k_1 C_{NO_2} + k_{1-} C_{MNPZ} \tag{2}$$

$$\frac{dC_{MNPZ}}{dt} = k_1 C_{NO_2} - k_{1-} C_{MNPZ} - k_2 C_{MNPZ} \tag{3}$$

The rate equations were initially numerically integrated with a time step of 0.001 days. The parameters k_1, k_{1-}, k_2, and initial nitrite concentration were fitted to the data using a simple least squares approach. Numerical regressions at 120 °C, 135 °C, and 150 °C all determined the reverse nitrosation reaction constant (k_{1-}) to be zero. The regression has prompted a new MNPZ kinetics model with both MNPZ formation and decomposition reactions as irreversible:

$$NO_2^- \underset{k1}{\rightarrow} MNPZ \underset{k2}{\rightarrow} Byproducts \tag{4}$$

$$\frac{dC_{NO_2}}{dt} = -k_1 C_{NO_2} \tag{5}$$

$$\frac{dC_{MNPZ}}{dt} = k_1 C_{NO_2} - k_2 C_{MNPZ} \tag{6}$$

Both differential equations can be solved analytically using Laplace transforms:

$$C_{NO_2^-} = C_{NO_2^- i} * e^{-k_1 t} \tag{7}$$

$$C_{MNPZ} = C_{NO_2^- i} * \frac{k_1}{k_2 - k_1} \left(e^{-k_1 t} - e^{-k_2 t}\right) \tag{8}$$

The parameters k_1, k_2, and $C_{NO_2^- i}$ were fitted to the data and regressed using a simple least squares approach. $C_{NO_2^- i}$ represents the amount of nitrite that reacts to form PZ, so it directly measures the nitrosamine yield from the nitrosation reaction. The parameters were initially regressed for each individual experiment and the results are shown in Table 1.

Table 1: Regressed Parameters

Parameters	120 °C	135 °C	150 °C
k_1*10^6 (s^{-1})	420±40	3640±2600	Instant
k_2*10^6 (s^{-1})	3.6±0.13	11.2±0.14	26±0.8
NO_{2i}^- (mmol/kg)	42.8±0.5	50±1	6/35±1
$NO_{2i\,Model}^-/NO_{2i\,\mathrm{Grav}}^-$	0.96±0.01	1.02±0.02	0.99/0.98±0.03

Each regression has an R^2 value greater than 0.99 so the new model matches MNPZ kinetics very well. Almost all MNPZ formation occurs in the first hour at 135 °C and 150 °C, which is too fast to analyze properly. This means the regressed k_1 values above 120 °C do not affect the model, which is apparent in their large standard errors. The regressed nitrite values match the gravimetric nitrite values, suggesting near perfect yield of MNPZ.

Temperature Dependence

All four experiments were normalized by the initial nitrite so that they could more easily be regressed together and represented on a single plot. The k_1 and k_2 values were modeled based on the Arrhenius equation with the temperature centered around 120 °C:

$$k_{1,2}(T) = k_{1,2}(120\ ^\circ\mathrm{C}) * e^{\frac{Ea_{1,2}}{R}\left(\frac{1}{393}-\frac{1}{T}\right)} \tag{9}$$

Without good data for k_1 at 135 °C or 150 °C, E_{a1} has no real meaning in the regression model so a default value of 70 kJ/mol was chosen for E_{a1} based on previous research (Ashouripashaki, 2011). The other three parameters were regressed using a simple least squares approach. The results are shown below in Table 2 and Figure 1. The point at 0.36 days for the 150 °C data is an outlier and was not used in the regression. The dashed line represents the quantification limit for a 5x dilution of the data at 150 °C. The values for k_2 from regressing the experiments together are not statistically different than the values for k_2 from regressing the experiments individually, which suggests that an Arrhenius model is a good fit for temperature dependence. Standard errors and covariance for the three regressed parameters still need to be determined.

Table 2: Regressed Parameters for Arrhenius Dependence

Parameters	Values
k_1(120)*10^6 (s^{-1})	430
Ea_1 (kJ/mol)	70 (Default)
k_2(120)*10^6 (s^{-1})	3.7
Ea_2 (kJ/mol)	92

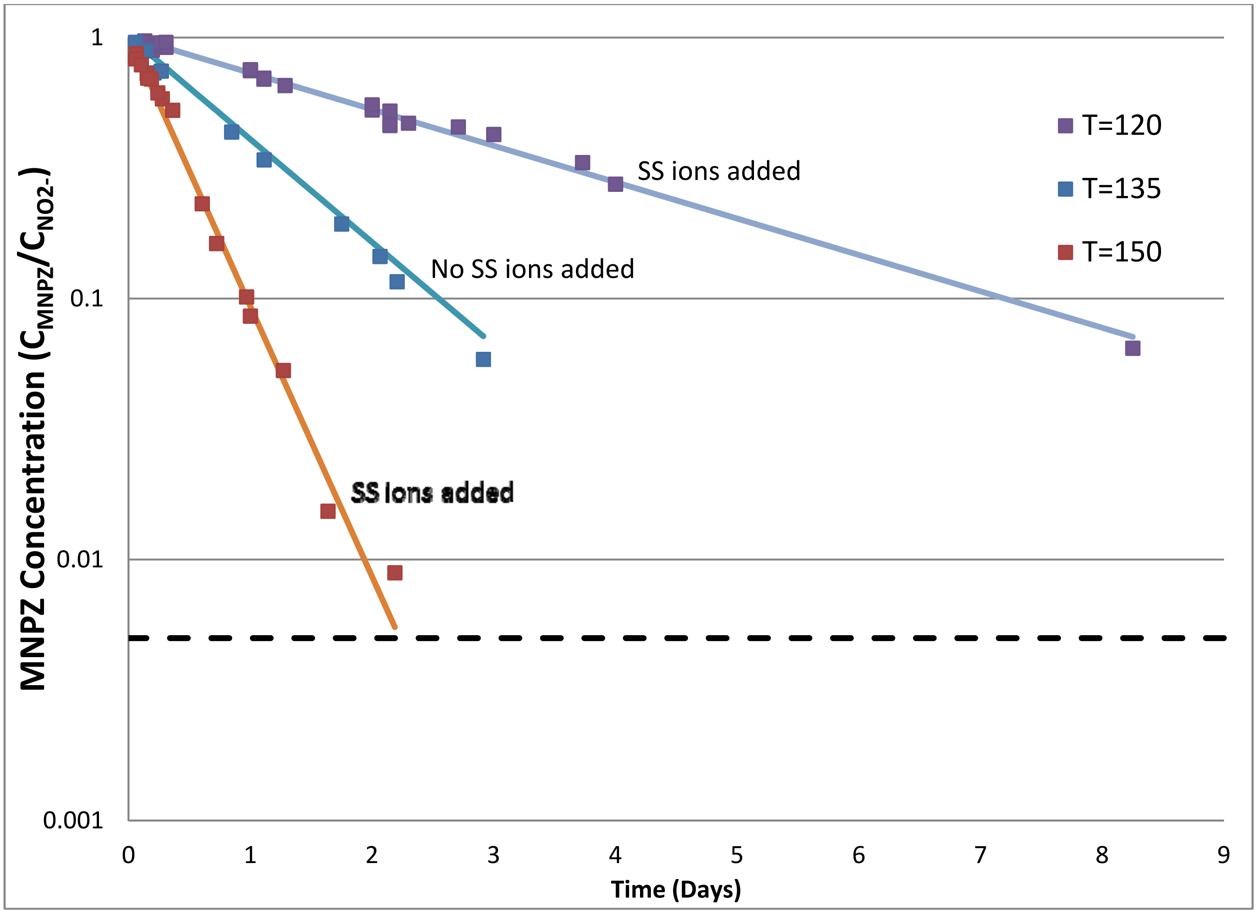

Figure 1: Kinetics for MNPZ formation and decomposition
Conditions: 8 m PZ, α = 0.3, T = 120 °C, 135 °C, 150 °C

Stainless Steel Ions

Stainless steel ions were not added to the experiment run at 135 °C. Furthermore, PZ is not corrosive at 135 °C, so this experiment should have very few metal ions in solution (Freeman, 2011). From the residual plot (Figure 2), a small bias can be seen in the 135 °C experiment, which could be attributed to the absence of metal ions. However, the 135 °C experiment was prepared from a different solution than the 120 °C and 150 °C experiments, so the solution had a slightly different concentration of PZ and a slightly different CO_2 loading. The bias could easily be attributed to these small changes in concentration instead. The bias is very small, so stainless steel ions do not play a significant role, if any role at all, in catalyzing MNPZ decomposition.

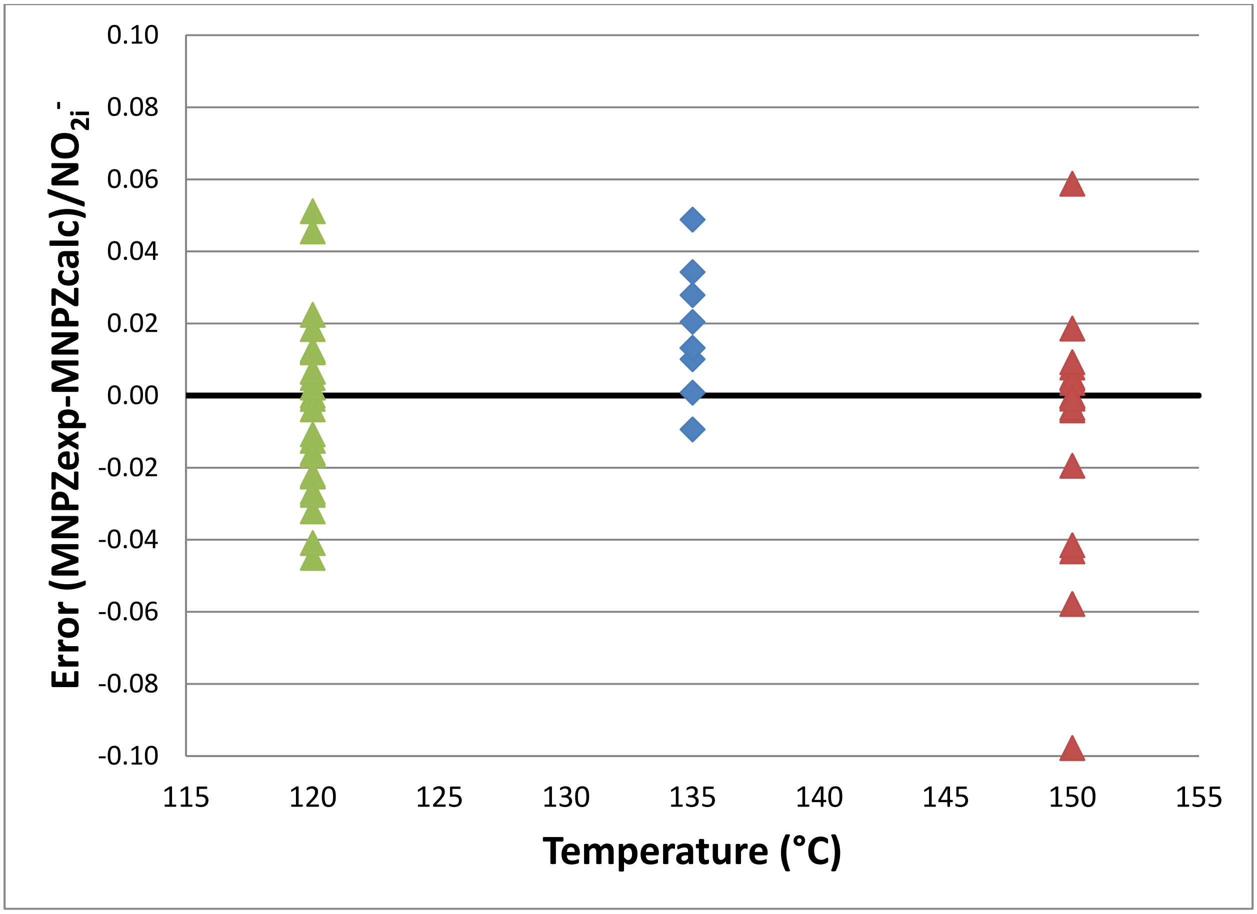

Figure 3: Residuals between the experimental data and the model

Role of Individual PZ Species

MNPZ kinetics are hypothesized to be a function of CO_2 loading and PZ concentration (Ashouripashaki, 2011). However, no clear trend has been found to explain MNPZ decomposition over a range of loadings. One possible explanation is that changing loading does not directly affect MNPZ decomposition, but instead causes PZ to speciate to different compositions. The experiment with sulfuric acid (H_2SO_4) in place of CO_2 isolates the effects of individual PZ species since there are no carbamates in the sulfuric acid solution. The nitrogens in the PZ solution were separated into three categories: protonated nitrogens, carbamated nitrogens, and free nitrogens. An 8 m PZ solution was loaded with H_2SO_4 so that the number of protonated nitrogens roughly matched the number of protonated nitrogens in a solution of 8 m PZ loaded with 0.3 mol CO_2/mol N. PZ speciation shown in Figure 4 below was extrapolated from low temperature speciation data (Frailie, 2010).

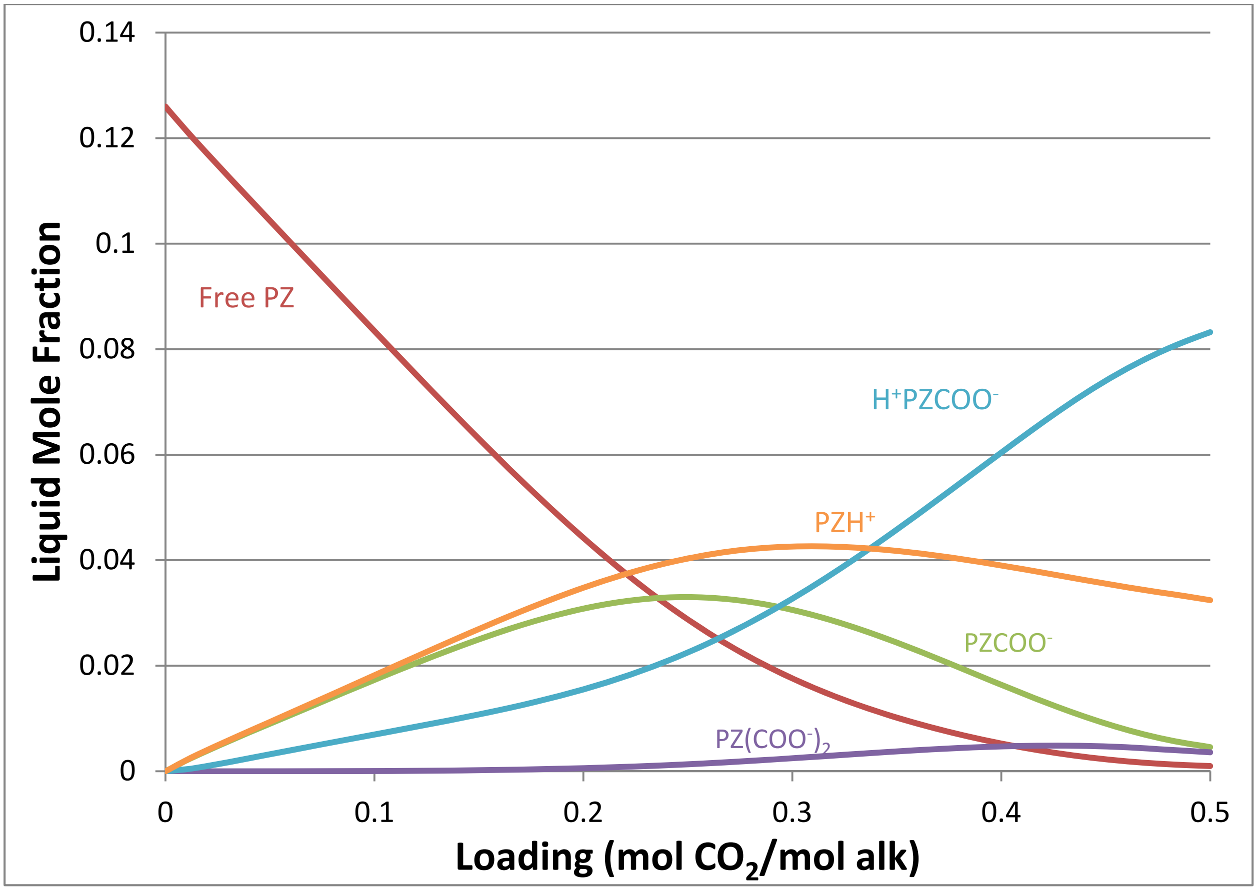

Figure 4: PZ speciation at 135 °C as a function of loading

The H_2SO_4 experiment was run at 135 °C and matched with the CO_2 experiment run at 135 °C. The theoretical PZ speciation and MNPZ kinetics are shown in Table 3 below, and the data along with the model are shown in Figure 5.

Table 3: Effect of PZ speciation on MNPZ kinetics

	H_2SO_4 Added	CO_2 Added
Free Nitrogen (m)	6.6	2.4
Protonated Nitrogen (m)	9.9	9.6
Carbamate Nitrogen (m)	0	4.0
k_1*10^6 (s^{-1})	61±3.5	3640±2600
k_2*10^6 (s^{-1})	13±0.7	11.2±0.14

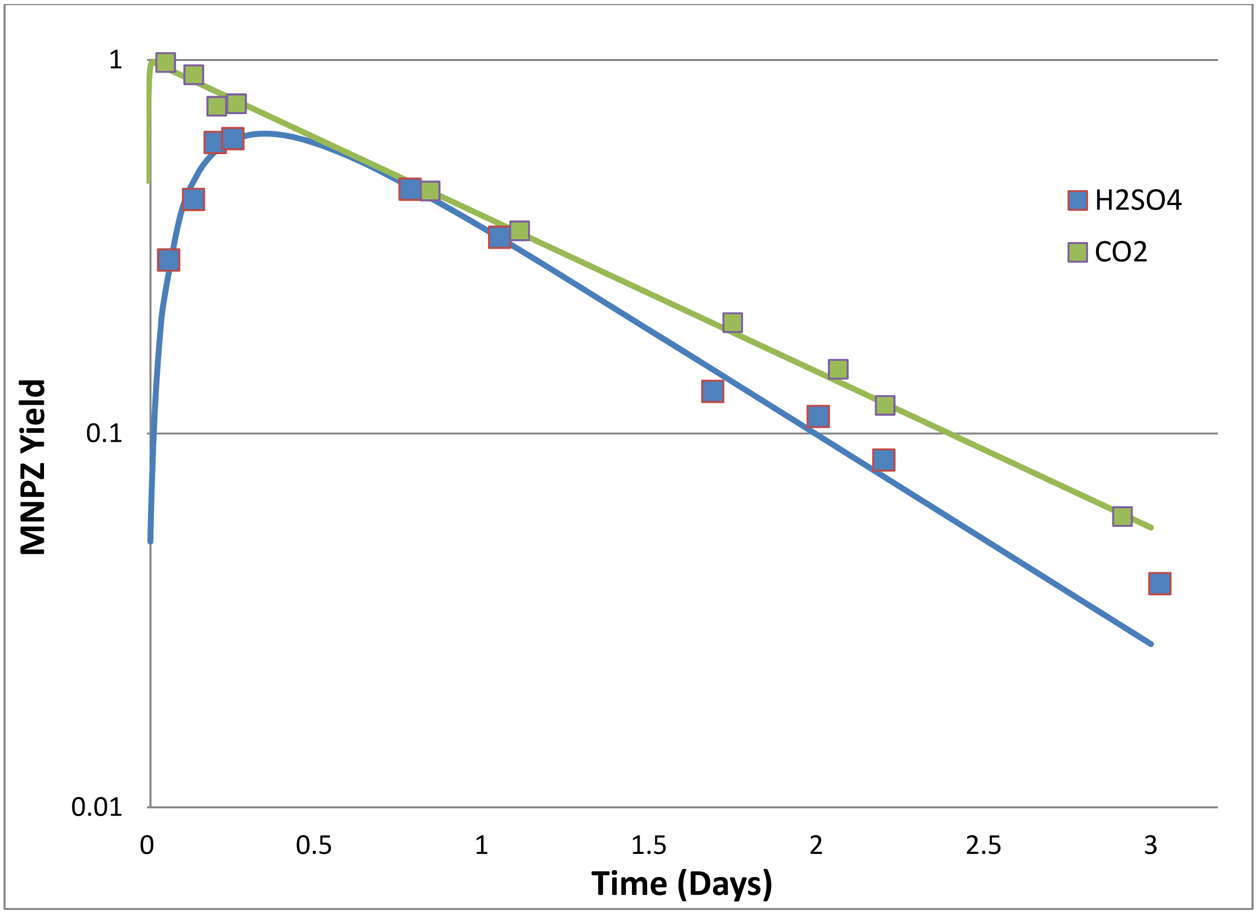

Figure 5: MNPZ kinetics in 8 m PZ at 135 °C

MNPZ formation was much faster with carbamate in solution, showing that the carbamate catalyzes the nitrosation reaction. However, the reaction still ran without any added CO_2. This could be a secondary pathway for nitrosation, or it could be caused by small amounts of CO_2 absorbed from the air when preparing the H_2SO_4 solution. A total inorganic carbon analysis will be performed to determine CO_2 content in the H_2SO_4 solution and conclude if there is a secondary nitrosation pathway.

The decomposition reaction had very similar rates for both experiments. Since carbamated nitrogen and free nitrogen concentrations are very different in the two experiments, MNPZ decomposition cannot be a first order function of either species. However, MNPZ decomposition could be a function of protonated PZ since that concentration was very similar for both experiments. Previous research suggests MNPZ decomposition is a first order function of an unknown PZ species concentration (Ashouripashaki, 2011). It is likely that MNPZ decomposition is first order with respect to protonated PZ, but further experiments over a range of loadings must be carried out to test this hypothesis.

Modeling Pilot Plant Data

The current pilot plant model has five necessary but reasonable assumptions which lead to the process diagram in Figure 6.

1. Nitrite reacts stoichiometrically to produce MNPZ.

Nitrite reacts over 100 times faster in the stripper sump than anywhere else in the system. Since the stripper sump also has a long residence time, all nitrite reactions will happen there. The high temperature experiments presented in this report show a stoichiometric yield of MNPZ under these conditions.

2. MNPZ only decomposes in the stripper sump.
   The sump has the longest residence time and highest temperatures.
3. All the NO_2 in the flue gas absorbs as NO_2^- in the absorber.
   This assumption will be tested in future work.
4. NO_2^- does not originate in large amounts from anywhere else.
   Some NO_2^- might come from PZ oxidation, which would explain the small amounts of MNPZ found at Pilot Plant 1 during the last campaign (Nielsen, 2011). However, these amounts are ten times less than the amount of NO_2^- expected in a real flue gas, so this NO_2^- source will be ignored for now.
5. The flue gas is 11% CO_2 and one mole of CO_2 is removed per liter of amine.

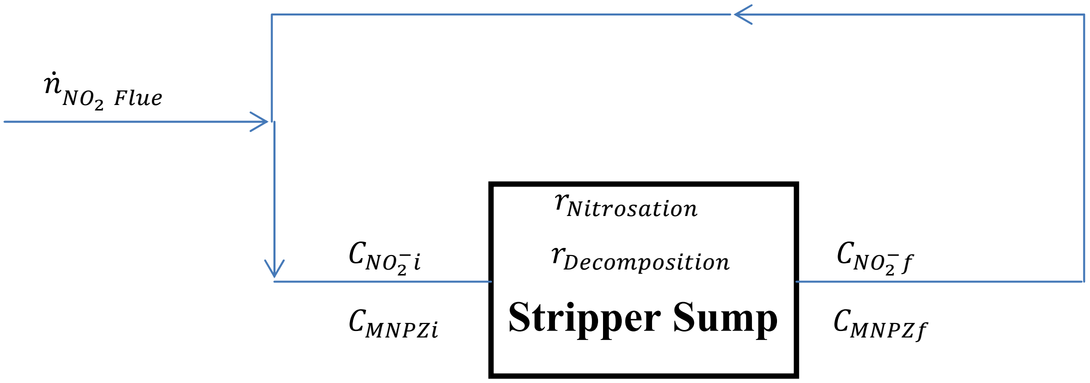

Figure 6: Schematic of steady state molar flow rates

Assuming constant density, the following four material balances can be written:

$Overall\ Nitrite$:
$$C_{NO_2^- i} = C_{NO_2^- f} + C_{NO_2^- FL} \tag{9}$$

$Nitrite\ Reacted\ In\ Sump$:
$$\frac{dC_{NO_2^-}}{dt} = C_{NO_2^- i} - C_{NO_2^- f} - k_1 C_{NO_2^- f} \tau_{sump} \tag{10}$$

$Overall\ MNPZ$:
$$C_{MNPZi} = C_{MNPZf} \tag{11}$$

$MNPZ\ in\ Sump$:
$$\frac{dC_{MNPZ}}{dt} = C_{MNPZi} - C_{MNPZf} + \tau_{sump}(k_1 C_{NO_2^- f} - k_2 C_{MNPZf}) \tag{12}$$

The time derivatives are zero at steady state, and the NO_2 gas molar flow rate can be converted to nitrite concentration. Solving the resulting four steady state mass balances simultaneously gives the steady state MNPZ concentration in the scrubber.

$$C_{NO_2^- Fl} = \frac{\dot{n}_{NO_2\ Fl}}{\dot{n}_{Fl}} * \frac{100\ moles_{Fl}}{11 moles_{CO_2 Fl}} * \frac{10\ moles\ CO_2}{9\ moles_{CO_2 removed}} * \frac{1\ mole_{CO_2 removed}}{1\ L} \tag{13}$$

$$C_{MNPZ} = \frac{C_{NO_2^- Fl}}{k_2 \tau_{sump}} \tag{14}$$

For a sump running at 150 °C with a residence time of 8 minutes and 1 ppm NO_2 in the flue gas, the expected steady state MNPZ concentration will be 0.8 mM MNPZ. This concentration can be lowered by increasing the MNPZ decomposition rate constant, increasing the stripper sump volume, or decreasing the inlet nitrite concentration.

Furthermore, the mass balances can be iterated with the derivatives to give the response time to reach steady state. The total time is equal to the time spent in the sump plus any time spent outside the sump. Figure 7 shows the same sump conditions as above with a total residence time 5 times greater than the sump residence time. It takes five days to reach 90% of steady state under these conditions.

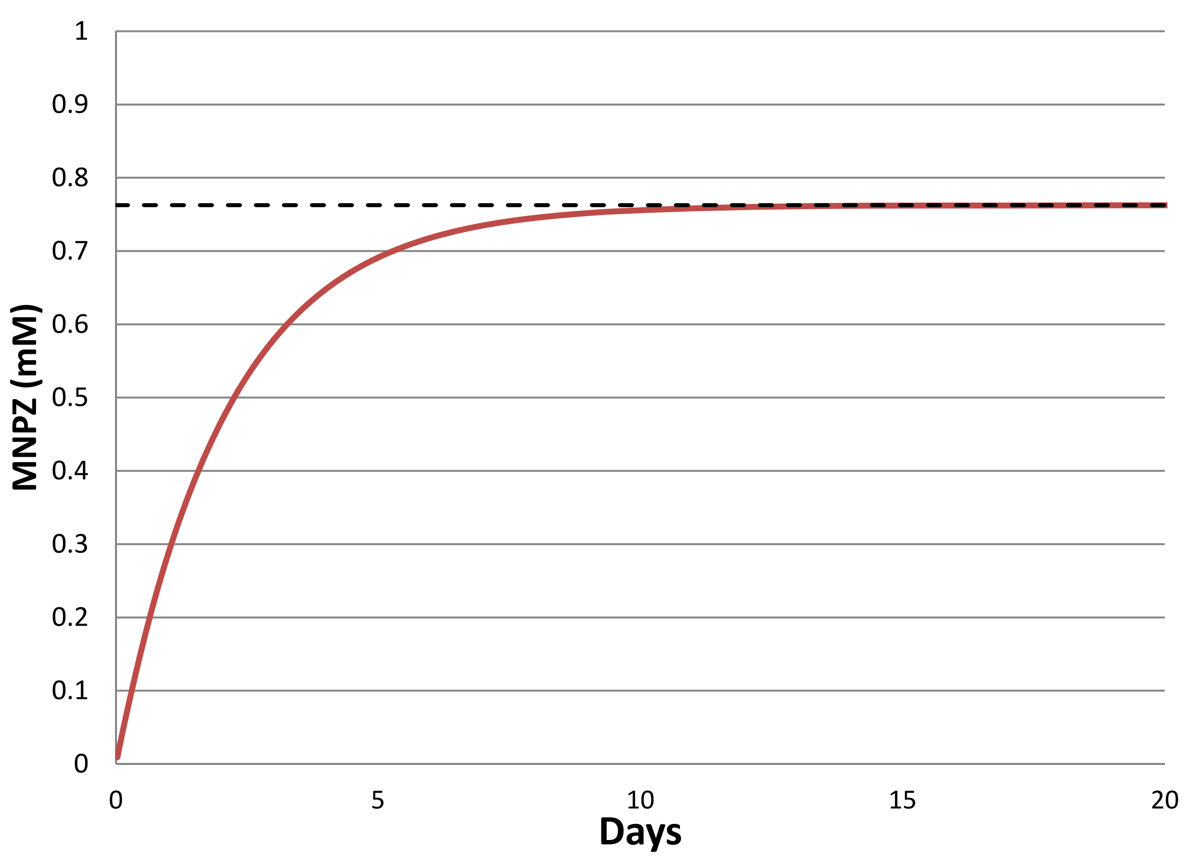

Figure 7: Response time to reach steady state

Conclusions

- MNPZ formation for 8 m PZ at 120 °C and a CO_2 loading of 0.3 is approximately $4*10^{-4}$ s^{-1}, formation at higher temperatures is too fast to analyze.
- MNPZ decomposition follows Arrhenius temperature dependence.

$$k_2(T) = 3.7 * 10^{-6} e^{\frac{92}{R}\left(\frac{1}{393}-\frac{1}{T}\right)}$$

- Both MNPZ formation and decomposition are irreversible reactions.
- Stainless steels do not significantly catalyze MNPZ decomposition.
- $PZCOO^-$ catalyzes MNPZ formation but not MNPZ decomposition.
- Neither MNPZ formation nor decomposition are first order functions of free PZ.

- MNPZ formation is not first order with respect to H^+PZ, but MNPZ is probably first order with respect to H^+PZ.
- The MNPZ steady state concentration is around 0.8 mM with a sump operating at 150 ^oC, a sump residence time of 8 minutes, and a flue gas NO_2 concentration of 1 ppm.
- It takes 5 days to reach 90% of steady state MNPZ concentration at 150 ^oC and a total residence time 5 times longer than the sump residence time.

Future Work

- Samples over a range of loading and PZ concentration will be analyzed to further refine the MNPZ kinetics model.
- Nitrosamine kinetics will be determined for other solvents and solvent blends.
- Nitrosamine kinetics will be determined for "real" solvent samples from pilot plants.
- Pilot plant modeling will be refined to take into account nitrite formation through PZ oxidation.
- The nonlinear regression model will be refined to give error and covariance of the parameters in the temperature dependent kinetics model.

References

Freeman SA. *Thermal degradation and oxidation of aqueous piperazine for carbon dioxide capture.* The University of Texas at Austin. Ph.D. Dissertation. 2011.

Garcia H, Keefer L, Lijinsky W, Wenyon CEM. "Carcinogenicity of nitrosothiomorpholine and 1-nitrosopiperazine in rats." *Cancer Res Clin Oncol.* 1970;74:179–184.

Rochelle GT, et al. "CO_2 Capture by Aqueous Absorption, Third Quarterly Progress Report2011." Luminant Carbon Management Program. The University of Texas at Austin. 2011.

Rochelle GT, et al. "CO_2 Capture by Aqueous Absorption, Second Quarterly Progress Report2010." Luminant Carbon Management Program. The University of Texas at Austin. 2010.

Appendix

Temperature Dependence

Temperature (°C)	120
PZ (m)	7.960
Nitrite (mmol/kg)	44.451
loading (mol CO_2/mol N)	0.300
Fe2+ (mM)	0.400
Cr3+ (mM)	0.100
Ni2+ (mM)	0.050

Time (Days)	MNPZ (mmol/kg)
0.00	0.00
0.06	38.60
0.06	37.28
0.13	41.63
0.13	41.13
0.19	38.38
0.19	39.61
0.26	40.25
0.26	40.94
0.31	39.34
0.31	41.11
1.00	32.03
1.00	32.31
1.11	29.97
1.11	29.72
1.28	28.07
2.00	22.64
2.00	23.68
2.15	19.75
2.15	22.40
2.30	20.14
2.71	19.49
3.00	18.25
3.73	14.23
4.00	11.76
8.25	2.77

Temperature (°C)	135
PZ (m)	8.0
Nitrite (mmol/kg)	49.2
Loading (molCO2/mol N)	0.296
Cr3+ (mM)	0
Ni2+(mM)	0
Fe 2+(mM)	0

Time (Days)	MNPZ (mMol/kg)
0	0
0.06	48.14
0.14	44.64
0.21	36.76
0.27	37.34 (Not regressed)
0.85	21.81
1.11	17.06
1.75	9.69
2.07	7.27
2.21	5.82
2.91	2.93

Temperature (°C)	150
PZ (m)	7.960
Nitrite (mmol/kg)	6.005
loading (mol CO_2/mol N)	0.300
Fe2+ (mM)	0.400
Cr3+ (mM)	0.100
Ni2+ (mM)	0.050

Time (Days)	MNPZ (mMol/kg)
0.00	0.00
0.06	4.80
0.10	4.56
0.16	4.05
0.24	3.56
0.36	3.05
0.60	1.34
0.97	0.59

Temperature (°C)	150
PZ (m)	7.960
Nitrite (mmol/kg)	36.390
loading (mol CO_2/mol N)	0.300

Fe2+ (mM)	0.400
Cr3+ (mM)	0.100
Ni2+ (mM)	0.050

Time (Days)	MNPZ (mmol/kg)
0.00	0.00
0.06	30.13
0.15	25.19
0.19	24.06
0.28	20.20
0.72	5.64
1.00	2.97
1.27	1.840
1.64	0.53
2.19	0.31

Sulfuric Acid

Temperature (°C)	135
PZ (m)	8.23
Nitrite (mmol/kg)	82.38
Acid (m)	2.47
Fe 2+(mM)	0.40
Cr 3+(mM)	0.10
Ni2+(mM)	0.05

Time (Days)	MNPZ (mMol/kg)
0	
0.06	24.73
0.14	35.92
0.20	51.05
0.26	52.25
0.79	38.27
1.05	28.46
1.69	11.01
2.01	9.43
2.20	7.21
3.03	3.37

Safe Operating Practices:
Handling Swagelok Cylinders for Thermal Degradation Experiments

by Omkar Namjoshi

Never work by yourself while preparing, tightening, or untightening cylinders. Always make sure someone else is in one of the labs.

Proper PPE must be worn while handling cylinders. This includes wearing a lab coat, safety glasses or goggles, and nitrile or latex gloves. Heat resistant leather gloves must be worn on top of the nitrile glove when placing cylinders in and out of the oven.

Cylinders must be capable of handling corrosive liquids at temperatures greater than 175 °C and pressures greater than 150 barg. The 10 ml Swagelok cylinders are all capable of handling this rating. Catastrophic failure can occur if the cylinder is not rated for this service.

1. Loading samples in the cylinder.
    a. Use a 10 ml pipette and place about 7 ml of solution in the cylinder (in standard 10 ml cylinders). If using a non-standard size, fill the cylinder to about 70% of volume.
    b. Load cylinders in a ventilated hood for particularly volatile, toxic, or foul-smelling solutions.
2. Torquing and tightening the cylinders.
    a. There is no set value that the cylinder needs to be torqued to – Swagelok (manufacturer of the cylinders) recommends that the cylinder be tightened between a quarter turn to half turn past hand tight. Some cylinders cannot be tightened by hand appreciably.
    b. Once the sample is loaded in the cylinder, tighten by hand as much as possible. Weigh the cylinder mass and record. Also make a note of any markings, etc., on the cap of the cylinder that was opened – this makes it easier to open the right side of the cylinder.
    c. Put the cylinder in the vise and clamp the vise on the nut of the cylinder as tightly as you can. Use the small ratchet and, without using too much force, tighten the cylinder as tightly as you can. The cap should thread into the nut quickly and smoothly, even for old cylinders. You will notice that there will be a point at which you have to use force to tighten the cylinder further – this is the Swagelok definition of “hand-tight.”
    d. To fully tighten and seal the cylinder, use the torque wrench, and set torque to a value of 60 ft-lb for cylinders with a ½” diameter cap nut. Torque the cylinder to this specification. Caution: tightening the cylinder beyond this value may lead to cylinder seal damage, which can lead to cylinder failure.
3. Placing the cylinder in the oven.
    a. Make sure that the ventilation is drawing air from the convection oven prior to placing cylinders inside.
    b. Open the oven. Slowly crack the open door away from the line of fire and check to see if any gases are escaping from the door. **Caution**: If there are any gases coming out, leave the door cracked slightly to allow the ventilation system to suck in the ambient air through the oven so any contaminants can be vented to the

   outside. Using a leather glove, place the cylinders on one of the oven racks. Close the oven door.
   c. Tape a list of all cylinders to the oven and clearly indicate what the solvent composition is. List any additives (metals, nitrite, etc.) in the solvent and if there is a potential for making toxic products, such as nitrosamines, clearly indicate on the list somewhere.
4. Removing cylinders.
   a. Using a leather glove, remove the cylinder and place it on the lab bench to cool. Record which cylinder is removed and weigh it. Use the same precautions as described in the above section when opening the oven door.
   b. Consider putting the cylinder in either a ventilated space or in the refrigerator (within a box).
5. Opening cylinders.
   a. **Caution:** Before opening the cylinder, ensure that the cylinder has cooled to room temperature (25 °C) or below. If the cylinder is not cooled, its contents will be under pressure, and could result in loss of containment.
   b. Slowly open the cylinder with a 15” wrench. Opening it slowly will relieve any residual pressure in the cylinder; opening it too quickly can also result in a containment loss.
   c. Once the cap becomes loose, use the ratchet to unscrew the cylinder.
   d. If the cap does not come off (still swaged inside), use the ratchet to pry the cap off. Sometimes the seals can become stuck. The cylinder will likely not be under much pressure at this time. Consider wearing a faceshield while performing this task.
   e. Put the cylinder contents in a vial and label it.
6. Cleaning cylinders.
   a. Ensure that the cylinder is completely free of any free liquid (i.e., has been drained).
   b. Rinse the cylinder with DI water.
   c. Place the rinsed (and open) cylinder in a Nalgene PP tub. Put a small quantity of hand soap in the tub and fill the tub with DI water prior to placing the cylinder in.
   d. Allow the cylinder to soak in the soap solution for several days. This removes any residual water-soluble contamination within the cylinder.
   e. After soaking, remove the cylinder and rinse with DI water a couple of times. Scrape the cylinder with a brush to remove any residue left inside and follow with at least three final DDI washes.
   f. Dry the cylinder in an oven that is designated for cleaning equipment. Set temperature to 60 °C and place the cylinders on the rack or in the Nalgene PP tub.
   g. Decant the liquid into the sink.